Dissertation
submitted to the
Combined Faculty of the Natural Sciences and for Mathematics
of Heidelberg University, Germany
for the degree of
Doctor of Natural Sciences

Put forward by

M.Sc. Daniel Roman Paul
born in Gießen

Oral examination: 21st July 2021

Electron recombination studies of rotationally cold CH^+ ions at the Cryogenic Storage Ring

Referees:

Prof. Dr. Andreas Wolf
Prof. Dr. André Schöning

Elektronenrekombinationsexperimente an rotationsgekühlten CH^+ Ionen im kryogenen Speicherring CSR

Die nachfolgende Arbeit befasst sich mit experimentellen Untersuchungen der Dissoziativen Rekombination (DR) an rotationsgekühlten CH^+ Ionen. Der experimentelle Teil wurde am Elektronenkühler des kryogenen Speicherrings CSR durchgeführt, innerhalb dessen Elektronen- mit Ionenstrahlen überlagert wurden. Als Vorbereitung wurden CH^+ Ionen bis zu 100 s im $T < 10$ K kalten Strahlungsfeld des CSR gespeichert, sodass lediglich die drei niedrigsten Rotationszustände besetzt waren. Deren relative Besetzungen und ihre zeitliche Entwicklung wurden darüber hinaus durch Photoionisation charakterisiert.
Mit den in dieser Arbeit entwickelten Methoden wird der Wirkungsquerschnitt für die DR-Reaktion im Bereich der Kollisionsenergien $0 - 1.3$ eV in Form eines Ratenkoeffizienten für überlagerte Strahlen vermessen und in einen Plasmaratenkoeffizienten umgerechnet. Letzterer kann für Modellierung chemischer Reaktionen in interstellaren Molekülwolken benutzt werden. Besonders relevant für diese Umgebung ist der reine $J = 0$ Plasmaratenkoeffizient, der mithilfe zeitabhängiger Messungen an dem fortwährend kühlenden Ionenensemble eingegrenzt wird.
Positions- und zeitaufgelöste Messungen der DR Fragmente ermöglichen die Charakterisierung der atomaren Kohlenstoff- und Wasserstoff-Produktzustände und die Bestimmung von Fragment-Winkelverteilungen. Entsprechende Experimente werden bei Kollisionsenergien von 0 meV, 8 meV, 70 meV und 320 meV durchgeführt. Die Ergebnisse geben Einblick in die Symmetrie von kurzlebigen, dissoziativen Zuständen des CH Moleküls, die an der DR Reaktion beteiligt sind.

Electron recombination studies of rotationally cold CH^+ ions at the Cryogenic Storage Ring

The present work is concerned with an experimental study of the Dissociative Recombination (DR) process for rotationally cold CH^+ ions. Experiments were conducted at the electron cooler of the Cryogenic Storage Ring (CSR) facility, a merged-electron-ion-beams setup. By storing CH^+ ions up to 100 s in the $T < 10$ K CSR environment, an ensemble of the lowest three rotational states was produced and time-dependent populations were additionally characterized via photodissociation.
With the methods developed in this work, the DR cross section is obtained in the collision energy range of $0 - 1.3$ eV as a merged-beams rate coefficient and converted into a plasma rate coefficient, which can be used for modeling the chemistry in interstellar clouds. A confinement for the pure $J = 0$ plasma rate is provided for this purpose, resulting from time-dependent measurements on the continually cooling rotational ensemble in CSR.
Imaging and arrival time detection of DR fragments are used for characterizing final atomic carbon and hydrogen states and angular fragment distributions. Here, collision energies of 0 meV, 8 meV, 70 meV and 320 meV are investigated. As a result, conclusions about the symmetry of intermediate dissociative states of the CH molecule, participating in the DR reaction, can be drawn.

Contents

List of Figures

List of Tables

Acronyms

COBRA Correlation of Spot Brightness and Pulse Amplitude

COMPACT Cold Movable Particle Counter

CSR Cryogenic Storage Ring

DE Dissociative Excitation

DR Dissociative Recombination

FWHM Full Width at Half Maximum

HTS High-Temperature Superconductor

ISM Interstellar Medium

KER Kinetic Energy Release

KIDA Kinetic Database for Astrochemistry

LLR Longitudinal-Longitudinal Relaxation

LTE Local Thermodynamic Equilibrium

MBRC Merged-Beams Rate Coefficient

MCMC Markov Chain Monte Carlo

MCP Microchannel Plate

MOCCA Molecular Camera

MPIK Max-Planck-Institut für Kernphysik

MQDT Multichannel Quantum Defect Theory

NICE Neutral Imaging in Cold Environment

NIST National Institute of Standards and Technology

OPO Optical Parametric Oscillator

PDR Photon Dominated Region

PEC Potential Energy Curve

PES Potential Energy Surface

PHD Pulse Height Distribution

RF Radio Frequency

TLR Transverse-Longitudinal Relaxation

TSR Test Storage Ring

UHV Ultra High Vacuum

UMIST University of Manchester Institute of Science and Technology

Chapter 1

Introduction

Understanding the formation and evolution of the Universe has been an ever persisting ambition of mankind. Today, the extreme environmental conditions still raise many questions that are pursued with great effort in physics, starting from the Big Bang and the unknown but most abundant part of matter - dark matter and dark energy - through the formation of stars and planets to the origin of life.

The Interstellar Medium (ISM) resembles a very dilute and cold environment in the Universe with densities of only hundreds to thousands of particles per cubic centimeter and temperatures of $30 - 100\,\mathrm{K}$ (Snow and McCall 2006). Despite the low probability of particle collisions in ISM diffuse clouds, the enormous time scales relevant for this environment allow a very efficient formation of molecules. To this date, over 200 distinct molecular species have been detected, including some building blocks of life like water and smaller carbohydrates (McGuire 2018). The rich chemistry responsible for molecular formation in diffuse clouds is mainly driven by ion-neutral reactions and electron collisions due to the absence of three-body collisions. In particular, the reaction of a positively charged molecular ion with a negative electron releases a significant amount of excess energy, leading to a dissociation of the molecule. This process, denoted as Dissociative Recombination (DR), terminates molecular formation chains and forms neutral molecules.

In contrast to conditions on Earth, molecules in diffuse clouds are not exposed to intense infrared radiation and can, thus, undergo radiative deexcitation towards their lowest vibrational and rotational states. As the surrounding material is mostly transparent for infrared light, molecules can radiatively release energy and effectively cool the cloud. This cooling process supports the gravitational collapse of dense clouds in the star formation process (Lepp, Stancil, and Dalgarno 2002).

The majority of detected molecules with more than four constituents contains carbon. In dense clouds, reactions of carbohydrates with molecular hydrogen can efficiently synthesize bigger molecules, even up to the largest detected fullerenes (C_{60}), as visual-

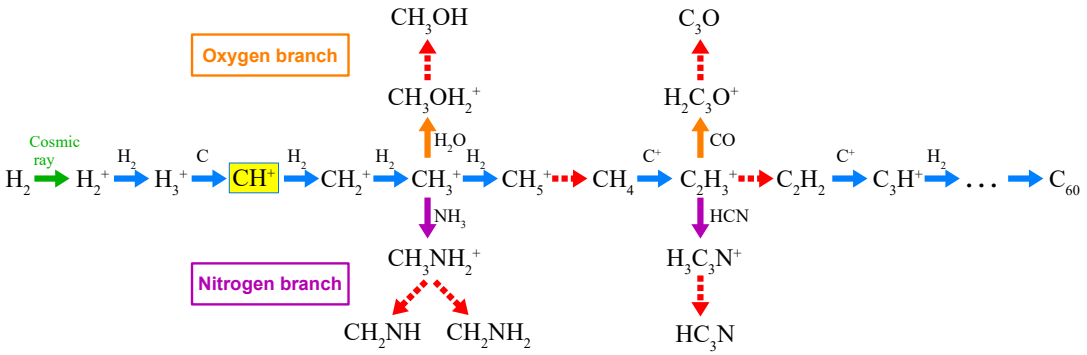

Figure 1.1: Carbon chemistry in dense molecular clouds. DR reactions are represented by the red, dashed arrows. The role of the CH^+ ion as starting point of the carbon chain is highlighted. The scheme is based on a summary of the $H_3{}^+$-induced chemical reactions in McCall 2001 and was simplified for presentation purposes.

ized in Figure 1.1. A key species for the carbon formation chain and, in fact, the first discovered molecular ion in the ISM is the methylidyne cation CH^+. It was initially detected by absorption line spectroscopy (Dunham 1937) and its spectroscopic fingerprint could later be assigned to CH^+ with help of a gas discharge experiment (Douglas and Herzberg 1941). Already in these times the CH^+ discovery demonstrated the possibilities of combining spectroscopic information from space and laboratory experiments in order to draw conclusions about the Universe.

Despite of its early detection, the abundance of CH^+ ions found in the ISM can still not be fully explained with today's knowledge. In diffuse clouds the by far most efficient known production mechanism is

$$C^+ + H_2 \longrightarrow CH^+ + H \tag{1.1}$$

and requires either a vibrationally excited hydrogen molecule or an energy input of $\Delta E \approx 4300\,\mathrm{K}$ (Gerlich, Disch, and Scherbarth 1987). Both requirements can barely be met in cold, diffuse clouds. Thus, numerous astrophysical models have been developed, promoting reaction 1.1 by mechanical heat input into the ISM. Among other processes, magneto-hydrodynamic shocks (Draine and Katz 1986) and turbulent dissipation (Myers, McKee, and Li 2015) are proposed to form local, high-temperature regions inside the diffuse cloud, which could explain the observed CH^+ abundances. However, neither the production nor destruction reaction rates for CH^+ are known precisely for ISM conditions due to the fact that experimental studies with slow and internally, especially rotationally, cold ions are technically very challenging. Those reaction rates are needed for judging about the validity and extent of heating processes in case of the CH^+ abundance modeling.

DR of CH^+ ions acts as one destruction process in the ISM. Theoretical calculations of its cross section (Chakrabarti et al. 2018, Mezei et al. 2019) are extremely difficult because of the variety of electronic, vibrational and rotational states involved in the reaction dynamics and the fact that two continua (the dissociative and electronic one) are

involved. A comprehensive experimental study of the process in the room-temperature Test Storage Ring (TSR) was conducted by Amitay et al. 1996. However, they could neither address low collision energies, owing to limited experimental energy resolution, nor the cross section of rotationally cold ions, which are both elementary for collisions in the ISM.

Cryogenic storage rings have been developed in the recent decades with the major advantage of performing clean collision experiments of vibrationally and, partly, also rotationally cold ions of many masses. The Cryogenic Storage Ring (CSR) is currently the only one capable of probing electron-ion collisions. Recent CSR studies on the DR of HeH^+ revealed remarkable dependencies of reaction rates on the ions' rotational state and allowed to provide state-specific rate coefficients for astrophysical application (Novotný et al. 2019).

In this work DR experiments with internally cold CH^+ ions were conducted at CSR, with the main goal of closing the gap between previously mentioned room-temperature results and the ISM-relevant low-temperature rates. Therefore, CH^+ ions were stored in a $T < 10\,\mathrm{K}$ environment until only their lowest three rotational states were populated. Simultaneous experimental probing of the time-dependent rotational state populations allows to infer possible differences between the state-specific reaction rates.

An overview of the DR process is given in chapter 2, together with latest theoretical results on the CH^+ rotational-state-dependent cross section and other theoretical and experimental results. In chapter 3 a description of the CSR facility, the neutral fragment detector and the electron cooler, the main technical project of this work, is provided. Merged electron-ion collision experiments at CSR necessitate the characterization of both beams, the data acquisition system and the neutral detector, which is described in chapter 4 in a general manner. As a major technical part of this work, a comprehensive evaluation of the electron collision energy distribution is presented, which can be used to compare theoretical cross sections to CSR rate coefficients and generate astrophysically-relevant plasma rate coefficients. Experimental details of specifically the CH^+ beamtime can be found in chapter 5, summarizing the storage and electron cooling of the CH^+ beam as well as results on its measured, electron enhanced rotational cooling in CSR. Additionally, a major part of analysis steps towards the results in following chapters is given.

The main experimental results on the DR rate coefficient of internally cold CH^+ ions are presented in chapter 6. Aside from the energy dependence study, it includes storage-time-dependent results for detection of possible rotational state effects. Finally, a temperature-dependent plasma rate coefficient is calculated and its implications for the CH^+ destruction in the diffuse ISM are discussed. Additional results for the DR dynamics can be extracted from a spatially- and time-resolved detection of the reaction products in chapter 7. Here a, compared to TSR results, improved 3D imaging technique is used to determine the energy release in the DR process as well as the angular fragmentation characteristics and the final state branching ratios. The results are suited to serve as additional information for theoretical description of the CH^+ DR. Ultimately,

chapter 8 concludes with a summary of the achieved results and an outlook towards further experimental and theoretical improvement possibilities.

Chapter 2

Dissociative recombination of CH^+

Astrophysical relevance of electron-ion collisions, especially of the Dissociative Recombination (DR) process, served as one motivation for experimental and theoretical studies on this topic. Even though DR has been a research topic for more than 70 years now, still not even a handful of molecular systems can be considered as fully understood to date. Over the whole time period, theoretical calculations of DR cross sections were followed with substantial effort and methods are still being improved nowadays. The major complication of current theory is to deal with the high amount of electronically, vibrationally and rotationally excited states, leading to a variety of interfering channels and resonances in the cross section. Still, for detailed astrochemistry calculations, theoretical studies bear the advantage of easily extractable state-resolved cross sections.

Only recently, such state-resolved DR cross sections could be measured at CSR for the HeH^+ ion (see chapter 1). The results were further used as a benchmark for comparing calculated cross sections obtained from a state-of-the-art Multichannel Quantum Defect Theory (MQDT) treatment with energy-dependent quantum defects (Čurík, Hvizdoš, and Greene 2020), showing a remarkable match between theory and experiment. Despite the fact that theoretical descriptions of the DR process are progressing promisingly for systems with a low number of electrons, experimental comparisons are still required at the current stage.

This chapter intends to give a general overview of electron collision processes with molecular cations and, in particular, the DR process (section 2.1). Here, the predominantly used MQDT approach for the calculation of DR cross sections is also presented. In section 2.2 recent calculations of Potential Energy Curves (PECs), inelastic collision and DR cross sections for the CH^+ ion will be shown. Section 2.3 summarizes other theoretical and experimental DR results and will be concluded in section 2.4 by formulating the most important open questions to be addressed later in this work.

2.1 Electron collisions with molecular cations

2.1.1 Molecular structure calculations

Description of molecular collision processes in general requires knowledge about the molecular structure. It can be fundamentally derived from the stationary Schrödinger equation (Haken and Wolf 1992)

$$H\Psi(\vec{R}_k, \vec{r}_i) = E\Psi(\vec{R}_k, \vec{r}_i) \tag{2.1}$$

$$H = -\sum_k \frac{\hbar^2}{2m_k}\Delta_k - \sum_i \frac{\hbar^2}{2m_\mathrm{e}}\Delta_i + \frac{e^2}{4\pi\varepsilon_0}\left(\sum_{k,l<k}\frac{Z_k Z_l}{\left|\vec{R}_k - \vec{R}_l\right|} + \sum_{i,j<i}\frac{1}{\left|\vec{r}_i - \vec{r}_j\right|} - \sum_{i,k}\frac{Z_k}{\left|\vec{r}_i - \vec{R}_k\right|}\right) \tag{2.2}$$

where $\vec{r}_i$ denote the electronic, $\vec{R}_k$ the nuclear coordinates, Z_k the nuclear charge states, m_k the nuclear masses, m_e the electron mass and Δ_k and Δ_i are the Laplace operators corresponding to $\vec{R}_k$ and $\vec{r}_i$, respectively. The Hamilton operator H includes the kinetic terms of all particles as well as their mutual Coulomb interactions as potential terms. Often, the fast movement of electrons is treated separately from the slow nuclear motion (*Born-Oppenheimer approximation*) and the total wavefunction is split into a nuclear and electronic part

$$\Psi(\vec{R}_k, \vec{r}_i) = \Psi_\mathrm{nu}(\vec{R}_k)\Psi_\mathrm{el}(\vec{R}_k, \vec{r}_i) \tag{2.3}$$

Consequently, the Schrödinger equation can be also split into a nuclear and electronic part, which are solved separately. The full solution, in form of the energy eigenvalues of the Hamilton operator, can be expressed approximately as

$$E(\vec{R}_k) = U_n(\vec{R}_k) + E_\mathrm{vib}(v) + E_\mathrm{rot}(J) \tag{2.4}$$

and includes the electronic, vibrational and rotational energy of the molecule, which depend on their respective quantum numbers (n, v and J). $U_n(\vec{R}_k)$ describes the electronic energy dependence on the nuclear coordinates and is often used to visualize molecular states as so-called *Potential Energy Surfaces*. In the special case of diatomic molecules, the multi-dimensional dependence of those surfaces reduces to a simple dependence $U_n(R)$, where R is the scalar internuclear distance. $U_n(R)$ is referred to as the Potential Energy Curve (PEC) and used for describing molecular state properties.

In general, molecular structure calculations underlie a high complexity, owing to mutual interactions between the electrons at non-spherical symmetry. Additionally, in some cases the *Born-Oppenheimer approximation* breaks down and nuclear motion has to be considered together with the electronic movement. Nowadays, only very few molecular systems can be calculated exactly. For all other systems, approximate theories are used, e. g., the *Hartree-Fock Self Consistent Field Method*, *Configuration Interaction* and *Density Functional Theory* (Haken and Wolf 1992), to name some of them.

2.1.2 Collision reactions

Due to the attractive Coulomb potential, collisions between electrons and molecular cations typically underlie a high cross section. In the diffuse ISM environment (see chapter 1) they are a main driver of ion chemistry, together with ion-neutral collisions.

Here, a diatomic molecular ion of structure $AB^+(n, v, J)$ in electronic state n, vibrational state v and rotational state J is considered, where A and B are neutral atoms. The most important reactions can be summarized as

$$AB^+(n,v,J) + e(\epsilon) \longrightarrow AB^{**} \longrightarrow AB^+(n,v,J) + e(\epsilon') \quad \text{(elastic collision)}$$
$$AB^+(n,v,J) + e(\epsilon) \longrightarrow AB^{**} \longrightarrow AB^+(n',v',J') + e(\epsilon') \quad \text{(inelastic collision)}$$
$$AB^+(n,v,J) + e(\epsilon) \longrightarrow AB^{**} \longrightarrow A(n') + B(n'') + E_{KER} \quad \text{(dissociative recombination)}$$
$$AB^+(n,v,J) + e(\epsilon) \longrightarrow AB^{**} \longrightarrow A(n') + B^+(n'') + e(\epsilon') \quad \text{(dissociative excitation)}$$

where ϵ is the kinetic energy of the incident electron, ϵ' of the scattered electron and n, v, J (n', v', J') the initial (final) electronic, vibrational and rotational state quantum numbers of the molecular ion. For atomic products n' and n'' denote electronic states. The concept of all these collisions can be generalized to polyatomic molecular ions. In that case, the dissociation fragments can be molecules or atoms.

A common feature of all those reactions is the formation of a highly excited compound molecule AB^{**} which decays on timescales of ps to fs (Davies et al. 2000). The reaction is either terminated by an autoionization process of the excited compound, resulting in the emission of the scattered electron (elastic or inelastic collision) or by dissociation of the molecule (Dissociative Recombination (DR) or Dissociative Excitation (DE)).

Elastic collisions do not change the internal state of the ion. Due to the high mass difference of the two collision partners, the ion momentum is barely influenced, while the electron trajectory can be redirected significantly. They are important as driver for electron cooling, as will be discussed in chapter 3.2.1.

In contrast to elastic collisions, the internal state of the ion is altered in inelastic collisions, leading to an excitation ($\epsilon' < \epsilon$) or deexcitation ($\epsilon' > \epsilon$) of the molecule. For astrophysical and other applications, these processes do not directly drive chemical reactions. However, in case other dominant reactions are internal-state dependent, or even selective, inelastic collisions may catalyze those by changing internal state populations of the molecule (Faure et al. 2017). As inelastic collisions for rotational states have to be considered for DR experiments presented in this work, chapter 2.2.2 will discuss recent calculations on this process for CH^+ ions.

A higher relevance for astrochemistry (see chapter 1) and also colder plasma regions of nuclear fusion reactors (Alman, Ruzic, and Brooks 2000) is given by dissociative reactions. Dissociative Recombination (DR) acts as the main dissociative process at low collision energies. Here, the excited molecular compound fragments into two neutral products, binding the primary electron during the process. Consequently, the excess energy release in this regularly exothermic reaction is distributed among the heavy

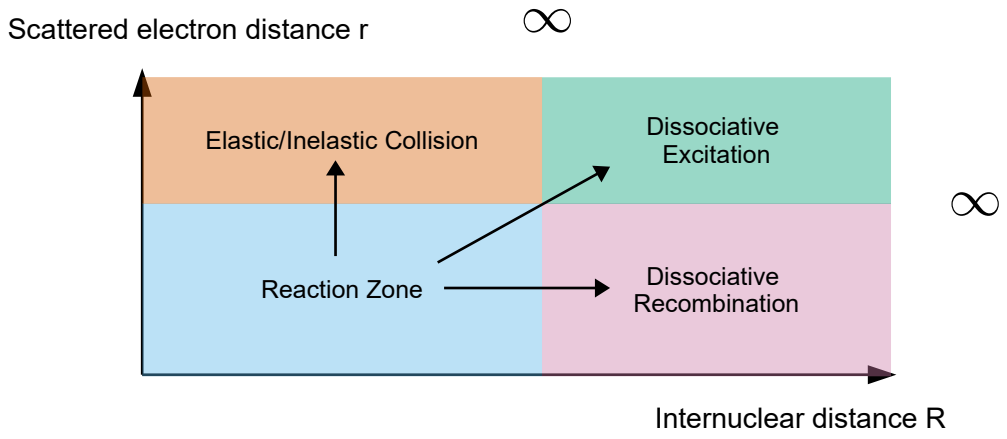

Figure 2.1: Collision space for electron collisions with molecular ions. The different reactions, discussed in the beginning of this section, are categorized by the internuclear distance and scattered electron distance. The scheme is based on Tennyson 2010.

fragments in form of kinetic energy and, therefore, denoted as Kinetic Energy Release (KER). More information about the DR terminology, dynamics and theoretical treatment will be provided in the next section.

Dissociative Excitation (DE) competes with DR as a molecular destruction reaction. In this process, the electron transfers energy into an electronically excited state of the molecule of dissociative nature, without being captured permanently. In the Franck-Condon region of the molecular ground state, such excited states are typically located several eV above the initial molecular state and result in a threshold character of the Dissociative Excitation (DE) process. Hence, DE does not occur in low-temperature environments like the ISM (see chapter 1), while its importance for fusion reactors becomes obvious.

For all applications underlying the above described collision processes, the calculation or measurement of their energy-dependent cross section $\sigma(\epsilon)$, which can depend on the initial molecular state, is of major interest. As an input for such calculations, detailed knowledge of the molecular structure (section 2.1.1) is necessary. Considering the previously mentioned reactions in the coordinate space of the internuclear distance R and radial distance of the primary electron r, all processes can be visualized in a common manner (see Figure 2.1). In all cases, the electron advances into the interaction zone. The interplay between the ion core and the scattered electron either results in autoionization ($r \to \infty$), in DR ($R \to \infty$) or DE ($r \to \infty$ and $R \to \infty$). This motivates the treatment of all three collision processes in a unified theory, as it is done in Multichannel Quantum Defect Theory (MQDT). A brief summary of this theory is presented, along with the calculation of DR cross sections, in the following section.

2.1.3 Dissociative recombination

One of the collision processes discussed in the previous section is Dissociative Recombination (DR). This process was first discussed in the literature by Bates 1950 as explanation for fast recombination in microwave plasma experiments. Decades later, first calculations on its cross section predicted a $\sigma(\epsilon) \sim 1/\epsilon$ dependence (Giusti-Suzor, Bardsley, and Derkits 1983), which mainly describes the *direct* DR process. When propagating this dependence to a rate coefficient ($\alpha \sim \langle\sigma\sqrt{\epsilon}\rangle$) an energy dependence of $\alpha \sim 1/\sqrt{\epsilon}$ ($\alpha \sim 1/\sqrt{T}$) is resulting from an energy (temperature) driven direct DR process. The more complex *indirect* process additionally causes resonances in the cross section spectrum and is therefore also called *resonant*. The considerations in this chapter are mainly following the review of Florescu-Mitchell and Mitchell 2006.

The nature of both DR mechanisms can be explained qualitatively on the base of PECs in Figure 2.2, starting from a bound electronic state of the molecular ion (AB^+ in blue) in its vibrational ground state. Typically, neutral (AB) PECs are calculated in the adiabatic picture, where the nuclear movement is assumed to be slow enough that the electrons can rapidly adjust to reach the potential minimum of the system (Born-Oppenheimer approximation). In this picture, molecular potential curves of similar symmetry cannot cross each other (*avoided crossing*). This approximation breaks down in case of DR, where the intermediate, highly excited compound core AB^{**} (see section 2.1.2) dissociates on a sub fs timescale. Thus, the PEC associated with AB^{**} crosses several adiabatic PECs of same symmetry. Such a *dissociative states* is of purely repulsive character and is displayed in orange. Due to the highly dynamic character of states in this *diabatic* picture, calculation of dissociative states is cumbersome. However, they are essentially needed for DR cross section calculations, as will be shown later in this section.

In the *direct* process (Figure 2.2 a)) the incident electron is immediately captured into the dissociative state AB^{**}, which fragments into the two neutral components. As no discrete energy levels are present in the dissociative state, no resonances are expected. Instead, for dissociative states located above the ionic ground state in the Franck-Condon region a threshold energy has to be overcome, which often lies beyond several eV. In most molecular systems, however, dissociative states below the ionic ground state are available and lead to a $\sigma(\epsilon) \sim 1/\epsilon$ dependence of the cross section, as discussed above.

In contrast to the *direct* process, the *indirect* one proceeds via an intermediate step. The primary electron is captured into a bound, neutral Rydberg state (AB^*). In Figure 2.2 b) this Rydberg state converges to the ionic ground state and is, thus, located slightly below. If the electron energy matches the difference between the vibrational ground state of the ion and a vibrationally excited Rydberg state, a resonant process is driven, leading to a characteristic feature in the energy spectrum. In case a dissociative state crosses the short-lived Rydberg state, a reconfiguration of electronic states (orange circle) can occur leading to the dissociation of the molecule via AB^{**}. Indirect

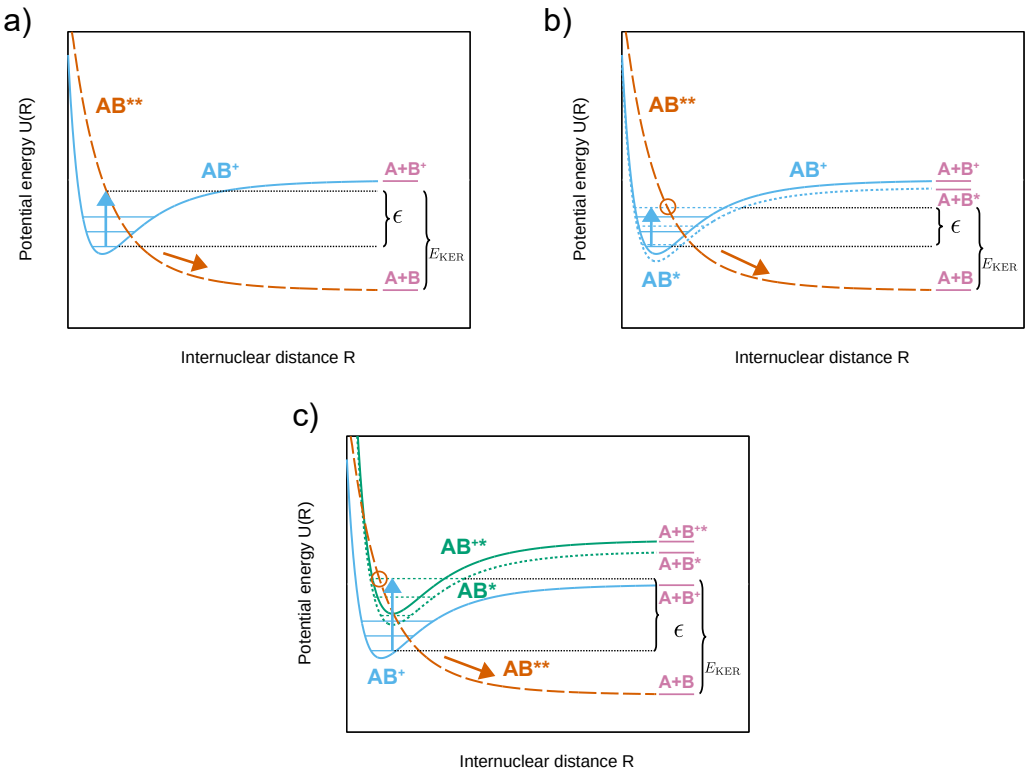

Figure 2.2: Schematic description of different DR mechanisms. a): *Direct* DR, b): *Indirect* DR via a ground state ion core, c): *Core-excited indirect* DR. Ionic states are indicated as solid lines, Rydberg states as short-dashed and dissociative states as long-dashed lines. Vibrational levels of bound states are displayed, as well as the electron collision energy ϵ and the Kinetic Energy Release E_{KER}.

DR processes via Rydberg states converging to the ionic ground state typically result in narrow resonances when new vibrational or rotational states become energetically accessible. Inaccessible channels are denoted as *closed*, while accessible channels are called *open*.

A mechanism of also indirect nature but with different effects for the DR cross section is the *core-excited indirect* process (Figure 2.2 c)). Here, the intermediate Rydberg state converges to an electronically excited ion core (AB^{+*}), which is crossed by the dissociative state. In contrast to the normal indirect process, the coupling between the ground state and the core-excited Rydberg state is of electronic character and results in typically broader resonances in the cross section spectrum (Carata et al. 2000).

In all cases, the excess energy of the DR reaction, which is split among the two fragments as Kinetic Energy Release (KER) (see section 2.1.2), is indicated in the subfigures. It reveals information about the ionic molecular PEC, as the energy conservation requires

$$E_0 + \epsilon = E(\mathrm{A} + \mathrm{B}) + E_{\mathrm{KER}} \tag{2.5}$$

where E_0 is the potential energy of the ionic vibrational ground state and $E(\mathrm{A}+\mathrm{B})$ the potential energy of the atomic final channel. Substituting the first by the usually better known atomic limit $E(\mathrm{A}+\mathrm{B}^+)$ and the dissociation energy $D_0 = E(\mathrm{A}+\mathrm{B}^+) - E_0$ one gets

$$D_0 = E(\mathrm{A}+\mathrm{B}^+) - E(\mathrm{A}+\mathrm{B}) + \epsilon - E_{\mathrm{KER}} \tag{2.6}$$

giving rise to the determination of the dissociation energy by measuring E_{KER} with the precise knowledge of the electron energy ϵ.

Cross section calculation

Multichannel Quantum Defect Theory (MQDT) resembles a widely used approach to calculate cross sections for the DR process and other collision processes (see section 2.1.2). The main ideas shall be outlined in this section and follow closely the review of Florescu-Mitchell and Mitchell 2006.

The major complication in DR calculations is the infinite number of Rydberg states (electronic quantum numbers $n \in \{1, ..., \infty\}$) that have to be taken into account in the indirect process. MQDT handles this issue by summarizing all Rydberg states in a single *channel* defined by the orbital angular momentum quantum number of the Rydberg electron (l) and the projection of the orbital angular momentum of all electrons onto the internuclear axis (Λ). The concept of working with initial and final *channels* instead of the contributing molecular states reduces the problem to a finite dimension.

Before MQDT can be applied, the PECs of the contributing states are required (see section 2.1.1). For the quantification of the Rydberg PECs, a dimensionless *quantum defect* $\mu_{l,\Lambda}(R)$ is introduced. The quantum defect describes the deviation of potential differences between Rydberg ($U_{n,l}(R)$) and ionic ($U_{\mathrm{ion}}(R)$) states from the simple Rydberg formula via

$$U_{n,l}(R) - U_{\mathrm{ion}}(R) = -\frac{1}{2(n-\mu_{l,\Lambda}(R))^2} \tag{2.7}$$

Conversely to atomic treatment, the quantum defect for molecules depends on the internuclear distance.

In analogy to Figure 2.1, the collision space is divided into three regions:

- region I: The *reaction zone* is characterized by small values for $r < r_0$ and $R < R_0$. Here, the scattered electron faces the same interactions as the other electrons and the molecule can be treated under the *Born-Oppenheimer approximation*.
- region II: The *intermediate zone* ($R < R_0$, $r_0 < r < r_{\mathrm{as}}$), where the scattered electron is still influenced by the combined interaction with the nuclei and other electrons. However, the electron is so far away that the angular velocity around the nucleus is comparable to the nuclear rotation. In that case, the *Born-Oppenheimer approximation* is no longer valid, as the electron is coupled to nuclear movement.

- region III: The *asymptotic zone* ($r > r_{\mathrm{as}}$) is defined such that only the long-range Coulomb interaction is affecting the scattered electron. The collisional final state is distinguished by either a finite value of R (autoionization channel) or $R \to \infty$ (dissociation channel).

Defining $\vec{q}$ as the coordinates of the bound electrons, the wave function in region I (Ψ^{I}) can be constructed from the three components:

- Ion-electron continuum states in vibrational state v_i and with scattered electron energy ϵ:

$$\Psi_{\mathrm{c},v_i\epsilon}(\vec{q},\vec{r},\vec{R}) = \psi_{v_i\epsilon}(\vec{q},\vec{r},\vec{R})\chi_{v_i}(\vec{R}) \tag{2.8}$$

- Rydberg states with quantum number n in vibrational state v_i:

$$\Psi_{\mathrm{r},nv_i}(\vec{q},\vec{r},\vec{R}) = \psi_n(\vec{q},\vec{r},\vec{R})\chi_{nv_i}(\vec{R}) \tag{2.9}$$

- Dissociative states d_j:

$$\Psi_{d_j}(\vec{q},\vec{r},\vec{R}) = \Phi_{d_j}(\vec{q},\vec{r},\vec{R})F_{d_j}(\vec{R}) \tag{2.10}$$

where each wave function is given by a product of a first (electronic) and second (nuclear) component. The total wave function can be expressed as an expansion of the latter three:

$$\Psi^{\mathrm{I}}(\vec{q},\vec{r},\vec{R}) = \sum_{i=1}^{N_v}\int_0^\infty c_{v_i}(\epsilon)\Psi_{\mathrm{c},v_i\epsilon}\,\mathrm{d}\epsilon + \sum_{n=1,i=1}^{\infty,N_v} c'_{nv_i}\Psi_{\mathrm{r},nv_i} + \sum_{j=1}^{N_d} c''_{d_j}\Psi_{d_j} \tag{2.11}$$

where the dependence $(\vec{q},\vec{r},\vec{R})$ of the wave functions was dropped for simplification. N_v and N_d denote the number of vibrational and dissociative states considered and their sum is limited to the total number of electrons in the MQDT method. The quantities $c_{v_i}(\epsilon)$, c'_{nv_i} and c''_{d_j} are the coefficients for the continuum, Rydberg and dissociative states, respectively.

The previously described wave function needs to satisfy the Schrödinger equation (equation 2.1), where the Hamiltonian representation is chosen such that radial coupling between dissociative and the other two states vanishes. Still, the ion-continuum and Rydberg functions stay eigenfunctions of the Hamiltonian, leading to the terminus of a *quasi-diabatic* representation. Here, three additional quantities are required as input for the MQDT calculations:

- Electronic couplings between continuum and dissociative states:

$$V_{ij}(\epsilon,R) = \langle\psi_{v_i\epsilon}|H_{\mathrm{el}}|\Phi_{d_j}\rangle \tag{2.12}$$

- Electronic couplings between Rydberg and dissociative states:

$$V_{nj}(\epsilon,R) = \langle\psi_n|H_{\mathrm{el}}|\Phi_{d_j}\rangle \tag{2.13}$$

- Radial coupling between Rydberg and continuum states:

$$V_{ni,j}(\epsilon, R) = \left\langle \Psi_{\mathrm{r},nv_i} \left| \frac{\partial}{\partial R} \right| \Psi_{\mathrm{c},v_i\epsilon} \right\rangle \tag{2.14}$$

While *direct* DR is driven by the first coupling element, the latter two are responsible for the *indirect* process.

Once all of the previously mentioned input parameters have been calculated by other methods (see section 2.1.1), the MQDT calculations can be applied. The collisional part of MQDT in the reaction zone I shows analogies to quantum mechanic two-body scattering theory (Sakurai 1994). Here, a solution of the stationary Schrödinger equation

$$(H_0 + \hat{V})\psi = E\psi \tag{2.15}$$

is desired for the two-body wave function ψ including the scattering potential matrix $\hat{V}$ as well as the Hamilton operator for the undisturbed system (no scattering)

$$H_0\phi = E\phi \tag{2.16}$$

The incoming ψ^- and outgoing ψ^+ wave functions are related to ϕ by the Lippmann-Schwinger equation (Lippmann and Schwinger 1950):

$$\psi^{+/-} = \phi + \frac{1}{E - H_0 \pm i\varepsilon}\hat{V}\psi^{+/-} \tag{2.17}$$

By defining the transition matrix $\hat{T}$ via

$$\hat{V}\psi^+ = \hat{T}\phi \tag{2.18}$$

and $\hat{G} = (E - H_0 \pm i\varepsilon)^{-1}$ as Greens operator of the Hamiltonian, the Lippmann-Schwinger equation transforms into a full matrix form (Sakurai 1994)

$$\hat{T} = \hat{V} + \hat{V}\hat{G}\hat{T} \tag{2.19}$$

It can be used to calculate the transition matrix $\hat{T}$ that relates the outgoing wave with the undisturbed system. A quantity of usually highest interest is the scattering matrix $\hat{S}$, which can be calculated from the transition matrix. It relates the outgoing to the incoming wave and is frequently used to calculate cross sections.

In MQDT calculations a key quantity for obtaining the full wave function in region I (Ψ^{I}) is the interaction matrix $\hat{K}$ of dimension $(N_v + N_d, N_v + N_d)$, which can be calculated from a Lippmann-Schwinger equation

$$\hat{K} = \hat{V} + \hat{V}\hat{G}\hat{K} \tag{2.20}$$

and, thus, can be seen as a transition matrix correlating the undisturbed solution to Ψ^{I}. While the matrix elements of $\hat{K}$ define the coefficients in equation 2.11, the potential

matrix $\hat{V}$ is built from the coupling elements (equations 2.12-2.14) and PECs. $\hat{G}$ is constructed as Greens operator, as described previously. Equation 2.20 is solved iteratively, starting from $\hat{K} = \hat{V}$ in the first order and inserting the calculated value into the right hand side of equation 2.20 in the following iteration. However, due to the demanding computational power, only first or second order calculations are predominantly achieved (Chakrabarti et al. 2018).

The wave functions in region II and III are calculated via *frame transformation* from the matrix elements of $\hat{K}$, the regular and irregular Coulomb functions (as solution to the point-like particle scattering problem in a central Coulomb field, Gaspard 2018) and the quantum defect $\mu_{l,\Lambda}(R)$ (see equation 2.7). From the wave function coefficients, one obtains a scattering matrix $\hat{X}$ of similar dimension as $\hat{K}$, which contains energetically *open* (o) and *closed* (c) channels and relates incoming to outgoing channels. Since only energetically open channels are accessible as final channels, it is transferred to a physical scattering matrix

$$\hat{S} = \hat{X}_{\mathrm{oo}} - \hat{X}_{\mathrm{oc}}(\hat{X}_{\mathrm{cc}} - \exp(-2i\pi\hat{\nu}_i))^{-1}\hat{X}_{\mathrm{co}} \tag{2.21}$$

where $\hat{\nu}_i$ is a diagonal matrix with elements $(E_{v^+} - E)^{-1/2}$ for all closed channels, E is the total and E_{v^+} the ionic vibrational state energy.

As previously mentioned, the physical scattering matrix $\hat{S}$ is of great importance, as all quantities describing the collision process can be derived from it. The most important information, the energy-dependent DR cross section for a single dissociation channel d_j, state symmetry *sym* (parity and spin), l and Λ can be extracted from (Florescu-Mitchell and Mitchell 2006 and Chakrabarti et al. 2018)

$$\sigma^{\mathrm{sym},l,\Lambda}_{j,v_0}(\epsilon) = \frac{\pi}{4\epsilon}\rho^{\mathrm{sym},\Lambda}\left|S^l_{d_j,v_0}\right|^2 \tag{2.22}$$

where $\rho^{\mathrm{sym},\Lambda}$ denotes the spin multiplicity ratio between neutral final and ionic initial state. The partial cross section is summed up over all channels and quantum numbers for obtaining the total cross section for the initial vibrational state v_0

$$\sigma_{\mathrm{tot},v_0}(\epsilon) = \frac{\pi}{4\epsilon}\sum_{\mathrm{sym},\Lambda}\rho^{\mathrm{sym},\Lambda}\sum_{j,l}\left|S^l_{d_j,v_0}\right|^2 \tag{2.23}$$

Hereby, the different l components of the scattering matrix, reflecting the scattered electron orbital angular momentum, are referred to as *partial waves*. If a DR cross section is dominated by a single partial wave, the atomic fragments underlie a characteristic angular distribution with respect to the internuclear axis, as will be discussed below.

The here presented sketch of the MQDT method is far from being comprehensive. Further information on this topic can be found in Florescu-Mitchell and Mitchell 2006, where also rotational degrees of freedom are discussed. Furthermore, the basics of MQDT have been extended by different theory groups. One example can be found in the *frame transformation* between region II and III, where an energy-dependent treatment of the quantum defect $(\mu_{l,\Lambda}(R,\epsilon'))$ and the Coulomb functions was developed in Gao and Greene 1990 and extended in Hvizdoš, Greene, and Čurík 2020. With a suitable

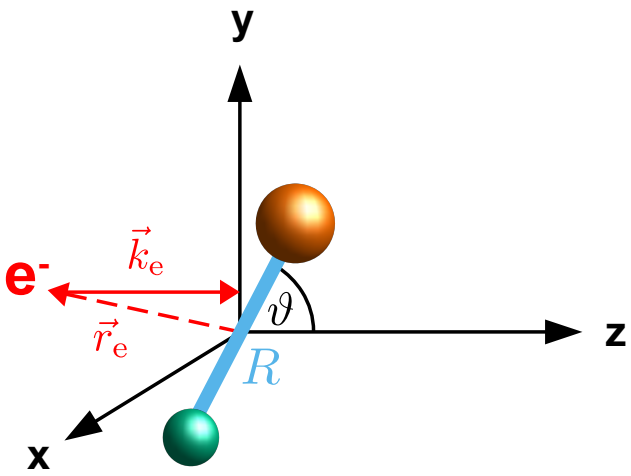

Figure 2.3: Coordinate system for description of the DR process. The origin is defined as the molecule's center of mass, while the z-axis is aligned along the electron beam trajectory. The choice of coordinate system follows Guberman 2004.

choice of continuum PECs, the incorporation of dependencies on the asymptotic kinetic energy of the scattered electron in the body frame is feasible in the calculation. As discussed in the beginning of this chapter, the extended MQDT with energy-dependent quantum defects showed a remarkable match to experimental data for the HeH^+ system. However, the choice of suitable theory always has to be adapted to the studied molecular system. In this respect, MQDT, among other methods, is a still evolving approach for calculating DR cross sections.

Angular fragment distribution

Complementary to the above discussed cross section, experimental DR studies allow to infer the angular characteristics of the fragmentation process. Theoretical treatment of angular fragmentation probabilities was initiated for *dissociative attachment* by Dunn 1962 and later on extended by a calculation framework of O'Malley and Taylor 1968. As the nature of *dissociative attachment* is similar to the cationic DR process, their results can be also applied to DR, which was several decades later explicitly shown by Guberman 2004.

Figure 2.3 presents the choice of coordinate system for the collision of an electron (wave vector $\vec{k}_e$) with a molecular, diatomic target. Here, the collision is mainly characterized by the orientation of the molecular axis with respect to $\vec{k}_e$, which is given in spherical coordinates by the polar (ϑ) and azimuthal (φ) angles. Assuming that the scattering electron is initially represented by a plane wave perpendicular to the z-axis, the collision is symmetric in φ and angular distributions are independent of that angle, which also follows from the calculations in Guberman 2004. In this work ϑ is defined as the polar angle with respect to the heavy fragment, such that $0 < \vartheta < \frac{\pi}{2}$ if the heavy

fragment is located at positive values ($z_h > 0$) and $\frac{\pi}{2} < \vartheta < \pi$ for $z_h < 0$.

A common assumption used in the previously mentioned calculations is the *axial recoil approximation* (Zare 1967). For most molecular ions, the dissociation proceeds on faster time scales than the molecule's rotational period. Guberman 2004 associates the dissociation time scales to a vibrational period, which is typically more than 100 times faster than a single rotation. Thus, during the dissociation process the molecule does not rotate and the trajectories of the neutral fragments directly reflect the orientation of the internuclear axis. A slightly different formulation of the *axial recoil approximation* condition is given by the comparison of the Kinetic Energy Release (KER) (E_{KER}, see Figure 2.2) to the rotational energy E_{rot}. If $E_{\mathrm{KER}} \gg E_{\mathrm{rot}}$, the approximation is valid. However, for low KERs in the meV regime the validity breaks down. It should be emphasized that the validity of the axial recoil approximation is a necessary criterion for inferring the angular dependence of the DR cross section from the angle of incident electrons with respect to the molecular axis (ϑ in Figure 2.3).

By describing the incident electron as an expansion of Coulomb waves and propagating its wave function through the coupling elements (equations 2.12-2.14) into the DR cross section, Guberman 2004 shows that the angular fragmentation probability is given by scaled Legendre-polynomials $A_{l,m}P_{2l}(\cos\vartheta)$. Those polynomials can be attributed to single partial waves (l, m), corresponding to the primary electron orbital angular momentum l and its projection along the internuclear axis m. While l defines the order of the Legendre-polynomial, both quantities influence the magnitude of the scaling factor $A_{l,m}$. For all combinations with $l \leq 3$ Guberman 2004 gives the angular distribution and the dissociative state symmetry for a given ionic state, which is defined by the partial wave. As the results will be used for interpretation in chapter 7, they are summarized in Table 2.1.

In case the DR process is not driven by a single partial wave, an appropriate description of angular fragmentation probability is given by (O'Malley and Taylor 1968)

$$W(\vartheta) = \sum_{l=0}^{\infty} a_{2l} P_{2l}(\cos\vartheta) \tag{2.24}$$

representing a weighted sum of all partial waves. Hereby, the dominant contribution is given by $l = 0$ and $l = 1$. To the author's best knowledge no experiment yet could prove a significant contribution of higher orders. It is noteworthy that only even indices of the Legendre polynomials are resulting from the calculations, indicating a symmetry of ϑ (electron approaches light atom first) and $\pi - \vartheta$ (electron approaches heavy atom first) for DR.

Further considerations for angular and fragment distance distributions in collision experiments, working with an ensemble of electrons and molecules, will be given in chapter 4.4.2 and used for interpretation of dominant partial waves and state symmetries in chapter 7.

Table 2.1: DR angular fragmentation probabilities and dissociative state symmetries for different partial waves. The here presented information for heteronuclear, diatomic molecules is extracted from Table I and III of Guberman 2004 and was truncated to the relevant ($l \leq 2$) partial waves for this work.

Electron partial wave	l	m	Angular distribution	Ionic state	
				Σ^+	Π
				Neutral dissociative state	
$s\sigma$	0	0	1	Σ^+	Π
$p\sigma$	1	0	$3\cos^2\vartheta$	Σ^+	Π
$p\pi$	1	1	$\frac{3}{2}\sin^2\vartheta$	Π	Σ^+ Σ^- Δ
$d\sigma$	2	0	$\frac{5}{4}(3\cos^2\vartheta - 1)^2$	Σ^+	Π
$d\pi$	2	1	$\frac{15}{2}\sin^2\vartheta\cos^2\vartheta$	Π	Σ^+ Σ^- Δ
$d\delta$	2	2	$\frac{15}{8}\sin^4\vartheta$	Δ	Π Φ

2.2 Indication of recent CH^+ theory

Astrophysical relevance of the CH^+ ion (see chapter 1) triggered many theory groups for developing and improving models for the molecular structure and collision cross sections. Moreover, its closed shell electron configuration in the ground state bears advantages for theoretical treatment. In this section recent calculations of the CH^+ and CH PECs as well as of inelastic and DR cross sections are presented.

2.2.1 Potential energy curves

A complementary calculation of CH^+ and CH PECs has been performed in Chakrabarti et al. 2017 and Chakrabarti, Ghosh, and Choudhury 2019. The CH^+ PECs were obtained by *Configuration Interaction* calculations with *Slater Type Orbitals* taken from other literature. Consequently, the authors computed CH PECs with the help of the *R-Matrix* method. For the interpretation of experimental results in the course of this work, the combined data for both systems seem very appropriate as the DR process relies on both data sets, underlying the same energy scale. For such a comparison, the authors provided the numerical data of both publications.

In this section molecular states are designated with $^{2S+1}\Lambda^{+/-}$ with the quantum numbers S (total spin), Λ (projection of the orbital angular momentum onto the internuclear axis) and where $+/-$ describes the reflection symmetry. Atomic states are labeled with $^{2S+1}L^{(o)}$ with total spin S, orbital angular momentum L and the optional o standing for odd parity, which is dropped in case of even parity. Before presenting the PECs, a few minor modifications and extensions have been applied to the data that

shall be summarized in the following points:

- The energy $E_{0,\min}$ was extracted from the minimum of the ionic ground state PEC. All PECs were shifted such that $E_{0,\min} = 0$.
- The energy axis was changed from Hartree units to eV.
- Atomic dissociation limits of CH were added to the graphs. Hereby, the energy of the dissociation limit $C(^3P) + H(1\,s)$ of the CH ground state (Amitay et al. 1996), was determined via the dissociation energy $D_e = 3.291\,eV$ (Chakrabarti, Ghosh, and Choudhury 2019). Further dissociation limits were calculated from the carbon atomic level energies[1] in the National Institute of Standards and Technology (NIST) database with respect to the previously mentioned channel.
- Ionic dissociation limits of CH^+ were added to the graphs. The level of the limits $C(^3P) + H^+$ and $C^+(^2P) + H(1\,s)$ were calculated with respect to the neutral $C(^3P) + H(1\,s)$ level from the ionization energies of hydrogen[2] and carbon[3]. From those two states the energy levels of higher excited ones were calculated with the carbon atomic level energies[1], ionic level energies[4] and hydrogen atomic level energies[5] from the NIST database.

Following the above described procedure, adiabatic PECs of the CH^+ ion were plotted and the result is shown in appendix Figure A.1, split into subfigures for the two spin states. The neutral PECs for the CH molecule are presented in appendix Figures A.2-A.5. Here, each subfigure is dedicated to a combined state symmetry $^{2S+1}\Lambda^{+/-}$ and, additionally, includes the lowest six CH^+ PECs. Chakrabarti, Ghosh, and Choudhury 2019 do not only provide adiabatic but also diabatic states, which are distinguished by their line style in the figures. Due to the high complexity of diabatic calculations, only four diabatic CH states are known to this point. They are labeled by $^{2S+1}\Lambda^{+/-\prime}$.

Since the purpose of chapter 7 is to study DR predominantly in the sub-eV range, not all of the previously mentioned states have to be considered. In this domain only the lowest four atomic final channels are accessible, from which previous DR experiments indicated that the $C(^1D) + H(1\,s)$ and $C(^1S) + H(1\,s)$ channels are of special importance (see section 2.3). Therefore, the collection of neutral PECs was condensed to a selection dissociating into these two limits. The resulting curves are presented in Figure 2.4.

[1] https://physics.nist.gov/cgi-bin/ASD/energy1.pl?conf_out=1&term_out=1&level_out=1&j_out=1&lande_out=1&perc_out=1&biblio=1&spectrum=C%20I (24.02.2021)
[2] https://physics.nist.gov/cgi-bin/ASD/ie.pl?spectra=H&units=1&at_num_out=on&el_name_out=on&seq_out=on&shells_out=on&level_out=on&e_out=0&unc_out=on&biblio=on (24.02.2021)
[3] https://physics.nist.gov/cgi-bin/ASD/ie.pl?spectra=C&units=1&at_num_out=on&el_name_out=on&seq_out=on&shells_out=on&level_out=on&e_out=0&unc_out=on&biblio=on (24.02.2021)
[4] https://physics.nist.gov/cgi-bin/ASD/energy1.pl?conf_out=1&term_out=1&level_out=1&j_out=1&lande_out=1&perc_out=1&biblio=1&spectrum=C%20II (24.02.2021)
[5] https://physics.nist.gov/cgi-bin/ASD/energy1.pl?conf_out=1&term_out=1&level_out=1&j_out=1&lande_out=1&perc_out=1&biblio=1&spectrum=H%20I (24.02.2021)

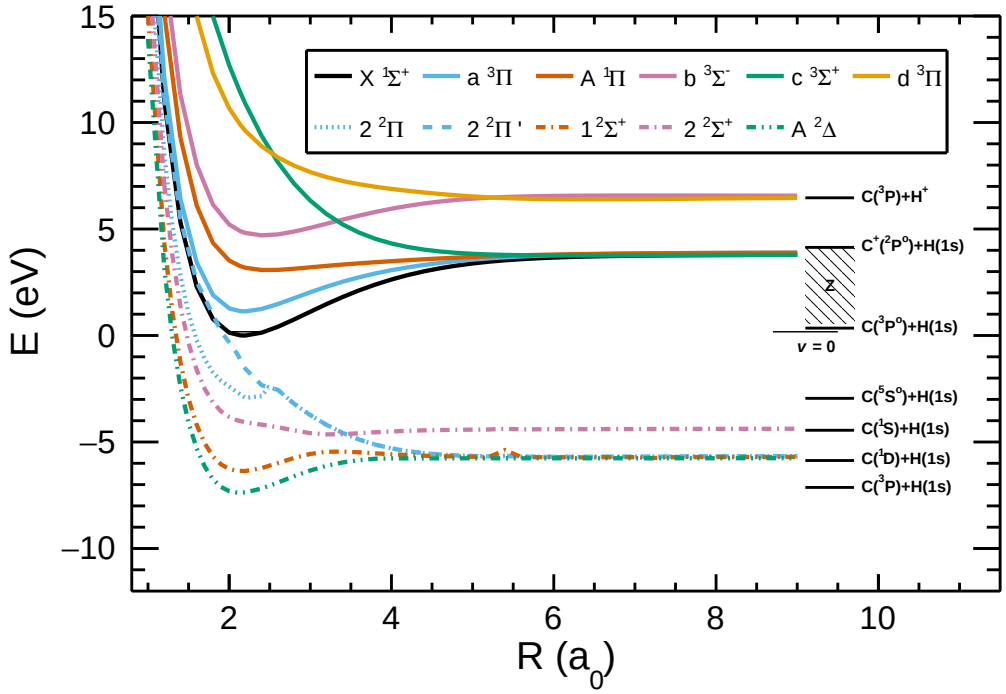

Figure 2.4: Selected Potential Energy Curves (PECs) of the CH^+ and CH molecule, dissociating into the $C(^1D) + H(1s)$ and $C(^1S) + H(1s)$ limit. Ionic curves are drawn as solid curves, where the $v = 0$ level of the electronic ground state is indicated on the right. The symmetry of adiabatic neutral PECs can be distinguished by their line style, where Π: dotted line, Σ^+: dashed-dotted lines, Δ: dashed-double-dotted line. The diabatic $2\,^2\Pi'$ state is drawn as dashed curve. Atomic dissociation limits were added as black lines on the right. Here, the region 'Z' contains a variety of channels corresponding to the $C(n) + H(1s)$ Rydberg series.

The electronic ground state configuration of the CH^+ ion is given by $1\sigma^2 2\sigma^2 3\sigma^2 (X^1\Sigma^+)$ and corresponds to a closed σ shell. Further properties of this state are listed in Table 2.2. They were extracted from spectroscopic measurements of Hakalla et al. 2006 and Doménech et al. 2018. Here, B_0 and D_0 denote the rotational and centrifugal distortion constant in the vibrational ground state, where rotational levels are approximately given by

$$F_v(J) = B_v J(J+1) - D_v[J(J+1)]^2 \tag{2.25}$$

Rotational constants for the other vibrational states can be calculated from

$$B_v = B_e - \alpha(v + 0.5) \tag{2.26}$$

Furthermore, r_e stands for the equilibrium radius. A summary of the first five rotational energies, calculated from the above described parameters, can be found in Table 2.3.

In the lowest excited states a 3σ electron from the $X^1\Sigma^+$ state is lifted into a higher shell. As the next higher shell is given by 1π, the first two excited states are of Π character. While most of the higher lying states are decaying fast, the first excited $a^3\Pi$ state is

Table 2.2: Molecular structure parameters for the CH^+ ground state ($X^1\Sigma^+$). The values are extracted from Hakalla et al. 2006 and Doménech et al. 2018 (superscript (a)). r_e was transferred into units of Bohr radii.

B_0 (cm^{-1}) [a]	$10^3 \times D_0$ (cm^{-1}) [a]	ω_e (cm^{-1})	B_e (cm^{-1})	α (cm^{-1})	r_e (a_0)
13.931 357 64(13)	1.382 657(67)	2857.560(22)	14.177 461(75)	0.9162(18)	2.137 061 6(57)

Table 2.3: Rotational state energies of the $X^1\Sigma^+(v = 0)$ state. The values are calculated from B_0 and D_0 in Table 2.2 with help of equation 2.25.

Rotational state	Rotational energy (meV)	Rotational energy/k_B (K)
$J = 0$	0	0
$J = 1$	3.454	40.1
$J = 2$	10.357	120.2
$J = 3$	20.703	240.2
$J = 4$	34.477	400.1

of metastable character and further discussed below. Even though other excited states are not participating as initial states for DR in this work, their corresponding Rydberg series can contribute in the intermediate step of the *core-excited indirect* process (see section 2.1.3).

Out of the variety of neutral PECs (see appendix A.2) only four adiabatic curves are coupled to the most important $C(^1D) + H(1\,s)$ and $C(^1S) + H(1\,s)$ dissociation limits. They are dedicated to three different symmetries, which can only interact with each other through rotational coupling. The two Σ^+ states, however, indicate an avoided crossing around $R = 3.2\,a_0$, which can play a role in the dissociation process. It should be emphasized that the $2\ ^2\Sigma^+$ state is the only one coupled to the $C(^1S) + H(1\,s)$ dissociation limit.

A fast dissociation processes is better described in the diabatic picture. In this case, only one diabatic state, dissociating into the lowest four energy levels, is known. It is of $^2\Pi$ symmetry and connects the adiabatic $2\ ^2\Pi$ state with the ionic ground state. The latter is crossed near its vibrational ground state, resulting in a considerable Franck-Condon overlap of the two states. At $R = 3.5\,a_0$ the diabatic state crosses the $2\ ^2\Sigma^+$ state, leading to a possible rotational coupling. Consequences for the DR process will be discussed in section 2.2.3 and 2.3.

Metastable $a^3\Pi$ state

As mentioned before, the first electronically excited $a^3\Pi$ state of the CH^+ ion is of metastable character. Its excitation energy of $T_e = 1.1816(62)\,\text{eV}$ was determined by spectroscopy in the TSR storage ring (Hechtfischer et al. 2007). Moreover, in a DR experiment at TSR (Amitay et al. 1996) its lifetime τ_m could be measured by separating its characteristic KER values from the ones of the ground state and by comparing the storage time decay of both DR signals. Their experiment resulted in

$$\begin{aligned} \tau_m &= 7.0(10)\,\text{s} \\ P_m(t=0) &= 65(5)\,\% \\ \frac{\sigma_0}{\sigma_m} &= 0.43(15) \end{aligned} \tag{2.27}$$

where $P_m(t = 0)$ the initial relative population of metastable state ions in their CH^+ beam and $\frac{\sigma_0}{\sigma_m}$ the DR cross section ratio between ground state and metastable state at their lowest reachable collision energies. Further information about the metastable DR process will be provided in section 2.3.

The long lifetime of the $a^3\Pi$ state can be explained by the fact that a dipole transition to the $X^1\Sigma^+$ ground state is forbidden due to the different spin quantum numbers of the two states. Hechtfischer et al. 2007 conducted theoretical studies on the metastable decay, with the result that the main deexcitation process proceeds via configuration mixing with the $A^1\Pi$ state (compare Figure 2.4), which allows for a dipole transition to the ground state. Their studies reveal that this configuration mixing depends on the metastable vibrational state, rotational state and parity. Thus, the before discussed lifetime of $\tau_m \approx 7\,\text{s}$ is actually an average of all contributing substates.

An interesting result of Hechtfischer et al. 2007 is that the rovibrational ground state with f parity ($a^3\Pi(v = 0, J = 0, f)$) does not allow for configuration mixing. Consequently, the fastest possible transition to the ground state is of magnetic dipole character and, thus, this particular substate is expected to show a significantly higher lifetime than τ_m. A rovibrational cooling simulation of Hechtfischer et al. 2007 furthermore estimates a fraction of 1% of the initial metastable ions to end up in this *dark state*. However, no experimental evidences for the existence of the dark state have been found, yet.

2.2.2 Rotational cooling by radiation and by inelastic collisions

In a cold blackbody radiation environment, excited states of a molecule decay by *radiative cooling* through dipole interactions on a time scale defined by the surrounding temperature T, the dipole moment d_0 and the transition frequency ω as shown in Hilborn 1982:

$$A = \frac{2\omega^3 d_0^2}{3\varepsilon_0 hc^3} \tag{2.28}$$

The latter quantity is called the Einstein coefficient for spontaneous emission. For rotational transitions ($J \to J-1$) a correction for the dipole moment and the degeneracy

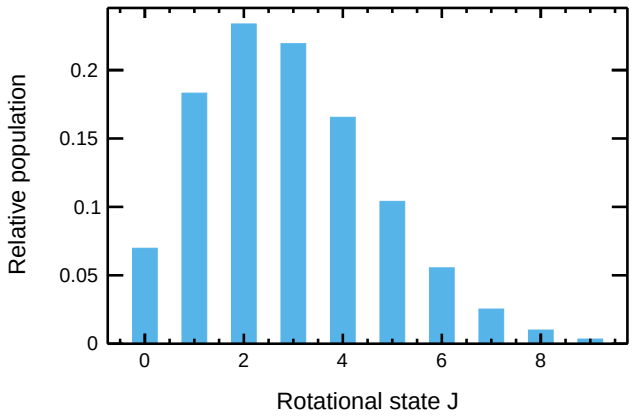

Figure 2.5: 300 K Boltzmann distribution of CH^+ rotational states.

of rotational states has to be included, as shown in Meyer 2018, such that

$$A_{J,J-1} = \frac{16\pi^3\nu^3 d_0^2}{3\varepsilon_0 hc^3}\frac{J}{2J+1} \tag{2.29}$$

The linear frequency ν can be approximated by the rotational spacing $\nu = 2cB_0J$ with the rotational constant B_0, leading to

$$A_{J,J-1} = \frac{128\pi^3 B_0^3 d_0^2}{3\varepsilon_0 h}\frac{J^4}{2J+1} \tag{2.30}$$

For CH^+ the characteristic decay times $\frac{1}{A_{J,J-1}}$ for the lowest states can be derived with help of the rotational constant listed in Table 2.2 and from the dipole moment $d_0 = 0.3505\,\text{eÅ}$ measured in Penning trap mass spectrometry by Cheng et al. 2007 to

$$\begin{aligned}\frac{1}{A_{1,0}} &= 156\,\text{s}\\ \frac{1}{A_{2,1}} &= 16\,\text{s}\\ \frac{1}{A_{3,2}} &= 4\,\text{s}\end{aligned} \tag{2.31}$$

On these time scales an ensemble of ions will approach the environmental temperature T, resulting in an equilibrium described by a Boltzmann distribution. Such a distribution for CH^+ ions is presented in Figure 2.5 for a room-temperature ($T = 300\,\text{K}$) environment. Plenty of rotational states are populated under these conditions, with the distribution maximum around $J = 2$ and $J = 3$. From the figure it becomes evident that an ion ensemble occupying purely the lowest rotational states can only be reached in a cryogenic environment.

In contrast to exclusive interaction with the radiation field, as described above, frequent inelastic collisions (see section 2.1.2) can change the rotational state population of an ion ensemble. Thus, when hunting for internal-state-dependent effects, an estimate of inelastic collision cross sections is necessary.

For the CH^+ ion Hamilton, Faure, and Tennyson 2015 conducted *R-Matrix* calculations and obtained an electron energy dependent cross section $\sigma_{J\to J'}(\epsilon)$ $(J' > J)$ of the excitation process, which has been provided by the authors. It should be noted that the calculations for $\Delta J = 1$ $(\Delta J > 1)$ were only carried out down to $\epsilon = 10\,\text{meV}$ $(\epsilon = 30\,\text{meV})$ and extrapolated by the authors to the respective excitation threshold by a $\sigma(\epsilon) \sim 1/\epsilon$ dependence, as predicted by the Wigner law (Faure et al. 2006). Cross sections for the de-excitation process $(\sigma_{J'\to J})$ can be linked to the excitation ones by the principle of detailed balance (Faure et al. 2006)

$$\sigma_{J'\to J}(\epsilon) = \frac{g_J}{g_{J'}} \frac{\epsilon + (E_{J'} - E_J)}{\epsilon} \sigma_{J\to J'}(\epsilon + (E_{J'} - E_J)) \tag{2.32}$$

where $g_{J'} = 2J' + 1$, $g_J = 2J + 1$ are the statistical weights of the two states and $E_{J'}$, E_J their rotational energies (see Table 2.3).

Figure 2.6 shows the electron impact excitation and deexcitation cross section for selected transitions in two different energy ranges. Subfigure a) summarizes the whole energy range up to 0.8 eV. The overall shape of the cross section is less steep than a $\sigma(\epsilon) \sim 1/\epsilon$ dependence. On top of that, resonances are appearing at 0.15 eV, 0.4 eV, 0.64 eV and 0.74 eV, which are slightly shifted between the individual transitions. Subfigure b) provides a closer look into the energy region $0 - 0.03\,\text{eV}$, where all cross sections are almost identical to a $\sigma(\epsilon) \sim 1/\epsilon$ dependence, also for the values in the non-extrapolated region (see above). The individual excitation thresholds are clearly visible in subfigure b).

As the deexcitation cross section is calculated from equation 2.32, it can be approximated by

$$\sigma_{J'\to J}(\epsilon) = \frac{g_J}{g_{J'}} \sigma_{J\to J'}(\epsilon) \tag{2.33}$$

only in the two special cases of either $\sigma_{J\to J'}(\epsilon) \sim 1/\epsilon$ or for $\epsilon \gg E_{J'} - E_J$. While the first condition is fulfilled in the resonance-free low energy region, the second holds for energies beyond 0.1 eV for the lower J states. Thus, the excitation and deexcitation cross sections are fairly proportional with a constant resulting solely from the statistical weights $\frac{g_J}{g_{J'}}$.

Over the whole energy range, transitions with $\Delta J = 1$ dominate the excitation and deexcitation cross sections. They outrange the next lower $\Delta J = 2$ cross section by factors of two and five, respectively. This behavior is expected for molecules with a strong dipole moment (Faure et al. 2006) like the CH^+ molecule. $\Delta J = 3$ transitions are already an order of magnitude lower than the dominant ones and can therefore be neglected.

From Figure 2.6 qualitative conclusions about inelastic collision effects on the rotational cooling of a CH^+ ion ensemble in cold environments can be extracted. First, for electron energies below the first excitation threshold (3.5 meV), rotational cooling is solely supported by electron-ion collisions. At higher energies the excitation cross section exceeds the deexcitation by a factor of three. Thus, in the energy range

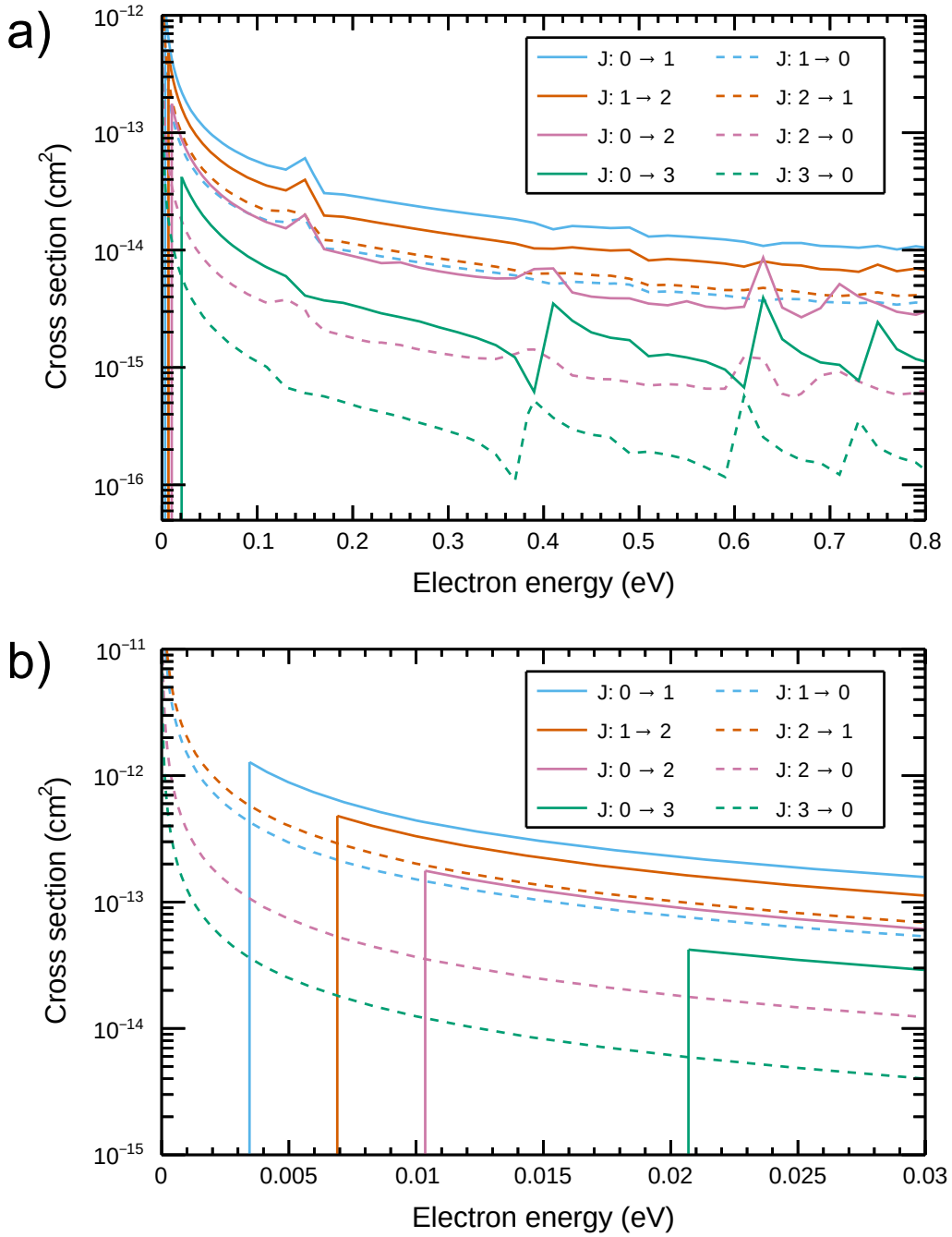

Figure 2.6: Rotational state-to-state inelastic cross sections. The data for excitation cross sections stem from Hamilton, Faure, and Tennyson 2015. Deexcitation cross sections were calculated with help of detailed balance (equation 2.32).

$(3.5 - 6.9\,\mathrm{meV})$, the $J = 0$ state is effectively heated while rotational cooling for $J > 1$ state is still enhanced by the electrons.

Quantitative estimates of inelastic collision effects on rotational state populations require a specification of the electron density and energy distribution the ions are exposed to. For this work inelastic collision have to be considered, as their absolute cross section is comparable to the probed DR process (see following section). A specific discussion about rotational cooling and an experimental probing of such will be provided in chapter 5.5.

2.2.3 Dissociative recombination cross section

Calculations of DR cross sections for the CH^+ ion have been pursued actively in the last decades. An overview of different approaches and results will be given in section 2.3. Here, the most recent results from Mezei et al. 2019 are presented. Their calculations are based on MQDT (see section 2.1.3) and have been extended by a treatment of individual rotational states of the $X^1\Sigma^+(v = 0)$ initial state. The authors provided their numerical results for the sake of comparisons with experimental data in the course of this work, which include data for $J = 0 - 10$.

The rotational-state-dependent cross sections for the lowest four states, which are most relevant to this work, are shown in Figure 2.7. Subfigure a) contains an overview of the full calculated energy range up to 0.8 eV. The energy dependence of the cross section is characterized by a multitude of resonances. Most of the resonances are common for all rotational states but their magnitude can depend on J. However, some of them are only present for certain rotational states, e. g., the two $J = 0$ resonances around 0.1 eV. The overall trend of the cross section reveals a slightly steeper decrease than expected from a pure $\sigma(\epsilon) \sim 1/\epsilon$ cross section for *direct* DR only (see section 2.1.3).

The origin of the resonances can be better understood from a magnified view onto the low-energy range ($\epsilon < 30\,\mathrm{meV}$, subfigure b)). The narrowest resonances are caused by new rotational channels opening up, i. e., becoming energetically accessible. Due to the increasing rotational spacing for higher J states, the density of these resonances shrinks with increasing J. In contrast to that, subfigure b) includes two prominent and broad resonances at 0.01 eV and 0.02 eV. They result from the opening of vibrational channels. In some cases, such channels can be closed before the threshold only for some rotational states. E. g., for the 0.02 eV resonance a vibrational channel is purely opening up for the $J = 0$ state but is already open for all higher states. Comparing to the overview picture in subfigure a), it becomes obvious that most of the J-specific vibrational resonances can be assigned to the $J = 0$ state.

One observation that can be derived from Figure 2.7 b) is the fact that rotational resonances are only visible up to energies corresponding to $\Delta J = 2$ transitions in the CH^+ molecule (vertically dashed lines in the figure). This can be attributed to the fact that the accessible Rydberg states in the *indirect* DR process are limited by the partial waves considered in the MQDT calculation. In this case, Mezei et al. 2019 only

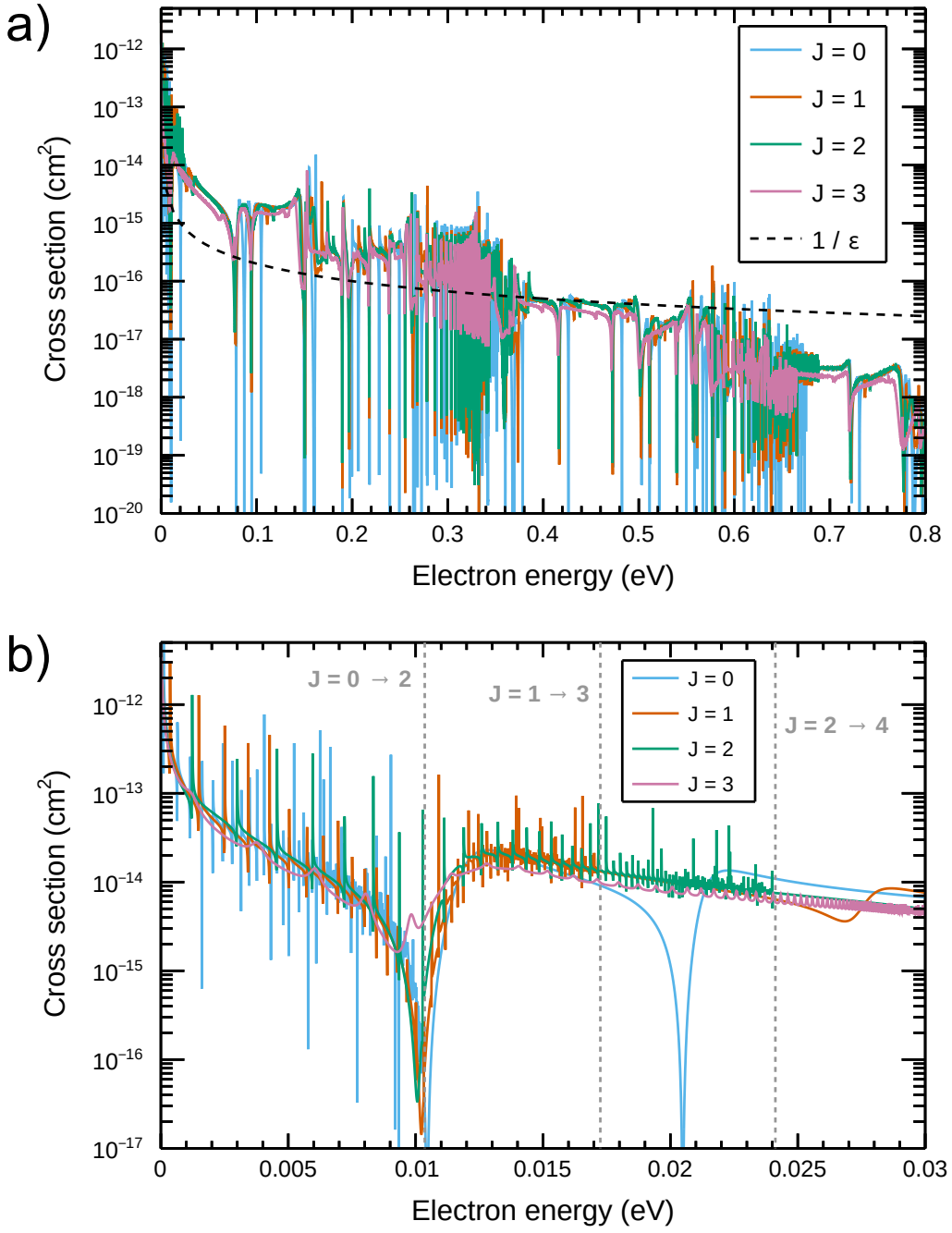

Figure 2.7: Rotational-state-dependent DR cross section calculation results from Mezei et al. 2019. a): Overview of the full calculated energy range. The data are compared to a $\sigma(\epsilon) \sim 1/\epsilon$ cross section, indicated as black dashed line. b): A view onto the low-energy ($\epsilon < 30\,\mathrm{meV}$) range. The rotational thresholds for $\Delta J = 2$ excitation of the CH^+ ion in its vibrational ground state (Table 2.3) are indicated by gray vertical lines.

calculated p-type partial waves, thus allowing only for intermediate Rydberg states converging to the $\Delta J = 2$ higher ionic PEC.

From an experimental point of view, the narrow, rotational resonances can not be resolved in most cases. With a high-resolution experiment, however, the vibrational resonances become partly accessible. The here presented theoretical results will be used for a comparison with experimental results in chapter 6.7.

2.3 Overview of previous research and results

The most recent theoretical calculations presented in the last section are not the only approach to the CH^+ DR cross section. In fact, substantial theoretical and experimental work on the topic has emerged over the last 40 years. It is instructive to look at this development in order to achieve the best possible knowledge about its cross section and final channels, which haven't been discussed in the previous section. In this section theoretical and experimental literature on the CH^+ DR is reviewed chronologically and summarized to formulate open questions on the topic in section 2.4.

In 1978, experimental knowledge about the CH^+ DR cross section was gained by a single-pass merged-beams measurement, where the results are presented in Mitchell and McGowan 1978 and Mul et al. 1981. As single-pass experiments work directly with an internal state ensemble from the used ion source, they tried to quench vibrationally excited states as well as the electronic metastable $a^3\Pi$ state (see Figure 2.4) by adding buffer gases into the source. With that, they optimized on the minimum DR cross section and stated that their measured values belong to vibrational ($v = 0$) and electronic ($X^1\Sigma^+$) ground state.

On the theory side, Takagi, Kosugi, and Le Dourneuf 1991 were the first group calculating the CH^+ cross section with the MQDT approach. A major achievement of their paper is the quantification of the $2^2\Pi'$ diabatic state (see Figure 2.4), which crosses the ionic $X^1\Sigma^+$ state PEC close to $v = 0$. To this date, it is the only known diabatic dissociative state driving the low-energy DR process. Their absolute cross section turned out to be a factor of three lower than in the previously mentioned single-pass experiment, but depends drastically on the exact position of the $2^2\Pi'$ state.

During the 1990s, merged-beams storage ring experiments were established, leading to an energy-resolution improvement as well as to better defined ion state ensembles compared to single-pass experiments. In the course of this development, a major experimental step for the CH^+ DR was taken by Amitay et al. 1996 at the Test Storage Ring (TSR) located at the Max-Planck-Institut für Kernphysik (MPIK). Similar to the results of this work, they complemented cross section measurements by the position detection of DR fragments, thus giving rise to the addressed final dissociation channels. In their measurements they could distinguish the metastable $a^3\Pi$ state cross section

Table 2.4: Kinetic energy releases and final channel branching ratios for DR of the CH^+ $X^1\Sigma^+(v = 0)$ ground state. The table information is extracted from Amitay et al. 1996 Table I.

Electron energy (eV)	Dissociation channel	E_{KER} (eV)	Branching ratio (%)
0	$C(^1D) + H(1\,s)$	5.92	79 ± 10
	$C(^1S) + H(1\,s)$	4.50	21 ± 10
0.11	$C(^3P) + H(1\,s)$	7.29	0^{+15}_{-0}
	$C(^1D) + H(1\,s)$	6.03	75 ± 25
	$C(^1S) + H(1\,s)$	4.61	25 ± 25
0.28	$C(^3P) + H(1\,s)$	7.46	0^{+15}_{-0}
	$C(^1D) + H(1\,s)$	6.20	75 ± 25
	$C(^1S) + H(1\,s)$	4.78	25 ± 25
1.18	$C(^3P^o) + H(1\,s)$	0.88	25^{+30}_{-25}
	$C(^1P^o) + H(1\,s)$	0.68	20^{+30}_{-20}
	$C(^3D^o) + H(1\,s)$	0.42	45 ± 15
	$\{C(^1D), C(^1S)\} + H(1\,s)$	$\{7.10, 5.68\}$	10 ± 7

from the $X^1\Sigma^+$ state and ensure that their probed ion ensemble is in the vibrational ground state.

Their measured cross section, in contrast to Mitchell and McGowan 1978, revealed a number of broad resonances in the energy range $0.08 - 2\,eV$. Such resonances were not compatible with the theory from Takagi, Kosugi, and Le Dourneuf 1991, as all of their predicted features could not be experimentally probed with the limited energy resolution of $\Delta E > 15\,meV$. Consequently, the discovered broad resonances were interpreted as resulting signal from *core-excited indirect* processes (see section 2.1.3), which were not yet included in any theoretical treatment.

The measured final channels at TSR, including their branching ratios and Kinetic Energy Releases (KERs) (see section 2.1.3), are listed in Tables 2.4 and 2.5 for the $X^1\Sigma^+$ ground state and $a^3\Pi$ metastable state, respectively. In case of the ground state, only four channels are available for energies $\leq 0.28\,eV$, as can be seen in Figure 2.4. From these four, only the $C(^1D) + H(1\,s)$ and $C(^1S) + H(1\,s)$ channels were observed in the experiment with significant branching ratios, which is the main argument for the PEC selection in Figure 2.4. While the major contribution of the $C(^1D) + H(1\,s)$ channel is expected from the dissociation limit of the diabatic $2^2\Pi'$ state, the existence of the $C(^1S) + H(1\,s)$ channel could not be explained directly. Amitay et al. 1996 proposed two possible interpretations:

- **Hypothesis I**: An interaction of the diabatic state with the $2^2\Sigma^+$ state through rotational coupling could result in a transition between the two PECs during

Table 2.5: Kinetic energy releases and final channel branching ratios for DR of the CH^+ metastable $a^3\Pi(v = 0)$ state. The table information is extracted from Amitay et al. 1996 Table I.

Electron energy (eV)	Dissociation channel	E_{KER} (eV)	Branching ratio (%)
0	$C(^3P^o) + H(1\,s)$	0.90 ± 0.05	7 ± 5
	$C(^1P^o) + H(1\,s)$	0.70 ± 0.05	8^{+25}_{-8}
	$C(^3D^o) + H(1\,s)$	0.44 ± 0.05	85^{+15}_{-25}

predissociation. In that case, a significant fraction of DR events could end up in the $C(^1S) + H(1\,s)$ channel without affecting the initial capture into the $2^2\Pi'$ state.

- **Hypothesis II**: A yet unknown diabatic state of $^2\Sigma^+$ character could be competing with the $2^2\Pi'$ state in the initial capture process. Such a state could dissociate into the $C(^1S) + H(1\,s)$ channel directly.

To this date, the TSR cross section and final state measurements have not been further improved experimentally. While their cross section will be used for comparison in chapter 6.1, chapter 7 references to their final state information.

In the year 2000 and motivated by the TSR results, Carata et al. 2000 conducted further MQDT calculations. They included *core-excited* Rydberg states to be able to reproduce the broad resonances seen in the experiment. In total, five Rydberg series were considered, where one converges to the $X^1\Sigma^+$ ground state and two to the excited $a^3\Pi$ and $A^1\Pi$ states each. Even though they could reproduce the broad character of the *core-excited* resonances, they were not able to match their positions and intensities to the TSR data. Furthermore, they conducted a rotational coupling calculation for the transition of the $2^2\Pi'$ state into the $2^2\Sigma^+$ state, resulting in a probability of $\approx 10^{-4}$. Thus, their results are incompatible with **Hypothesis I** about the $C(^1S) + H(1\,s)$ final channel, discussed previously.

Theoretical work on the CH^+ final state branching ratios was later on initiated by Guberman 2005, who earlier on published general considerations on angular fragment distributions (see section 2.1.3). He proved that the TSR fragment distance distribution could be reproduced even without a contribution of the $C(^1S) + H(1\,s)$ channel if the angular fragment distribution is not of isotropic character but rather follows a mixture of $p\pi$ ($\sim \sin^2\vartheta$) and $d\pi$ ($\sim \sin^2\vartheta\cos^2\vartheta$) partial waves (see Table 2.1). Afterwards, the $C(^1S) + H(1\,s)$ channel was not considered again by theoretical works.

In recent years DR cross section calculations were updated by Chakrabarti et al. 2018. In their MQDT calculations they used the same input data as Carata et al. 2000, also including *core-excited* Rydberg states. With improved computational power, they could include more vibrational states and evaluate the Lippmann-Schwinger equation 2.20 to second order, which turned out to change observed resonances significantly.

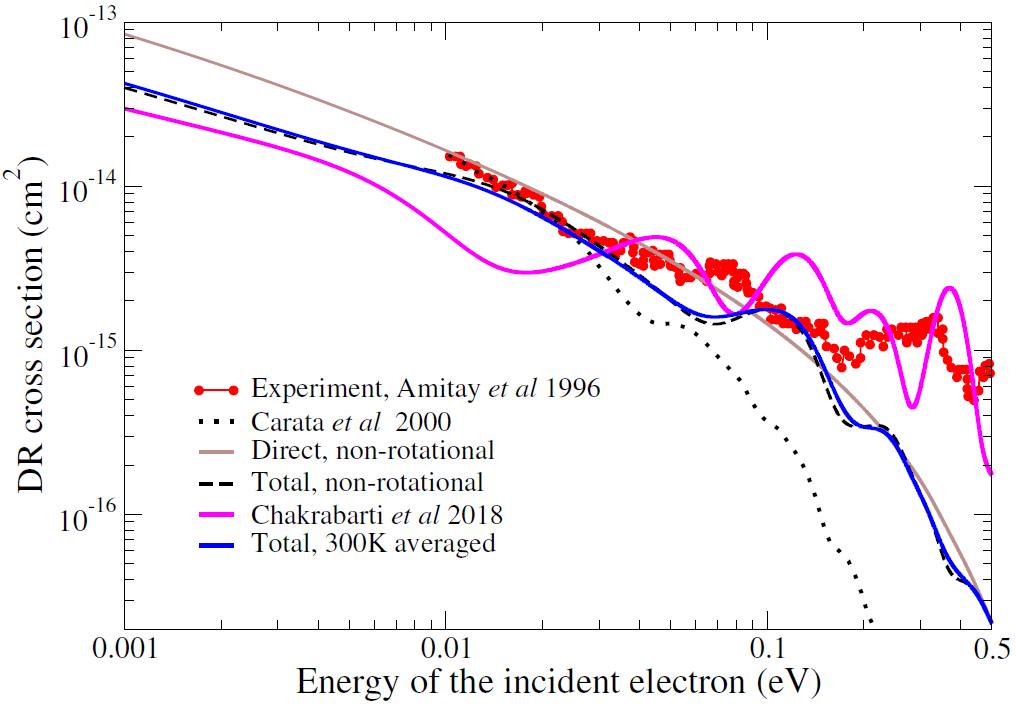

Figure 2.8: Comparison of latest theoretical and experimental CH^+ DR cross sections. The Figure is extracted from Mezei et al. 2019 and includes the results of other literature cited in the text.

In the course of the calculations from Mezei et al. 2019, presented in section 2.2.3, rotational states were included into the MQDT formalism. To this point, the rotational and *core-excited* approach can not be unified in one calculation due to the high computational demand. By a convolution of their cross section (and other theoretical results) with the TSR experimental resolution, they provide a comparison of different experimental and theoretical results in the energy range $0.001 - 0.5\,\text{eV}$ that is shown in Figure 2.8 and discussed in the following.

In the displayed range the TSR results indicate a few resonances, which exceed the general trend of the data by a factor of $1.5 - 4$. The different theoretical approaches can reproduce the absolute scale of the measured cross section quite well in the intermediate energy range of $0.03 - 0.2\,\text{eV}$. However, the *core-excited* calculation of Chakrabarti et al. 2018 falls short at low energies around $0.015\,\text{eV}$, while the rotational treatment deviates strongly above $0.2\,\text{eV}$. Here, the *core-excited* states seem to be the important driver of DR. The resonance positions measured at TSR are not reproduced by both theories. In total, the figure indicates that a combined treatment of core-excited and rotational effects might be a necessary improvement.

Even though the TSR measurement served as theoretical benchmark now for more than 20 years, two weaknesses should be pointed out here: First, the absolute scaling uncertainty of their measurement is stated to be around 50%, making precise abso-

lute comparisons impossible. Second, the energies below 10 meV could not be measured because of their limited energy resolution. Even the behavior up to 50 meV might be influenced by that effect. Especially in this region, corresponding to a temperature equivalent of $T < 120\,\mathrm{K}$, the cross section is extremely relevant for astrophysical processes in the ISM (see chapter 1). To date, the relevant rates had to be extrapolated from TSR results or extracted from theory. However, Figure 2.8 shows a discrepancy in the slopes of both results, which might continue into the low-energy regime.

2.4 Open questions

Based on the previously presented overview of the current experimental and theoretical status, open questions on the CH^+ DR process can be formulated, which shall be addressed in the course of this work. They are concerned with the energy dependence of its cross section and the final channel branching ratios:

- **How does the experimental cross section continue into the astrophysically relevant low energy range?**
  At TSR only energies down to 10 meV could be measured and the results close to that are resolution limited. Especially the $0 - 10\,\mathrm{meV}$ range is of importance for the ISM (see chapter 1). Measurements in this range require a high-resolution electron-ion collision experiment.

- **What is the precise absolute value of the cross section?**
  Absolute scaling of the TSR data is limited by a 50% uncertainty. Nowadays, merged-beams experiments in storage rings can achieve uncertainties around 20% (Novotný et al. 2019) and the limit can be improved.

- **How does the cross section of rotationally cold CH^+ ions look like?**
  The rotational population ensemble probed in TSR is expected to be close to Figure 2.5 and differs significantly from ISM conditions. Reproducing these conditions on Earth is only possible in a cryogenic environment. Previous experiments on the DR process of HeH^+ revealed significant J-state-dependencies of its cross section (see chapter 1), while theory estimates rather small effects for CH^+ (black dashed curve versus blue curve in Figure 2.8).

- **Can the $C(^1S) + H(1s)$ final channel be unambiguously observed experimentally?**
  The $C(^1S) + H(1\,s)$ channel was detected with a small branching ratio in Amitay et al. 1996 but later on the detection was criticized by Guberman 2005. MQDT is not able to distinguish between different final channels. Thus, an improved experimental approach is required to clarify the $C(^1S) + H(1\,s)$ puzzle.

- **How do final channel branching ratios evolve with electron energy?** Despite the issue described in the latter point, all branching ratios measured at TSR underlie high statistical uncertainties, such that the secondary channel in most cases can not be claimed as a significant detection. Imaging measurements at storage rings have evolved over the years and nowadays data acquisition systems are capable of higher data transfer rates, enabling an improved experimental access.

All of the questions above can be answered by improving the TSR experiment in a cryogenic storage ring with a high-resolution electron collision target. The experimental part of this work was conducted at the Cryogenic Storage Ring (CSR), which combines these properties, as presented in the next chapters. The first three questions will be addressed in chapter 6, in the course of CH^+ DR rate measurements, while chapter 7 is concerned with the last two questions, using an improved imaging approach.

Chapter 3

An electron-ion merged-beams setup for rotationally cold molecules

Dissociative Recombination (DR) of the CH^+ ion has been an active research topic over a long time. In chapter 2 the current experimental and theoretical state was presented, concluding with five questions to be addressed. A major experimental challenge for answering those questions is given by a demanded high energy resolution and cold internal state population of the measured ions.

Electron collision experiments with internally cold molecules require thermalization of the molecular species in a low-temperature environment. Plasma afterglow experiments achieve this thermalization by collisional processes with residual gas and are currently capable of reaching internal temperatures down to 30 K (see Plašil et al. 2018). This experimental method, however, goes at the expense of three body collisions in the apparatus. Moreover, the control over collision energy distributions is limited since all collisions are determined by the plasma properties.

Fast merged-beams techniques offer a different experimental approach. For perfectly aligned, merged electron and ion beams, the collision energy in the center of mass system is given by (Larsson 2005)

$$E_{\mathrm{CM}} = \mu \left[\sqrt{\frac{E_{\mathrm{e}}}{m_{\mathrm{e}}}} - \sqrt{\frac{E_{\mathrm{ion}}}{m_{\mathrm{ion}}}} \right]^2 \tag{3.1}$$

where m_{e}, m_{ion} and μ are the electron, ion and reduced mass, E_{e} is the kinetic energy of the electrons and E_{ion} the kinetic energy of the ions. Collision energies in such experiments can be reduced close to zero without the need of storing particles at rest. Furthermore, the collision energy distributions are determined by the electron and ion beam energy spread only and are typically narrower than a thermal distribution.

Merged-beams experiments in single-pass configuration bear the disadvantage of probing vibrationally excited molecular ions, mainly defined by the ion source con-

ditions. By storing molecules in a room-temperature vacuum chamber, they interact with the blackbody radiation field, leading to vibrational relaxation. Therefore, the development of ion storage rings has paved the way for vibrationally cold collision experiments, starting in 1993 (Forck et al. 1993). Energy stored in molecular rotations, on the contrary, is much lower than in vibrations. All molecules stay rotationally excited in a room-temperature environment, as the first excitation energy is confined by the upper limit given by the H_2 molecule: $E_{J=1} = 170.5\,\mathrm{K} \times k_\mathrm{B}$ (Bishop and Shih 1976). Thus, cryogenic storage rings have been developed and became state-of-the-art devices for collision studies with rotationally cold molecular ions in the last decade. In such environments molecules with a finite dipole moment interact with the surrounding blackbody radiation field and their internal degrees of freedom are effectively cooled.

The Cryogenic Storage Ring (CSR) (von Hahn et al. 2016), located at the Max-Planck-Institut für Kernphysik (MPIK), offers the possibility for electron-ion collision experiments with internally cold ions. Hydride ions, like the CH^+ ion, relax to their lowest rovibrational levels and can undergo electron collision in the CSR electron cooler. In this merged-beams configuration collision energies down to the meV regime can be addressed. Since the CSR is a fully electrostatic storage ring, mass-independent storage of different species is possible, allowing for experiments with heavy molecular ions or even clusters. This chapter intends to give an overview of the CSR facility, its low-temperature electron cooler and the fast neutral imaging detector used for DR experiments.

3.1 The Cryogenic Storage Ring

The experiments presented in this work were conducted at the Cryogenic Storage Ring (CSR) facility. A comprehensive description of the storage ring setup and functionality is given by von Hahn et al. 2016. In this section a short overview of the facility will be given.

A schematic view of the Cryogenic Storage Ring (CSR) is shown in Figure 3.1. Ion beams are generated in various ion sources that can be mounted on two different high-voltage platforms for acceleration with upper voltage limits of 60 kV and 300 kV, respectively. For experiments involving the electron cooler, high acceleration voltages are typically targeted in order to simplify the electron cooling process. After the acceleration step, ions are guided through a transfer line with several beam diagnostic elements as well as two magnetic quadrupole doublets and two electric quadrupole triplets for optimizing the beam quality. Additionally, an electrostatic deflector (chopper) is installed in this beamline. By switching the high-voltage on its deflector plates, it can be used as a fast beam dump. It can be further utilized to record the ion free background count rate (*dark count rate*) of any detector. A more detailed description of ion sources

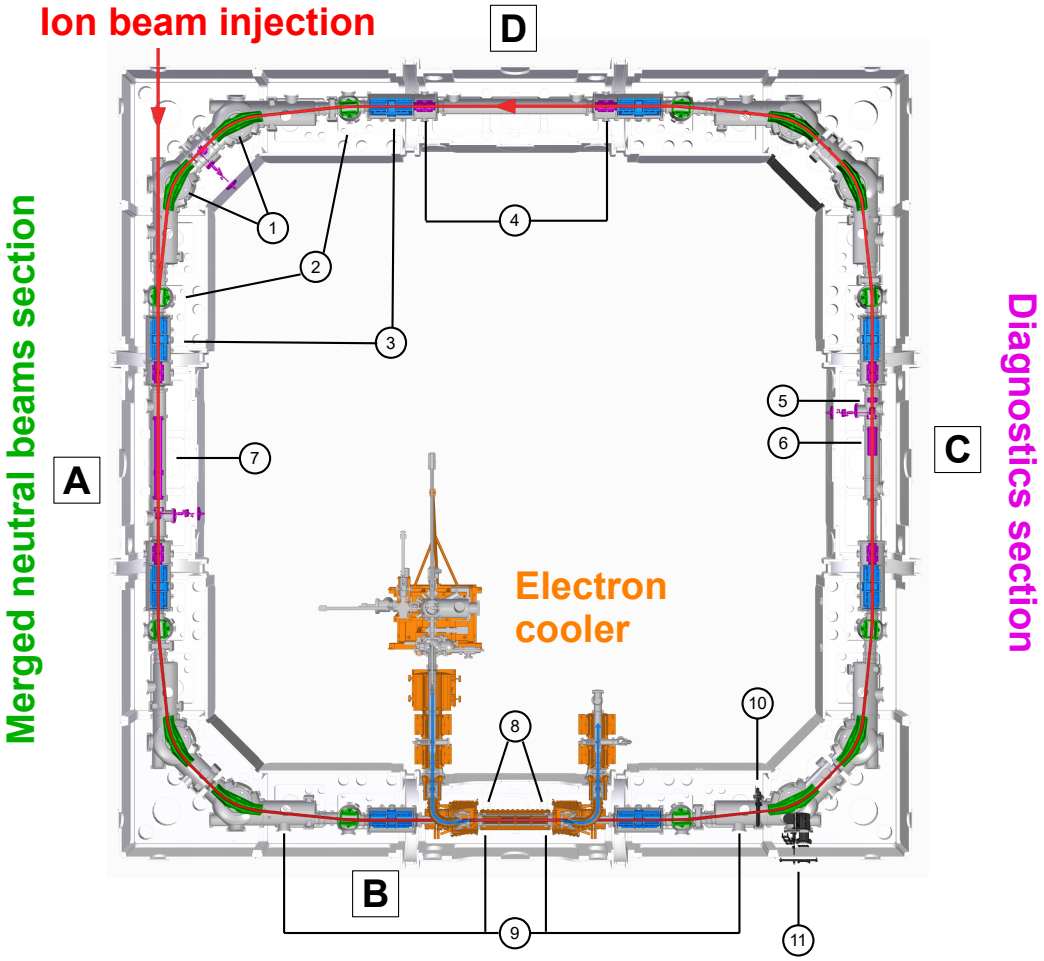

Figure 3.1: Schematic setup of CSR. The ion beam is injected on the top left and circulates counterclockwise. Four deflection elements in each corner (green) define the closed orbit: 39° deflectors (1) and 6° deflectors (2). Two quadrupole doublets per straight section (blue) are used for focusing (3). Beam diagnostics elements are shown in purple: position pickups (4), current (5) and Schottky pickup (6) and RF bunching system (7). The electron cooler is located in the bottom section with additional wire scanners for electron and ion beam (8). Viewport positions for laser experiments are indicated (9). Collision products are detected by a movable charged particle counting detector COMPACT (10) and a fast neutral imaging detector NICE (11).

and the transfer beamline can be found in von Hahn et al. 2016 and Grussie 2016.

The ion beam is injected at the beginning of section A into the storage ring with a circumference of $C_0 = 35.12(5)\,\mathrm{m}$ (Novotný et al. 2019). In each corner of CSR two electrostatic 6° deflectors and 39° deflectors are installed. The beam is focused with help of two quadrupole doublets in each straight section. In order to inject and consequently store the ion beam after the first revolution, the first 6° deflector is changed from zero to nominal voltage by a high-voltage switch. On the timescale of a revolution (μs), the final voltage is not completely reached, thus resulting in a drift of the closed ion beam orbit during the first hundred to thousand revolutions.

Experiments are mainly conducted in the four straight sections (A-D) of CSR. Section A is dedicated to neutral-ion merged-beams studies with an additional extraction section for analyzing collision products at the end of the section (not shown in the figure). Additionally, a Radio Frequency (RF) bunching system is installed here. At the expense of a reduced ion beam lifetime, bunched ion beams offer a much higher detection sensitivity and are, e. g., used for ion beam number determination, center of charge detection and electron cooling diagnostics.

Section C (ion beam diagnostics section) is equipped with two capacitive current pickup electrodes, detecting mirror charges of the revolving ion beam. The Schottky pickup is designed for observation of coasting beam Schottky noise signal and is in general more sensitive. However, since the Schottky pickup signal does not show a linear response to the stored number of ions and because of the high pickup length, it is not advantageous for absolute current measurements. For this purpose the shorter current pickup was implemented.

In section B of Figure 3.1 photon collision experiments can be performed by guiding laser beams (including the beam from an Optical Parametric Oscillator (OPO) system) through several viewports installed in CSR. One pathway for merged-beams and two for crossed-beams configuration are accessible here.

Most relevant for the purpose of this work is the electron cooler, located also in section B. This device is used on the one hand for phase-space electron cooling of ion beams in order to reduce beam size and velocity spread. Two wire scanners (scrapers) in the electron cooler section are used to find and characterize the electron-ion beam overlap. On the other hand, the electron cooler is used as high-resolution collision target in a merged-beams configuration. A detailed description of the electron cooler will be given in section 3.2.

Collision products from photon or electron collisions are detected in the corner after section B. Because of their different charge-to-mass ratio compared to the main ion species, they are separated by the first 6° deflector from the main beam. The Cold Movable Particle Counter (COMPACT), described in Spruck et al. 2015, is a movable, cryogenic, single particle detector on the basis of Microchannel Plate (MCP) detection. It is typically used for collecting charged products. Due to its low *dark count rate* ($< 0.1\,\mathrm{Hz}$), it is the preferred detector to study reactions with low cross sections. The Neutral Imaging in Cold Environment (NICE) detector (Becker 2016) is limited to

collection of neutral fragments. A combination of MCP single-particle detection and a phosphor screen allows to image fragment positions. Transverse electron cooling can be diagnosed with NICE and fragmentation kinematics of collision products can be studied. Thus, this detector was used for all experiments in the course of this work and is described in more detail in section 3.3.

In each section, except section B, two capacitive position pickups are placed. With the principle of a sliced electrode, voltage differences between both slices give rise to the center of charge of the ion beam. The functionality and design of the position pickups as well as a comprehensive view on all diagnostic elements of CSR can be found in Vogel 2016.

As a major feature, the CSR beamline is housed in a separate isolation vacuum chamber that acts as a cryostat for the whole beamline. Wall temperatures around 4 K are achieved by a closed-cycled liquid helium system. A commercial helium refrigerator liquefies the gas down to temperatures of 2 K. In CSR the liquid is guided through cooling lines attached to copper blocks, which act as cryopumps. With four additional cycles through the ring, each of them bearing warmer helium than the previous, lines with nominal temperatures of 2 K, 5 K, 40 K and 80 K are available. In order to prevent 300 K blackbody radiation from the outer vacuum chamber to warm up the cold surfaces, two aluminum shields have been installed between the inner and outer vacuum chamber, which are connected to the 40 K line (inner shield) and 80 K line (outer shield). For further details on the cryogenics, the reader is referred to von Hahn et al. 2016.

3.2 The CSR electron cooler and collision target

In CSR operation the electron cooler is used in a twofold manner. One the one hand, it provides the possibility of electron cooling for ions with masses smaller than 160 u. On the other hand, energy-resolved electron-ion collision experiments can be performed by tuning the electron energy. The major challenge in both cases is given by the shaping and guidance of an electron beam at extremely low energies, down to 1 eV. While recent experiments in other low-energy storage rings (see Hunt et al. 2020) have proven phase-space electron cooling at energies of 55 eV, the usual energy range of the CSR electron cooler is even lower. Additionally, the cryogenic environment of CSR necessitates the minimization of heat inputs by the electron cooler. A special design to meet these requirements has been developed in the work of Shornikov 2012, constructed in the works of Vogel 2016 and Wilhelm 2019 and commissioned for electron cooling in Wilhelm 2019. Within this section, the design of the CSR electron cooler shall be presented.

Figure 3.2 shows a schematic overview of the electron cooler. The whole setup is covered by a solenoidal magnetic field that allows for guidance of low-energy elec-

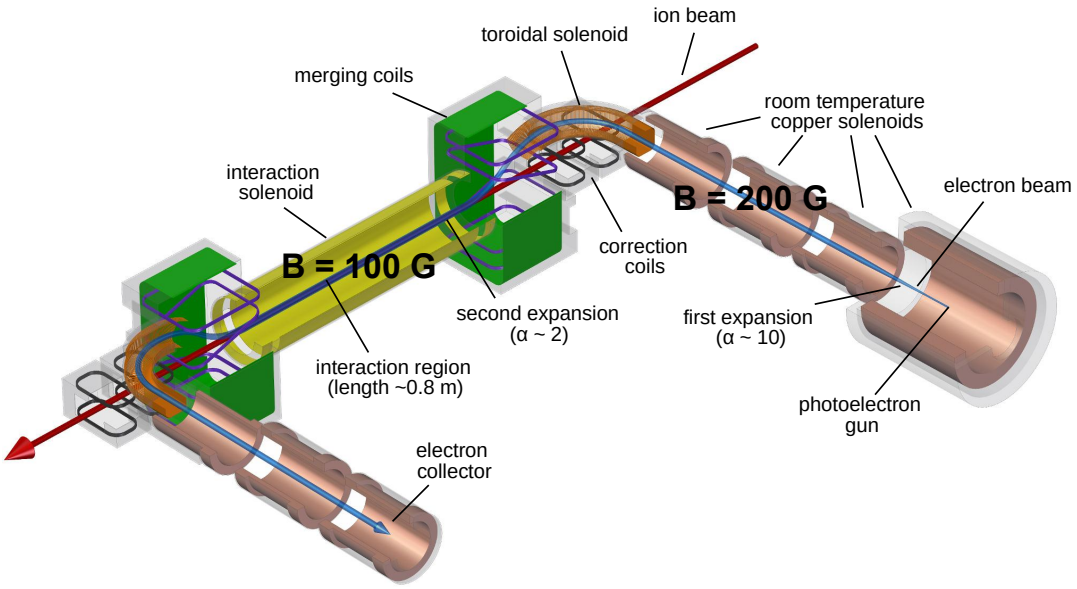

Figure 3.2: Schematic view of the CSR electron cooler, extracted from Wilhelm 2019. The ion trajectory is displayed as red, the electron trajectory as blue arrow.

tron beams. The beam is produced from different GaAs photocathodes with negative electron affinity. A deposition of thin cesium and oxygen layers onto the semiconductor surface shifts the conduction band energy level below the vacuum level, making the photoelectric effect to generate free electrons more efficient. While commonly used thermocathodes bear the disadvantage of a broad thermal energy distribution of the emitted electrons, room-temperature photocathodes offer the possibility for high-resolution experiments. However, this comes at the cost of a higher operational complexity. In order to prepare and clean such cathodes, a separate vacuum chamber setup is used that has already been in operation for years at TSR and is described in detail in the work of Weigel 2003. Information about the activation procedure of such photocathodes is given in the works of Weigel 2003 and Krantz 2009. In the current setup quantum efficiencies (number of electrons per photon) of $8 - 20\,\%$ are achieved, depending on the surface quality of the specific cathode. The corresponding number of electrons is sufficient to produce a space-charge limited electron beam.

After the electron beam production region, a set of three copper solenoid magnets is installed, followed by the transition between the room-temperature vacuum chamber and the CSR cryostat. In the CSR area the electron beam is bent by 90° in the horizontal plane and by 30° vertically in the toroidal solenoid. Merging of the inclined electron beam and the ion beam below the latter is achieved by a dipole field from the merging coils. In the interaction solenoid electron and ion beam are fully overlapped. Symmetrically to the merging section, the two beams are de-merged and the electron beam is guided to and dumped in the electron collector. Most of the magnets inside

the cryogenic section of CSR were constructed from High-Temperature Superconductor (HTS) material for eliminating resistive heat inputs into the cold vacuum chamber.

A part of the special and unique design of this electron cooler is concentrated in the merging section. Typically, electrons and ions in other electron coolers are overlapped within the toroidal section. However, because of the low ion energies in CSR, the ion beam would be deflected beyond the acceptance limit by the toroidal magnetic field in such a configuration. Moreover, this deflection is not compensable by a simple dipole field, as discussed in Fadil et al. 2006. Thus, merging inside the CSR electron cooler is achieved within a weaker dipole field. The resulting distortion of the ion beam trajectory by this field is compensated by two additional HTS racetrack-type correction coils, before and after the electron cooler (see Figure 3.2).

For electron beam related experiments it is crucial to control the beam position and its angle in the interaction zone. This is achieved with seven pairs of copper-made steering coils (the only magnets not made out of HTS material) at several positions in the electron cooler setup. Each pair contains a horizontal and vertical steering unit. Three of them are placed in the gun-side part of the cooler (first room-temperature solenoid, toroid and merging section) for controlling the beam position. One pair is spread over the interaction zone and introduces a constant angle. Symmetrically to the gun-side steerers, three pairs are located in the collector section to compensate for position shifts and hit the electron collector.

A commonly included feature in electron coolers is the reduction of the solenoidal field from the electron gun towards the interaction region. This induces an *adiabatic magnetic expansion*, which is described in more detail in chapter 4.2.2. For the price of a decreased electron density, the electron beam size is increased and its transverse temperature is reduced by this technique. In the CSR electron cooler the solenoidal magnetic field is lowered in two steps from the electron gun ($B_{\mathrm{gun}} = 2000\,\mathrm{G}$) to the room-temperature region after acceleration ($B_{\mathrm{acc}} = 200\,\mathrm{G}$) and finally to the interaction region ($B_{\mathrm{int}} = 100\,\mathrm{G}$). The ratio of magnetic fields from electron gun to a certain section with field strength B in the electron cooler is called *expansion factor*:

$$\alpha = \frac{B_{\mathrm{gun}}}{B} \tag{3.2}$$

Figure 3.3 summarizes the magnetic fields (top) as well as the electrodes (center) and electric potentials (bottom) from electron gun to collector for the setup used in this work. For better illustration the beam path has been linearized. In the central part of the figure all electrodes are drawn with solid and all coils as dotted lines.

In the electron gun section, the GaAs photocathode is illuminated in transmission configuration from the backside by a 500 mW infrared laser diode ($\lambda = 805\,\mathrm{nm}$). The electron beam extracted from the cathode at potential $-U_0$ is shaped and current-controlled by the combination of a Pierce and two extraction electrodes at potentials relative to the cathode of U_{pierce} and U_{ext}. A barrier electrode set to U_{barrier}, slightly above ground potential, prevents back-streaming of ions produced by residual gas ionization of the electron beam.

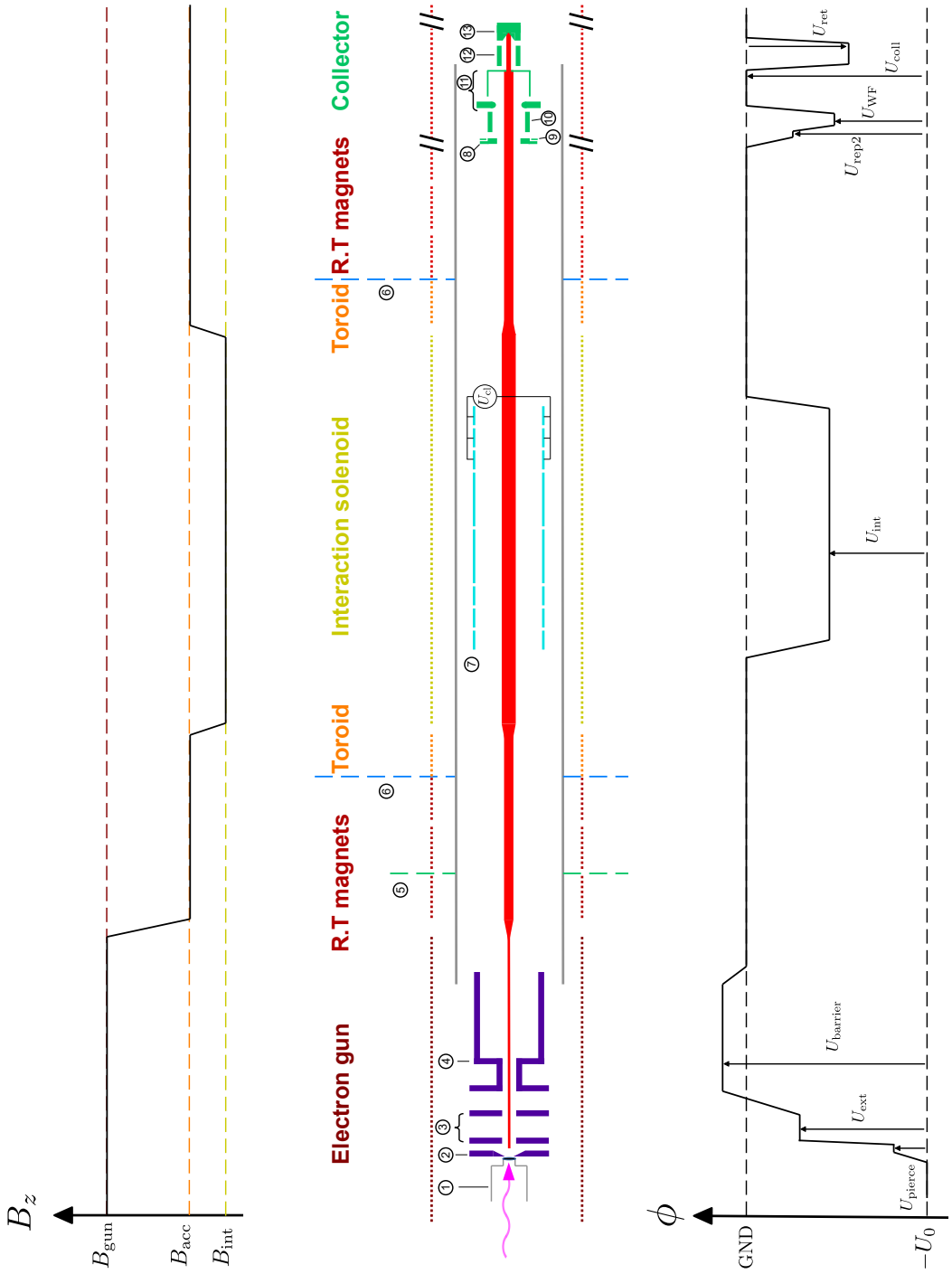

Figure 3.3: Potentials and magnetic fields along the electron beam path inside the CSR electron cooler. (1-4): electron gun, (1): photocathode, (2): Pierce electrode, (3): extraction electrodes, (4): barrier electrode, (5): position of the gun-side Faraday cup, (6): room-temperature transitions, (7): drift-tube electrodes, (8)-(13): collector Faraday cup, (8): repeller electrode, (9): secondary electron collector, (10): Wien filter electrodes, (11): collection electrodes, (12): retarding electrode, (13): analyzer cup. See text for more information.

After propagating through the equipotential region of the room-temperature magnets and toroid, the electron beam enters the interaction zone. As indicated in Figure 3.3, the main interaction region is split into eight drift-tube elements where each of them can be operated at a different voltage. In this work, however, all drift-tube elements were set to the same base voltage U_{int}. As an inadvertent effect, ions produced in the interaction zone by residual gas collisions can be captured in the electron beam potential like in an electron beam ion trap. To counteract this effect, the last three drift-tube elements are sliced in two halves and a small voltage U_{cl} is applied between each pair. This clearing voltage does not affect the magnetically guided electron beam since the potential in the drift-tube center is unaltered. However, resting ions are attracted towards the negative electrode and removed from the interaction zone.

The electron beam is de-merged after the interaction zone, passes another equipotential region and is finally guided into the electron collector. The design and functionality of all individual collector electrodes is described in detail in the work of Lohmann 2015. At the cup entrance a repeller electrode (U_{rep2}) and a Wien filter potential (U_{WF}) are set to negative voltages against ground to suppress backstreaming of secondary electrons. It turned out that using the magnetic field of the Wien filter is not necessary for trapping of secondary electrons. On the backside of the repeller electrode, a secondary electron collector is installed. Its potential (U_{sec}) is not shown in the figure since the main beam is not affected by it. The collection electrodes, involving the main Faraday cup and an additional aperture are typically operated close to ground potential ($U_{\mathrm{coll}} \approx U_0$). The main cup itself contains a pinhole with a diameter of 0.8 mm used for electron beam profile and energy distribution measurements, with help of a grounded analyzer cup for electron collection and a retarding field electrode for energy scans at voltage U_{ret}.

A similar electron collector without the entrance electrodes (U_{rep2}, U_{WF} and U_{sec}) was developed and implemented in the work of Wilhelm 2019 close to the electron gun. Its position in the setup is indicated as number (5) in Figure 3.3.

It should be noted that all voltages, except for the retarding field electrode, are with respect to cathode potential. They are driven by power supplies on a common high-voltage platform, which was developed in the work of Rimmler 2017. The full electronic connection scheme is also described there.

Cryogenic operation of CSR and the electron cooler requires active cooling of the High-Temperature Superconductor (HTS) magnets. Therefore, a closed-cycle helium or neon cooling system was developed, implemented on top of the electron cooler and commissioned in the works of Shornikov 2012 and Lion 2015. A cold head is designed to cool gaseous neon into the liquid phase and pump it through a tubing system in CSR that is heat-connected at several places with the HTS material and its transitions to other materials. During the commissioning of the electron cooler, it turned out that using gaseous helium, with the advantage of lower system complexity but at the cost of its lower heat capacity compared to liquid neon, is sufficient for cooling the hottest parts of the HTS material well below the critical temperature of 100 K. In operation

an additional safety margin is added, leading to a maximum allowed temperature of 90 K at the hottest measured parts. Further discussion on the temperature development during the CH^+ beamtime can be found in section 5.1.

3.2.1 Electron cooling

The position and settings of all ion optics elements inside a storage ring define an ideal ion beam trajectory, the *closed orbit*, and an ideal revolution frequency. Due to a finite phase-space distribution of the ion beam at injection, all ions in the stored beam experience oscillations around the closed orbit, referred to as *betatron oscillations*, and around the center revolution frequency, referred to as *synchrotron oscillations*. The phase space occupied by the ion beam is defined as emittance ϵ and can be split into a horizontal (ϵ_x), vertical (ϵ_y) and longitudinal (ϵ_L) component. It depends on convention if the emittances are given as phase space area containing 68 % (ϵ_σ), 90 % (ϵ_{90}) or 95 % ($\epsilon_{2\sigma}$) of all stored ions. A comprehensive view on synchrotron and betatron oscillations is given in Hinterberger 2008.

One method for damping betatron and synchrotron oscillations is the application of electron cooling, which has been proposed by Budker 1967. The principle of electron cooling is presented in Figure 3.4. Electrons and ions are overlapped in the electron cooler section with matched average velocities $\langle v_{\mathrm{ion},\parallel}\rangle$ and $\langle v_{\mathrm{e},\parallel}\rangle$. In the co-moving beam frame of the ions (also referred to as center of mass system), both particles species interact via Coulomb collisions. As a consequence of all collisions, an average, velocity-dependent collision force acts on the ions that is qualitatively shown for longitudinal motion in Figure 3.4 b). For small deviations between ion and electron velocity ($v_{\mathrm{ion},\parallel} - \langle v_{\mathrm{e},\parallel}\rangle$), this cooling force is approximately linear and serves as a friction force on individual ions, ultimately damping synchroton and betatron oscillations.

The latter considerations only hold in case of matched mean velocities. If the mean ion velocity, however, slightly differs from the mean electron velocity, the cooling force accelerates or decelerates the whole ion beam until mean velocities are matched. This effect is referred to as *dragging*. In case of extreme velocity differences, the force acting on ions is negligible.

Electron cooling of ion beams offers several benefits:

- By reducing the transverse ion beam emittance, the ion beam is compressed. This is helpful to guarantee a full overlap for merged-beams experiments.
- The momentum spread of the ion beam is reduced together with the beam emittance, paving the way for high-resolution experiments. In case of CSR, however, the electron velocity spread usually defines collision energy distributions, even for uncooled ion beams.
- Different heating processes in storage rings limit ion storage times. Electron cooling can, in principle, counteract these heating processes and increase beam lifetimes.

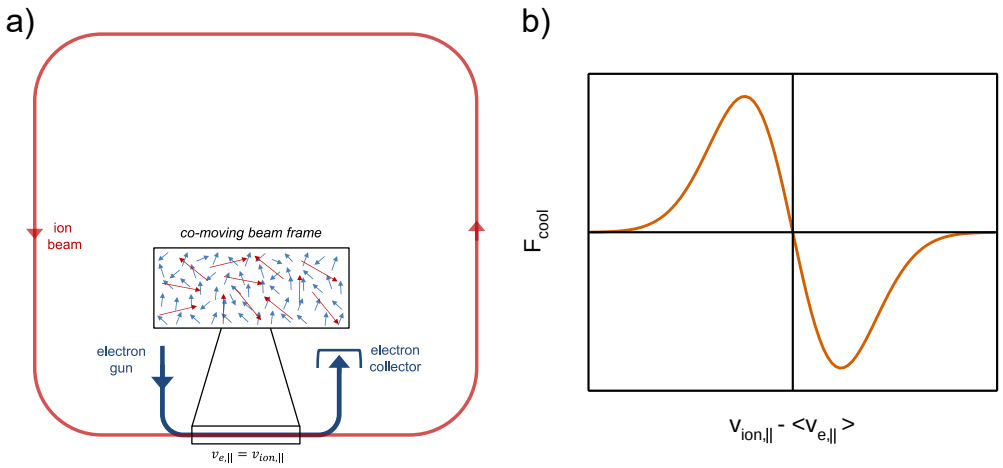

Figure 3.4: Principle of electron cooling. a): The ion beam (red) is overlapped with a velocity-matched electron beam (blue) in the electron cooler section. Interactions between electrons and ions in the co-moving beam frame are illustrated in the center of the picture. The figure is extracted from Wilhelm 2019. b): Qualitative dependence of the longitudinal cooling force on the velocity difference of individual ions to the mean electron velocity (see Poth 1990).

- If electron and ion velocities are not fully matched in the beginning, electron cooling can drag the ion beam, as described previously, and define the ion beam velocity. This is advantageous for knowledge of the precise collision energy distribution in high-resolution merged-beams experiments.

Hence, electron cooling is typically applied before electron-ion collision experiments. For velocity-matching of both beams, the energy of the electron beam in lab frame is given by the cooling energy

$$E_{\mathrm{cool}} = \frac{m_{\mathrm{e}}}{m_{\mathrm{ion}}} E_{\mathrm{ion}} = \frac{m_{\mathrm{e}} f_{\mathrm{rev}}^2 C_0^2}{2} \tag{3.3}$$

where C_0 is the storage ring circumference and f_{rev} is the revolution frequency of the ion beam, which is typically determined experimentally. Because of the low electron and ion energies in CSR, all calculations in this work are done non-relativistically.

3.2.2 Drift-tube deceleration mode

At the low electron energies used in the CSR electron cooler, especially for cooling of heavy ions, the space charge potential of the electron beam becomes important. For high electron densities n_e, as present in the gun section, it is even possible to stop electrons completely due to the high negative space charge. Therefore, the electron cooler is designed for two operation modes:

In *standard mode* all drift-tube elements in the interaction region are grounded and the electron energy is determined by the cathode potential. In contrast to that, the *drift-tube mode* operation facilitates a constant cathode potential and the electron energy is set by the difference between the cathode and the variable drift-tube potential. As it will be shown in this section, the deceleration from ground to the negative drift-tube potential rises the possibility for higher electron densities in the interaction zone.

In drift-tube mode the electron energy in the lab frame of the interaction zone E_{lab} for electrons in the beam center is defined mostly by the potential U_{int} (see Figure 3.3). During experiments this voltage is typically switched fast between cooling and experimental conditions. A sub-millisecond fast power supply is used to provide this voltage. At a given setting, the lab frame electron energy is given by

$$E_{\mathrm{lab}} = eU_{\mathrm{int}} - e|U_{\mathrm{sc}}| - e(W_{\mathrm{int}} - W_{\mathrm{cath}}) \tag{3.4}$$

where $W_{\mathrm{int}} - W_{\mathrm{cath}} \approx 2.5\,\mathrm{V}$ is the difference of work functions between interaction zone and cathode (also called *contact potential*) and is slightly depending on the cathode properties, e is the elementary charge and U_{sc} is the space charge potential of the electron beam. The latter can be approximated by the potential minimum of a cylindrically symmetric electron beam of radius r_{beam} with constant density n_{e} in a potential-fixed tube with radius $r_{\mathrm{tube}} > r_{\mathrm{beam}}$, leading to

$$U_{\mathrm{sc}} = -\frac{n_{\mathrm{e}} e r_{\mathrm{beam}}^2}{4\varepsilon_0}\left(1 + 2\ln\left(\frac{r_{\mathrm{tube}}}{r_{\mathrm{beam}}}\right)\right) \tag{3.5}$$

For the CSR electron cooler $r_{\mathrm{tube}} = 50\,\mathrm{mm}$ and the electron density is defined by the electron current I_{e} over

$$n_{\mathrm{e}} = \frac{I_{\mathrm{e}}}{e\pi r_{\mathrm{beam}}^2}\sqrt{\frac{m_{\mathrm{e}}}{2E_{\mathrm{lab}}}} \tag{3.6}$$

I_{e} is measured on the collector cup and can be controlled by the extraction and Pierce voltage. With equations 3.4, 3.5 and 3.6 the set voltage for a desired lab energy can be calculated. Reversely, extracting a lab energy from a given drift-tube voltage is achieved by solving the three equations alternately in an iterative procedure with an initial condition of $U_{\mathrm{sc}} = 0$. At typical conditions in the CSR electron cooler, the space charge potential amounts to $U_{\mathrm{sc}} = 0 - 1\,\mathrm{V}$.

The electron current drawn from the photocathode is usually not limited by the laser power but by the space charge resulting from an electron cloud in front of the cathode (space-charge-limited operation). Here, the electron current dependence on extraction voltage is given by the Child-Langmuir law (Child 1911)

$$I_{\mathrm{e}} = PU_{\mathrm{ext}}^{3/2} \tag{3.7}$$

where $P \approx 0.5\,\mu\mathrm{A/V}^{3/2} = 0.5\,\mu\mathrm{perv}$ is the perveance of the CSR electron gun setup, measured in Wilhelm 2019. Since the extraction voltage is limited by the acceleration voltage U_0,

$$I_{\mathrm{e,max}} = PU_0^{3/2} \tag{3.8}$$

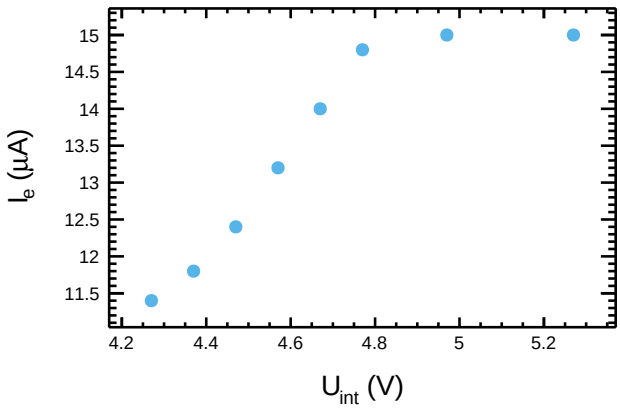

Figure 3.5: Drift-tube current breakdown by space-charge effects. The electron current above $U_{\mathrm{int}} = 5.3\,\mathrm{V}$ stays constant.

describes the maximum achievable electron current in standard mode. For cooling of heavy ions ($U_0 \approx 1\,\mathrm{V}$) electron beam currents are limited to values below $1\,\mu\mathrm{A}$.

This limit can be overcome by operating in drift-tube mode. By accelerating electrons first with a high cathode potential $U_0 \approx 20\,\mathrm{V}$ to ground potential and afterwards decelerating them in the negative potential of the drift-tubes, the electron current is now no longer limited by the perveance of the electron gun but by space-charge conditions inside the drift-tubes. Here, an effective perveance of the interaction zone can be defined by

$$I_{\mathrm{e,max}} = P_{\mathrm{int}} U_{\mathrm{int}}^{3/2} \tag{3.9}$$

and was measured to $P_{\mathrm{int}} = 4.1\,\mu\mathrm{perv}$ in a test setup before the final construction of the CSR electron cooler in the work of Shornikov 2012.

An estimate for the perveance of the current setup can be obtained by lowering the drift-tube voltage U_{int} at a given electron gun setting until a breakdown of I_{e} (the electron current transported through the drift-tube and measured at the collector) occurs because of the space-charge limits in the interaction zone. Such a measurement is presented in Figure 3.5. For high voltages of U_{int}, the electron current is limited by the gun perveance and stays constant. The breakdown occurs at $U_{\mathrm{int}} = 4.8\,\mathrm{V}$. By subtracting the cathode contact potential from the measured voltage, the perveance for electron current transport through the drift-tube can be estimated to

$$P_{\mathrm{int}} \approx \frac{I_{\mathrm{e,max}}}{(U_{\mathrm{int}} - W_{\mathrm{int}} - W_{\mathrm{cath}})^{3/2}} = 4.3\,\mu\mathrm{perv} \tag{3.10}$$

which is close to the test setup result. A thorough determination of the drift-tube perveance would, however, require the measurement of several breakdown curves and a correction for space-charge potentials, as described in chapter 3.2.1 of Shornikov 2012. Since such a measurement is likely to degrade photocathodes and therefore stands in conflict with other experimental plans, it was not prioritized in this work.

3.2.3 Collision target operation

In electron collision experiments the electron cooler is tuned to energies different from the cooling energy. Since electron collision experiments are typically conducted with an electron-cooled ion beam, the average ion velocity is given by

$$\langle v_{\mathrm{ion}} \rangle = \sqrt{\frac{E_{\mathrm{cool}}}{2m_{\mathrm{e}}}} = \sqrt{\frac{E_{\mathrm{ion}}}{2m_{\mathrm{ion}}}} \tag{3.11}$$

where the ion velocity spread can be neglected. A single electron with energy E_{lab} possesses a collision energy in the ion center of mass frame that can be calculated analogously to equation 3.1:

$$E_{\mathrm{CM}} = m_{\mathrm{e}} \left[\sqrt{\frac{E_{\mathrm{lab}}}{m_{\mathrm{e}}}} - \sqrt{\frac{E_{\mathrm{cool}}}{m_{\mathrm{e}}}} \right]^2 = \left(\sqrt{E_{\mathrm{lab}}} - \sqrt{E_{\mathrm{cool}}} \right)^2 \tag{3.12}$$

where the reduced mass has been approximated by the electron mass.

For collision experiments, however, the velocity spread of the electron beam has to be considered. In this case, the center of mass collision energy is statistically distributed with the distribution function determined by a parameter E_{d} that is called *detuning energy*, where

$$E_{\mathrm{d}} = \left(\sqrt{E_{\mathrm{lab,0}}} - \sqrt{E_{\mathrm{cool}}} \right)^2 \tag{3.13}$$

and $E_{\mathrm{lab,0}}$ stands for the lab frame energy calculated by equation 3.4, neglecting the statistical distribution of electron energies. In chapter 4.2.2, electron velocity and collision energy distributions will be derived in detail.

3.3 A fast neutral fragment imaging detector

In DR experiments the Neutral Imaging in Cold Environment (NICE) detector is utilized for detecting neutral reaction products. It is capable of measuring not only collision rates but also fragment positions and the difference of fragment arrival times, which enables an event-by-event analysis of fragmentation kinematics. Therefore, the NICE detector was used for the purpose of this work.

Particle detectors used in CSR require a specific design. Apart from their operation in cryogenic environment, they have to withstand Ultra High Vacuum (UHV) conditions and be bakeable to temperatures around 250°C. The choice of detector technology is further limited by the constraint of a high detection efficiency in the keV particle energy range. As a solution for a fast neutral detector with imaging capabilities, NICE uses the combination of a MCP-based single particle detector and a phosphor screen. It was designed and commissioned in the work of Becker 2016 and was already used for rate

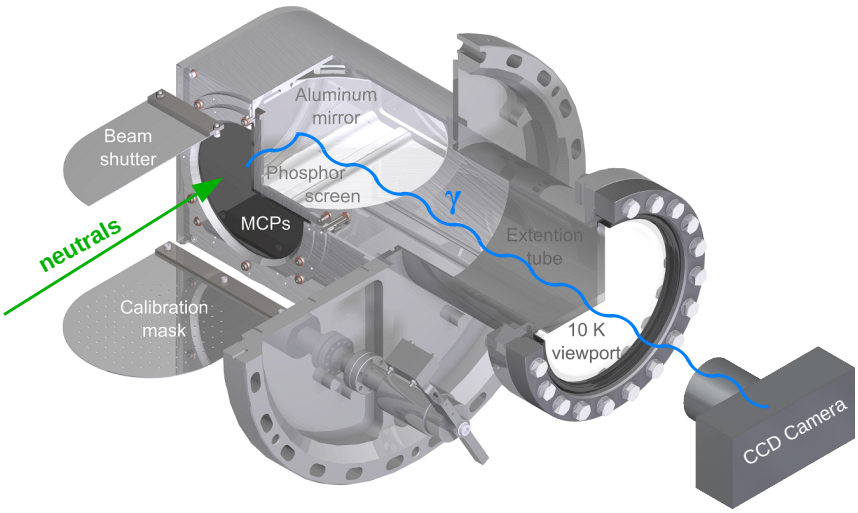

Figure 3.6: Simplified model of the NICE detector. Neutral particles cause electron avalanches in the MCP stack that are converted into photons on a phosphor screen. A CCD camera is utilized for detecting impact positions. The central part of the figure was developed by Dr. Arno Becker and was amended by particle trajectories and the camera for illustration purposes.

and imaging measurements of DR in Novotný et al. 2019. A short summary of the detection principle shall be given here.

A model of NICE is presented in Figure 3.6. Neutral fragments hitting the detector cause electron avalanches in the Chevron-type MCP stack. An avalanche propagates to the phosphor screen, where visible photons are emitted on the timescale of nanoseconds. The light is deflected by a 90° aluminum mirror out of the infrared-tight experimental-vacuum and isolation-vacuum view ports. To protect the detector in case of too high particles fluxes, a mechanical shutter in form of a thin aluminum plate is mounted in front of the MCP and can be moved by a rotary feedthrough. The same holds for a calibration mask that is equipped with a pattern of holes spaced by 10 mm. As presented in section 4.5.1 the mask is used for calibrating fragment distances.

Electron avalanches hitting the phosphor screen result in electronic pulses on top of the high DC supply voltage. The induced electronic signal is capacitively decoupled by a special circuit, described in Becker 2016. It is utilized as trigger for the data acquisition system (see chapter 4.4). Furthermore, the signal is obtained as electronic waveform and digitized with sampling times of 1 ns in order to obtain timing information for detection of multiple fragments. Due to the high impedance of the MCPs at cryogenic temperatures ($\approx$ TΩ), the detector is actively heated to $\approx$ 40 K, where count rates of $\approx$ 5 kHz can be reached without observable saturation effects.

Outside the vacuum chamber a fast CMOS camera (*Microtron EoSens CL*) collects and transmits images of light spots arising from the phosphor screen, with shutter triggered by the electronic signal. The camera interface is capable of transferring at

frame rates of 1 kHz at a typically used resolution of 512×512 pixel. Saturation of the camera at higher impact rates leads to losses of imaging data. However, the count rate data are resolved and stored also for higher rates, as explained above.

One property of the NICE detector is a constant signal, arising homogeneously from the detector surface, even when no ions are stored in CSR. This signal is referred to as *dark counts* and appears at a rate of $R_{\mathrm{dark}} \approx 50\,\mathrm{Hz}$, depending slightly on the detector settings. Dark counts in MCP-based detectors are expected to be caused by cosmic ray induced showers of secondary particles and by inner radioactivity of the MCP material (Fraser, Pearson, and Lees 1987). The signal is typically measured in an ion-beam-off-phase and subtracted as a constant background. Further discussion on the *dark count rate* within the CH^+ beamtime is given in appendix C.1.1.

Chapter 4

Beam characterization, data acquisition and analysis procedures

The CSR merged-beams apparatus presented in the previous chapter is capable of high-resolution, absolute rate measurements. Both features require a detailed knowledge of the two particle beam currents and their energy distributions. This chapter is intended to give an overview of the relevant ion and electron beam parameters. The principle for absolute ion current measurements is explained in section 4.1, while the electron beam profile, density and velocity distribution is discussed in section 4.2. Especially for the latter, a comprehensive evaluation was aimed for in this work, as it is of crucial importance for comparison of cross sections with measured rate coefficients for any collisional process in the CSR electron cooler, as explained in section 4.3.

General properties of the data acquisition system used for electron collision experiments at CSR are presented in section 4.4, explaining the concept of rate and imaging measurements. In order to analyze acquired data, some detector calibration procedures have to be followed in section 4.5. All considerations in this chapter are intended to provide general information about collision experiments with the CSR electron cooler. Details about CH^+ specific measurements and analysis steps will be given in chapter 5.

4.1 Ion beam current measurement

For collision experiments at CSR, a major step towards absolute rate measurements is to ensure that the ion beam is small enough to be covered by a constant density electron beam. In that case, all necessary information for absolute calibration is given by the ion current, or the directly associated number of ions N_{ion} in the storage ring, and by the electron beam density in the interaction zone $n_{\mathrm{e,int}}$ (see equation 3.6).

In order to obtain ion numbers, the ion beam is bunched by the RF cavity and its mirror charge is detected by the capacitive current pickup (see Figure 3.1). Here, a waveform of the bunched ion beam signal is obtained. Due to the fact that this signal is weak compared to environmental electronic noise, the total waveform is split into sub-waveforms corresponding to exactly one ion revolution each. An average of all sub-waveforms is calculated to obtain a clear voltage signal $U_{\mathrm{p}}(t)$ of the ion bunches in the storage ring. The connection between ion number N_{ion} and time-dependent pickup voltage is derived in Vogel 2016 as

$$N_{\mathrm{ion}} = \frac{C_{\mathrm{p}} C_0}{z e L_0 T_0 G} \int_0^{T_0} U_{\mathrm{p}}(t)\,\mathrm{d}t \tag{4.1}$$

where C_{p} is the measured capacity of the current pickup detection system, C_0 the CSR circumference, z the ion charge state, $L_0 = 30\,\mathrm{mm}$ the pickup length, G the amplifier gain, and $T_0 = f_{\mathrm{rev}}^{-1}$ the ion revolution time for a single turn. The pick-up capacity has been measured at room temperature to $C_{\mathrm{p,warm}} = 97.3(13)\,\mathrm{pF}$ in Vogel 2016. In cryogenic operation it is expected to decrease slightly and an additional uncertainty margin is added in the same work. Moreover, the input transistor of the cryogenic amplifiers had to be exchanged several times since the capacity measurement was conducted, such that a total uncertainty of 5% is estimated and $C_{\mathrm{p}} = 96.0(48)\,\mathrm{pF}$. The specific procedure for measuring the ion current in the CH^+ beamtime is summarized in chapter 5.7.

4.2 Electron beam characterization

As discussed in the previous section, a broad and constant density electron beam is advantageous in the electron-ion interaction zone. Furthermore, the electron velocity distribution is of important knowledge for cooling and collision experiments. Thus, the following subsections are concerned with the description and optimization of the electron beam profile and velocity distribution.

4.2.1 Beam profile optimization and density

The shape of the electron beam profile is mainly influenced by the Pierce and extraction electrode settings, which belong to the electron gun (Figure 3.3). A systematic study of beam profiles at the gun-side Faraday cup was done in the course of this work and is presented here.

In order to record a profile, the electron beam is scanned over the main cup pinhole by the horizontal and vertical steering coils in the first room-temperature solenoid. The profile is obtained by measuring the current going through the pinhole to the analyzer cup I_a as function of the steering currents. The deflection introduced by the steerers for a room-temperature solenoid current of $I_\mathrm{acc} = 10.8\,\mathrm{A}$ was calibrated to the steerer currents I_x and I_y in the work of Wilhelm 2019 and led to calibration factors of

$$\begin{aligned} k_x &= 4.180\,\mathrm{mm/A} \\ k_y &= 4.098\,\mathrm{mm/A} \end{aligned} \tag{4.2}$$

that are used to determine the absolute size of the electron beam.

For interpreting beam profiles the adiabatic magnetic expansion (see section 3.2) from electron gun to other regions of lower magnetic field strength has to be considered. Hereby, the beam radius increases from the cathode r_cath to the low-field section by

$$r_\mathrm{beam} = \sqrt{\alpha} r_\mathrm{cath} \tag{4.3}$$

where α is the expansion factor.

Figure 4.1 shows electron beam profiles obtained for different settings of U_pierce and U_ext. In each contour plot the profile is compared to the expected beam size (red circle) for an effective cathode radius of $r_\mathrm{cath} = 1.2\,\mathrm{mm}$ and an expansion factor of $\alpha = 12.56$, as expected from the magnetic field strengths. All profiles show increased densities on the left side, indicating a general tilt that is more prominent for low extraction voltages (top row). For a constant U_ext the electron beam size scales with U_pierce, which is a desirable effect. However, at too high pierce voltages additional peaks in the profile appear on the top left and the tilt increases slightly. For a constant setting of U_pierce, the electron beam size increases with U_ext and the tilt gets less prominent.

A compromise between high electron beam sizes and most homogeneous profiles is given by the two pictures in the center column. The matrix shown in Figure 4.1 was extended by several more voltage combinations. From those measurements an optimal setting of U_pierce for each value of U_ext can be obtained. The dependence is summarized in Figure 4.2 and serves as a standard for the electron gun setup. Each point in the diagram corresponds to a different electron current I_e, which increases with higher values of U_ext. Further details on this dependence were already given in section 3.2.2.

Profile scans, as shown in this section, can be used to infer the effective cathode radius. The corresponding procedure is described in detail on page 88 of Wilhelm 2019 and is used frequently in this work. r_cath depends on the electron gun settings and, additionally, can be changing slightly due to the cathode surface properties. The

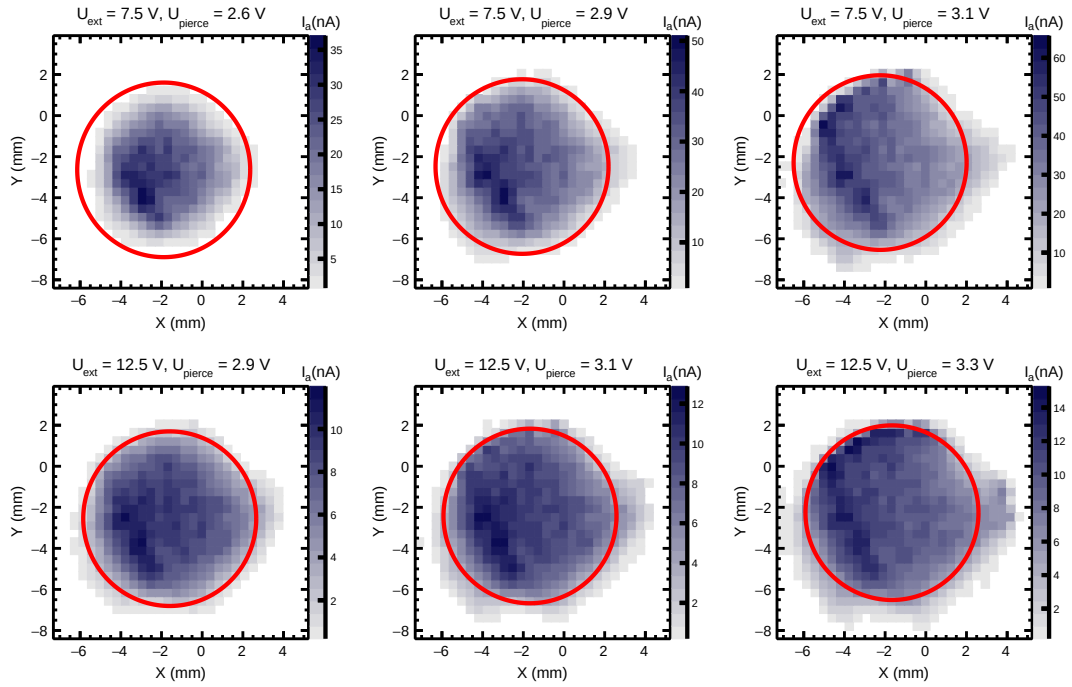

Figure 4.1: Electron beam profiles for different potential settings. The top and bottom row show different extraction voltages, while the Pierce voltage is scanned from left to right. A circle centered to the center of charge with a radius of 4.25 mm is added into each diagram, corresponding to an effective cathode radius of $r_{\mathrm{cath}} = 1.2\,\mathrm{mm}$. The color axis corresponds to the measured analyzer cup current I_{a}.

uncertainty of the radius ($\Delta r_{\mathrm{cath}} = 0.05\,\mathrm{mm}$) was determined from differences between gun-side and collector-side measurements and is slightly overestimated to account for uncertainties introduced by the algorithm in the determination of r_{cath}.

The previously mentioned tilt in the profiles violates the approximation of a constant-density electron beam, which is especially evident for low electron currents ($I_{\mathrm{e}} < 5\,\mu\mathrm{A}$). In the course of this work, the dependence of the tilt on the photocathode laser alignment was checked. Over a broad range of settings the profile did not show any response while for very specific laser positions it could be influenced at the cost of minimizing the electron current. The measurements indicate that the laser beam covers the full cathode surface in standard alignment. Hence, the tilt in the electron beam profiles is likely caused by a misalignment of the electron gun electrodes, most likely the Pierce electrode, which is closest to the cathode surface. Due to the low-energy and low-current regime of the CSR electron cooler it is, however, unclear whether it is possible at all to generate homogeneous profiles under these conditions. In case of higher electron currents the profile usually approaches a constant density and the measurement of densities via effective cathode radii (equations 3.6 and 4.3) is a reasonable way to calculate absolute rate coefficients.

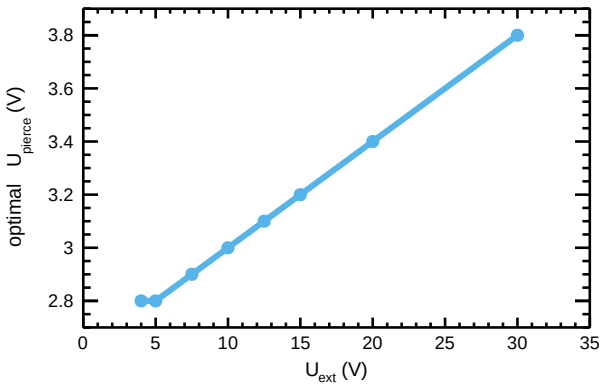

Figure 4.2: Electron gun settings for homogeneous beam profiles. The optimal combination of Pierce and extraction voltage on this line is determined by the desired electron current I_e. The corresponding values I_e for the displayed data points from left to right are: 0.5 μA, 1.4 μA, 5.4 μA, 11.7 μA, 19.8 μA, 28.1 μA, 44.4 μA and 108.4 μA.

4.2.2 Velocity and energy distributions

Efficient electron cooling as well as high-resolution experiments require a low electron beam velocity and energy spread. In the cylindrically symmetric field of the electron cooler, it is reasonable to define a longitudinal and transverse electron beam temperature according to Pastuszka et al. 1996 by

$$T_{\parallel} = \frac{m_e}{k_B}\left(\langle v_{\parallel}^2\rangle - \langle v_{\parallel}\rangle^2\right) \tag{4.4}$$

$$T_{\perp} = \frac{m_e}{k_B}\langle v_{\perp}^2\rangle \tag{4.5}$$

where $v_{\parallel}$ stands for the longitudinal and $v_{\perp}$ for the transverse velocity of an electron. The mean value of the transverse velocity is assumed to be negligible. Publications and works on electron cooling and collision experiments in storage rings typically assume an electron velocity distribution in lab frame as given in Pastuszka et al. 1996:

$$f(\vec{v}) = \sqrt{\frac{m_e}{2\pi k_B}}^3 \frac{1}{T_{\perp}\sqrt{T_{\parallel}}} \times \exp\left(-\frac{m_e v_{\perp}^2}{2k_B T_{\perp}} - \frac{m_e(v_{\parallel} - \langle v_{\parallel}\rangle)^2}{2k_B T_{\parallel}}\right) \tag{4.6}$$

which is called a flattened Maxwellian distribution. It assumes a thermalization of the longitudinal and transverse degrees of freedom, separately. However, thermalization between longitudinal and transverse degrees of freedom is neglected due to the strong magnetic guiding field in the electron cooler.

Since knowledge of electron velocity and energy distributions is essential for inferring cross sections from merged-beams rate coefficients (see section 4.3), the validity of the flattened Maxwellian assumption is examined here and transverse and longitudinal temperatures are discussed. For all considerations in this section, it is assumed that the

magnetic guiding field decouples the longitudinal and transverse degrees of freedom such that the total velocity distribution can be factorized into

$$f(\vec{v}) = f(v_\perp) f(v_\parallel) \tag{4.7}$$

Transverse velocity distribution

A low transverse temperature in CSR experiments is achieved initially by extracting electrons from a room-temperature cathode ($k_B T_{\perp,\mathrm{gun}} = 25\,\mathrm{meV}$). Since the transverse degrees of freedom are thermalized already at the cathode surface and acceleration/deceleration is taking place only in the longitudinal direction, the transverse electron velocity distribution stays Maxwellian over the whole electron cooler:

$$f(v_\perp) = \frac{m_\mathrm{e}}{2\pi k_\mathrm{B} T_\perp} \exp\left(-\frac{m_\mathrm{e} v_\perp^2}{2 k_\mathrm{B} T_\perp}\right) \tag{4.8}$$

With help of a magnetic adiabatic expansion of the electron beam from a high solenoidal field in the electron gun of B_gun to lower magnetic fields (see section 3.2), the transverse temperature can be reduced further, as discussed in Pastuszka et al. 1996:

$$T_\perp = \frac{B}{B_\mathrm{gun}} T_{\perp,\mathrm{gun}} = \frac{T_{\perp,\mathrm{gun}}}{\alpha} \tag{4.9}$$

Typical values for the magnetic fields in the room-temperature section after acceleration and in the interaction zone are $B_\mathrm{acc} = 200\,\mathrm{G}$ and $B_\mathrm{int} = 100\,\mathrm{G}$, leading to expansion factors of $\alpha_\mathrm{acc} = 10$ and $\alpha_\mathrm{int} = 20$. For an ideal adiabatic expansion, a lower limit of the transverse temperature can be calculated to

$$T_{\perp,\mathrm{min}} = 1.25\,\mathrm{meV} \tag{4.10}$$

Previous experiments at TSR have shown that such low temperatures cannot be reached even for a cathode cooled to $T_\mathrm{c} \approx 100\,\mathrm{K}$ (Novotný et al. 2013). Hence, the transverse temperature in the current setup is assumed to be higher than the theoretical minimum with a value of

$$T_\perp = 2 - 3\,\mathrm{meV} \tag{4.11}$$

As a dependence on the electron cooler operation parameters has not been studied up to now, this value is assumed to be constant. An experimental determination of $T_\perp$ is planned for the future.

Longitudinal velocity distribution - finite cathode temperature acceleration

In contrast to the transverse velocity distribution, the longitudinal one cannot be assumed to be thermalized from the beginning. The acceleration in the gun section and deceleration in the drift-tube region are fast processes. This section aims to calculate the longitudinal velocity distribution after acceleration for a finite cathode temperature T_c.

In space-charge limited emission mode an electron cloud is established in front of the photocathode that acts as a virtual cathode. The velocity distribution in this cloud can be assumed thermalized to the cathode temperature. Jansen 1990 approximates the virtual cathode by a hollow container with a small hole, from which electrons can be extracted. It is deduced that only electrons with positive velocities, which is half of the Maxwellian distribution, are able to leave the container. Additionally, the electron density outside the container is weighted by the particle flux compared to the inside. The corresponding velocity distribution of emitted electrons, therefore, only contains positive velocities and is additionally weighted by $v_\parallel$:

$$f_\mathrm{i}(v_\parallel) = A v_\parallel \Theta(v_\parallel) \exp\left(-\frac{m_\mathrm{e} v_\parallel^2}{2 k_\mathrm{B} T_\mathrm{c}}\right) \tag{4.12}$$

where A is a normalization factor and $\Theta(x)$ is the Heaviside step function. Since A is wrongly calculated in Jansen 1990, it is determined here by integrating the distribution over the whole space

$$\int_{-\infty}^{\infty} f_\mathrm{i}(v_\parallel)\,\mathrm{d}v_\parallel = A\frac{k_\mathrm{B} T_\mathrm{c}}{m_\mathrm{e}} \equiv 1 \tag{4.13}$$

leading to

$$f_\mathrm{i}(v_\parallel) = \frac{m_\mathrm{e}}{k_\mathrm{B} T_\mathrm{c}} v_\parallel \Theta(v_\parallel) \exp\left(-\frac{m_\mathrm{e} v_\parallel^2}{2 k_\mathrm{B} T_\mathrm{c}}\right) \tag{4.14}$$

With

$$E_\parallel = \frac{m_\mathrm{e}}{2} v_\parallel^2 \tag{4.15}$$

the distribution can be transformed into energy space:

$$f_\mathrm{i}(E_\parallel) = \frac{\mathrm{d}v_\parallel}{\mathrm{d}E_\parallel} f(v_\parallel) = \frac{1}{k_\mathrm{B} T_\mathrm{c}} \Theta(E_\parallel) \exp\left(-\frac{E_\parallel}{k_\mathrm{B} T_\mathrm{c}}\right) \tag{4.16}$$

Accelerating all electrons by a common voltage U shifts the distribution to

$$f_T(E_\parallel) = \frac{1}{k_\mathrm{B} T_\mathrm{c}} \Theta(E_\parallel - eU) \exp\left(-\frac{E_\parallel - eU}{k_\mathrm{B} T_\mathrm{c}}\right) \tag{4.17}$$

Back-transforming into velocity space yields the accelerated velocity distribution

$$f_T(v_\parallel) = \frac{\mathrm{d}E_\parallel}{\mathrm{d}v_\parallel} f(E_\parallel) = \frac{m_\mathrm{e}}{k_\mathrm{B} T_\mathrm{c}} v_\parallel \Theta\left(v_\parallel - v_\mathrm{acc}\right) \exp\left(-\frac{m_\mathrm{e} v_\parallel^2/2 - eU}{k_\mathrm{B} T_\mathrm{c}}\right) \tag{4.18}$$

where $v_\mathrm{acc} = \sqrt{2eU/m_\mathrm{e}}$. The longitudinal temperature of the accelerated system can be calculated with equation 4.4, requiring the mean velocity and mean squared velocity as inputs

$$\langle v_\parallel \rangle = \int_{-\infty}^{\infty} v_\parallel f_T(v_\parallel)\,\mathrm{d}v_\parallel = \frac{m_\mathrm{e}}{k_\mathrm{B} T_\mathrm{c}} \int_{v_\mathrm{acc}}^{\infty} v_\parallel^2 \exp\left(-\frac{m_\mathrm{e} v_\parallel^2/2 - eU}{k_\mathrm{B} T_\mathrm{c}}\right) \mathrm{d}v_\parallel \tag{4.19}$$

which can be solved analytically to

$$\langle v_\parallel \rangle = \frac{1}{2}\sqrt{\frac{2k_\mathrm{B}T_\mathrm{c}}{m_\mathrm{e}}}\left[\sqrt{\pi}e^a\left(1-\mathrm{erf}\left(\sqrt{a}\right)\right)+2\sqrt{a}\right] \tag{4.20}$$

with $a = \frac{eU}{k_\mathrm{B}T_\mathrm{c}}$ and $\mathrm{erf}(x)$ representing the Gauss error function. The mean squared velocity is given by

$$\langle v_\parallel^2 \rangle = \int_{-\infty}^{\infty} v_\parallel^2 f_T(v_\parallel)\,\mathrm{d}v_\parallel = \frac{m_\mathrm{e}}{k_\mathrm{B}T_\mathrm{c}}\int_{v_\mathrm{acc}}^{\infty} v_\parallel^3 \exp\left(-\frac{m_\mathrm{e}v_\parallel^2/2 - eU}{k_\mathrm{B}T_\mathrm{c}}\right)\mathrm{d}v_\parallel \tag{4.21}$$

with analytical solution

$$\langle v_\parallel^2 \rangle = \frac{2k_\mathrm{B}T_\mathrm{c}}{m_\mathrm{e}}(a+1) \tag{4.22}$$

Inserting both mean values into equation 4.4 leads to the longitudinal temperature of

$$k_\mathrm{B}T_\parallel = k_\mathrm{B}T_\mathrm{c}\left(2(a+1)-\frac{1}{2}\left[\sqrt{\pi}e^a\left(1-\mathrm{erf}\left(\sqrt{a}\right)\right)+2\sqrt{a}\right]^2\right) \tag{4.23}$$

Typically, the acceleration energy is significantly higher than the thermal energy ($a \gg 1$), allowing for a Taylor expansion in $1/a$:

$$k_\mathrm{B}T_\parallel = k_\mathrm{B}T_\mathrm{c}\left(\frac{1}{2a}-\frac{1}{a^2}+O\left(\frac{1}{a^3}\right)\right) \tag{4.24}$$

The first term of the expansion is identical with the kinematic compression formula that is commonly used in publications (see Orlov et al. 2006) and also resulting from the calculations in Jansen 1990:

$$k_\mathrm{B}T_\parallel = \frac{(k_\mathrm{B}T_\mathrm{c})^2}{2eU} \tag{4.25}$$

Longitudinal velocity distribution - finite acceleration voltage noise

In previous considerations it was assumed that the acceleration voltage is fixed. However, in the experiment it has been observed that electronic noise ΔU between cathode and ground potential is of the order of or even higher than thermal energies $k_\mathrm{B}T_\mathrm{c}$. In this section a negligible cathode temperature is assumed and electrons are accelerated by a Gaussian voltage distribution, leading to a Gaussian electron energy distribution after acceleration:

$$f_\mathrm{n}(E_\parallel) = \frac{1}{\sqrt{2\pi e^2\Delta U^2}}\exp\left(-\frac{(E_\parallel - eU)^2}{2e^2\Delta U^2}\right) \tag{4.26}$$

The distribution is transformed into the velocity space

$$f_\mathrm{n}(v_\parallel) = \frac{m_\mathrm{e}v_\parallel}{\sqrt{2\pi e^2\Delta U^2}}\exp\left(-\frac{(m_\mathrm{e}v_\parallel^2/2 - eU)^2}{2e^2\Delta U^2}\right) \tag{4.27}$$

and the mean velocity can be calculated as

$$\langle v_\parallel \rangle = \int_{-\infty}^{\infty} v_\parallel f_\mathrm{n}(v_\parallel)\,\mathrm{d}v_\parallel = \frac{m_\mathrm{e}}{\sqrt{2\pi e^2 \Delta U^2}} \int_0^{\infty} v_\parallel^2 \exp\left(-\frac{(m_\mathrm{e} v_\parallel^2/2 - eU)^2}{2e^2\Delta U^2}\right) \mathrm{d}v_\parallel \tag{4.28}$$

Solving the integral leads to

$$\begin{aligned}\langle v_\parallel \rangle = v_\mathrm{acc} \frac{\pi}{4\sqrt{2\pi\sigma^2}} e^{-\frac{1}{4\sigma^2}} \Bigg[& I_{-1/4}\left(\frac{1}{4\sigma^2}\right) + (2\sigma^2+1) I_{1/4}\left(\frac{1}{4\sigma^2}\right) \\ & + I_{3/4}\left(\frac{1}{4\sigma^2}\right) + I_{5/4}\left(\frac{1}{4\sigma^2}\right)\Bigg]\end{aligned} \tag{4.29}$$

with $\sigma = \frac{e\Delta U}{eU}$ and $I_n(x)$ being the modified Bessel function of first kind. The electronic noise is assumed to be significantly smaller than the mean acceleration voltage. Consequently, the result can be Taylor-expanded for $\sigma \ll 1$:

$$\langle v_\parallel \rangle = v_\mathrm{acc}\left(1 - \frac{1}{8}\sigma^2 + O(\sigma^4)\right) \tag{4.30}$$

Calculation of the mean squared velocity yields

$$\langle v_\parallel^2 \rangle = \int_{-\infty}^{\infty} v_\parallel^2 f_\mathrm{n}(v_\parallel)\,\mathrm{d}v_\parallel = \frac{m_\mathrm{e}}{\sqrt{2\pi e^2 \Delta U^2}} \int_0^{\infty} v_\parallel^3 \exp\left(-\frac{(m_\mathrm{e} v_\parallel^2/2 - eU)^2}{2e^2\Delta U^2}\right) \mathrm{d}v_\parallel \tag{4.31}$$

which can be solved to

$$\langle v_\parallel^2 \rangle = v_\mathrm{acc}^2 \left[\frac{1}{2} - \frac{1}{2}\mathrm{erf}\left(\frac{-1}{\sqrt{2}\sigma}\right) + \frac{1}{\sqrt{2\pi}}\sigma e^{-\frac{1}{2\sigma^2}}\right] \tag{4.32}$$

Taylor expansion for small σ results in

$$\langle v_\parallel^2 \rangle = v_\mathrm{acc}^2\left(1 + O(\sigma^2 e^{-\frac{1}{2\sigma^2}})\right) \approx v_\mathrm{acc}^2 \tag{4.33}$$

where the exponential term can be safely neglected compared to the polynomial terms in $\langle v_\parallel \rangle$.

With help of equation 4.4, the longitudinal temperature can be extracted as

$$k_\mathrm{B} T_\parallel = \frac{eU}{2}\left(\sigma^2 + O(\sigma^4)\right) \approx \frac{(e\Delta U)^2}{2eU} \tag{4.34}$$

The result is comparable to equation 4.25, where the thermal energy spread $k_\mathrm{B}T_\parallel$ has been replaced by the Gaussian acceleration voltage spread $e\Delta U$.

Longitudinal velocity distribution - combined temperature and noise effects

In the last two sections the longitudinal velocity distributions for finite cathode temperature (equation 4.18) and finite electronic noise (equation 4.27) were derived. Considering both effects together requires a convolution of both velocity distributions, which

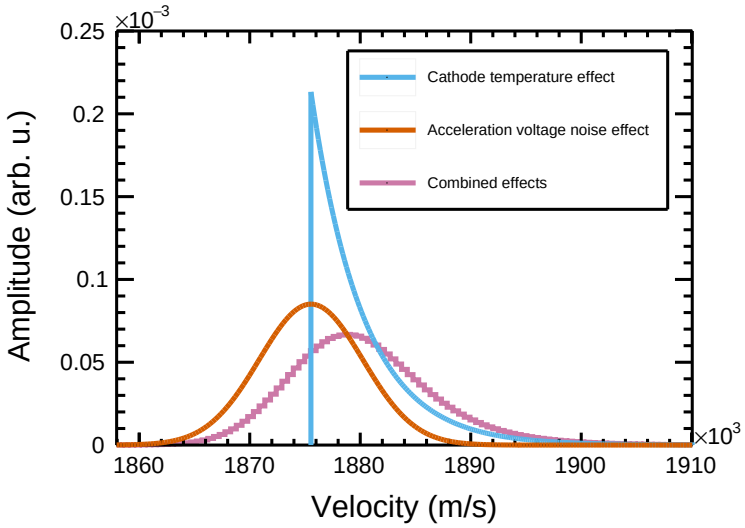

Figure 4.3: Electron velocity distributions after acceleration. The blue curve considers only broadening due to finite cathode temperature ($k_\mathrm{B}T_\mathrm{c} = 50\,\mathrm{meV}$), while the orange curve solely includes a Gaussian noise on the acceleration voltage ($e\Delta U = 50\,\mathrm{meV}$). The combined effect is presented as pink curve. All distributions assume a mean acceleration voltage of $\langle U \rangle = 10\,\mathrm{V}$.

is analytically impossible. Instead, a Monte Carlo based approach is chosen in this section.

Equation 4.18 is an exact solution for a fixed voltage U. By parametrizing the voltage according to a Gaussian distribution with mean value $\langle U \rangle$ and standard deviation ΔU and taking samples $U_i (i \in \{1, ..., n\})$, the combined velocity distribution is approximated by an average over all individual, fixed-voltage distributions:

$$f(v_\parallel) = \frac{1}{n} \sum_{i=1}^{n} f_T(v_\parallel, U_i) \tag{4.35}$$

Figure 4.3 presents velocity distributions for the combination of cathode temperature and acceleration voltage noise as well as for the individual effects. The distributions assume $k_\mathrm{B}T_\mathrm{c} = 50\,\mathrm{meV}$, $e\Delta U = 50\,\mathrm{meV}$ and $\langle U \rangle = 10\,\mathrm{V}$. The temperature-based distribution shows a sharp cut around $v_\mathrm{acc} = 1.876 \times 10^6\,\mathrm{m/s}$ due to the assumption of a half-Maxwellian before acceleration. Moreover, the distribution is asymmetric with a significantly higher mean value than v_acc. In contrast to that, the noise-based distribution is approximated well by a Gaussian distribution around a mean value close to v_acc. The resulting combined distribution is still slightly asymmetric but does not show a sharp cutoff any more.

The temperature of the combined distribution can be calculated from the mean ve-

locity of the histogram and the individual bin contents $f(v_{\parallel,j}), j \in \{1, ..., m\}$ by

$$\begin{aligned} k_\mathrm{B}T_\parallel &= m_\mathrm{e}\left(\langle v_\parallel^2\rangle - \langle v_\parallel\rangle^2\right) = m_\mathrm{e}\langle v_\parallel^2 - \langle v_\parallel\rangle^2\rangle \\ &= \frac{\sum_{j=1}^{m} f(v_{\parallel,j})\left(v_{\parallel,j}^2 - \langle v_\parallel\rangle^2\right)}{\sum_{j=1}^{m} f(v_{\parallel,j})} \end{aligned} \tag{4.36}$$

This evaluation was done for several combinations of $k_\mathrm{B}T_\mathrm{c}$ and $e\Delta U$ and shows a perfect agreement to the formula

$$k_\mathrm{B}T_\parallel = \frac{(k_\mathrm{B}T_c)^2 + (e\Delta U)^2}{2e\langle U\rangle} \tag{4.37}$$

In further considerations this formula will be applied whenever $k_\mathrm{B}T_\mathrm{c} \ll e\langle U\rangle$ and $e\Delta U \ll e\langle U\rangle$. For typical operational conditions of the CSR electron cooler with $k_\mathrm{B}T_\mathrm{c} = 25\,\mathrm{meV}$ and $e\langle U\rangle \approx 20\,\mathrm{eV}$ as well as an electronic noise of $e\Delta U = 100\,\mathrm{meV}$ (see section 4.2.3), the longitudinal temperature before the interaction zone amounts to

$$k_\mathrm{B}T_{\parallel,\mathrm{acc}} = 0.27\,\mathrm{meV} \tag{4.38}$$

Thermalization and timescales

The considerations in previous sections revealed that electron beam velocities do not necessarily follow a Maxwellian distribution. However, during the path of flight from cathode to interaction zone, electron-electron interactions can lead to a thermalization of the distribution. In order to estimate timescales for such a thermalization process, the electron beam is approximated by a one-component plasma. According to Kudelainen et al. 1982 the timescale for thermalization can be estimated to the inverse plasma frequency

$$t_\mathrm{therm} = \frac{2\pi}{\omega_\mathrm{p}} = 2\pi\sqrt{\frac{\varepsilon_0 m_\mathrm{e}}{n_\mathrm{e}e^2}} \tag{4.39}$$

and transformed into a thermalization length via

$$L_\mathrm{therm} = \sqrt{\frac{2E_\mathrm{lab}}{m_\mathrm{e}}}t_\mathrm{therm} \tag{4.40}$$

This quantity becomes large for low electron densities and high electron energies. An estimate for rather extreme values (high L_therm) in the CSR electron cooler operation is given by an energy of $E_\mathrm{lab} = 20\,\mathrm{eV}$ and densities of $n_\mathrm{e,gun} = 2\times10^6\,\mathrm{cm}^{-3}$, $n_\mathrm{e,acc} = 2\times10^5\,\mathrm{cm}^{-3}$ and $n_\mathrm{e,int} = 1\times10^5\,\mathrm{cm}^{-3}$ in the gun section, room-temperature section and interaction zone, respectively. This corresponds to thermalization path lengths in the three sections of

$$\begin{aligned} L_\mathrm{therm,gun} &= 0.21\,\mathrm{m} \\ L_\mathrm{therm,acc} &= 0.66\,\mathrm{m} \\ L_\mathrm{therm,int} &= 0.93\,\mathrm{m} \end{aligned} \tag{4.41}$$

Even in this worst-case estimate, the electron beam is almost thermalized after the high-field magnet of length 0.2 m but definitely in the room-temperature region. Therefore, a flattened Maxwellian velocity distribution, as given in equation 4.6, is a reasonable approximation. However, the deceleration in the $L_{\mathrm{int}} \approx 0.8\,\mathrm{m}$ long drift-tube does not allow the electron beam to thermalize immediately again in the interaction zone.

Relaxation effects

As pointed out in the previous sections, the longitudinal temperature of the electron beam is typically at least an order of magnitude smaller than the transverse one due to the kinematic compression effect. During the thermalization process, collisions between electrons can, in principle, transfer energy from the transverse into longitudinal degrees of freedom, which is referred to as Transverse-Longitudinal Relaxation (TLR) (Dikansky et al. 1988). This effect is suppressed in strong magnetic fields, i. e., when the minimum distance between electrons r_{min} is larger than their Larmor radius $\rho_\perp$. Kudelainen et al. 1982 give expressions for both quantities:

$$\begin{aligned} \rho_\perp &= \frac{\sqrt{2 k_\mathrm{B} T_\parallel m_\mathrm{e}}}{e B_\mathrm{gun}} \\ r_\mathrm{min} &= \min\left[\frac{e^2}{4\pi\varepsilon_0 k_\mathrm{B} T_\parallel}, n_\mathrm{e}^{-1/3}\right] \end{aligned} \tag{4.42}$$

While $\rho_\perp$ is maximized for high longitudinal temperatures and low magnetic field strengths, r_{min} is given by the first term for typical CSR electron cooler operation and scales inversely with temperature. In case of $k_\mathrm{B} T_\parallel = 0.3\,\mathrm{meV}$ and $B_\mathrm{gun} = 2000\,\mathrm{G}$ both quantities amount to

$$\begin{aligned} \rho_\perp &= 0.29\,\mu\mathrm{m} \\ r_\mathrm{min} &= 4.7\,\mu\mathrm{m} \end{aligned} \tag{4.43}$$

Consequently, the effect of TLR can be neglected.

After a sudden acceleration in the gun section, electron scattering effects are able to minimize the potential energy of the beam. This additional relaxation effect is called Longitudinal-Longitudinal Relaxation (LLR) and is, for magnetized beams, even able to form crystalline structures. Due to collisions in the beam, the longitudinal temperature is increased in the LLR process. Dikansky et al. 1988 give an expression for the increase:

$$\Delta k_\mathrm{B} T_\parallel = C \frac{e^2}{4\pi\varepsilon_0} n_\mathrm{e}^{1/3} \tag{4.44}$$

where C is a factor of order unity, characterizing the acceleration process and final structure of the electron beam. Orlov et al. 2006 give values between $C = 0.9$ and $C = 1.9$ and come the conclusion that a constant value of C is not matching experimental results. In this work, however, $C = 1.9$ is assumed since no explicit formula for the dependence on other experimental parameters is known.

Equation 4.44 raises the question, which electron density to insert, because of its continuous change over the acceleration region and when passing different potential regions. As described in Dikansky et al. 1988, relaxation calculations typically assume an ideal Pierce geometry, including only the Pierce and extraction electrode. After extraction the electron density assumes the highest value of the whole cooler section. All other relaxations caused by density changes are assumed to increase the temperature much less than the initial step. Therefore, the electron density after extraction $n_{\mathrm{e,ext}}$, corresponding to an energy of E_{ext}, should be used.

A third effect that should be considered for the transverse temperature arises from the adiabatic magnetic expansion of the electron beam. Due to energy conservation, the heat removed from the transverse degrees of freedom is added to the longitudinal one, as discussed in Krantz 2009. Hence, a correction factor of $\left(1+(\alpha-1)^2\alpha^{-2}\right)$ is included together with the LLR relaxation term for estimating the final longitudinal temperature:

$$k_{\mathrm{B}}T_{\parallel} = \left(1+\left(\frac{\alpha-1}{\alpha}\right)^2\right)\frac{(k_{\mathrm{B}}T_{\mathrm{c}})^2}{2e\langle U\rangle} + \frac{(e\Delta U)^2}{2e\langle U\rangle} + C\frac{e^2}{4\pi\varepsilon_0}(n_{\mathrm{e,ext}})^{1/3} \tag{4.45}$$

Drift-tube deceleration

The previous sections prove that for the conditions present in the CSR electron cooler, a thermalized electron beam with a flattened Maxwellian velocity distribution (equation 4.6) can be assumed after the acceleration region, with temperatures given in equations 4.11 and 4.45. The deceleration in the drift-tubes, however, leaves a non-thermalized distribution for part of the interaction zone. Differences to a Maxwellian distribution shall be evaluated in this section.

In the longitudinal component the velocity distribution before the drift-tube section is Maxwellian:

$$f(v_{\parallel}) = \sqrt{\frac{m_{\mathrm{e}}}{2\pi k_{\mathrm{B}}T_{\parallel}}}\exp\left(-\frac{m_{\mathrm{e}}(v_{\parallel}-\langle v_{\parallel}\rangle)^2}{2k_{\mathrm{B}}T_{\parallel}}\right) \tag{4.46}$$

and is transformed into energy space by

$$f(E_{\parallel}) = \frac{\mathrm{d}v_{\parallel}}{\mathrm{d}E_{\parallel}}f(v_{\parallel}) = \sqrt{\frac{1}{4\pi k_{\mathrm{B}}T_{\parallel}E_{\parallel}}}\exp\left(-\frac{m_{\mathrm{e}}\left(\sqrt{2E_{\parallel}/m_{\mathrm{e}}}-\langle v_{\parallel}\rangle\right)^2}{2k_{\mathrm{B}}T_{\parallel}}\right) \tag{4.47}$$

Compared to the significant deceleration in the drift-tube, the mean velocity before the interaction section differs only slightly from the acceleration velocity and $\langle v_{\parallel}\rangle = v_{\mathrm{acc}}$ is assumed for further considerations, leading to

$$f(E_{\parallel}) = \frac{\mathrm{d}v_{\parallel}}{\mathrm{d}E_{\parallel}}f(v_{\parallel}) = \sqrt{\frac{1}{4\pi k_{\mathrm{B}}T_{\parallel}E_{\parallel}}}\exp\left(-\frac{\left(\sqrt{E_{\parallel}}-\sqrt{eU}\right)^2}{k_{\mathrm{B}}T_{\parallel}}\right) \tag{4.48}$$

The distribution is decelerated by the stopping voltage $U_\mathrm{s} = U - U_\mathrm{int}$ to

$$f_\mathrm{int}(E_\parallel) = \sqrt{\frac{1}{4\pi k_\mathrm{B} T_\parallel (E_\parallel + eU_\mathrm{s})}} \exp\left(-\frac{\left(\sqrt{E_\parallel + eU_\mathrm{s}} - \sqrt{eU}\right)^2}{k_\mathrm{B} T_\parallel} \right) \tag{4.49}$$

and back-transformed into velocity space

$$f_\mathrm{int}(v_\parallel) = \frac{\mathrm{d}E_\parallel}{\mathrm{d}v_\parallel} f_\mathrm{int}(E_\parallel) = \sqrt{\frac{1}{1 + v_\mathrm{s}^2/v_\parallel^2}} \sqrt{\frac{m_\mathrm{e}}{2\pi k_\mathrm{B} T_\parallel}} \exp\left(-\frac{m_\mathrm{e}\left(\sqrt{v_\parallel^2 + v_\mathrm{s}^2} - v_\mathrm{acc}\right)^2}{k_\mathrm{B} T_\parallel} \right) \tag{4.50}$$

where $v_\mathrm{s} = \sqrt{2eU_\mathrm{s}/m_\mathrm{e}}$. The resulting velocity distribution deviates from a Maxwellian. Nevertheless, numerical comparisons indicate that the deviation is small. In order to prove this analytically, the following criteria were checked that are necessary for an approximation by a Maxwellian:

1. A relevant range in $v_\parallel$ for the velocity distribution is defined as the highest four orders of magnitude of f_int, i. e., where $\frac{f_\mathrm{int}(v_\parallel)}{\max\{f_\mathrm{int}\}} > 10^{-4}$. This value was chosen because of the fact that the dynamic ranges in the count rates for measuring merged-beams rate coefficients with the CSR electron cooler and NICE detector are of the same order. The velocities marking the interval borders left and right of the distribution maximum are defined as $v_{\parallel,\mathrm{l}}$ and $v_{\parallel,\mathrm{r}}$, respectively.
2. Inside this range the factor $\sqrt{\frac{1}{1+v_\mathrm{s}^2/v_\parallel^2}}$ is approximately constant.
3. The exponent can be Taylor-expanded around the maximum $v_{\parallel,\mathrm{max}} = v_\mathrm{acc}^2 - v_\mathrm{s}^2$ to a quadratic term.
4. Higher order terms in the exponent are approximately constant between $v_{\parallel,\mathrm{l}}$ and $v_{\parallel,\mathrm{r}}$.

A detailed discussion of all criteria goes beyond the scope of this work. Still, the results shall be presented here.

Within the calculations it turned out that point 2. of the previous list is a much weaker restriction than points 3. and 4. and is, therefore, no longer considered. A Taylor-expansion of the exponential term yields

$$\begin{aligned} f_\mathrm{int}(v_\parallel) \approx & C \exp\left[\frac{m_\mathrm{e}\left((1 - v_\mathrm{s}^2/\langle v\rangle^2)(v_\parallel - \sqrt{\langle v\rangle^2 - v_\mathrm{s}^2})^2\right)}{2k_\mathrm{B} T_\parallel} \right] \\ & \times \exp\left[\frac{m_\mathrm{e}\left(\sqrt{1 - v_\mathrm{s}^2/\langle v\rangle^2} v_\mathrm{s}^2/\langle v\rangle^3 (v_\parallel - \sqrt{\langle v\rangle^2 - v_\mathrm{s}^2})^3\right)}{2k_\mathrm{B} T_\parallel} \right] \end{aligned} \tag{4.51}$$

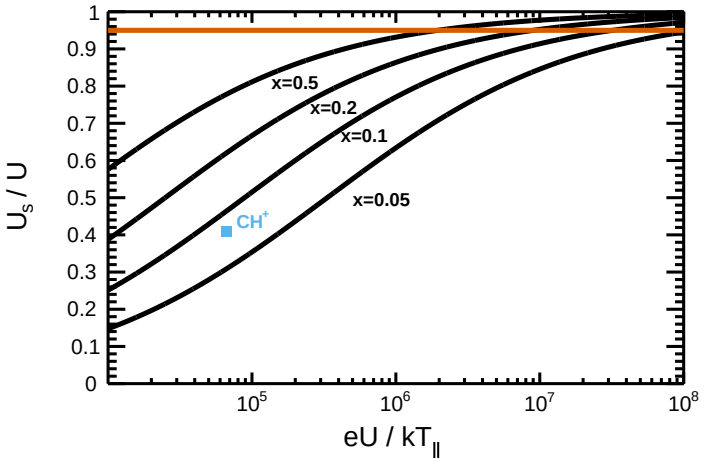

Figure 4.4: Drift-tube mode working parameters for thermalized velocity distributions. The parameter x (equation 4.52) defines the maximum deviation of the real velocity distribution $f_{\mathrm{int}}(v_\parallel)$ in the electron cooler interaction zone compared to a thermalized, i. e., Maxwellian velocity distribution over the range where $\frac{f_{\mathrm{int}}(v_\parallel)}{\max\{f_{\mathrm{int}}\}} > 10^{-4}$ holds. The initial acceleration voltage U, longitudinal temperature $T_\parallel$ after acceleration (equation 4.45), as well as the drift-tube stopping voltage U_s are defined by the electron cooler working parameters. For given settings, the electron velocity distribution after the deceleration step matches a Maxwellian distribution better than $1 - x$ if the corresponding point in the diagram lies below the black line for x. The blue square indicates the working conditions in the CH^+ beamtime, where a Maxwellian distribution is reproduced better than 90% but less than 95%. A red line on top of the graph shows the maximum deceleration for an interaction zone electron energy of $e(U - U_\mathrm{s}) = 1\,\mathrm{eV}$ and acceleration energy of $eU = 20\,\mathrm{eV}$.

The first exponential resembles a Gaussian function while the second one is the next higher order term $g(v_\parallel)$. The requirement of the latter varying only slightly in the range $[v_{\parallel,\mathrm{l}}, v_{\parallel,\mathrm{r}}]$ is expressed by a parameter x with

$$\left| \frac{g(v_\parallel)}{g(v_{\parallel,\max})} - 1 \right| < x \tag{4.52}$$

I. e., a value of $x = 0.1$ expresses that the higher order term is varying less than 10% in the important range of $f_{\mathrm{int}}(v_\parallel)$. A fixed value of x limits the assumption of a thermalized electron distribution in the interaction zone, depending on the working parameters of the electron cooler $\frac{U_\mathrm{s}}{U}$ and $\frac{eU}{kT_\parallel}$ as shown in Figure 4.4. The conditions in the CH^+ beamtime are such that a deviation of less than 10% from a thermalized distribution is expected. Especially for cooling of heavy ions (high $\frac{U_\mathrm{s}}{U}$) and low longitudinal temperatures, this approximation breaks down. At the cost of a lower electron density, it is possible to reduce the initial acceleration voltage U in order to counteract this effect.

From the Gaussian part of equation 4.51, the longitudinal temperature in the inter-

action zone can be calculated to

$$T_{\parallel,\mathrm{int}} = T_{\parallel}\frac{U}{U-U_\mathrm{s}} = T_{\parallel}\frac{U}{U_\mathrm{int}} \tag{4.53}$$

Voltage correction

Up to now, all voltages in this section were expected to directly relate to an electron energy loss or gain. However, due to the cathode contact potential and electron beam space charge potential, energy changes differ from their corresponding voltages, as expressed in equation 3.4. For this reason the energies E_int and E_acc are used further on instead of the voltages U_int and U. With E_int representing the electron energy in the drift-tube section and E_acc the energy after acceleration, expressions for the longitudinal temperatures in both sections are given by

$$k_\mathrm{B}T_{\parallel,\mathrm{acc}} = \left(1+\left(\frac{\alpha-1}{\alpha}\right)^2\right)\frac{(k_\mathrm{B}T_\mathrm{c})^2}{2E_\mathrm{acc}} + \frac{(e\Delta U)^2}{2E_\mathrm{acc}} + C\frac{e^2}{4\pi\varepsilon_0}(n_\mathrm{e,ext})^{1/3} \tag{4.54}$$

$$k_B T_{\parallel,\mathrm{int}} = k_\mathrm{B}T_{\parallel,\mathrm{acc}}\frac{E_\mathrm{acc}}{E_\mathrm{int}} \tag{4.55}$$

LLR term - energy scaling

The LLR temperature contribution was assumed to be constant up to the acceleration region. However, equation 4.53 manifests that the calculated LLR term in equation 4.54 is only valid for the extraction region and should be decreased further when accelerating the electron beam from E_ext to E_acc. Consequently, the expected longitudinal electron temperatures in the accelerated region and interaction zone are given by

$$k_\mathrm{B}T_{\parallel,\mathrm{acc}} = \left(1+\left(\frac{\alpha_\mathrm{acc}-1}{\alpha_\mathrm{acc}}\right)^2\right)\frac{(k_\mathrm{B}T_\mathrm{c})^2}{2E_\mathrm{acc}} + \frac{(e\Delta U)^2}{2E_\mathrm{acc}} + C\frac{e^2}{4\pi\varepsilon_0}(n_\mathrm{e,ext})^{1/3}\frac{E_\mathrm{ext}}{E_\mathrm{acc}} \tag{4.56}$$

$$k_B T_{\parallel,\mathrm{int}} = \left(1+\left(\frac{\alpha_\mathrm{int}-1}{\alpha_\mathrm{int}}\right)^2\right)\frac{(k_\mathrm{B}T_\mathrm{c})^2}{2E_\mathrm{int}} + \frac{(e\Delta U)^2}{2E_\mathrm{int}} + C\frac{e^2}{4\pi\varepsilon_0}(n_\mathrm{e,ext})^{1/3}\frac{E_\mathrm{ext}}{E_\mathrm{int}} \tag{4.57}$$

Including geometrical effects

The electron cooler geometry introduces additional broadening of the velocity distribution with respect to the ion beam axis due to the inclined overlap in the toroid region and the spatial potential dependence at the entrance and exit of the drift-tube region. Furthermore, in the transition to the drift-tubes the decreasing distance between electron beam and surrounding tube leads to a change in space charge potentials. All effects together have been included in a simulation as a major part of the work of Saurabh 2019, yielding a merged-beams collision energy distribution

$$f_\mathrm{mb}(E, E_\mathrm{d}; T_\perp, T_\parallel, X, U_\mathrm{sc}, U_\mathrm{s}) \tag{4.58}$$

where E is the distributed variable and describes the collision energy in the co-moving beam frame, E_d is the detuning energy (as defined in equation 3.13), X stands for the collision geometry, U_sc for the space charge potential and U_s for the stopping voltage in the drift-tube. Both temperatures, $T_\perp$ and $T_\parallel$, were assumed to have a constant value for the whole beam path. However, equations 4.56 and 4.57 show that the longitudinal temperature decreases for increasing electron energy.

Dr. Oldřich Novotný used a simplified version of the previously described collision geometry simulation, neglecting space charge effects, and extended it by the longitudinal temperature dependence on the electron energy, which varies along the electron beam trajectory. The resulting Monte Carlo simulation of the collision geometry is used to generate distributions

$$f_\mathrm{mb}(E, E_\mathrm{d}; T_\perp, T_\parallel(\alpha, E_\mathrm{lab}, T_\mathrm{c}, \Delta U, C, n_\mathrm{e,ext}, E_\mathrm{ext}), X, U_\mathrm{s}) \tag{4.59}$$

This extended approach makes use of equation 4.57 for the longitudinal temperature by inserting a variable lab frame electron energy E_lab.

The previous distribution can be used to convert cross sections into Merged-Beams Rate Coefficients (MBRCs) and vice versa (see section 4.3). An example for the electron collision energy distribution with and without averaged geometric effects ($f_\mathrm{mb}(E)$ and $f^*_\mathrm{mb}(E)$, respectively) is provided in Figure 4.5. The simulation results for the thermal distribution are obtained similarly to the calculations in this section and show a steep decrease, starting around the transverse temperature of $T_\perp = 2\,\mathrm{meV}$. In contrast to that, the electron cooler geometry introduces a high-energy tail, resulting from collisions in the toroid and ground potential region before and after the drift-tubes. The peak at $E_\mathrm{d} = 1\,\mathrm{eV}$ corresponds directly to the lab frame energy in the ground potential region ($E_\mathrm{acc} = 20\,\mathrm{eV}$).

4.2.3 Low-pass filters for improved energy spreads

The calculations carried out in section 4.2.2 have shown that electronic noise in the setup worsens the longitudinal temperature of the electron beam, especially if it exceeds the cathode-temperature-equivalent voltage of 25 mV.

The electron cooler potentials are provided by a common high voltage platform (see Rimmler 2017) in order to adapt to any change of the cathode voltage quickly. In the course of this work, it turned out that a high-frequent ($f > 1\,\mathrm{MHz}$) electronic noise is disturbing the high-voltage platform potential and, thus, propagates to all electrodes in the setup. A measurement of this noise is presented in Figure 4.6 a) and c) for the cathode potential and drift-tube potentials, respectively. It amounts to a peak-to-peak voltage of $\approx 200\,\mathrm{mV}$ and is consequently crucial for the longitudinal electron temperature.

A noise of this magnitude completely dominates the longitudinal electron velocity spread in the typical working regime of the CSR electron cooler. However, a reduction of the noise could not be achieved since the source could not be determined. Because of

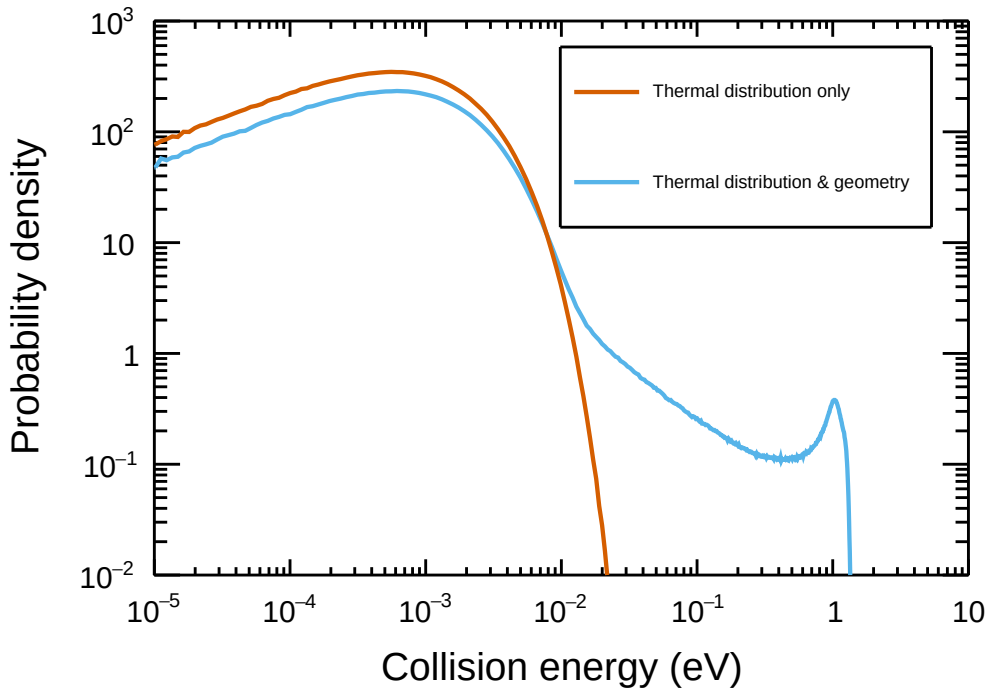

Figure 4.5: Simulated electron collision energy distributions for detuning energy $E_\mathrm{d} = 0\,\mathrm{eV}$. A transverse temperature of $T_\perp = 2\,\mathrm{meV}$ is assumed. The longitudinal temperature along the whole trajectory is, in both cases, obtained from equation 4.57 with a variable energy $E_\mathrm{int} \to E$. The plot assumes an acceleration energy $E_\mathrm{acc} = 20\,\mathrm{eV}$, interaction energy $E_\mathrm{int} = 11.8\,\mathrm{eV}$, extraction energy $E_\mathrm{ext} = 9.0\,\mathrm{eV}$, extraction electron density $n_\mathrm{e,ext} = 1.5 \times 10^7\,\mathrm{cm}^{-3}$, cathode temperature $T_\mathrm{c} = 25\,\mathrm{meV}$ and electronic noise $e\Delta U = 100\,\mathrm{meV}$.

its high frequency, it is possible to dampen the noise with low-pass filters that have been developed in the course of this work. The design of the first-order filters is presented in Figure 4.7 and depends on the properties of the electrodes they are attached to. For collision experiments electron energies are typically changed on a sub-millisecond timescale. Therefore, a cutoff frequency of $f_\mathrm{cut} = 10\,\mathrm{kHz}$ was chosen for all filters. Figure 4.6 b) and d) show the effect of the filters. The initial $\approx 200\,\mathrm{mV}$ peak-to-peak voltage is dampened to $\approx 10\,\mathrm{mV}$ in the high-frequency component. A 50 Hz component is left over after filtering that could be also attributed to the high-voltage platform.

Additional requirements for the filters are provided by the design voltage of the high-voltage platform ($0 - 1000\,\mathrm{V}$). For most of the electrodes, this does not collide with the standard filter design (Figure 4.7 a)) since the used 10 nF capacitors are available with specifications up to 1 kV. In contrast to that, some electrodes (cathode, Pierce and extraction electrode) have to provide/collect an electron current in the μA range. For the standard filter design a resistance of $10\,\mathrm{k\Omega}$ would cause a significant voltage drop from power supply to the electrode. Hence, in the design in subfigure b), a low resistance of $200\,\Omega$ and a corresponding capacitance of 500 nF was implemented instead. With

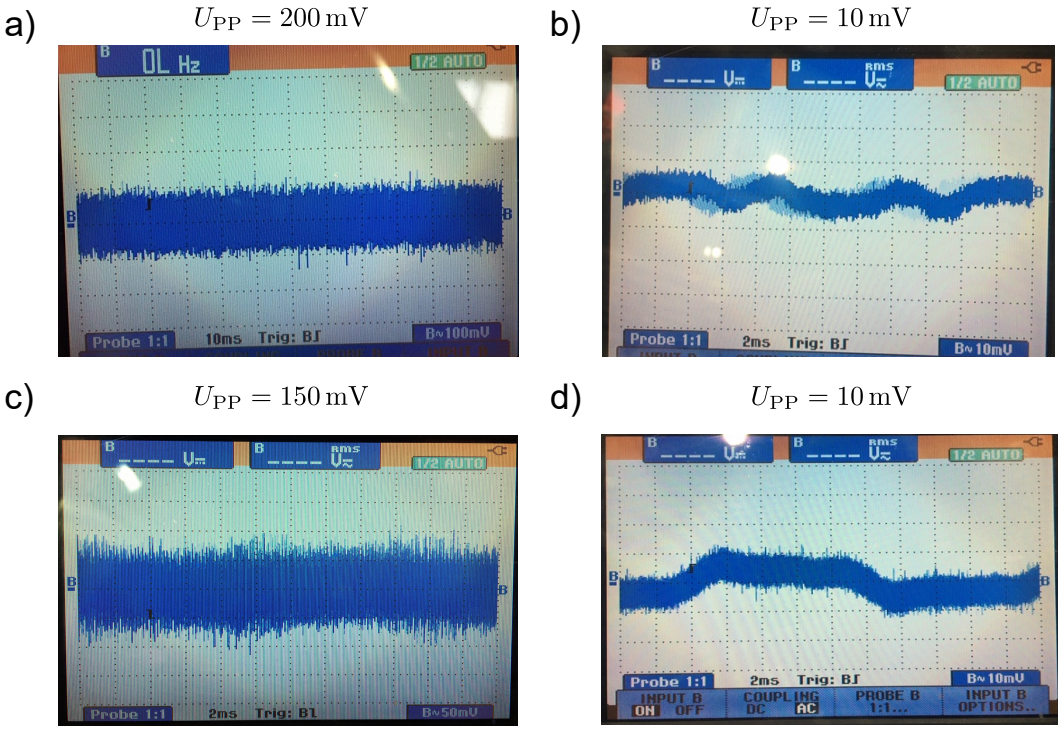

Figure 4.6: Electronic noise on relevant electron cooler electrodes. The situation with and without the low-pass filters in Figure 4.7 is compared. Measured peak-to-peak voltages U_{PP} are displayed on top of each waveform. a): Cathode without filter, b): Cathode with filter, c): Drift-tubes without filter, d): Drift-tubes with filter.

the reduced capacity a voltage drop of $0.33\,mV/\mu A$ was measured. Since the electron current is typically constant for electron collision measurement, this voltage drop will only appear as offset in the contact potential when the electron energy is optimized on cooling.

The extraction electrode potential, in specific, is toggled by a fast high-voltage switch on the platform in order to control the electron current in an on-off manner. It turned out that the switch does not supply enough current to reach the final voltage below a millisecond if the filter in subfigure b) is attached. An additional capacitive load of $1\,\mu F$ (Figure 4.7 c)) was added between the power supply and the extraction switch in order to solve this problem.

First tests with all filters revealed that the reduced noise improves the electron energy distribution measured with the retarding field analyzer of both Faraday cups. Furthermore, for electron cooled ion beams attaching the filters turned out to increase ion beam lifetimes and reduce their emittance significantly. The filter configuration, however, is only applicable for the drift-tube mode. In standard operation mode of the electron cooler, the high-voltage platform potential is defined by a combination of a fast and slow power supply. Attaching the filters to the cathode potential introduces

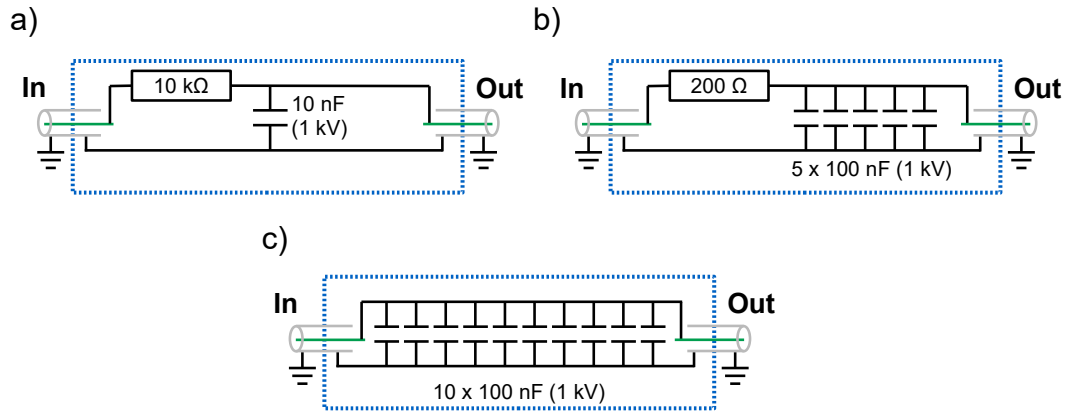

Figure 4.7: Low-pass filter and buffer capacity design for the electron cooler drift-tube mode. a): Low-pass filter for drift-tube voltages and barrier electrode. b): Low-pass filter for cathode, Pierce and extraction electrode. c): Buffer capacity for extraction switch. Inputs and outputs are realized by SHV cables and plugs.

an additional capacitance that can not be charged fast enough by the combination of both power supplies.

In order to test the filter functionality in collision experiments, a dedicated beamtime is foreseen in future. Here, a recombination signal that is sufficiently narrow in energy domain will be obtained with and without the low-pass filters. Such a measurement also allows to infer the longitudinal and transverse temperature of the electron beam in the interaction zone.

4.3 Cross sections, rate coefficients and plasma rates

Ultimately, the goal of rate measurements with the CSR electron cooler is to extract energy resolved cross sections $\sigma(E)$ of any electron-ion collision process. Due to the finite electron energy spread, the experimentally observed reaction rate cannot be directly connected to cross section but only to the Merged-Beams Rate Coefficient (MBRC). The latter is representing the convolution of $\sigma(E)$ with the electron collision energy distribution f_{mb} (equation 4.59) and is given by (Novotný et al. 2013)

$$\alpha_{\mathrm{mb},L_{\mathrm{full}}}(E_{\mathrm{d}}) = \int_0^\infty \sigma(E) v f_{\mathrm{mb}}(E, E_{\mathrm{d}})\,\mathrm{d}E \tag{4.60}$$

Here, v stands for the electron velocity in the ion beam frame and the multi-parameter notation of f_{mb} was reduced to the single parameter E_{d}, which stands for the electron beam detuning energy (equation 3.13). This parameter is typically scanned by adjusting the electron beam acceleration voltage.

In the equation above, the rate coefficient is related to the full overlap length L_{full} of electrons and ions in the electron cooler. As a convention raised in a previous publication (Novotný et al. 2019), this MBRC is normalized to an effective cooler length l_{e} defined by

$$\frac{l_{\mathrm{e}}}{L_{\mathrm{full}}} = \frac{\max\{f_{\mathrm{mb}}(E, E_{\mathrm{d}} = 0\,\mathrm{eV})\}}{\max\{f^{*}_{\mathrm{mb}}(E, E_{\mathrm{d}} = 0\,\mathrm{eV})\}} \tag{4.61}$$

where f^{*}_{mb} is the purely thermal distribution as shown in Figure 4.5. l_{e} resembles an estimate for the overlap length, where the mean collision energy is close to the detuning energy.

With the latter convention the MBRC is given by

$$\alpha_{\mathrm{mb}}(E_{\mathrm{d}}) = \frac{L_{\mathrm{full}}}{l_{\mathrm{e}}} \int_0^{\infty} \sigma(E) v f_{\mathrm{mb}}(E, E_{\mathrm{d}})\,\mathrm{d}E \tag{4.62}$$

This definition will be used for all further calculations in this work. Since the MBRC is not a fundamental physical quantity, such a scaling of rate coefficients can be applied, as long as equation 4.62 is used for connecting MBRCs with cross sections.

When considering electron collisions in an astrophysical environment, like the ISM (see chapter 1), the collision energies are often expected to follow a Maxwell-Boltzmann distribution $f_{\mathrm{pl}}(E)$. In this case, the environment is modeled as a plasma of constant temperature T_{pl}. Here, a *plasma rate coefficient* can be defined that describes the temperature-dependent reaction probability. It is calculated as convolution of the collision cross section with the thermal distribution

$$\alpha_{\mathrm{pl}}(T_{\mathrm{pl}}) = \int_0^{\infty} \sigma(E) v f_{\mathrm{pl}}(E) dE = \int_0^{\infty} \sigma(E) v \sqrt{\frac{4E}{\pi (k_{\mathrm{B}} T_{\mathrm{pl}})^3}} \exp\left(-\frac{E}{k_{\mathrm{B}} T_{\mathrm{pl}}}\right) dE \tag{4.63}$$

This convolution is straight-forward when the energy dependence of the cross section is known. However, for experimental data, only the MBRC is measured, which is a cross section convolved for the specific merged-beams energy distribution (see equation 4.62). In this case, cross sections cannot be obtained analytically but by a numerical deconvolution procedure and finally be convolved into the plasma rate coefficient.

In the deconvolution procedure the cross section energy spectrum is binned into n energy intervals E_i. The cross sections σ_i are assumed to be constant within each bin and are fitted in a χ^2 minimization procedure to reproduce the experimental MBRC. Details about the method are given in the appendix of Novotný et al. 2013. In contrast to this publication, here, the first energy bin in the cross section spectrum was treated differently. Instead of a constant cross section, it is modeled by $\sigma(E) = \frac{\sigma_0}{E}$, describing a *direct* DR process. Furthermore, the updated merged-beams collision energy distribution (equation 4.59) is used.

The result of the deconvolution procedure is a binned histogram of the cross section that can be convolved with a Maxwell-Boltzmann distribution (equation 4.63) to obtain an experimental plasma rate coefficient. After this convolution the fact that a discretized cross section was used does not play a major role because of the broad thermal collision energy distribution, which anyhow averages out possible narrow artifacts in the reconstructed cross section.

Rovibrational state effects

In general, cross sections can depend on the rovibrational state (v, J) of the molecule and are often provided in such a form by theoretical calculations (see chapters 2.2.2 and 2.2.3). They can be convolved to state-dependent rate coefficients via

$$\alpha_{\mathrm{mb},v,J}(E_d) = \frac{L_{\mathrm{full}}}{l_{\mathrm{e}}} \int_0^\infty \sigma_{v,J}(E) f_{\mathrm{mb}}(E, E_{\mathrm{d}})\, \mathrm{d}E \tag{4.64}$$

Such rate coefficients can be constructed from theoretical cross sections, which was done in this work for both, inelastic (Figure 2.6) and DR (Figure 2.7) cross sections. The results will be used in chapter 5.5 and 6.7, respectively.

On the experimental side, rovibrational states are deexciting radiatively in the cryogenic environment of CSR. Therefore, storage-time-dependent (t) MBRC measurements offer the possibility for obtaining results with different state population mixtures. Novotný et al. 2019 presented a method for extracting $\alpha_{\mathrm{mb},v,J}(E_{\mathrm{d}})$ from time-dependent MBRCs $\alpha_{\mathrm{mb}}(E_{\mathrm{d}}, t)$. If the populations $P_{v,J}(t)$ are known, the rate coefficient can be expressed as

$$\alpha_{\mathrm{mb}}(E_{\mathrm{d}}, t) = \sum_{v,J} P_{v,J}(t)\, \alpha_{\mathrm{mb},v,J}(E_{\mathrm{d}}) \tag{4.65}$$

By measuring $\alpha_{\mathrm{mb}}(E_{\mathrm{d}}, t)$ at several time intervals, a system of linear equations is solved to calculate state-dependent MBRCs from experimental rate coefficient data. A similar approach will be used in chapter 6.4 for analysis of the low-energy storage time dependence of the CH^+ DR process.

In analogy to the general formalism above, state-dependent MBRCs can be deconvolved into cross sections and converted into state-dependent plasma rate coefficients $(\alpha_{\mathrm{pl},v,J}(T_{\mathrm{pl}}))$. This will be carried out in chapter 6.5 for experimental and in chapter 6.7 for theoretical data.

4.4 Data acquisition and analysis

All experimental data presented in this work were obtained with help of the NICE detector (chapter 3.3). Here, the acquired data can be split into two categories: timing and camera data. For rate measurement evaluations solely the electronic signal from the phosphor screen (timing data) is used. Additionally, the camera data is included for imaging measurements.

After digitizing the electronic detector signal from the phosphor screen (see chapter 3.3) into waveforms, they are analyzed online (on CPU) to extract the number of pulses N_{p} as well as the arrival time t_{p}, amplitude A_{p} and integral I_{p} for each pulse. Storage of the individual waveforms is not intended, as it would limit the maximum detection rate significantly.

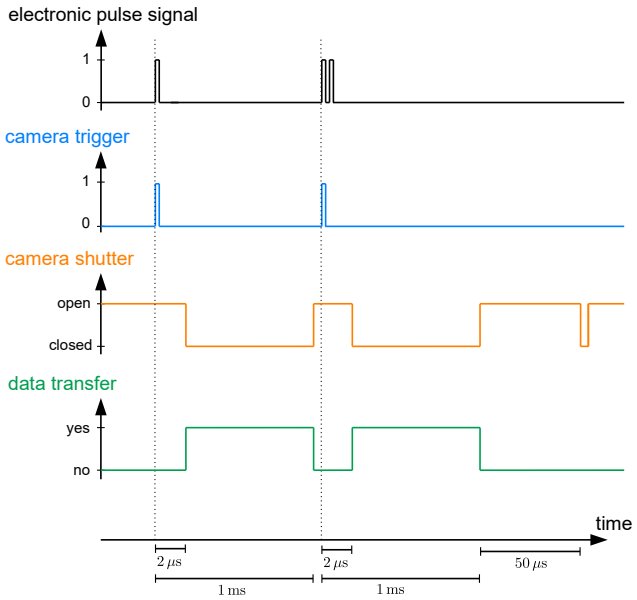

Figure 4.8: Simplified scheme of the NICE data acquisition timing - not to scale. The vertical dotted lines indicate starts of events.

The camera data are obtained by evaluation of individual frames. An online spot search algorithm is used to assign neighboring illuminated pixels to a single spot. Only relevant information is stored for each frame, which is the number of spots N_s as well as their pixel-positions x_s, y_s, amplitudes A_s and integrals I_s. Due to the fact that individual spots usually cover few pixels, it is possible to determine positions on a sub-pixel resolution by their center of intensity. Both data categories are obtained separately and synchronized offline on an event-by-event basis, together with additional information (e. g., injection number, measurement scheme, electron energy). The software of the data acquisition system was developed by Dr. Oldřich Novotný.

In Figure 4.8 the timing of the data acquisition system is visualized. The discriminated electronic signal from the phosphor screen is used as trigger for the camera. The camera itself is continuously integrating the incident light. Once triggered, the camera acquires for additional 2 μs in order to detect other fragments from the same collision event. Then, the camera shutter is closed and the data are transferred to the frame grabber, which takes approximately 1 ms. After transmission, the camera shutter is opened again and waits for the next trigger. Accumulation of stray light and other faint light sources is avoided by refreshing the camera every 50 μs without transferring data if no trigger arrives in this time window.

Electron collision experiments at CSR are typically realized by a fast and frequent adjustment of the electron beam energy, also called *wobbling*. Especially for measuring low values of E_d, the electron beam can drag the ion beam to different velocities due to the shape of the cooling force (see section 3.2.1). To prevent such dragging effects, the electron beam energy is for most of the time set to cooling energy (E_{cool}) and switched

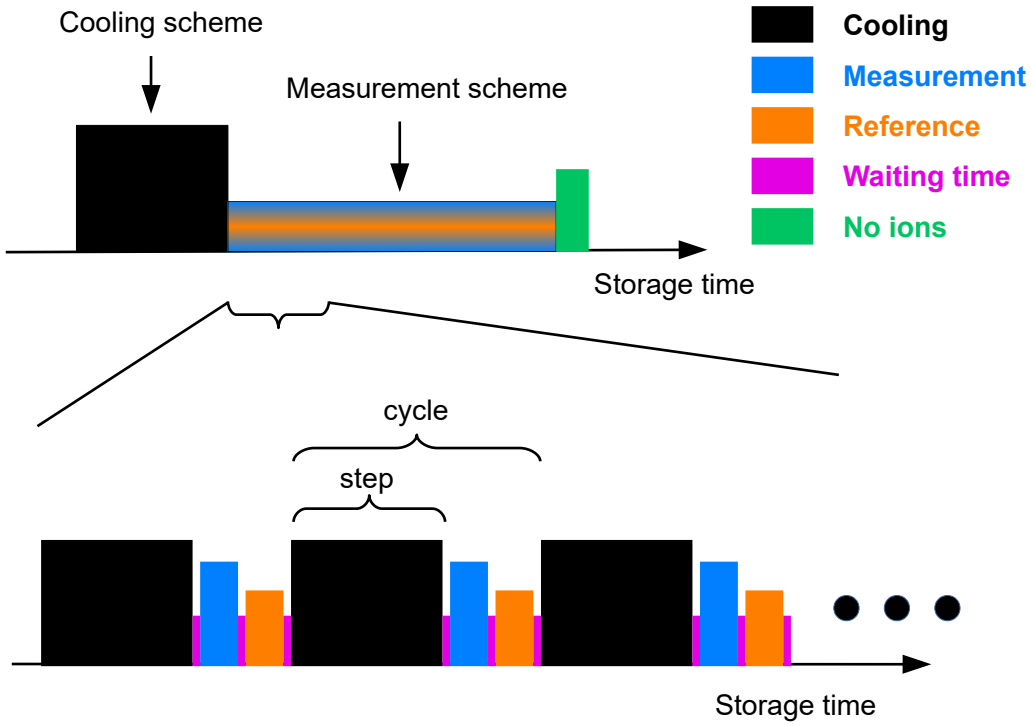

Figure 4.9: Measuring scheme for electron collision experiments. The whole measurement is split up into sub-units which are labeled from small to big as *step*, *cycle* and *scheme*. The often repeated *cycle* is composed of at least three different step types: electron cooling, measurement at variable E_d and a background reference. A waiting period is inserted between every step for voltage stabilization purposes.

to non-zero detuning energies only for short time intervals, on the order of tenths of milliseconds.

A visualization of the measuring scheme is presented in Figure 4.9. At first, the ion beam is solely electron cooled in a *scheme* of 'cooling only' type in order to reach a stable and small ion beam size as well as a defined energy. Afterwards, the measurement *scheme* is started. It is divided into several wobbling *cycles*, which are repeated typically for hundred to thousand times. Each cycle consists of a *cooling step*, a *measurement step* at desired E_d and a *reference step*, recording the residual gas induced background. The duration of the individual steps are typically between tenths to hundreds of milliseconds, where the *cooling step* is at least a factor of two longer than the others in order to minimize dragging effects. An additional ≈ 5 ms long waiting period is added between the *steps*, so that the electron energy can stabilize but no data are acquired yet.

The most obvious approach for the reference step is to switch off the electron beam and observe solely the ion beam induced signal. However, in preceding beamtimes it turned out that fast switching of the electron current often reduces the ion beam lifetime significantly. While for later beamtimes electron off steps could be included without

lifetime reduction, a different approach had to be chosen for the CH^+ beamtime. There, the electron beam energy was set to a fixed value of E_d, at which only a negligible electron induced signal is expected.

Additionally to the minimal configuration in Figure 4.9, other steps at fixed energies E_d can be included for normalization purposes. Including such steps is especially helpful if an ion-state-independent electron induced cross section is expected at this point.

The presented measurement scheme represents one *injection cycle*, where the ions are injected into CSR and the measurement is performed afterwards on the stored ion beam. At the end of each injection cycle, the ion beam is removed from the storage ring and the ion free background (*dark count rate*) is obtained. The statistical quality of the acquired data can be increased by repeating the injection cycles. Measurement conditions stay the same, except for fluctuations in the intensity of the injected ion beam. For long acquisition times it is convenient to split measurements into periods of several hours (*runs*). This is, e. g., helpful to analyze and correct for possible background pressure evolution.

4.4.1 Total rate measurements

The observables for rate measurements are the number of events in the cooling steps (N_{cool}), in the measurement steps (N_{meas}) and in the reference steps (N_{ref}). Here, in contrast to imaging measurements, it is not distinguished how many collision fragments were detected from a single reaction event. As the integration times t_{cool}, t_{meas} and t_{ref} of the individual steps are recorded, count rates R_{cool}, R_{meas} and R_{ref} can be obtained in each case by

$$R_i = \frac{N_i}{t_i} \tag{4.66}$$

with $i \in \{\text{cool}, \text{meas}, \text{ref}\}$. Those count rates are detected versus ion storage time and typically averaged over several steps. At the end of each injection, the ion beam is removed from the storage ring in order to measure the NICE dark count rate R_{dark} (see chapter 3.3) in a similar manner.

In section 4.3 the calculation of MBRCs from cross sections was explained. Reciprocally, the MBRC is extracted from experimental rates by the following considerations. At any given storage time, the detected count rate is given by

$$R_{tot} = R_{dark} + k_{res}\, n_{gas}\, N_{ion} + \alpha_{mb}\, \eta\, \frac{l_e}{C_0} N_{ion}\, n_e \tag{4.67}$$

The second term refers to residual gas induced collisions, where the rate is assumed to scale with residual gas density n_{gas} and number of ions N_{ion}. The remaining factor k_{res} describes an effective rate coefficient and is constant in this case. The third term of equation 4.67 summarizes the electron induced collisional rates. Here, η is the efficiency for detecting at least one fragment in the collision process, l_e the effective electron cooler length (equation 4.61), C_0 the CSR circumference and n_e the electron density in the center of the interaction zone. During measurement steps the total rate is given by

$R_{\mathrm{tot}} = R_{\mathrm{meas}}$. By summarizing the second term as $R_{\mathrm{res}} = k_{\mathrm{res}} n_{\mathrm{gas}} N_{\mathrm{ion}}$, the MBRC is calculated by

$$\alpha_{\mathrm{mb}} = \frac{R_{\mathrm{meas}} - R_{\mathrm{res}} - R_{\mathrm{dark}}}{\eta N_{\mathrm{ion}} n_{\mathrm{e}} l_{\mathrm{e}} / C_0} \tag{4.68}$$

In the reference step the electron induced signal vanishes and $R_{\mathrm{ref}} = R_{\mathrm{res}} + R_{\mathrm{dark}}$ holds, such that

$$\alpha_{\mathrm{mb}} = \frac{R_{\mathrm{meas}} - R_{\mathrm{ref}}}{\eta N_{\mathrm{ion}} n_{\mathrm{e}} l_{\mathrm{e}} / C_0} \tag{4.69}$$

Equation 4.69 is sufficient to calculate MBRCs. However, the determination of N_{ion} for each run is cumbersome and typically avoided. Instead, the ion number is deduced as

$$N_{\mathrm{ion}} = \frac{R_{\mathrm{res}}}{k_{\mathrm{res}} n_{\mathrm{gas}}} = \frac{R_{\mathrm{ref}} - R_{\mathrm{dark}}}{k_{\mathrm{res}} n_{\mathrm{gas}}} = \frac{R_{\mathrm{ref}} - R_{\mathrm{dark}}}{P_i} \tag{4.70}$$

where $P_i = k_{\mathrm{res}} n_{\mathrm{gas}}$ is proportional to residual gas pressure and, thus, called *pressure proxy*. The calculation of pressure proxies for the CH^+ beamtime, in specific, is discussed in chapter 5.7. Insertion of the previous equation into equation 4.69 yields

$$\alpha_{\mathrm{mb,rel}}(E_{\mathrm{d}}, t) = \frac{P_i}{\eta(E_{\mathrm{d}}) n_{\mathrm{e}}(E_{\mathrm{d}}) l_{\mathrm{e}} / C_0} \frac{R_{\mathrm{meas}}(E_{\mathrm{d}}, t) - R_{\mathrm{ref}}(t)}{R_{\mathrm{ref}}(t) - R_{\mathrm{dark}}} \tag{4.71}$$

where dependencies on detuning energy and storage time have been indicated explicitly. Since the absolute value of P_i is typically not known, equation 4.71 is used to calculate relative rate coefficients for all runs. At least one run needs to be evaluated with equation 4.69 for obtaining absolute MBRCs. The normalization procedure for all other runs is only valid if the residual gas density n_{gas} is constant within the run. Thus, fast pressure fluctuations inside the CSR have to be avoided.

4.4.2 Imaging measurements and distance distributions

For DR experiments with the CSR electron cooler, imaging measurements are a versatile tool for the study of fragmentation kinematics and can be used to infer branching ratios toward final product states (see discussion in chapter 2.3). Thus, imaging can be applied complementary to rate measurements presented in the previous section. The key for imaging experiments is the recording and evaluation of fragment positions on the detector, which is done with help of the NICE camera (see chapter 3.3 and beginning of section 4.4). Relevant information is encoded in the spatial distance and time difference between the individual fragments.

Under the *axial recoil approximation*, discussed at the end of chapter 2.1.3, the initial orientation of the molecule is preserved during the fragmentation process. Thus, fragment imaging even allows to detect angular collision probabilities and infer symmetries of the participating molecular states (Table 2.1). The first publication on two-dimensional (2D) fragment imaging at TSR was presented by Zajfman et al. 1995 and the method was soon used as a common experimental technique. By additionally measuring fragment time differences, it was further developed into three-dimensional (3D)

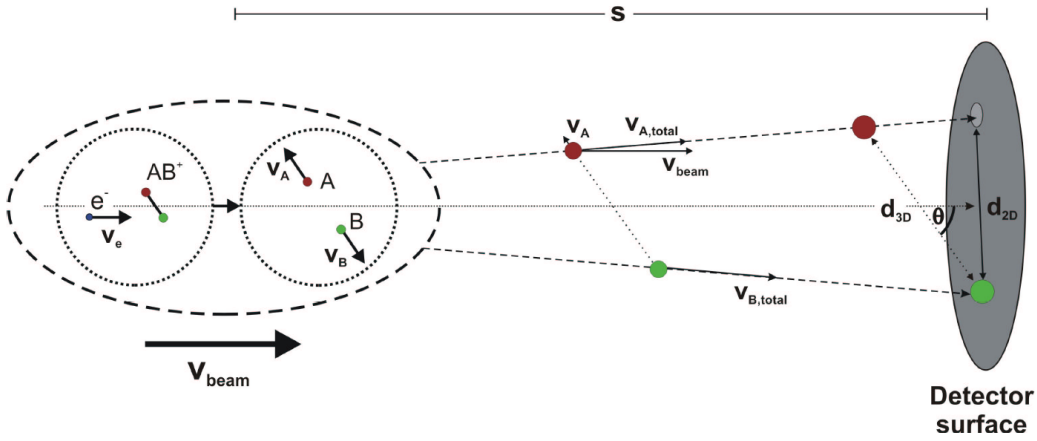

Figure 4.10: Fragment imaging kinematics for DR of diatomic molecules - extracted from Novotny 2004.

imaging in Novotny 2008 and Stützel 2011 at TSR. With detectable time differences on the order of 20 ns, the NICE detector offers the possibility for 3D imaging experiments on some molecular ions at CSR, including the CH^+ ion studied in this work.

The description of fragmentation kinematics for DR of diatomic molecules can be found in many works. The considerations in this part of the section follow the thesis of Novotny 2004, which contains derivations of all relevant probability distributions in the limit of a negligibly low KER E_{KER} (see chapter 2.1.3) compared to the ion beam energy E_{ion}. The results are later on corrected for fragment recoil effects, taking into account the change of E_{ion} by the KER in higher order.

The kinematics of a two-body fragmentation process are illustrated in Figure 4.10. The KER is distributed among both fragments while fulfilling the momentum conservation law. In the center of mass frame, this results in anti-parallel velocities $\vec{v}_{\mathrm{A}}$ and $\vec{v}_{\mathrm{B}}$ of both particles (A: heavy fragment, B: light fragment), which are transformed into the lab frame by the beam velocity $\vec{v}_{\mathrm{beam}}$. When both fragments impinge on the detector, a transverse distance d_{2D} on the detector screen can be observed. Additionally, the fragments arrive at different times and a longitudinal distance of $d_{\parallel} = v_{\mathrm{beam}}\Delta t$ can be defined, where $v_{\mathrm{beam}} = \sqrt{2E_{\mathrm{ion}}/m_{\mathrm{ion}}}$ is the absolute beam velocity and $\Delta t = t_{\mathrm{A}} - t_{\mathrm{B}}$ the arrival time difference, neglecting recoil effects. Both quantities can be added in square to define a 3D-distance

$$d_{\mathrm{3D}} = \sqrt{d_{\mathrm{2D}}^2 + d_{\parallel}^2} \tag{4.72}$$

All distances are scaling linearly with the path of flight between fragmentation position and detector surface s.

As discussed in chapter 2.1.3, DR collision events show a characteristic angular distribution $W(\vartheta)$, where ϑ denotes the angle between electron trajectory and molecular axis. In collision experiments all molecules are oriented randomly. Nevertheless, the electron beam defines a direction in the center of mass frame (see Figure 2.3) and DR

events with collision angles preferred by the $W(\vartheta)$ distribution are observed more often. As a consequence, collision experiments provide the possibility to sample the distribution $W(\vartheta)$ by observing the angular distribution of the detected fragmentation events. One exception to that is given at cooling energy, where ion and electron velocity match and no preferred direction exists in the center of mass frame. The experimental angular distribution becomes isotropic, independently of possible anisotropies in $W(\vartheta)$.

In analogy to chapter 2.1.3, the polar angle $\vartheta \in [0, \pi]$ is defined such that $\vartheta = 0$ describes fragmentation parallel to the electron/ion beam axis, with the heavy particle impinging the detector first ($d_\parallel > 0$). $\vartheta = \pi$ is similar but with light fragment arriving first ($d_\parallel < 0$) and $\vartheta = \pi/2$ indicates transverse fragmentation with both fragments arriving simultaneously. The fragmentation angle can, in first approximation, be directly measured as

$$\vartheta = \begin{cases} \arctan \frac{d_{2\mathrm{D}}}{d_\parallel} & d_\parallel > 0 \\ \pi + \arctan \frac{d_{2\mathrm{D}}}{d_\parallel} & \text{otherwise} \end{cases} \tag{4.73}$$

Since the whole process is cylindrically symmetric, the azimuthal angle φ is averaged over and is not considered in further analysis separately.

For a single DR event all kinematics depend on the unknown value of the event-detector distance s and the measured positions and impact times cannot give an insight into the fragmentation kinematics. When integrating over many events in the experiment, however, statistical distributions are obtained that characterize all physical quantities. A finite interaction length ΔL leads to equally distributed values for $s \in [s_1, s_2]$. In case of CSR, the mean distance between interaction zone and detector is $L = 3807\,\mathrm{mm}$, implying that $s_1 = L - \Delta L/2$ and $s_2 = L + \Delta L/2$. Further aspects have to be considered when analyzing statistical distributions:

- The values for $d_{2\mathrm{D}}$ and $d_\parallel$ are summed over all possible angles ϑ.
- Several final channels n with different KERs $E_{\mathrm{KER},n}$ (see chapter 2.1.3) can contribute to the distance distributions.

Novotny 2004 calculated probability distributions of a single channel n for isotropic fragmentation, i. e., for a normalized angular distribution $W(\vartheta) = 1/\pi$, resulting in

$$P_{n,\mathrm{iso}}(d_{3\mathrm{D}}) = \begin{cases} \frac{1}{\delta_n \Delta L} & s_1\delta_n \leq d_{3\mathrm{D}} \leq s_2\delta_n \\ 0 & \text{otherwise} \end{cases} \tag{4.74}$$

$$P_{n,\mathrm{iso}}(d_{2\mathrm{D}}) = \begin{cases} \frac{1}{\delta_n \Delta L}\left(\arccos\frac{d_{2\mathrm{D}}}{s_2\delta_n} - \arccos\frac{d_{2\mathrm{D}}}{s_1\delta_n}\right) & 0 \leq d_{2\mathrm{D}} \leq s_1\delta_n \\ \frac{1}{\delta_n \Delta L}\arccos\frac{d_{2\mathrm{D}}}{s_2\delta_n} & s_1\delta_n \leq d_{2\mathrm{D}} \leq s_2\delta_n \\ 0 & \text{otherwise} \end{cases} \tag{4.75}$$

$$P_{n,\mathrm{iso}}(d_{\parallel}) = \begin{cases} \frac{1}{2\delta_n \Delta L}\ln\frac{s_2}{s_1} & 0 \leq \left|d_{\parallel}\right| \leq s_1\delta_n \\ \frac{1}{2\delta_n \Delta L}\ln\frac{s_2\delta_n}{\left|d_{\parallel}\right|} & s_1\delta_n \leq \left|d_{\parallel}\right| \leq s_2\delta_n \\ 0 & \text{otherwise} \end{cases} \tag{4.76}$$

where

$$\delta_n = \frac{m_{\mathrm{A}} + m_{\mathrm{B}}}{\sqrt{m_{\mathrm{A}} m_{\mathrm{B}}}}\sqrt{\frac{E_{\mathrm{KER},n}}{E_{\mathrm{ion}}}} \tag{4.77}$$

When measuring angular distributions, the original distribution in the center of mass system is integrated over φ, leading to

$$W_{\mathrm{meas}}(\vartheta) = \int_0^{2\pi} W(\vartheta)\sin(\vartheta)\,\mathrm{d}\varphi = 2\pi W(\vartheta)\sin(\vartheta) \tag{4.78}$$

where the additional factor $\sin(\vartheta)$ stems from the spherical Jacobian matrix. Therefore, measured distributions have to be normalized by $1/\sin(\vartheta)$ to infer real angular distributions in the center of mass frame. As discussed at the end of chapter 2.1.3, expected angular distributions are given by a sum of Legendre polynomials (see equation 2.24). Even though theory predicts a symmetry for exchanging the heavy and light particle in a molecule (odd indices in the Legendre polynomials vanish), in this work both cases can be distinguished experimentally and a parameter a_1 is introduced for the Legendre polynomial $P_1(\cos\vartheta)$ for data modeling in chapter 7. Despite $a_1 = 0$ is expected from theoretical side, any significant experimental difference would be an interesting finding.

The lowest contributing orders/partial waves are given by

$$W(\vartheta) = 1 + a_1\cos\vartheta + \frac{a_2}{2}(3\cos^2\vartheta - 1) \tag{4.79}$$

where a_1 gives rise to asymmetries in the fragment arrival order and a_2 to asymmetries between transverse and longitudinal fragmentation with respect to the electron beam axis. Thus, they are referred to as *forward-backward anisotropy coefficient* and *longitudinal-transverse anisotropy coefficient*, respectively. By analyzing the fragment masses and correlating them with the arrival order (see sections 4.5.2 and 4.5.3), 3D imaging rises the unique possibility to study forward-backward asymmetries.

For non-isotropic distributions, the 3D distance distribution does, in first approximation, not differ from equation 4.74, which is a favorable feature for 3D fragment imaging experiments. The other two distance distributions, however, have to be adapted by averaging over all possible angles. With equation 4.79 and neglecting any forward-backward asymmetry ($a_1 = 0$), the 2D distance distribution is modified as

$$P_{n,2}(d_{2\mathrm{D}}) = P_{n,\mathrm{iso}}(d_{2\mathrm{D}}) + \begin{cases} \frac{a_2}{4\delta_n \Delta L}\left(\arccos\frac{d_{2\mathrm{D}}}{s_2\delta_n} - \arccos\frac{d_{2\mathrm{D}}}{s_1\delta_n}\right) - \\ \quad \frac{3a_2 d_{2\mathrm{D}}}{4\delta_n^2 \Delta L}\left(\sqrt{1-\left(\frac{d_{2\mathrm{D}}}{s_2\delta_n}\right)^2}/s_2 - \sqrt{1-\left(\frac{d_{2\mathrm{D}}}{s_1\delta_n}\right)^2}/s_1\right) & d_{2\mathrm{D}} \le s_1\delta_n \\ \frac{a_2}{4\delta_n \Delta L}\arccos\frac{d_{2\mathrm{D}}}{s_2\delta_n} - \frac{3a_2 d_{2\mathrm{D}}}{4s_2\delta_n^2}\sqrt{1-\left(\frac{d_{2\mathrm{D}}}{s_2\delta_n}\right)^2} & s_1\delta_n \le d_{2\mathrm{D}} \le s_2\delta_n \\ 0 & \text{otherwise} \end{cases} \tag{4.80}$$

In Figure 4.11 the most relevant distributions for the analysis in chapter 7 are presented. The combined contour plot of longitudinal and transverse distances (subfigure a)) is a circular arc where the intensity is suppressed for small transverse distances according to the $\sin(\vartheta)$ dependence of $W_{\mathrm{meas}}(\vartheta)$, as explained previously. The 3D distance distribution (subfigure b)) represents the radial distribution of subfigure a) and appears as a box function (compare equation 4.74). Subfigure c) shows angular distributions. In order to extract the fundamental angular fragment distribution $W(\vartheta)$, the measured distribution $W_{\mathrm{meas}}(\vartheta)$ is normalized by $\frac{1}{\sin(\vartheta)}$ and is isotropic in this example case.

Recoil effect correction

The previously derived distance distributions were calculated in the limit of an infinitely high ion beam energy compared to the Kinetic Energy Release (KER) in the fragmentation process. A reasonable measure for this limit is the ratio of the two velocities

$$v_{\mathrm{KER}} = \sqrt{\frac{2E_{\mathrm{KER}}}{M}} \tag{4.81}$$

$$v_{\mathrm{ion}} = \sqrt{\frac{2E_{\mathrm{ion}}}{M}} \tag{4.82}$$

where $M = m_{\mathrm{A}} + m_{\mathrm{B}}$ is the ion mass. For experiments at CSR, this ratio amounts to $r_v = \frac{v_{\mathrm{KER}}}{v_{\mathrm{ion}}} \approx 3 \times 10^{-3}$. In contrast to high-energy storage rings, for which the distance distributions were initially calculated, in this low-energy regime the fragment recoil during breakup considerably alters the time of flight towards the detector and a more detailed calculation of fragment distances is required. The following relations were derived in the course of this work and result in a method for a higher-order correction of this recoil effect.

As described previously, the fragment distances on the detector can be calculated by momentum and energy conservation in the center of mass frame and by transforming

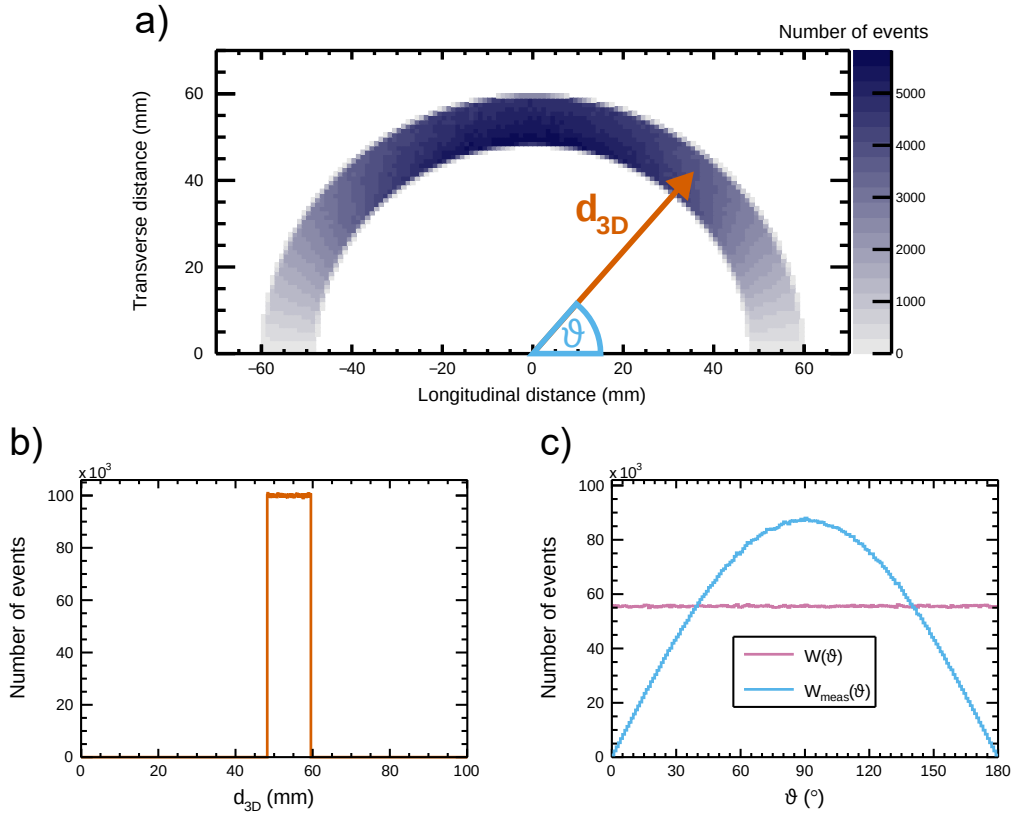

Figure 4.11: Ideal 3D imaging distributions. The combined distance distribution (a) consists of a circular arc. The determination of d_{3D} and ϑ is indicated as radial and angular component. The 3D distance distribution (b) is given by a box function. While the fundamental angular distribution $W(\vartheta)$ in (c) is isotropic, the measured one $W_{\mathrm{meas}}(\vartheta)$ is additionally weighted by $\sin(\vartheta)$ (see equation 4.78).

the resulting fragment velocities into the lab frame. Exact relations for all distances are given by

$$d_{\parallel} = s\frac{m_{\mathrm{A}}+m_{\mathrm{B}}}{\sqrt{m_{\mathrm{A}}m_{\mathrm{B}}}}r_v\frac{\cos(\vartheta)}{1-\frac{m_{\mathrm{A}}-m_{\mathrm{B}}}{\sqrt{m_{\mathrm{A}}m_{\mathrm{B}}}}r_v\cos(\vartheta)-r_v^2\cos^2(\vartheta)} \tag{4.83}$$

$$d_{2\mathrm{D}} = s\frac{m_{\mathrm{A}}+m_{\mathrm{B}}}{\sqrt{m_{\mathrm{A}}m_{\mathrm{B}}}}r_v\frac{\sin(\vartheta)-2\frac{\sqrt{m_{\mathrm{A}}m_{\mathrm{B}}}}{m_{\mathrm{A}}+m_{\mathrm{B}}}r_v\sin(\vartheta)\cos(\vartheta)}{1-\frac{m_{\mathrm{A}}-m_{\mathrm{B}}}{\sqrt{m_{\mathrm{A}}m_{\mathrm{B}}}}r_v\cos(\vartheta)-r_v^2\cos^2(\vartheta)} \tag{4.84}$$

$$d_{3\mathrm{D}} = s\frac{m_{\mathrm{A}}+m_{\mathrm{B}}}{\sqrt{m_{\mathrm{A}}m_{\mathrm{B}}}}r_v\frac{\sqrt{1-4\frac{\sqrt{m_{\mathrm{A}}m_{\mathrm{B}}}}{m_{\mathrm{A}}+m_{\mathrm{B}}}r_v\sin^2(\vartheta)\cos(\vartheta)+4\frac{m_{\mathrm{A}}m_{\mathrm{B}}}{(m_{\mathrm{A}}+m_{\mathrm{B}})^2}r_v^2\sin^2(\vartheta)\cos^2(\vartheta)}}{1-\frac{m_{\mathrm{A}}-m_{\mathrm{B}}}{\sqrt{m_{\mathrm{A}}m_{\mathrm{B}}}}r_v\cos(\vartheta)-r_v^2\cos^2(\vartheta)} \tag{4.85}$$

By neglecting the r_v and r_v^2 summands in the fractional terms, i. e., by neglecting the recoil effect, one can obtain the distributions presented in equations 4.74-4.76. With a finite value of r_v, however, the 3D distance is no longer independent of ϑ.

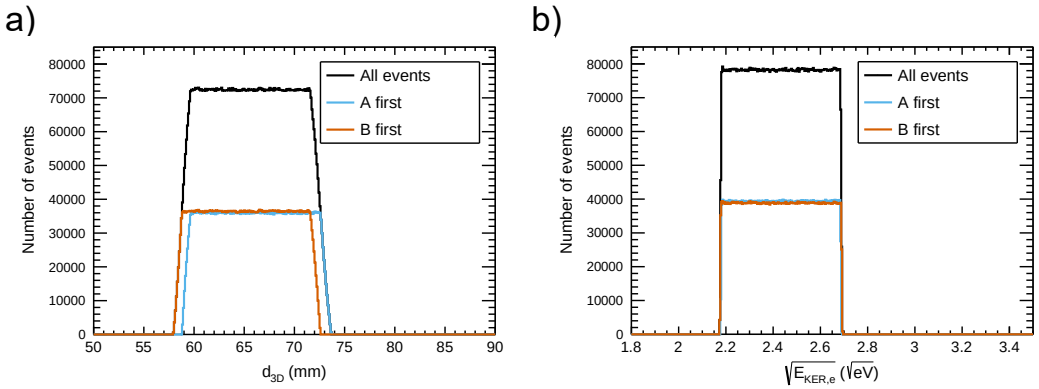

Figure 4.12: Simulation of a 3D distance distribution (a) and a distribution of the effective KERs (b) with recoil effect. Both simulations were conducted with 1×10^7 events, $\Delta L = 0.8\,\mathrm{m}$, $L = 3.807\,\mathrm{m}$, $E_{\mathrm{ion}} = 280\,\mathrm{keV}$, $E_{\mathrm{KER}} = 5.92\,\mathrm{eV}$, $m_{\mathrm{A}} = 12\,\mathrm{u}$ and $m_{\mathrm{B}} = 1\,\mathrm{u}$ (see text for parameter definitions). The conditions represent a quite extreme case for a high KER and high fragment mass difference. Resulting distributions are split up into events with heavy (A) and light (B) fragments arriving first. a): 3D distance distribution. b): Effective-KER distribution.

For calculations of the corrected distance distributions, normalized distributions $f(\vartheta) \sim W_{\mathrm{meas}}(\vartheta)$ (see equation 4.78) for the angle ϑ, and $f(s)$ for the detector distance are assumed as follows:

$$f(\vartheta) = \frac{1}{2} W(\vartheta) \sin(\vartheta) \Theta(\vartheta) \Theta(\pi - \vartheta) \tag{4.86}$$

$$f(s) = \frac{1}{s_2 - s_1} \Theta(s - s_1) \Theta(s_2 - s) \tag{4.87}$$

where $\Theta(x)$ is the Heaviside step function. The cumulative distribution function of any of the given distances $d_i \in \{d_{\parallel}, d_{2\mathrm{D}}, d_{3\mathrm{D}}\}$ is given by

$$F(d_i) = \iint_{\tilde{d}_i(s,\vartheta) < d_i} f(\vartheta) f(s)\, \mathrm{d}s\, \mathrm{d}\vartheta \tag{4.88}$$

and can be differentiated with respect to d_i to obtain the distance distribution function observed in experiments. $\tilde{d}_i(s, \vartheta)$ stands for the functional expressions in equations 4.83-4.85, which have to be inserted. In case of the here studied 3D distance distribution, the integral defies analytical evaluation. Hence, the extent of the recoil effect was studied with help of a Monte Carlo simulation.

The simulation results are presented in Figure 4.12 a) and reveal that the 3D distance distribution deviates from an ideal box function. For the total distribution the fragment recoil results in a smear-out of the box function edges. An interesting observation is that the sub-distribution for events with heavy fragments (A) arriving first ($\vartheta < \frac{\pi}{2}$) is shifted towards higher distances compared to the light fragments (B) first distribution. This can be explained by the fact that if the light fragment undergoes a backwards recoil, the two fragments, on average, experience a higher time of flight and can separate further.

Unfortunately, no closed analytical expression for the whole distribution can be derived and fitting of experimental data is only possible with a simulation or effective models.

In contrast to simulating distance distributions, a much simpler way for deriving angular distributions and the KER from imaging data is to calculate an event-based value for ϑ and E_{KER}. This can be done by solving the equation system 4.83 and 4.84 for both observables of physical interest. In order to obtain an analytical solution, the r_v^2 term in the denominator of equations 4.83 and 4.84 had to be neglected and it could be proven by simulation that for CSR-relevant conditions this approximation leads to almost unaltered distance distributions. The approximate solution is given by

$$\vartheta = \begin{cases} \arctan\left(\frac{d_{2\mathrm{D}}}{d_\parallel}(1-\frac{2m_\mathrm{A}m_\mathrm{B}}{C(s)})^{-1}\right) & d_\parallel > 0 \\ \pi + \arctan\left(\frac{d_{2\mathrm{D}}}{d_\parallel}(1-\frac{2m_\mathrm{A}m_\mathrm{B}}{C(s)})^{-1}\right) & \text{otherwise} \end{cases} \tag{4.89}$$

$$\sqrt{E_{\mathrm{KER}}} = \sqrt{E_{\mathrm{ion}}}\frac{m_\mathrm{A}+m_\mathrm{B}}{\sqrt{m_\mathrm{A}m_\mathrm{B}}}\frac{m_\mathrm{A}m_\mathrm{B}}{|C(s)|}\sqrt{1+\left(\frac{d_{2\mathrm{D}}}{d_\parallel}\frac{C(s)}{C(s)-2m_\mathrm{A}m_\mathrm{B}}\right)^2} \tag{4.90}$$

where

$$C(s) = \frac{s}{d_\parallel}(m_\mathrm{A}+m_\mathrm{B})^2 + m_\mathrm{A}^2 - m_\mathrm{B}^2 \tag{4.91}$$

As already explained previously, it should be noted that $d_\parallel$ can take positive or negative values, depending on the fragment arrival order.

If the detector distance s for an event would be known, equations 4.89 and 4.90 could be used to derive the full information about the physical quantities. The expression for ϑ is dominated by a s-independent term. Even for extreme cases at CSR, where the KER is so high that most fragments are not collected by the detector for geometrical reasons, the deviation of results from equation 4.73 to the real angle for single events is less than 0.1°. Thus, the simplified equation 4.73 actually acts as a good approximation for extracting angular distributions, independent of s.

In contrast to the angular term, the KER dependence on s is more crucial. Here, a practical solution is to calculate event-based effective KERs $E_{\mathrm{KER,e}}$ by approximating the detector distance by its mean value $s \approx L = 3807\,\mathrm{mm}$ such that

$$\sqrt{E_{\mathrm{KER,e}}} = \sqrt{E_{\mathrm{ion}}}\frac{m_\mathrm{A}+m_\mathrm{B}}{\sqrt{m_\mathrm{A}m_\mathrm{B}}}\frac{m_\mathrm{A}m_\mathrm{B}}{|C(L)|}\sqrt{1+\left(\frac{d_{2\mathrm{D}}}{d_\parallel}\frac{C(L)}{C(L)-2m_\mathrm{A}m_\mathrm{B}}\right)^2} \tag{4.92}$$

By back-substituting equations 4.83 and 4.84 it can be proven by Taylor expansion with respect to r_v that the dependence of $E_{\mathrm{KER,e}}$ on the real KER and angle is approximately given by

$$\sqrt{E_{\mathrm{KER,e}}}(s) = \sqrt{E_{\mathrm{KER}}}\frac{s}{L}\left(1+O\left(r_v\frac{\Delta L}{2L}\right)\right) \tag{4.93}$$

where the first order correction term, in comparison to the 3D distance, is additionally suppressed by the ratio of half the interaction zone length ($\Delta L/2$) to the mean detector

distance (L) with $\frac{\Delta L}{2L} \approx 0.1$. Consequently, the effective KER defined by equation 4.92 takes into account the recoil effect to an order-of-magnitude better extent than typically analyzed 3D distance distributions, which is underlined by simulation in Figure 4.12 b). In contrast to the smeared-out box function for 3D distances (subfigure a)), the effective-KER distribution can be well approximated by a box function with sharp edges, which can be proven analytically by propagating the dominant term in equation 4.93 through equations 4.86-4.88, resulting in

$$f\left(\sqrt{E_{\mathrm{KER,e}}}\right) = \begin{cases} \frac{L}{\Delta L \sqrt{E_{\mathrm{KER}}}} & \frac{s_1}{L}\sqrt{E_{\mathrm{KER}}} \leq \sqrt{E_{\mathrm{KER,e}}} \leq \frac{s_2}{L}\sqrt{E_{\mathrm{KER}}} \\ 0 & \text{otherwise} \end{cases} \tag{4.94}$$

For future imaging studies at CSR and other low-energy merged-beam experiments, it is recommended to observe the distribution of effective KERs (equation 4.93) and angles (equation 4.73). While the first can be fitted with equation 4.94, the latter can be normalized by $1/\sin(\vartheta)$ and be fitted with equation 4.79.

As a major advantage, the 3D imaging technique allows one to study the KER and angular distribution separately, while they are entangled for 2D and longitudinal distance distributions. In Novotný et al. 2010 3D imaging has already been applied for experiments on CF^+ ions at TSR. The first DR 3D imaging study at CSR, in particular on CH^+ ions, will be presented in chapter 7. It uses the here described recoil effect correction.

4.5 Detector calibration

In this section a few calibration procedures are presented that are generally applicable for imaging related experiments. In section 4.5.1 pixel coordinates of the camera are calibrated to millimeter distances. Section 4.5.2 is concerned with the assignment of fragment masses to individual camera event positions. Finally, the considerations in section 4.5.3 allow to assign fragment masses also to the timing data, i. e., to their arrival times.

4.5.1 Fragment distances

3D imaging measurements require a precise calibration of fragment distances on the phosphor screen. Those distances are obtained from spot positions (see section 4.4) in units of camera pixels first and later on converted into millimeters. The calibration in this work was achieved by observing carbon and hydrogen atoms, resulting from residual gas collision of CH^+, that are passing through holes in the calibration mask (see section 3.3) placed in front of the detector. In Figure 4.13 the integrated data for

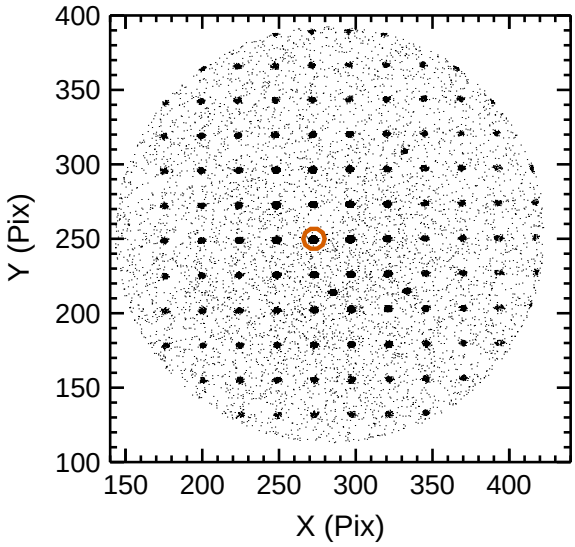

Figure 4.13: Imaging event positions recorded with calibration mask. The origin of the millimeter coordinate space is set to the center of the hole marked in orange.

all spots generated on the phosphor screen and observed by the camera is presented. An accumulation of imaging events in the holes of the calibration mask is clearly visible. All events with random intermediate positions are attributed to *dark counts* (see section 3.3).

In order to determine precise pixel positions of the mask hole-centers, all statistically significant clusters are fitted by two-dimensional Gaussian distributions and their centers are extracted as $(x_{\mathrm{pix}}|y_{\mathrm{pix}})$. The calibration mask is manufactured such that holes form a rectangular pattern with columns and rows spaced by 10 mm. The three holes that do not follow this pattern can be used for orientation. With the definition of the millimeter space origin as center of the highlighted hole in Figure 4.13, the millimeter position of all holes can be defined as exact. In principle, the dependence of $(x_{\mathrm{mm}}|y_{\mathrm{mm}})$ on $(x_{\mathrm{pix}}|y_{\mathrm{pix}})$ can be used to determine a calibration function.

After applying the proposed scaling procedure, different linear scaling factors for the x and y coordinate were obtained. A serious complication is given by the fact that the MCP rim becomes elliptical in the millimeter space with axis lengths differing by $\approx 3\%$, while it is round in the pixel domain (axis lengths deviation $< 0.5\%$). Furthermore, 2D distance distributions for horizontal and vertical breakups were studied separately, and revealed to be scaled with respect to each other in millimeter space, while they agree in pixel space. Both facts together indicate that the camera picture is negligibly distorted by any optical effects or a possible angle of the camera with respect to the axis of incident light. Consequently, the results are a strong indication that the horizontal and vertical scaling factors should be identical to a sub-percent precision and either the

horizontal or the vertical factor is determined incorrectly. The observed discrepancy seems to be attributed to the calibration mask, where two scenarios could be imagined as an explanation:

- The horizontal hole distances are reliable but not the vertical ones. In this case, the size of the visible MCP area (diameter: $D = 120\,\mathrm{mm}$) cannot be reproduced. In this calibration it appears smaller, which might be attributed to edge field effects on the detector rim.
- The vertical hole distances are reliable but not the horizontal ones. In this case, the size of the visible MCP area matches the expectation.

Considering the mounting of the calibration mask and the fact that it is turned along a vertical axis when moved in front of the detector, the first option seems more likely. An (on hardware level) erroneously introduced vertical tilting angle α compared to the ideal design orientation perpendicular to the ion beam trajectory could be a possible explanation. Details about a correction of this tilting angle and further considerations on this topic can be found in Jain 2020 and are not repeated here. Similar to that work, a tilting angle of $\alpha = 14.5(25)°$ is assumed here and all hole positions are corrected in a way that the vertical point distance is given by

$$\Delta y_{\mathrm{mm}} = 10\,\mathrm{mm}\cos\alpha \tag{4.95}$$

Figure 4.14 shows the dependence between ideal hole positions in millimeters and measured hole positions in pixels. Linear fits were applied to extract a calibration coefficient between pixel and millimeter coordinates

$$C_{\mathrm{pix},1} = 0.4131(25)\,\mathrm{mm/pix} \tag{4.96}$$

where the value and uncertainty are calculated from the mean value and deviation between calibrations for different angles α in the above mentioned range. The statistical uncertainties are about an order of magnitude lower and have been neglected.

The hypothesis on the existence of an erroneous vertical tilting angle could not have been tested by an independent method yet. Thus, for the imaging analysis in chapter 7 the possibility of horizontal hole distances being incorrect will be included as well. In this case a different value of $C_{\mathrm{pix},2} = 0.4261\,\mathrm{mm/pix}$ is obtained and both, $C_{\mathrm{pix},1}$ and $C_{\mathrm{pix},2}$, are propagated into a common scaling factor

$$C_{\mathrm{pix}} = 0.4196(65)\,\mathrm{mm/pix} \tag{4.97}$$

which includes their values in the given uncertainty range. It should be noted that both, $C_{\mathrm{pix},1}$ and $C_{\mathrm{pix},2}$, are common scaling factors for horizontal and vertical direction according to the reasoning presented before. They only differ by the choice for one of the two hypotheses, where either the vertical or the horizontal hole distance is not reliable. Hence, C_{pix} is also used for horizontal and vertical scaling.

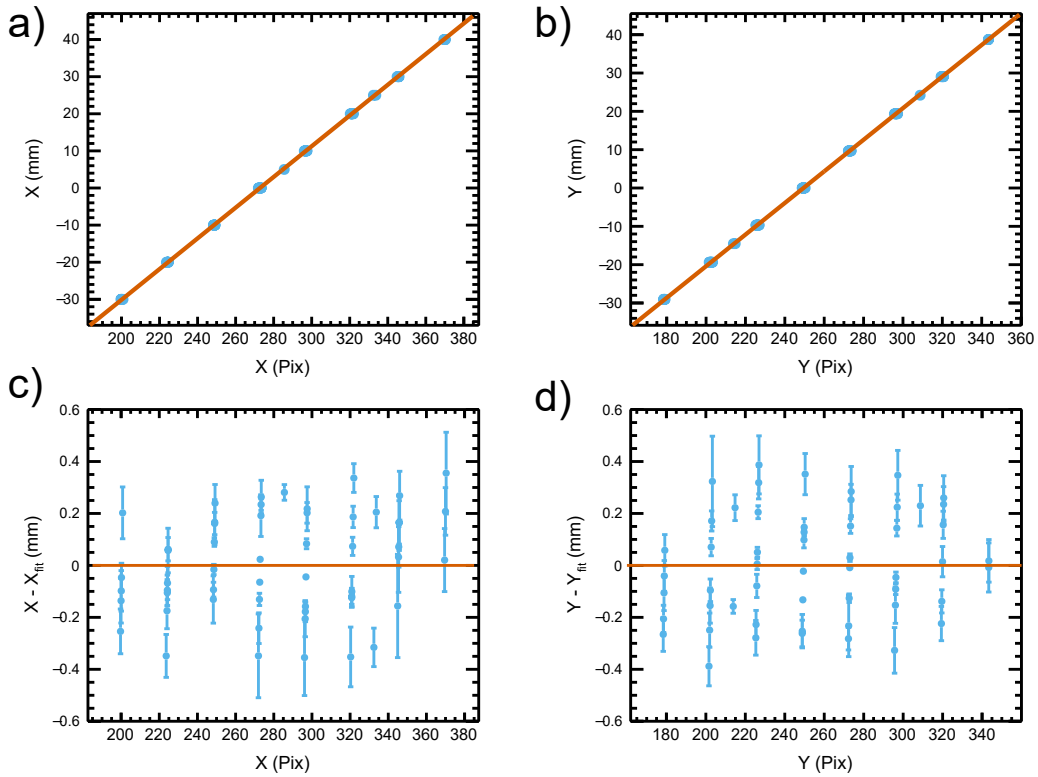

Figure 4.14: Linear fits and residuals for position calibration. In a) and b) the horizontal/vertical dependence between ideal and measured hole positions is shown and fitted by a linear function. c) and d) present the residuals of those fits.

Due to the high systematic uncertainty of C_{pix} no effort was put in trying more precise calibration functions in Figure 4.14, which would contain horizontal and vertical correlations and quadratic terms. For future beamtimes it is planned to study a system with a precisely known literature value for the KER in order to decide about the asymmetries in the mask and obtain a more precise calibration.

4.5.2 Mass assignment

Imaging-related experiments benefit from a situation where spots and pulses on the detector can be assigned to fragment masses using kinematic arguments. As already shown in section 4.4.2, mass assignment allows to determine asymmetries in the order of fragment arrival, also referred to as forward-backward asymmetry. The mass assignment procedure for the camera data will be presented in this section and is propagated to the timing data in the following section.

For functionality of the algorithm, all n DR fragments (n must be known) of the studied ion must be neutral and detected by the camera. The latter restriction can be achieved by a filter on events with the number of detected spots set as $N_{\mathrm{s}} = n$. Spot positions are defined by $\vec{s}_1, ..., \vec{s}_n$ and masses by $m_1, ..., m_n$. The goal of the algorithm

is to find the permutation $\sigma(i)$ which leads to the event center of mass

$$\vec{r}_{\mathrm{CM}} = \frac{1}{n}\sum_{i=1}^{n} m_{\sigma(i)}\vec{s}_i \tag{4.98}$$

that is closest to the average center of mass of all DR events $\vec{r}_{\mathrm{CM,g}}$, denoted as global center of mass. $\vec{r}_{\mathrm{CM,g}}$ also represents the center of the ion beam projected onto the detector plane. The determined permutation $\sigma(i)$ is the optimal mass assignment for the considered event.

Since the global center of mass is not known from the beginning, the mass assignment algorithm relies on an iterative procedure. First, a value for $\vec{r}_{\mathrm{CM,g}}$ is estimated visually from the position of all events. Afterwards the following steps are repeated:

1. Equation 4.98 is calculated for all possible permutations $\sigma_k(i)$ and each event k. The permutation with minimum distance between $\vec{r}_{\mathrm{CM},k}$ and $\vec{r}_{\mathrm{CM,g}}$ is chosen. This is done for all events with $N_{\mathrm{s}} = n$.

2. From the resulting permutations the new global center of mass is calculated as average over all $\vec{r}_{\mathrm{CM},k}$.

For DR events with $n = 2$ the procedure typically converges after three iterations. The algorithm is exact if all fragments arise from the same center of mass coordinates, i. e., for an infinitely narrow ion beam and correspondingly sharp distribution of all $\vec{r}_{\mathrm{CM},k}$, but introduces uncertainty if this is not the case, especially for fragmentation along the ion beam axis. Thus, a small ion beam profile as well as high KERs and very asymmetric fragment masses are desired for the mass assignment algorithm. In case of the CH^+ beamtime all of these criteria are fulfilled and the mass assignment is estimated to be reliable for $> 97\%$ of the events.

The previously discussed mass assignment algorithm gets much less reliable for high number of fragments, already starting at $n = 3$. Hence, an upgrade of CSR is planned to include a Molecular Camera (MOCCA) detector (Gamer et al. 2016 and Novotný et al. 2015). With this magnetic micro-calorimeter, fragment masses will be identified by their kinetic energy at an expected mass resolution of about $\frac{\Delta m}{m} \approx 10^{-4}$. Thus, fragment mass assignment will be independent of the above described approximate algorithm.

4.5.3 Correlation of spots and pulses

With the algorithm presented in the last section, mass assignment for individual spots in the camera data can be obtained. This data, however, are acquired independently of the timing data and do not provide any timing information. In order to still determine the order of fragment arrival, spot and pulse information has to be assigned to each other. Urbain et al. 2015 developed a method to achieve this assignment based on a detector design, where pulse intensity and spot brightness are correlated. The NICE detector was designed in a similar way. Therefore, the assignment procedure, denoted as

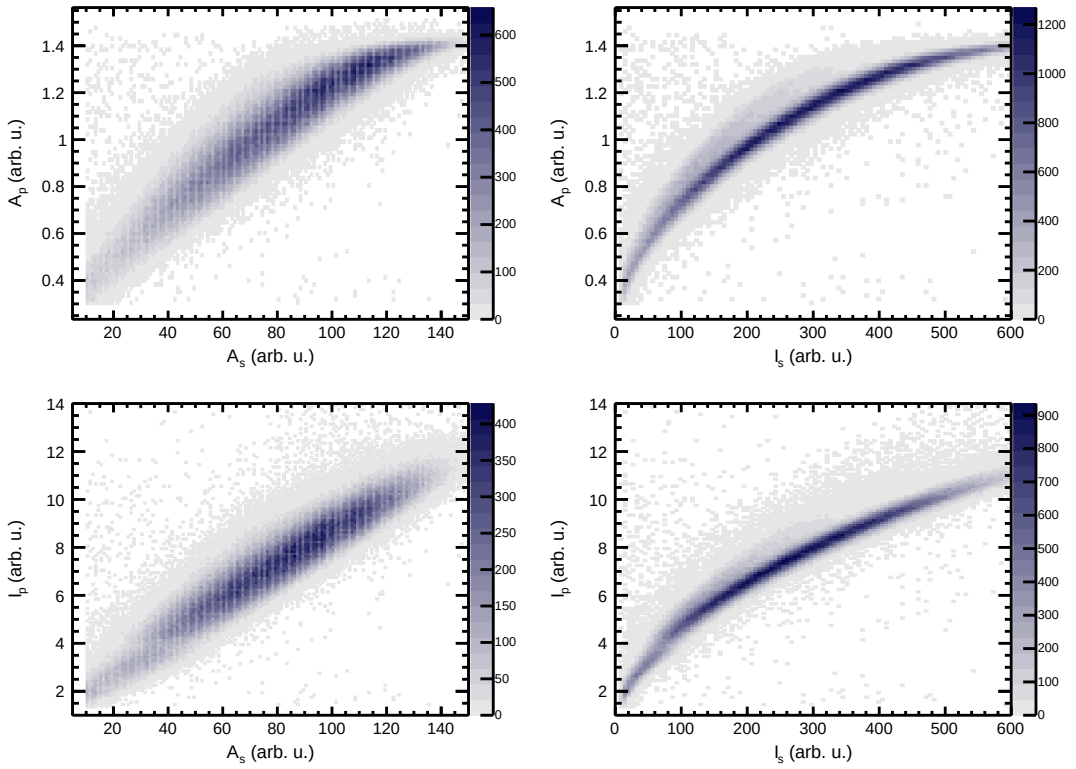

Figure 4.15: Correlation diagrams for amplitudes A and integrals I of spots and pulses - corresponding to the 'high-density campaign' detector voltages in Table B.1. The four diagrams represent all possible combinations of the two pulse-related variables A_p and I_p with the two spot-related variables A_s an I_s. The color scale indicates the number of detected events. The diagrams are representative also for the other detector voltage settings in Table B.1.

Correlation of Spot Brightness and Pulse Amplitude (COBRA) algorithm, was adapted and is described in detail for the application at CSR in Becker 2016. This section is concerned with a short summary of the principle while applying the algorithm to the obtained data.

Information about the pulse and spot response is encoded in the data within the pulse amplitude A_p and integral I_p as well as the spot amplitude A_s and integral I_s (see section 4.4). In principle, all observables can be used as correlation parameters. In order to determine the best combination, all possible correlation diagrams are presented in Figure 4.15. Filtering the events for the number of spots $N_\mathrm{s} = 1$ and number of pulses $N_\mathrm{p} = 1$ ensures that identical fragments are observed and that the spot and pulse properties (amplitudes/integrals) must be correlated. While both diagrams belonging to A_s show broad distributions, the spread in the two diagrams including I_s is rather narrow. Despite the fact that the dependence is non-linear, due to nonlinear response of the camera pixel signal to the observed light intensity, the correlation diagram for I_p and I_s was chosen for further analysis.

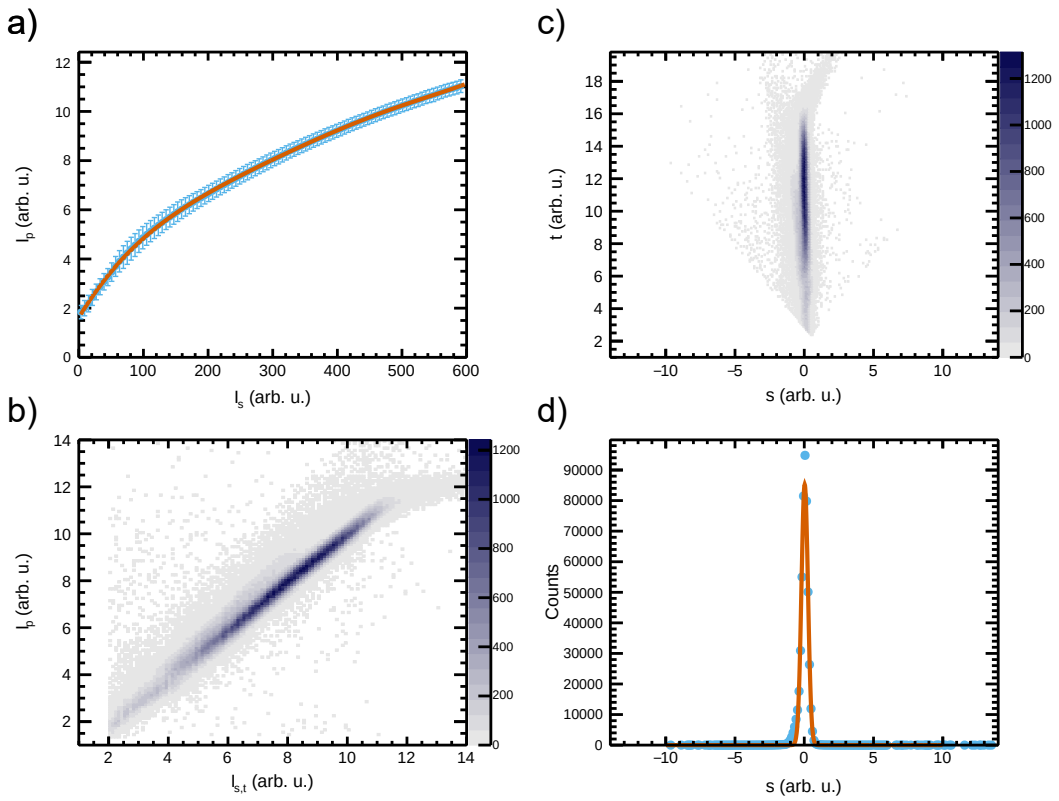

Figure 4.16: COBRA analysis diagrams for determination of the correlation spread. a): Mean values for the correlation diagram in Figure 4.15 fitted by a sixth order polynomial. b): Correlation diagram for transformed spot intensity and pulse intensity. c): Correlation diagram in b) rotated by 45°. d): Projection of c) onto axis s, fitted by a Gaussian function. See text for further explanations.

The first goal of the COBRA analysis is to determine the correlation spread $\sigma_{1\mathrm{hit}}$ from the $I_\mathrm{p}/I_\mathrm{s}$ correlation diagram in order to deduce a quality criterion for the pulse-spot assignment. The procedure has been described in detail in Becker 2016 and will be summarized here with help of Figure 4.16. From the correlation diagram in Figure 4.15 the mean value of I_p for each bin of I_s is extracted by a Gaussian fit and plotted in Figure 4.16 a). The error bars symbolize the Gaussian standard deviation obtained by the fits and visualize the imperfect correlation. The mean values as a function of I_s are fitted by a sixth order polynomial, referred to as correlation function $f_\mathrm{cor}(I_\mathrm{s})$.

With help of the correlation function, all coordinates I_s can be modified into the transformed spot intensity $I_{s,t} = f_\mathrm{cor}(I_\mathrm{s})$ and the correlation diagram can be plotted again in the coordinates I_p and $I_{s,t}$ (subfigure b)). For a quantitative analysis of the correlation spread, the distribution is rotated by 45° in subfigure c), where coordinates

have been transformed as follows:

$$t = \frac{I_{s,t} + I_\mathrm{p}}{\sqrt{2}}$$
$$s = \frac{I_{s,t} - I_\mathrm{p}}{\sqrt{2}} \tag{4.99}$$

Here, s is the relevant coordinate to determine the correlation spread. Finally, the histogram is projected onto the s axis and fitted by a Gaussian function, giving access to a correlation spread of $\sigma_\mathrm{1hit} = 0.234$ equal to the Gaussian standard deviation.

Now that the COBRA algorithm has been applied to single fragments, it can be transferred to detected double fragments ($N_\mathrm{s} = 2$ and $N_\mathrm{p} = 2$). For an event with two spot intensities $I_{\mathrm{s},1}$ and $I_{\mathrm{s},2}$, as well as two pulse intensities $I_{\mathrm{p},1}$ and $I_{\mathrm{p},2}$, the first step is to transform spot intensities into $I_{s,t,1}$ and $I_{s,t,2}$ by applying the correlation function. Both values, together with the pulse intensities, are further modified with equation 4.99 to obtain $s_{1,i}$ and $s_{2,i}$ for every possible combination of spot and pulse intensities. One of the combinations is valid if $s_{1,i} \leq \sigma_\mathrm{a}$ and $s_{2,i} \leq \sigma_\mathrm{a}$, where σ_a is called acceptance level. I. e., a valid combination does not deviate significantly from the main axis of the correlation diagram for both fragments. The whole event is declared as

- *invalid* if $s_{1,i} > \sigma_\mathrm{a}$ or $s_{2,i} > \sigma_\mathrm{a}$ for all combinations i.
- *valid* if $s_{1,i} \leq \sigma_a$ and $s_{2,i} \leq \sigma_\mathrm{a}$ for only one combination i.
- *ambiguous* if $s_{1,i} \leq \sigma_\mathrm{a}$ and $s_{2,i} \leq \sigma_\mathrm{a}$ for more than one combination.

For invalid and ambiguous events spots and pulses can not be assigned definitely. At the cost of reduced statistics, they are filtered out for 3D imaging related analysis. Residual gas collision measurements for an $N_2{}^+$ beam in Becker 2016 have revealed that an optimal value for the acceptance level, resulting in a minimum sum of invalid and ambiguous events, is given by

$$\sigma_\mathrm{a} = 2\sqrt{2\ln 2}\sigma_\mathrm{1hit} = 0.558 \tag{4.100}$$

which is identical with the Full Width at Half Maximum (FWHM) of the Gaussian fit in Figure 4.16 d).

The previously described algorithm was applied to all imaging related measurements presented in chapter 7. The here shown pulse and spot intensity distributions are corresponding to the 'high-density campaign' detector voltages in Table B.1. However, they are also representative for the other detector settings. In order to account for data-set-dependent effects, all data sets have been analyzed independently, leading to slightly varying values for the acceptance level. Furthermore, as Figure 4.16 indicates, the correlation of spots and pulse intensities is rather strong and results only in 15% of invalid and 11% of ambiguous events. A possible spatial dependence of the correlation, as discussed and applied in Becker 2016, is neglected in this work for the sake of reduced complexity.

Chapter 5

Storage of CH^+, runs and specific data analysis steps

All considerations and methodical updates presented in the previous chapter are generally applicable for electron-ion recombination experiments at CSR. Given the nature and the physical properties of each individual molecule, however, specific Dissociative Recombination (DR) experiments might necessitate further adaption of measurement schemes and inclusion of other experimental techniques. This chapter is dedicated to the CH^+ beamtime and first analysis steps towards the Merged-Beams Rate Coefficient (MBRC), whose results will be presented in chapter 6.

Sections 5.1 and 5.2 are concerned with the storage and electron cooling of CH^+ ions. In sections 5.3 and 5.4 a first analysis of imaging data is followed in order to determine a geometric detection efficiency for the DR fragments. As the internal states of the CH^+ ion are sensitive to inelastic electron collisions, its rotational state evolution is experimentally probed with help of a photodissociation technique in section 5.5. Furthermore, the influence of the population of the metastable excited $a^3\Pi$ state (chapter 2.2.1) is measured by 2D imaging in section 5.6, especially to estimate its influence on the CH^+ DR experiments.

The experimental conditions used for different measurement runs are shortly summarized in section 5.7 and a detailed view is provided in the appendix B.1 and B.2, for rate and imaging measurements, respectively. Section 5.7 furthermore includes the scaling uncertainty determined for rate measurements. A special emphasis in this work is put on a thorough description of pressure normalization as well as on a detailed uncertainty budget for absolute scaling of the MBRC, which can be found in appendix C.1.

5.1 CH^+ storage in CSR

For the experiments in this work, CH^+ ions were produced in a Penning ion source by fragmentation and ionization of methane gas. An analyzer magnet was used to separate CH^+ ions with a mass of approximately 13 atomic mass units (u) from other beam components on the high voltage platform. Isotopic molecular contaminants can be safely excluded, as typical atomic species inside the source (nitrogen, oxygen, hydrogen) cannot form a mass 13 u molecule. Additionally, a mass spectrum was recorded, showing that the amounts of mass 12 u and mass 13 u are comparable. Since the ion source chemistry is not expected to be different for $^{12}C^+$ and $^{13}C^+$, their natural abundance ratio ($\approx 100:1$) should be reflected in the mass spectrum. The additional height of the 13 u peak must therefore be attributed to $^{12}CH^+$, implying only a 1% contamination of $^{13}C^+$ in the mass 13 u beam. As electron recombination of atomic ions is typically much less probable than for molecules, the contamination of detected rates by $^{13}C^+$ is expected to be negligible.

The high voltage platform was set to an acceleration voltage of $\approx 280\,\mathrm{kV}$. From the initial ion source current of $300 - 800\,\mathrm{nA}$, around 50% could be transferred to CSR. Because of variations of the ion source conditions, those currents were not constant for the whole beamtime. However, in the experiment the ion number stored in CSR was determined independently (see sections C.1.2 and C.1.4). In first place, the CH^+ beam was RF-bunched, allowing to optimize the ion optic elements in the injection beamline. Additionally, the RF frequency gives a very precise ($10^{-4} - 10^{-5}$) determination of the revolution frequency in the ring, which was evaluated for the two different measurement weeks to

$$\begin{aligned} f_{\mathrm{rev},1} &= 57.9865\,\mathrm{kHz} \\ f_{\mathrm{rev},2} &= 57.9738\,\mathrm{kHz} \end{aligned} \tag{5.1}$$

As a major benefit, CSR offers the possibility for experiments in cryogenic environment. Additionally to active cooling of the whole experimental vacuum chamber with liquid helium (see section 3.1), the superconducting magnets in the electron cooler section were cooled by gaseous helium (see section 3.2). During the CH^+ beamtime the temperature development was followed by several resistive temperature sensors that are implemented in the experimental and isolation vacuum. In Figure 5.1 the temperature development for selected sensors is presented over the course of one of three beamtime weeks. In this week the electron cooler was operated twice for less than a day and then once for over two days. The operational times correspond to the common temperature increase in all sensors.

As thermal anchoring point for the current leads from outside the vacuum, the HTS terminals show the highest temperature. Due to safety reasons, the electron cooler is only operated if their temperature is below 90 K. This limit is almost reached in the displayed week. The terminals are cooled by the 80 K cooling line that is, for electron cooler beamtimes, typically operated at lower temperatures than its nominal

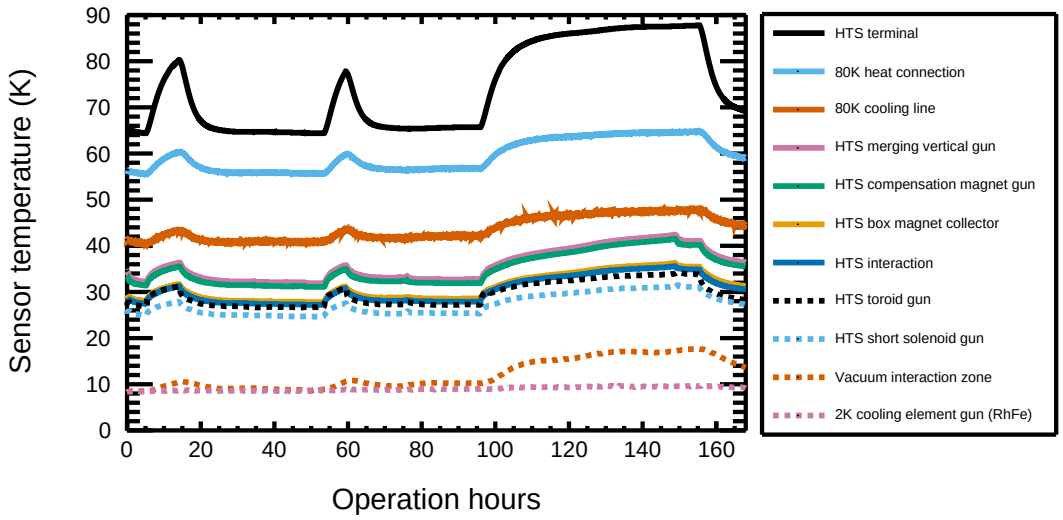

Figure 5.1: Temperature development on various sensors during a beamtime week. Sensors labeled by 'HTS' are measured on the superconducting magnets, except for the HTS terminal that is their common thermal anchoring point. The sensor with lowest temperature uses a rhodium-iron ('RhFe') resistive element, while all others are based on platinum (PT-1000).

value. Here, the cooling line temperature is around 50 K. The sensor labeled '80 K heat connection' monitors the temperature of a clamp connecting the 80 K line with the terminals. Judging by the 20 K difference between clamp and line, it becomes evident that the heat connection between these two elements is insufficient. For the future it is planned to improve cooling of the terminals by implementing an additional cold head in order to extend operation possibilities for the CSR electron cooler.

The sensors mounted directly to the HTS are reasonably cold (< 40 K) due to the separate cooling by gaseous helium, as explained in section 3.2. Furthermore, it is interesting to follow the experimental vacuum chamber temperature. The lowest temperature is achieved on the nominal 2 K cooling element, which is around 8 K for the conditions in the CH^+ beamtime. Small temperature fluctuations at this comparably high absolute value induce outgassing and freezing of cryopumped gas on the experimental chambers. Consequently, pressure fluctuations were observed during the three weeks of beamtime. The sensor in the electron cooler interaction region additionally follows the temperature trend of the electron cooler operation cycle. The obvious hypothesis that heat input from the electron cooler operation worsens the CSR vacuum pressure could already be confirmed.

Despite of the comparably high temperature, the conditions do barely affect rotational cooling of molecules, which is more dominated by the small fraction of 300 K radiation in the ring than by the CSR temperature. Pressure fluctuations partly affect normalization of DR signals but can be corrected for, as shown in appendix C.1.2. In recent beamtimes cooling element temperatures around 3 K could be achieved and reaching the design

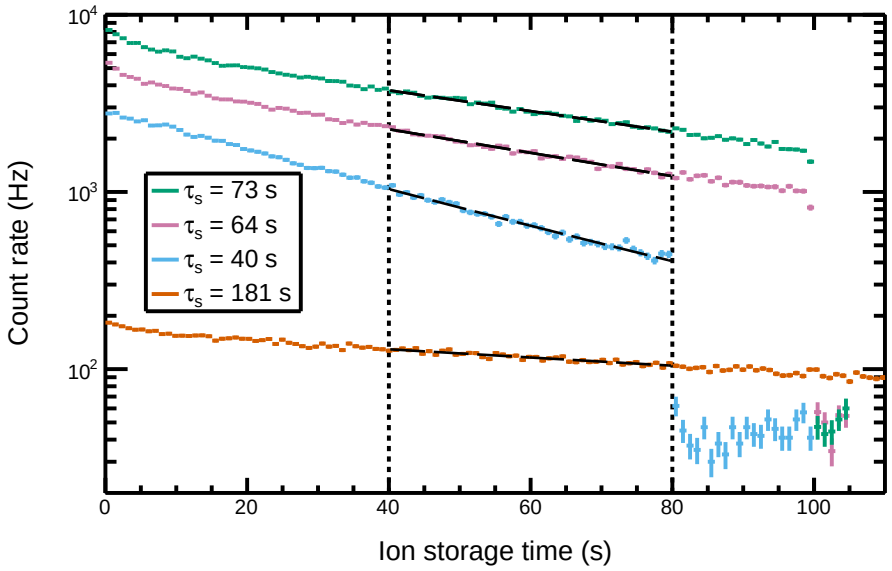

Figure 5.2: Lifetime curves for CH^+ ions in CSR. Various colors indicate measurements on different days of the beamtime. Exponential decays (black dashed lines) have been fitted for storage times of $40 - 80$ s. The detector *dark count rate* was measured for the blue curve after 80 s and for the green and pink curve after 100 s and has been considered as an offset in the exponential fits. Beam lifetimes extracted from the fits are shown in the legend. The lifetimes are not pressure limited, while the absolute count rate is affected by both, pressure and stored ion number.

goal of 2 K is planned for the near future.

In order to characterize storage conditions, neutral fragments resulting from residual gas collisions were detected on the NICE detector (section 3.3). Because of the low temperatures in CSR, all remaining residual gas is expected to be H_2, enabling three possible processes for the production of fast neutral fragments:

$$CH^+ + H_2 \longrightarrow C + H + X^+ \tag{5.2}$$

$$CH^+ + H_2 \longrightarrow C^+ + H + X \tag{5.3}$$

$$CH^+ + H_2 \longrightarrow C + H^+ + X \tag{5.4}$$

where X stands either for molecular hydrogen or two hydrogen atoms. X is not expected to impinge on the detector due to fact that the initial hydrogen molecule is at rest in the lab frame. The detector signal induced by the latter reactions is proportional to the number of ions in the ring. Thus, ion beam lifetimes can be measured by following the collisional count rate over storage time.

A comparison of different lifetime curves obtained on several days within the beamtime is shown in Figure 5.2. Lifetime curves in CSR usually show an initial non-exponential decay, followed by a reasonably exponential drop at higher storage times.

However, it has been observed for several systems that storage of low ion numbers results in significantly better lifetimes, indicating an ion-number-dependent loss process and a negligible pressure dependence. The orange curve with a lifetime of 181 s in Figure 5.2 might illustrate this behavior in comparison to the other three curves with lifetimes of $40 - 73$ s. Since ion numbers have not been measured for those data and it is known that the cryogenic conditions were not stable over the beamtime, leading to pressure fluctuations, the absolute count rates in Figure 5.2 are not reflecting the ion number only but the product of ion number and pressure.

A crucial parameter for optimizing storage conditions is the *working point*, which describes the combination of horizontal (Q_x) and vertical (Q_y) betatron tune values (see Hinterberger 2008). For certain values of both tunes, betatron oscillations are amplified. These *tune resonances* can either limit the lifetime of the ion beam or prevent storage completely. Electron cooling of ion beams can cause shifts of the working point by the presence of the electron beam space charge, leading to a focusing of the ion beam (lensing effect). Additionally, electron cooling reduces the ion beam size, causing a defocusing by the ion space charge itself (incoherent tune shift). An extended discussion about the working point, tune shifts and investigations for CSR-conditions can be found in chapter 2.1.2, 2.3.1 and 4.2.5 of Wilhelm 2019.

The working point of the storage ring can be controlled by the settings of the quadrupole doublets (see Figure 3.1). In case of the CH^+ beamtime, the quadrupole voltages in all sections of CSR were set up symmetrically, which is termed *standard mode*. In this mode the working point was optimized in order to increase the ion beam lifetime, with and without electron cooling simultaneously, by avoiding resonances in the tune diagram (Figure 5.3). This diagram represents all resonances of order $n = 1-4$. In general, lower order resonances affect beam storage more than those of higher order. The resonance-free region around $Q_x = 2.5 - 2.66$ and $Q_y = 2.5 - 2.66$ is promising for stable storage conditions. In that region the optimal working point was determined experimentally by scanning the quadrupole voltages and measuring the ion beam lifetime at storage times of $10 - 25$ s, similar to Figure 5.2.

The scan interval and results of the working point determination are displayed in Figure 5.4. Subfigure b) shows lifetime measurements at different points on the arrow in subfigure a). The blue data indicate that the region $Q_x = 2.49 - 2.57$ is not suited for long storage times due the variety of second and fourth order resonances. For high tunes above $Q_x = 2.69$, the red third order resonances complicate storage conditions. In the intermediate region, lifetimes above 100 s can be reached. It is interesting to note that even in this region peaks and dips in the lifetimes are visible. Those can tentatively be attributed to the fifth order tune resonances between $Q_x = 2.6$ and $Q_x = 2.65$. An untypical sensitivity to even fifth order resonances may be caused by the low-energy regime that CSR is working at.

When the magnetic field of the electron cooler (see section 3.2) is turned on (orange data in Figure 5.4 b)), the fifth order resonances are smeared out while other regions remain unchanged. With the application of electron cooling (pink data), the regions

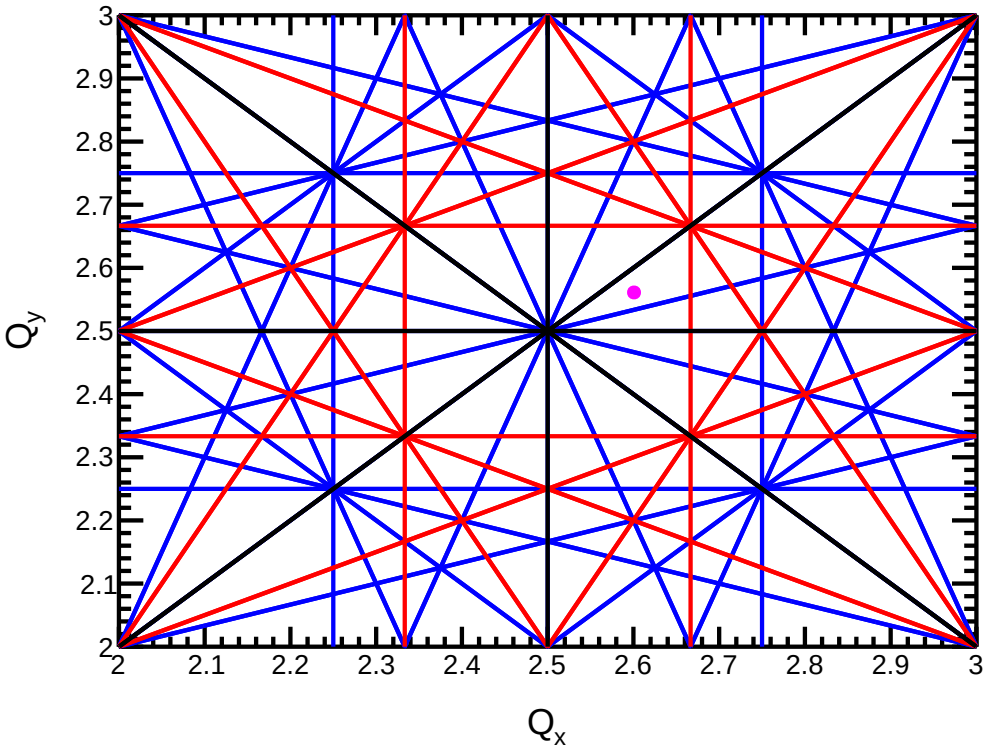

Figure 5.3: Tune diagram and working point in CSR. First order resonances are identical with the x- and y-axis, second order resonances are shown in black, third order resonances in red and fourth order resonances in blue. The chosen working point is marked as magenta circle.

$Q_x < 2.57$ and $Q_x > 2.65$ become inaccessible for ion storage. A possible explanation for this are electron-induced tune shifts, which are most critical in regions of resonances. In the accessible region lifetimes are reduced by at least factor of three. Possible reasons for this will be discussed in section 5.2. Considering all of the limitations above, the working point for this work has been set to

$$Q_x = 2.60 \qquad Q_y = 2.56 \tag{5.5}$$

As an additional observation, it should be emphasized that the peaks and dips in the electron cooled tune scan seem to be shifted compared to the uncooled data, indicating that electron-induced tune shifts can be seen in the working point scans. The magnitude of this shift is about $\Delta Q_x = 0.01$ and, thus, a factor of five higher than calculations done in chapter 4.2.5 of Wilhelm 2019. A detailed experimental study of electron-induced tune shifts goes beyond the scope of this work. Though, the results presented in this section motivate further experiments on this field for future operation of CSR.

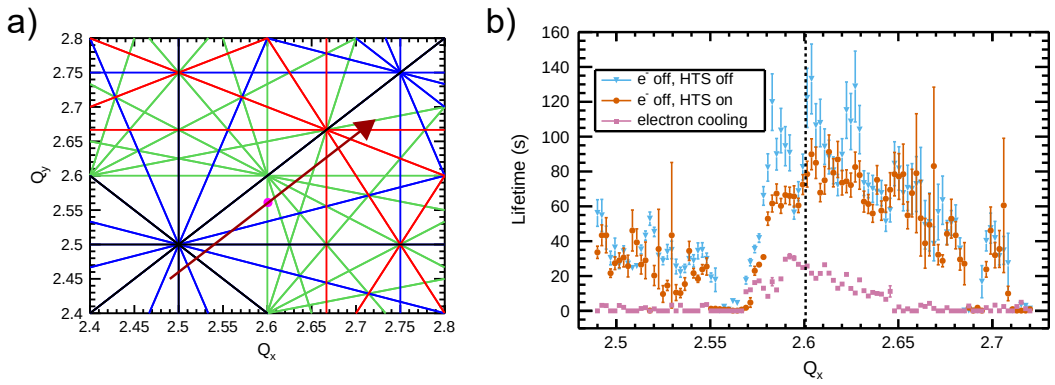

Figure 5.4: Working point determination by lifetime measurements. a): Detailed view on the tune diagram shown in Figure 5.3. Fifth order resonances are included in green, the optimal working point in magenta. Different discrete tunes on the brown arrow have been scanned in the displayed direction. b): Lifetimes of the CH^+ ion beam at different horizontal tunes on the arrow shown in a). Blue triangles: ion storage without electrons, orange circles: turning on all HTS magnets in the electron cooler section, pink squares: electron cooled ion beam. The black dashed line sits at the chosen optimal working point.

5.2 Electron beam parameters and cooling of CH^+ ions

In the CH^+ beamtime the electron cooler was operated at two different electron densities in the interaction zone of $n_{\mathrm{e,int,high}} = 6.6 \times 10^5\,\mathrm{cm}^{-3}$ and $n_{\mathrm{e,int,low}} = 3.4 \times 10^5\,\mathrm{cm}^{-3}$. The corresponding experimental campaigns are referred to as *high-density* and *low-density* campaign and allow to study different internal cooling behaviors of the molecule (see section 5.5). Common voltages for the electron cooler settings of both modes are summarized in Table 5.1 and can be compared to the electron cooler scheme in Figure 3.3. Here, the electron beam detuning energy E_d (see equation 3.13) was set by the interaction zone voltage U_int. Furthermore, its density was adjusted by U_pierce and U_ext, which control the electron current. As shown in chapter 4.2.1, the electron beam profile contains information about the effective cathode radius and can be used to calculate the electron density. In order to observe small density variations, various profile scans were conducted during the CH^+ beamtime, resulting in effective cathode radii in the range of

$$r_\mathrm{cath} = 1.08 - 1.19\,\mathrm{mm} \tag{5.6}$$

Due to the moderate currents in the CH^+ beamtime ($I_\mathrm{e} > 8\,\mu\mathrm{A}$), inhomogenities in the profile, as shown in chapter 4.2.1, are neglected and a constant density of the electron beam is assumed for further considerations.

Regarding the solenoidal guiding field in the electron cooler, standard magnetic field strengths of $B_\mathrm{gun} = 2000\,\mathrm{G}$, $B_\mathrm{acc} = 200\,\mathrm{G}$ and $B_\mathrm{int} = 100\,\mathrm{G}$ were used, leading to expansion factors of $\alpha_\mathrm{acc} = 10$ and $\alpha_\mathrm{int} = 20$.

Table 5.1: Electron cooler voltages for cooling of and collision experiments on CH^+. See Figure 3.3 and discussion around it for the definition of all voltages.

Voltages	U_0	U_{pierce}	U_{ext}	U_{barrier}	U_{int}	U_{cl}	U_{rep2}	U_{sec}	U_{WF}	U_{coll}	U_{ret}
Values (V)	23.0	2.9-3.1	7.0-11.5	30.0	11.0-24.0	4.0	16.5	20.0	13.6	30.0	0.0

A detailed discussion of the electron beam velocity and collision energy distribution was already given in chapter 4.2.2. In transverse direction no dependencies of the temperature on any electron cooler parameters, except for the expansion factor are known. Thus, a transverse temperature of

$$T_\perp = 2 - 3\,\text{meV} \tag{5.7}$$

is assumed in accordance with equation 4.11 and discussions around it.

For estimating the longitudinal temperature, equations 4.56 and 4.57 were evaluated for the two electron densities, corresponding to extraction energies of $E_{\text{ext,high}} \approx 9.0\,\text{eV}$ and $E_{\text{ext,low}} \approx 4.5\,\text{eV}$ as well as extraction densities of $n_{\text{e,ext,high}} = 1.5 \times 10^7\,\text{cm}^{-3}$ and $n_{\text{e,ext,low}} = 1.1 \times 10^7\,\text{cm}^{-3}$. An electronic noise of $e\Delta U = 100\,\text{meV}$ is entered since the noise filters described in chapter 4.2.3 have not yet been implemented at this point. With $k_\text{B}T_\text{c} = 25\,\text{meV}$, $\alpha_{\text{acc}} = 10$ and $\alpha_{\text{int}} = 20$ the longitudinal temperatures for both densities in the acceleration and interaction region result in

$$k_\text{B}T_{\parallel,\text{acc,high}} = 0.03\,\text{meV} + 0.25\,\text{meV} + 0.03\,\text{meV} = 0.31\,\text{meV} \tag{5.8}$$

$$k_\text{B}T_{\parallel,\text{acc,low}} = 0.03\,\text{meV} + 0.25\,\text{meV} + 0.01\,\text{meV} = 0.29\,\text{meV} \tag{5.9}$$

$$k_\text{B}T_{\parallel,\text{int,high}} = 0.05\,\text{meV} + 0.42\,\text{meV} + 0.05\,\text{meV} = 0.52\,\text{meV} \tag{5.10}$$

$$k_\text{B}T_{\parallel,\text{int,low}} = 0.05\,\text{meV} + 0.42\,\text{meV} + 0.02\,\text{meV} = 0.49\,\text{meV} \tag{5.11}$$

All previous equations show that the kinematic compression and LLR term contribute $\approx 10\%$ each to the longitudinal temperature, while the major contribution stems from the electronic noise. The noise reduction by the low-pass filters, described in section 4.2.3, is expected to reduce its contribution to a level comparable to the other effects in future.

In order to evaluate the full collision energy distribution, the approach described at the end of chapter 4.2.2 was followed, which considers the longitudinal temperature variation along the whole geometry of the electron cooler, angles between electron and ion beam in the merging section and the deceleration in the drift-tube. Figure 4.5 shows a representative example for a $E_\text{d} = 0\,\text{eV}$ distribution in the CH^+ high-electron-density mode.

For matching the merged electron and ion beam, the cooler settings for electron beam position, angle and velocity were optimized for longitudinal electron cooling of a bunched CH^+ beam. With help of the RF bunching system, the ion beam was divided

into $h = 4$ bunches by applying a frequency of $f_{\mathrm{rf}} = h f_{\mathrm{rev}}$ (see also equation 5.1). The Schottky pickup (Figure 3.1) was used to detect the mirror charges of the ion bunches at the second harmonic of f_{rf}. As explained in chapter 4.1 of Wilhelm 2019, the signal at this second harmonic frequency shows a significant increase when applying electron cooling. In order to obtain preliminary cooler settings, the magnitude of this increase was optimized. The cooling energies for CH^+ at revolution frequencies given in equation 5.1 are calculated with equation 3.3 to

$$\begin{aligned} E_{\mathrm{cool},1} &= 11.790(34)\,\mathrm{eV} \\ E_{\mathrm{cool},2} &= 11.785(34)\,\mathrm{eV} \end{aligned} \tag{5.12}$$

where the uncertainties are dominated by the ring circumference uncertainty.

A proof for electron cooling at an electron density of $n_{\mathrm{e}} = 6.3 \times 10^5\,\mathrm{cm}^{-3}$ is presented in Figure 5.5. Here, transverse cooling of a non-bunched (coasting) ion beam was studied. Simultaneously to electron cooling, neutral atoms are produced by DR and detected on the NICE detector (see section 3.3). The mass assignment algorithm presented in section 4.5.2 is used to determine the center of mass position for each recombination event, which is a projection of the molecule position in the interaction zone before the recombination process. Consequently, all detected center of mass positions together form a projection of the ion beam profile that can be studied as a function of storage time.

Figure 5.5 a) illustrates the cooling process for different ion storage times. Here, electron cooling was applied directly at injection ($t = 0$). A clear shrinking of the beam profile is visible. Typically, ion beam profiles in storage rings are assumed to be elliptical with major and minor axis aligned along the horizontal and vertical coordinate (see Hinterberger 2008). The here presented profiles in the cooling process of CH^+ ions are also elliptical. However, the major axis in the beginning is slightly turned clockwise compared to the vertical axis. During the cooling process the major axis is turning counter-clockwise. This effect is not yet completely understood. It is suspected that in low-energy storage rings the influence of the magnetic field from interaction solenoid and correction dipoles as well as the Earth's magnetic field lead to a coupling of horizontal and vertical degrees of freedom. Such an effect is under current investigation.

For a quantitative evaluation, the profiles at different storage times were fitted by a two-dimensional Gaussian distribution, turned by an angle φ to represent the turned elliptical profiles:

$$\begin{aligned} f(x,y) = A \exp\Bigg(&- \left(\frac{\cos^2\varphi}{2\sigma_1^2} + \frac{\sin^2\varphi}{2\sigma_2^2} \right) (x - x_0)^2 - \left(\frac{\sin^2\varphi}{2\sigma_1^2} + \frac{\cos^2\varphi}{2\sigma_2^2} \right) (y - y_0)^2 \\ &- \left(\frac{1}{\sigma_2^2} - \frac{1}{\sigma_1^2} \right) \sin\varphi \cos\varphi (x - x_0)(y - y_0) \Bigg) \end{aligned} \tag{5.13}$$

Here, σ_1 and σ_2 represent the major and minor ellipse axis size and x_0 and y_0 the horizontal and vertical center of the distribution, respectively. In Figure 5.5 b) the

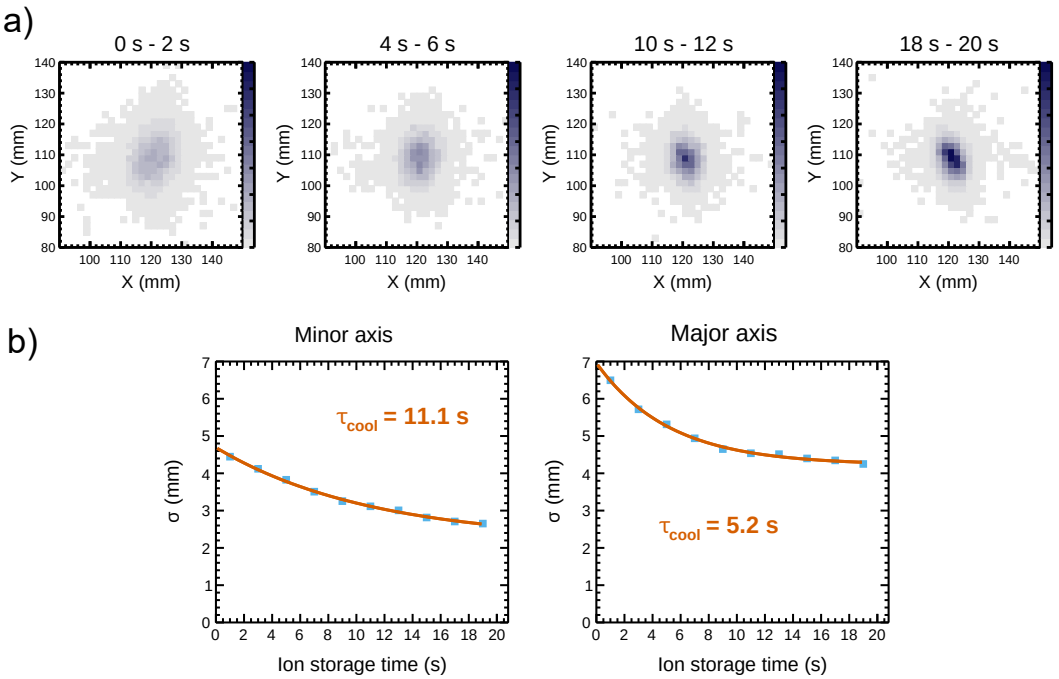

Figure 5.5: Transverse cooling of CH^+ ions. Subfigure a) shows projections of the ion beam, measured on the NICE detector, for different time intervals of the electron cooling process. The projections were fitted with equation 5.13. The Gaussian width for the minor and the major axis are plotted against ion storage time in subfigure b). The small error bars arising from the fits are covered by the data point sizes.

resulting values for σ_1 and σ_2 are plotted against storage time. From an exponential fit of the data, cooling times of

$$\begin{aligned} \tau_{\mathrm{cool},1} &= 11.1(11)\,\mathrm{s} \\ \tau_{\mathrm{cool},2} &= 5.2(4)\,\mathrm{s} \end{aligned} \tag{5.14}$$

can be extracted. The uncertainties are of statistical nature and are propagated through the exponential and two-dimensional Gaussian fits.

As discussed in Poth 1990, the cooling-time-dependence on ion mass, charge number Z and electron density is given by

$$\tau_{\mathrm{cool}} = \overline{\tau}\frac{m_{\mathrm{ion}}}{Z^2 n_{\mathrm{e}}} \tag{5.15}$$

where $\overline{\tau}$ is a proportionality factor that can depend on the electron and ion beam temperatures. CH^+ cooling times can be compared to values obtained for transverse cooling of HeH^+ ($\tau_{HeH^+} \approx 1.5\,\mathrm{s}$) and HD^+ ($\tau_{HD^+} \approx 1.0\,\mathrm{s}$) in Wilhelm 2019. For this

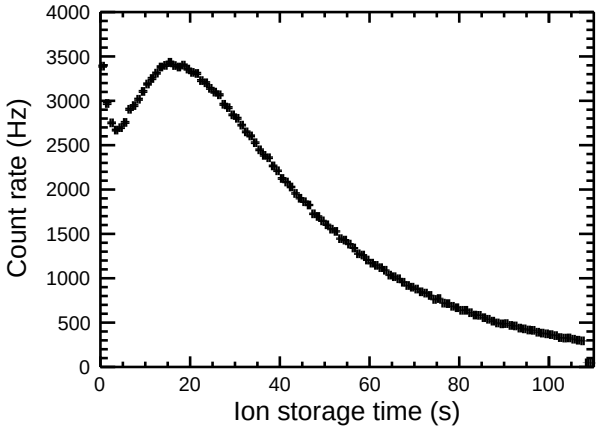

Figure 5.6: Ion collection effect for CH^+ ions. The observed count rate corresponds predominantly to DR events.

purpose $\overline{\tau}$ is evaluated for all measurements, resulting in

$$\begin{aligned} \overline{\tau}_{CH^+,1} &= 5.4 \times 10^{-5}\,\mathrm{cm}^{-3}\mathrm{s/u} \\ \overline{\tau}_{CH^+,2} &= 2.5 \times 10^{-5}\,\mathrm{cm}^{-3}\mathrm{s/u} \\ \overline{\tau}_{HeH^+} &= 1.9 \times 10^{-5}\,\mathrm{cm}^{-3}\mathrm{s/u} \\ \overline{\tau}_{HD^+} &= 1.4 \times 10^{-5}\,\mathrm{cm}^{-3}\mathrm{s/u} \end{aligned} \tag{5.16}$$

Compared to the lighter ions, CH^+ cooling times appear longer than expected. The high difference between the two ellipse axis should be emphasized especially, which has not been observed for the light ions in this extent. In general, electron cooling at CSR has turned out to be challenging for heavy ions up to now. The low-energy regime is very sensitive to effects of *dispersive electron cooling* that were already studied by Beutelspacher et al. 2003 at TSR. Due to a finite storage ring dispersion in the electron cooler section, a small displacement between electrons and ions can worsen cooling times and even introduce heating effects. In order to counteract this effect for future experiments, a storage mode with negligible dispersion in the electron cooler section is currently under investigation and has shown promising results for cooling of OH^+ ions.

Due to degradation of photocathodes and their slightly different surface qualities, the cooling voltage U_{cool}, corresponding to the cooling energy via equation 3.4, had to be adapted several times over the beamtime. A fine adjustment of this voltage was achieved with a third diagnostic method. In the course of the experiments, it was observed that the electron recombination count rate on the detector rises on the order of the cooling time as shown in Figure 5.6, even though the residual gas signal is continuously decreasing. This effect was ascribed to the fact that the ion beam at injection is broader than the electron beam. After transverse electron cooling, the electron-ion beam overlap improves, leading to an increase in the count rate. The fact that this collection effect was very prominent only for a small range of cooling voltages, on the order of 20 mV,

led to the conclusion that it can be used as a sensitive method for optimization of transverse cooling.

It should be mentioned at this point that the previous interpretation is not unequivocal. Another possible explanation is that the increased count rate stems from rotational-state-dependent DR, as studied in chapter 6.4. Depending on the electron energy, rotational state populations are changed due to inelastic collisions (see chapter 2.2.2 and section 5.5). Even if this is the cause of the increasing count rate, optimizing on the effect would be reasonable because inelastic cooling is expected to be most efficient at the exact cooling energy (Figure 2.6).

Electron cooling at CSR offers the possibility for collision experiments in a new low-energy regime. The work of Wilhelm 2019 presents a detailed study on this topic with several diagnostic approaches. Since the focus of this work lies on electron recombination experiments, further considerations in this section would fall out of the scope.

5.3 Detector data characterization

As a first step for the later analysis, data obtained in the DR experiments of CH^+ shall be characterized in this section, following the definitions in chapter 4.4. Most events with small pulse amplitudes of $|A_\mathrm{p}| < 0.3\,\mathrm{V}$ could be identified as electronic noise and were filtered out of the data sets.

An example of imaging data for CH^+ events with electron beam set to $E_\mathrm{d} = 0 - 40\,\mathrm{meV}$ after this filter process is given in Figure 5.7. It is representative for the low-energy DR ($E_\mathrm{d} < 280\,\mathrm{meV}$), where two channels with high KER are expected (see Table 2.4), and will therefore be discussed in the following.

Due to the high KER and correspondingly high transverse fragment distances, the distribution of spot positions for two-fragment events (subfigure a)) indicates that the detector is completely filled with events, which is a serious complication for obtaining distance distributions. While the carbon atoms are mainly located in the high intensive center, the hydrogen atoms are spread over the complete MCP aperture. A maximum transverse distance between both species of

$$d_\mathrm{2D,max} = 122\,\mathrm{Pix} \approx 51\,\mathrm{mm} \tag{5.17}$$

was determined, all higher distances are affected by the detector size and the distance distributions presented in chapter 4.4.2 become invalid. However, when considering only lower transverse fragment distances, e. g., by angular cuts on ϑ (see chapter 4.4.2), comparison to ideal distributions is reasonable.

The circular outer rim in Figure 5.7 a) represents the MCP aperture with a diameter of $D \approx 120\,\mathrm{mm}$. On the left hand side a cutout becomes visible, which is caused by the shadow of a mirror holder for the laser setup inside the CSR beamline. For imaging

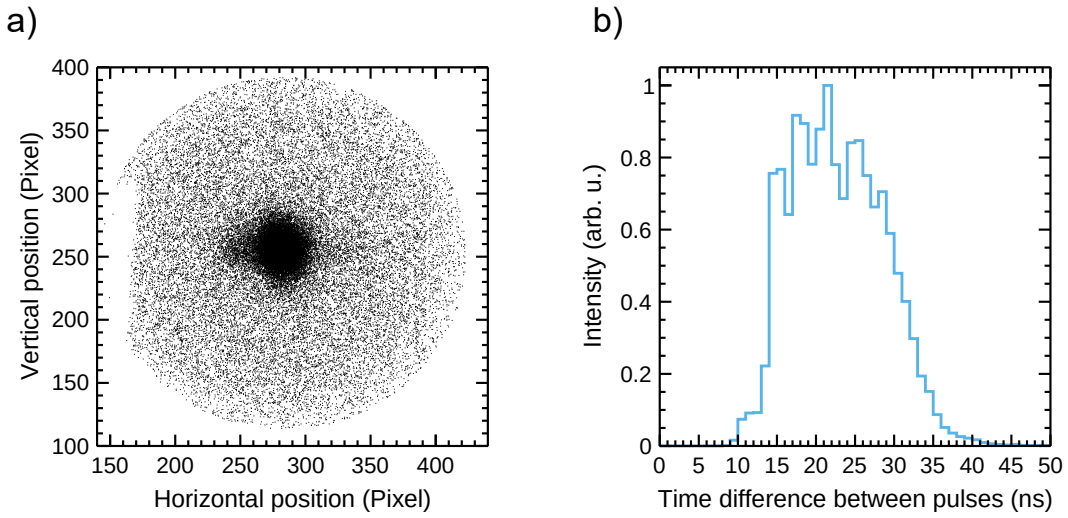

Figure 5.7: Typical example of imaging data at $E_d = 0 - 40\,\text{meV}$. The data are filtered on $N_s = 2$ and $N_p = 2$ events, where DR dominates residual gas induced events. Subfigure a) represents an integration over all transverse impact positions. Subfigure b) shows the distribution of time difference between pulses.

related measurements in chapter 7, this cutout was corrected by a data cut on the azimuthal angle range $155° < \varphi < 210°$. As explained in section 4.4.2, from theoretical considerations a fragmentation probability dependence on φ can be neglected. Still, the experimental geometry, especially the vertical inclination between electron and ion beam in the electron cooler merging region (Figure 3.2), might introduce a small azimuthal asymmetry, which is neglected here.

In Figure 5.7 b) the distribution of time differences for DR dominated double-fragment events ($N_s = 2$ & $N_p = 2$) is presented. The shape of the distribution shows a strong suppression of short time differences below 14 ns. This is due to overlapping of pulses, which cannot be separated reliably by the applied algorithm. Thus, for the analysis in chapter 7, only times $\Delta t \geq 15\,\text{ns}$ are considered as reliable. In contrast to the expected longitudinal distribution in equation 4.76, the distribution is not flat over most part of the range but shows a pattern of sharp peaks on its maximum, exceeding the statistical uncertainty of the data. Such a pattern cannot be created even from multiple DR channels with different KER values and only two channels should be observable anyhow (see Table 2.4). The behavior is expected to originate from the amplification stage of the signal processing and is not yet fully understood. It is considered as a possible time jitter in the analysis.

Further characterization of the measured data is possible by analyzing Pulse Height Distributions (PHDs). PHDs for different combinations of N_s and N_p are presented in Figure 5.8. They correspond to the 'low-density campaign' detector voltages of Table B.1. The contributing events can be explained as follows:

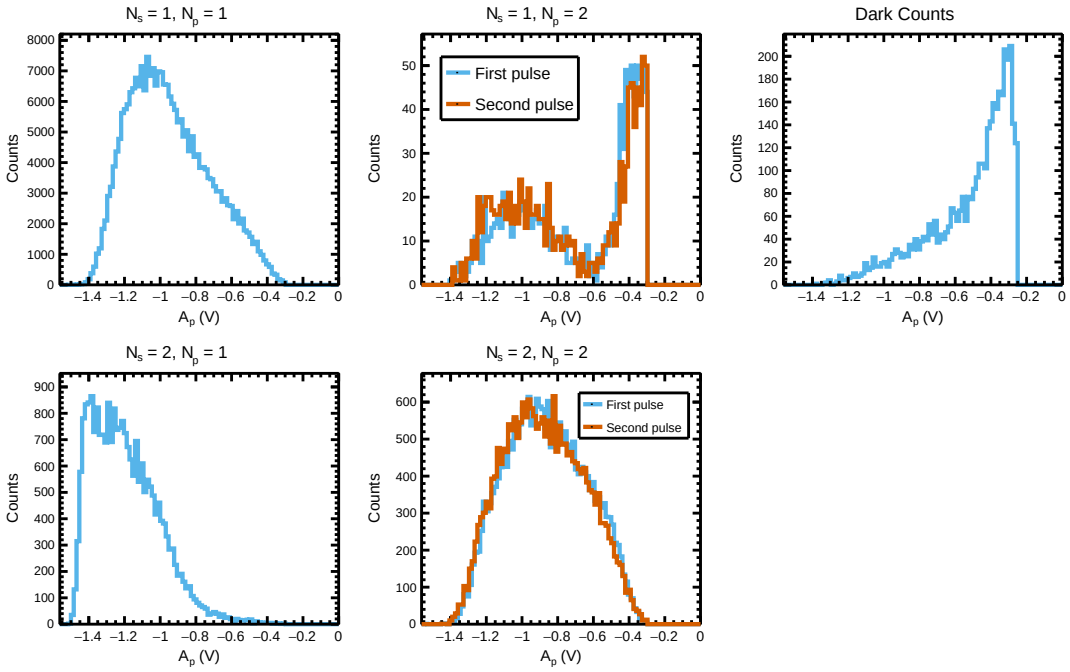

Figure 5.8: Pulse height distributions for the NICE detector, typical for CH^+ DR measurements with electron beam at $E_d = 0 - 40\,\text{meV}$. The distributions were obtained for the 'low-density campaign' detector voltages of Table B.1. N_s stands for the number of spots and N_p for the number of pulses detected. In case of $N_p = 2$, distributions for both pulses are shown separately. Note that due to the negative amplitudes, high absolute amplitudes are located at the left side of the distributions.

The distribution for ($N_s = 1$, $N_p = 1$) contains DR events, where only one of the two particles is detected because of the limited detection efficiency (see section 5.4). Furthermore, residual gas collisions mostly produce single neutral particles, which also fall into this category.

In rare cases, two pulses are detected with only a single spot. As the distribution for ($N_s = 1$, $N_p = 2$) shows, one of the pulses in those events has a low amplitude. It is possible that for less-intense electron avalanches on the MCP, the phosphor screen does not provide enough light to be detected by the camera. The analysis of time differences proved that most of the events are indeed real DR fragments while a small fraction of random coincidences between two separate events in the time window of $2\,\mu s$ (Figure 4.8) also occurs.

Events with $N_s = 2$ can be predominantly assigned with real DR processes. In case of $N_p = 1$, the two fragments are arriving so close in time ($\Delta t < 14\,\text{ns}$) that the pulse detection algorithm can not separate both pulses any more. As a consequence, both pulses add up and the PHD is shifted towards higher pulse amplitudes. For events with $N_p = 2$, both fragments are arriving with a time difference high enough to be separated. The PHD shows a more pronounced signal at low pulse amplitudes compared to ($N_s = 1$, $N_p = 1$), which is more affected by residual gas events. A tentative conclusion

is that residual gas induced events are caused by neutral carbon atoms, thus providing slightly higher pulse amplitudes on average because of their higher mass, while a fully detected DR event always contains carbon and hydrogen. Most residual gas collisions are therefore expected to follow reaction 5.4, while a small fraction of the other two processes (reactions 5.2 and 5.3) can clearly not be excluded.

The PHD of *dark counts* (see chapter 3.3) is also presented in Figure 5.8 and shows an exponential trend. For total DR rate measurements, the *dark count rate* is of importance and measured separately. A detailed analysis of dark count rates is provided in appendix C.1.1. The here presented characterization of events is used further in the next section in order to determine the CH^+ specific detection efficiency.

5.4 CH^+ specific detection efficiency

MCP based detectors, like the NICE detector, suffer from a limited detection efficiency due to the fact that particles impinging in-between two channels do not generate electron avalanches. This intrinsic detection efficiency was studied already in Novotný et al. 2019 for the NICE detector and amounts to a value of

$$p = 0.617(9) \tag{5.18}$$

In case of measuring fragments from CH^+ DR, expected KERs above 4 eV (see Table 2.4) as well as the mass asymmetry of both fragments, result in high fragment distances at the NICE detector. As shown in Figure 5.7 a), the whole surface is filled with hydrogen fragments and it is expected that a non-negligible fraction of them does not fit on the detector at all. Therefore, the detection efficiency for hydrogen fragments reduces to

$$p_\mathrm{H} = p p_\mathrm{g} \tag{5.19}$$

where p_g is the geometric hydrogen detection efficiency, arising from the detector size, and p is the MCP detection efficiency. As an additional complication, the value for p_g is not fixed but depends on the branching ratios of the DR final channels and, thus, becomes a function of detuning energy $p_\mathrm{g}(E_\mathrm{d})$. While for detuning energies up to 280 meV high energetic channels are dominating, higher detuning energies will result in the opening of new low-energetic channels (see Table 2.4). Therefore, $p_\mathrm{g}(E_\mathrm{d})$ depends mostly on the branching ratios of the ^{1}D and ^{1}S channel up to $E_\mathrm{d} = 280$ meV and is expected to increase to almost 100% at higher detuning energies, when the KER becomes smaller.

In order to determine $p_\mathrm{g}(E_\mathrm{d})$, the ratio of detected single fragments to double fragments $r_\mathrm{S/D}$ is studied for several detuning energies. Both, experiment (Amitay et al. 1997) and theory (Chakrabarti et al. 2017), indicate that the Dissociative Excitation

(DE) reaction (chapter 2.1.2) is negligible for electron energies below 2 eV, which is the upper limit of E_d studied in this work. Thus, after subtraction of residual gas induced background events, the remaining signal is solely caused by DR. Since for DR all events are expected to produce two fragments, the following probabilities can be calculated:

- Both fragments are detected: $p_D = p^2 p_g$
- C atom is not detected but H atom is: $p_{S,1} = (1-p)pp_g$
- C atom is detected but H atom does not hit the MCP surface: $p_{S,2} = p(1-p_g)$
- C atom is detected but H atom does not hit a MCP channel: $p_{S,3} = pp_g(1-p)$
- One fragment is detected: $p_S = p_{S,1} + p_{S,2} + p_{S,3}$
- At least one fragment is detected: $\eta = p_S + p_D$.

From these, the ratio of single to double fragment events is given by

$$r_{S/D} = \frac{p_S}{p_D} = \frac{1}{p} - 2 + \frac{1}{pp_g} \tag{5.20}$$

If $r_{S/D}$ is measured, the previous equation can be solved to extract the geometric hydrogen detection efficiency

$$p_g(E_d) = \frac{1}{p(2 + r_{S/D}(E_d)) - 1} \tag{5.21}$$

as well as the *trigger efficiency*

$$\eta(E_d) = p + \frac{p - p^2}{p(2 + r_{S/D}(E_d)) - 1} \tag{5.22}$$

The latter quantity is needed for absolute scaling of DR rate measurements (see chapter 4.4.1). Here, all events with at least one fragment are contributing to the measured count rate.

A procedure to determine $r_{S/D}$ shall be shortly summarized here. In first approximation single fragments are events with $N_s = 1$ and double fragments can be assigned to $N_s = 2$. However, as Figure 5.8 and the discussion around showed, some events can be misassigned with that approach. By analyzing pulse height distributions and time differences between pulses, misassignments are corrected and events that still cannot be interpreted are counted and their number is introduced as systematic uncertainty. The procedure results in the number of single fragments (S_{on}, S_{off}) and double fragments (D_{on}, D_{off}) for the electron on and electron off measurements, respectively. It is imperative to subtract both values from each other to obtain the electron induced quantities. However, due to higher count rates in the electron on state and the limited camera speed, saturation effects occur. This saturation effectively reduces the electron on and

electron off count rates differently. In order to correct for saturation, the electron on data are scaled by a factor C_{sat} such that

$$r_{\mathrm{S/D}} = \frac{C_{\mathrm{sat}} S_{\mathrm{on}} - S_{\mathrm{off}}}{C_{\mathrm{sat}} D_{\mathrm{on}} - D_{\mathrm{off}}} \tag{5.23}$$

Even for a non-saturated camera system the factor C_{sat} involves the total measurement times of both intervals, i. e., $C_{\mathrm{sat}} = \frac{t_{\mathrm{off}}}{t_{\mathrm{on}}}$, because S_{on} and S_{off} are not normalized by the measurement time. The most precise estimate for the saturation effect can be obtained by comparing camera data with timing data. The latter is able to deal with higher count rates, which are practically not affected by saturation. The real fraction between the number of electrons off ($N_{\mathrm{el,off}}$) and on ($N_{\mathrm{el,on}}$) events is given by the ratio determined from electronic measurements

$$f_{\mathrm{el}} = \frac{N_{\mathrm{el,on}}}{N_{\mathrm{el,off}}} \tag{5.24}$$

In contrast to that, the data acquisition system flags the events for which the camera could record images and was not busy transmitting data, which is the main saturation effect. Those events show a different fraction between electrons on and off measurements

$$f_{\mathrm{cam}} = \frac{N_{\mathrm{cam,on}}}{N_{\mathrm{cam,off}}} \tag{5.25}$$

The latter fraction is lower due to a higher saturation in the electrons on measurement. Consequently, a quantitative estimate for saturation is given by the ratio of both fractions

$$C_{\mathrm{sat}} = \frac{t_{\mathrm{off}}}{t_{\mathrm{on}}} \frac{f_{\mathrm{el}}}{f_{\mathrm{cam}}} \tag{5.26}$$

With the knowledge of C_{sat} and $r_{\mathrm{S/D}}$, $p_{\mathrm{g}}(E_{\mathrm{d}})$ can be determined. Unfortunately, the data statistics do not allow to extract a value for all detuning energies probed in the rate coefficient measurements (see chapter 6). Still, an analysis was conducted for the detuning energies 0 eV, 8 meV, 70 meV, 320 meV and an additional interval of $0.5 - 1.3$ eV. The results for $p_{\mathrm{g}}(E_{\mathrm{d}})$ and $\eta(E_{\mathrm{d}})$ are presented in Figure 5.9. Both quantities are significantly decreasing in the range of $E_{\mathrm{d}} = 8 - 320$ meV, which can be attributed to the higher electron energy added to the system, on the one hand, and by possible changes in DR channel branching ratios (see chapter 7.5), on the other hand. Above $E_{\mathrm{d}} = 320$ meV new low-energy channels are opening up, as explained in the beginning of this section, and the geometric efficiency rises again.

Since the detection efficiency depends on detuning energy, relative DR rates have to be normalized to $\eta(E_{\mathrm{d}})$, as shown in appendix C.1. A pragmatic approach to normalize all measured detuning energies is to interpolate the measured values for $\eta(E_{\mathrm{d}})$ with a spline. The resulting curve is shown together with the data in Figure 5.9. Here, the fundamental limits of $\eta_{\mathrm{max}} = (2-p)p = 0.8536$ ($p_{\mathrm{g}} = 1$) and $\eta_{\mathrm{min}} = p = 0.6174$ ($p_{\mathrm{g}} = 0$) cannot be overcome. For this reason, the functional form of $\eta(E_{\mathrm{d}})$ is forced to saturate when reaching η_{max} at the high detuning energies.

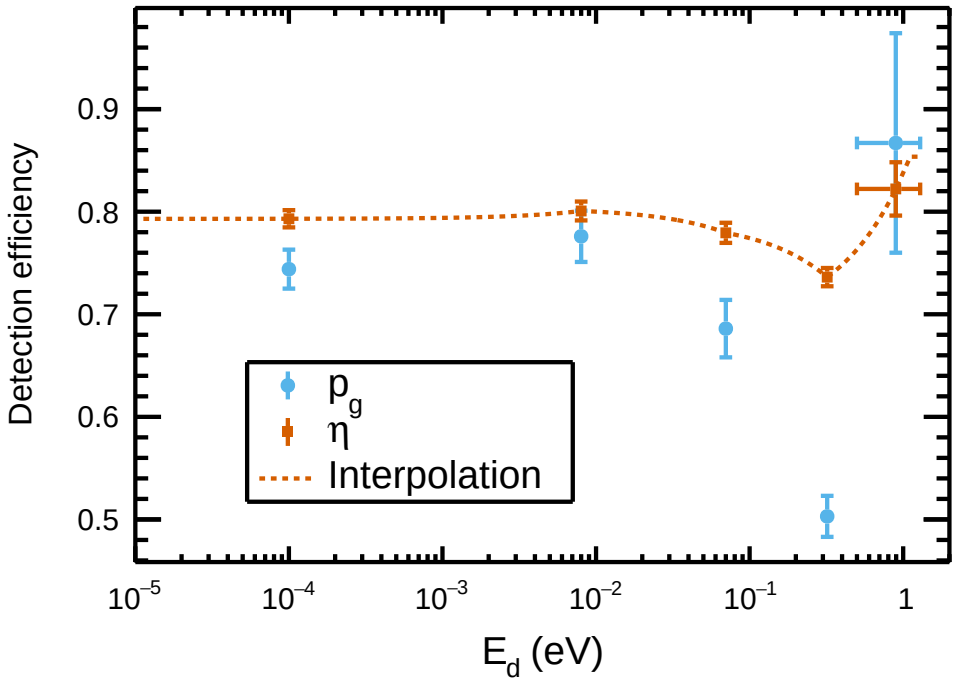

Figure 5.9: Geometric detection efficiency p_g and trigger efficiency η for CH^+. The data points for $E_d = 0\,\text{eV}$ were shifted to $E_d = 0.1\,\text{meV}$ for the sake of presentation. The orange data points for η are interpolated and slightly extrapolated by a spline. Above $E_d = 1\,\text{eV}$ the spline is changed into a horizontal line because the maximum possible trigger efficiency η_{max} (see text) is reached.

5.5 Rotational cooling measurements

As discussed in chapter 2.2.2, molecular ions stored in CSR are influenced by the blackbody radiation field and, additionally, by inelastic collisions with the overlapped electron beam. Qualitative estimates in that chapter led to the conclusion that both effects are relevant for the rotational state population evolution of CH^+. For DR experiments it was demonstrated in chapter 4.3 that quantitative knowledge of rotational state populations $P_J(t)$ is crucial for extracting state-dependent MBRCs.

The rotational energy of the CH^+ $J = 3$ state already amounts to $240\,\text{K} \times k_B$ (see Table 2.3) and is far beyond the CSR temperature. Therefore, a mixture of $J = 0$, $J = 1$ and $J = 2$ is expected during DR measurements, from radiative considerations only. Room-temperature storage ring measurements, as in Amitay et al. 1996, instead work with a rotational state ensemble close to the 300 K distribution shown in Figure 2.5.

In previous experiments at CSR, photodissociation of CH^+ (O'Connor et al. 2016) and photodetachment of OH^- (Meyer et al. 2017) ions were studied. Both processes show a significant and known dependence on J and could be used to characterize rota-

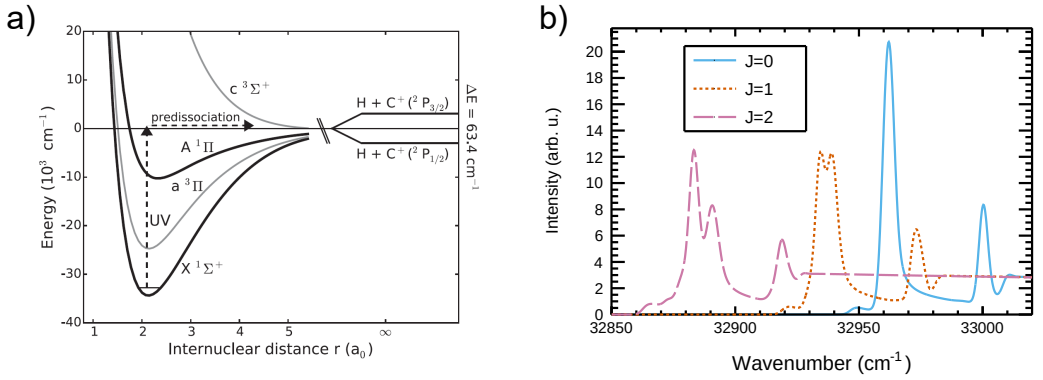

Figure 5.10: Near-threshold photodissociation of CH^+. a): The photodissociation process visualized on PECs, where the fine-structure splitting of the C(^{2}P) atomic limit is responsible for resonances in the cross section. The figure is taken from O'Connor et al. 2016. b): Wavenumber-dependent cross section for the photodissociation process of the three lowest rotational states convolved with a $4\,\mathrm{cm}^{-1}$ laser line width. The data were provided by O'Connor et al. 2016.

tional cooling. In those experiments effective blackbody radiation field temperatures of $T_{\mathrm{csr}} = 20\,\mathrm{K}$ and $T_{\mathrm{csr}} = 15\,\mathrm{K}$ could be extracted. More recent experiments (see Novotný et al. 2019) used these results to simulate the CSR radiation field as a composition of a $T_{\mathrm{csr}} = 10\,\mathrm{K}$ and a $T_{\mathrm{rt}} = 300\,\mathrm{K}$ radiation field, where the latter contribution from inevitable room-temperature openings of the storage ring amounts to a small fraction of $\epsilon_{\mathrm{rt}} < 5\%$.

Because of the relevance of inelastic collisions for CH^+ and in order to not solely rely on theory cross sections (Figure 2.6), a major goal of the CH^+ beamtime was to additionally measure the rotational state population evolution via photodissociation and use the results for the evaluation of state-specific DR rates. The methodology behind the population measurement was already explained in O'Connor et al. 2016 and a separate publication on inelastic electron collisions with CH^+ is currently in progress (Kálosi et al. 2021). A short summary of the methods and results relevant for this work is given here.

The photodissociation process

$$\mathrm{CH}^+ + \gamma \longrightarrow \mathrm{C}^+ + \mathrm{H} \tag{5.27}$$

was already studied in great detail in Hechtfischer et al. 2002, both, experimentally and theoretically. Its mechanism is visualized in Figure 5.10 a) on the base of PECs (compare Figure 2.4). A specific feature of the three lowest PECs of CH^+ is the fine structure splitting in the $C^+(^2P)$ dissociation limit, which is correlated with several PECs. At wavenumbers around the dissociation energy of $D_0 \approx 30\,000\,\mathrm{cm}^{-1}$, the only dipole-allowed transition from the ground state is $X^1\Sigma^+ \longrightarrow A^1\Pi$, which converges to the upper fine structure limit $\mathrm{H} + \mathrm{C}^+\,(^2\mathrm{P}_{3/2})$. If the photon energy is sufficient to

dissociate into the lower fine structure limit $H + C^+ (^2P_{1/2})$ but not into the upper one, a non-adiabatic coupling of PECs at high internuclear distance is responsible for a dissociation into the lower fine structure level. This near-threshold photodissociation process is of resonant character and, in specific, depends on the CH^+ rotational state.

Hechtfischer et al. 2002 observed this near-threshold photodissociation first experimentally and, later on, calculated cross sections to match the observed spectra. Detailed information about the long range coupling process is also provided in their work. Their calculated cross sections for CSR-relevant rotational states, convolved with an expected experimental linewidth of $4\,cm^{-1}$, are presented in Figure 5.10 b).

From an experimental point of view, the photodissociation process in the CH^+ beamtime was studied by overlapping the stored ion beam with a laser beam, produced by an OPO, at grazing angle. The two most distantly spaced viewports in Figure 3.1 were used to couple the beam into and out of the experimental vacuum chamber. Since the OPO generates a high-intensity, pulsed laser beam with a pulse length of $\approx 5\,ns$, the NICE detector gets saturated when hit by the reflected laser beam. Therefore, the detector was switched off during laser shots and activated again afterwards to collect the neutral hydrogen fragments, arriving with an additional time of flight of $2\,\mu s$. Because of the low absolute cross section for the photodissociation process, a high number of ions was needed. The detector was switched off during the cooling step (see appendix B.1 for details about detector switching), while collecting data only in the measurement and reference step (see chapter 4.4).

In the course of the CH^+ beamtime, population measurements were conducted for radiative decay without the influence of electrons, for a combination of electrons velocity-matched to the ion beam and off, as well as for conditions similar to DR measurements. The first two results are in preparation for publication (Kálosi et al. 2021) and reveal that the inelastic cooling of rotations is significantly influenced by electron collisions at used electron densities, as expected from theory. For the purpose of this work, however, only the results relevant for DR conditions shall be discussed. The analysis of the photodissociation data was conducted by Dr. Ábel Kálosi, who provided the results that will be used for interpretation of the time dependence of the DR rate (MBRC) in chapter 6.4.

Figure 5.11 represents the rotational populations for high- and low-electron-density data (section 5.2). The corresponding electron detuning energy ranges for high-density run set 4-5 (subfigure a)) and low-density run set 7-9 (subfigure b)) are defined in Tables B.4 and B.5. Due to limited measurement time, only these two energy ranges could be probed. The population for $J = 1$ has not been measured independently but calculated from the other two by the reasonable assumption that the sum of all three states amounts to 100%. Any contribution from higher rotational states is expected to be less than 1% from simulations.

The statistical quality of the laser-probed data, especially for low electron densities, is rather poor, owing to the low absolute photodissociation cross section of CH^+ and the low intensity of the OPO in the ultra-violet range. In order to qualitatively interpret

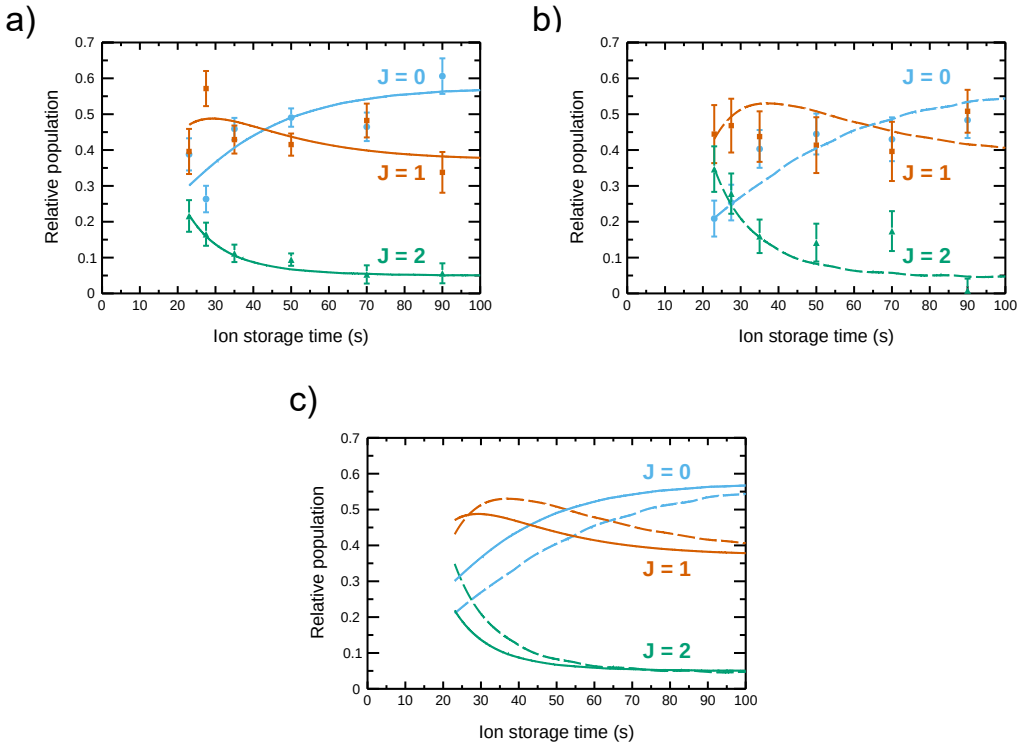

Figure 5.11: Rotational state populations for high and low electron density. Rotational cooling models with calculated inelastic cross sections from Hamilton, Faure, and Tennyson 2015 (see text) are included as guiding lines a): high-density measurements for conditions of run set 4-5 in Table B.4. b): low-density measurements for conditions of run set 7-9 in Table B.5, c): Comparison of high-density (solid line) and low-density (dashed line) cooling behavior.

the rotational cooling behavior, an inelastic cooling model was developed by Dr. Ábel Kálosi, using the pure radiative data from Kálosi et al. 2021 and the calculated rotational (de-)excitation cross sections from Figure 2.6. The result of the measurements in Kálosi et al. 2021 is that those cross sections are able to predict electron-induced rotational cooling correctly within the knowledge of the CSR electron cooler energy distribution. Therefore, it is assumed that modeling of the here presented DR conditions is possible. The model results are shown in Figure 5.11 a) and b) for the two different electron densities as solid lines and are compared to each other in Figure 5.11 c).

The comparison of the population evolution for both densities shows an increase of $P_{J=0}(t)$ and a decrease for $P_{J=2}(t)$ of about a factor of two at storage times between 21 s and 100 s. In contrast to that, $P_{J=1}(t)$ changes only slightly. The biggest difference between high- and low-density rotational cooling can be found by comparing their temporal behavior. At $t = 21$ s the high electron density is responsible for an already colder rotational state distribution than at low density. As both densities drive the final populations to similar limits, the difference between both data sets shrinks with storage

time. Consequently, the remaining change of $J = 0$ and $J = 2$ relative populations within the observed time window of $21 - 100\,\mathrm{s}$ is larger for the low-density case.

Even though a statistical improvement of both data sets would be desired, the observed changes of the $J = 0$ and $J = 2$ populations are large enough to detect any significant rotational dependence of the DR rate coefficient through a time dependence of the state-averaged DR MBRC. The results will be presented in chapter 6.4. For analysis of rotational state effects in these measurements, the statistical scatter of the measured rotational populations might introduce unwanted artifacts. Since the physical nature of the cooling process does not allow for sudden population changes, the smooth model curves in Figure 5.11 c) are used in that case.

For the sake of completeness, it should be mentioned that any population of vibrationally or electronically excited states, except for the metastable $a^3\Pi$ state, discussed in the following section, can be neglected. The discussion in Amitay et al. 1996 shows that, even for room-temperature storage rings, lifetimes for other states are below 1 s. Thus, for the CH^+ beamtime, none of these states is expected to be represented at 21 s.

5.6 Experimental analysis of the metastable $a^3\Pi$ state population

The CH^+ molecule possesses several electronically excited states and the first excited $a^3\Pi$ state is of metastable character with a lifetime of $\tau_\mathrm{m} \approx 7.0\,\mathrm{s}$ (chapter 2.2.1). The state information in equation 2.27 obtained at TSR (Amitay et al. 1996) revealed that a considerable fraction of ions can be populated in the metastable state when producing CH^+ in a hot ion source. Since the experiments in this work were done with a different ion source, the metastable population at ion beam injection into the CSR as well as the temporal population evolution needs to be checked by a similar analysis as given in Amitay et al. 1996.

For characterization of the metastable state in this section, CH^+ DR fragment distances on the NICE phosphor screen were measured in order to apply a 2D imaging analysis (chapter 4.4.2). This technique allows to distinguish the high KERs of the $X^1\Sigma^+$ ground state (Table 2.4) from the low KERs of the metastable $a^3\Pi$ state (Table 2.5) at collision energies close to 0 eV. The expected probability distribution for 2D distances was already shown in equation 4.75 and shall be repeated here:

$$P_{n,\mathrm{iso}}(d_\mathrm{2D}) = \begin{cases} \frac{1}{\delta_n \Delta L}\left(\arccos\frac{d_\mathrm{2D}}{s_2\delta_n} - \arccos\frac{d_\mathrm{2D}}{s_1\delta_n}\right) & 0 \le d_\mathrm{2D} \le s_1\delta_n \\ \frac{1}{\delta_n \Delta L}\arccos\frac{d_\mathrm{2D}}{s_2\delta_n} & s_1\delta_n \le d_\mathrm{2D} \le s_2\delta_n \\ 0 & \text{otherwise} \end{cases} \tag{5.28}$$

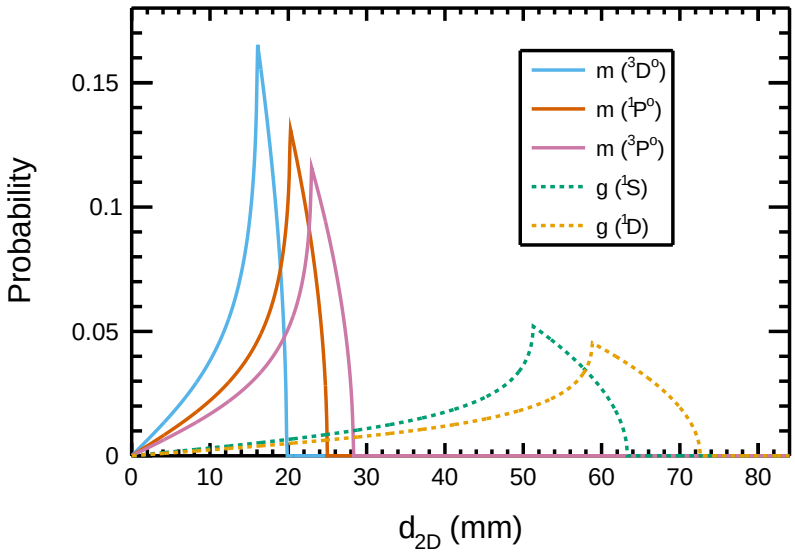

Figure 5.12: Ideal 2D distance distributions of metastable and ground state CH^+ DR final channels. The isotropic distributions ($a_2 = 0$) reflect equation 5.28 assuming the parameters relevant for the CH^+ beamtime, as well as the KERs listed in Table 2.4 and 2.5 for the possible final channels found at TSR. The solid lines indicate DR channels of the metastable $a^3\Pi$ state, while the dashed lines stand for the $X^1\Sigma^+$ ground state channels.

with

$$\delta_n = \frac{m_A + m_B}{\sqrt{m_A m_B}} \sqrt{\frac{E_{KER,n}}{E_{ion}}} \tag{5.29}$$

The previous distribution does not use the recoil effect correction derived in chapter 4.4.2, as it turned out that the 2D distance distribution is much less affected by the correction than other distance distributions. Furthermore, it assumes an isotropic angular distribution, which is approximately given for collision energies close to 0 eV because of the symmetry in the collision geometry (see chapter 4.4.2).

Figure 5.12 illustrates the expected 2D distance distributions at CSR for all DR final channels of the CH^+ ground state (Table 2.4) and metastable state (Table 2.5) observed at TSR. Each channel shows a characteristic peak whose position is given by the KER of the reaction and can compared to experimental distributions. Since the metastable and ground state KER values differ significantly from each other, both contributions can be well separated. The storage time dependence of summed up intensity of the metastable channels compared to the intensity of the ground state channels gives rise to the metastable state decay, as will be derived below.

In the CSR experiment, 2D distance distributions were studied for different storage times ($0 - 72$ s) for observation of the metastable state decay. This was done by overlapping the stored CH^+ ion beam with an electron beam in the CSR electron cooler. A similar measurement scheme as described in chapter 4.4 was applied, where the elec-

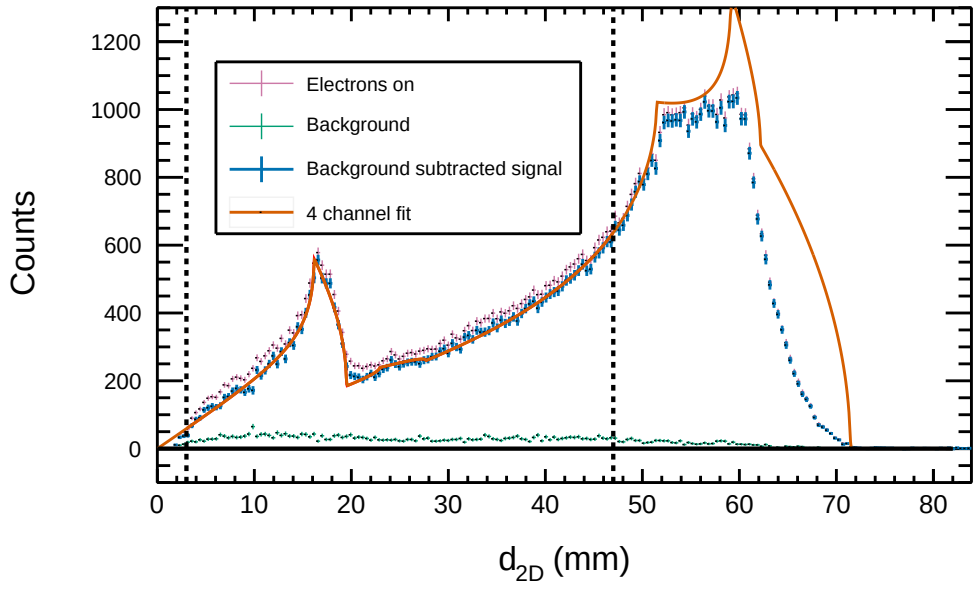

Figure 5.13: 2D fragment imaging of metastable and ground state CH^+ ions. The data measured with electrons at $E_d = 0\,eV$ and background are shown separately. The background subtracted signal (dark blue) is fitted by four individual channels. Two vertical dashed lines indicate the signal range where DR events can be detected without disturbances. More information is given in the text.

tron beam is switched between cooling energy ($E_d = 0\,eV$) and off on a ≈ms timescale, allowing to subtract the residual gas induced background signal.

As a first analysis step, data for all storage times were merged. The resulting 2D distance distributions are shown in Figure 5.13 for data with the electron cooler set to $E_d = 0\,eV$, as well as for the residual gas background. The signal measured in the cooling step was scaled by a saturation factor $C_{sat} = 0.384$, derived as explained in section 5.4, and the background is subtracted to obtain the electron induced fragment distribution.

The data show a pronounced peak around 17 mm that is attributed to the metastable state $^3D^o$ channel (compare Figure 5.12). Moreover, a clear signal from ground state channels is visible at higher distances. Unfortunately, fragments belonging to these channels can not be fully detected due to the limited size of NICE, as discussed in section 5.3. Thus, the signal shape of the ground state channels differs from Figure 5.12. Vertical lines are added to the figure to symbolize the left and right border of the non-distorted distances. At lower distances, spots on the screen arrive so close that they cannot reliably be separated by the NICE camera.

In principle, the distribution can be fitted by a sum of 2D distance distribution functions, as provided in equation 5.28. In this case, a four channel fit function was used to consider two metastable state channels ($^3P^o$ and $^3D^o$) and two ground state channels (^1D and ^1S). The metastable $^1P^o$ channel does not show any significant intensity in

the measured data and is thus neglected in the fit. Furthermore, the more general 2D distance distribution $P_{n,2}(d_{2D})$ (equation 4.80) was used instead of equation 5.28, which also allows for anisotropic angular distributions. The resulting fit function is given by

$$P(d_{2D}) = I_0 \sum_{n=1}^{4} f_n P_{n,2}(d_{2D}) \tag{5.30}$$

where I_0 is a normalization factor and f_n the relative integral of channel n compared to the ^{1}D channel ($f_4 = 1$). The purpose of this fitting process is to extract intensities of the individual channels. An independent determination of KERs is not intended due to the detector cutoff at high distances. For this reason, the KERs of the high energy channels were fixed to the values from Table 2.4. Additionally, the integral ratio for the two high energy channels had to be fixed to the results obtained by 3D imaging (see chapter 7.5) to $f_3 = 0.48$. The anisotropy factors were first fixed to $a_2 = 0$ for all channels because of the fact that no anisotropy is expected for $E_d = 0\,\text{eV}$, as discussed above. During the analysis, however, it turned out that a non-zero anisotropy coefficient of $a_2 \approx 0.3$ for the strongest metastable channel is needed to reproduce the data. Since the aim of this section is to predominantly evaluate integral ratios, this anisotropy was included as a free parameter.

The fit result is visualized as orange line in Figure 5.13 and describes the data quite well in the fit range between both vertical lines. The following fit parameters for the metastable channels were obtained:

$$\begin{aligned} f_1 &= 0.1216(20) \\ E_{\text{KER},1} &= 0.4376(27)\,\text{eV} \\ f_2 &= 0.0122(16) \\ E_{\text{KER},2} &= 0.882(12)\,\text{eV} \end{aligned} \tag{5.31}$$

Uncertainties given in the latter equations only reflect fit uncertainties. While the KERs are expected to be dominated by systematic uncertainties of the distance calibration (section 4.5.1), the integral ratios are unaffected by possible shifts of the distributions in millimeter space. Thus, statistical uncertainties for all f_n are expected to reflect their total uncertainty. Values for both KERs and relative intensities are well within the uncertainties given in Table 2.5. In contrast to the dominant $^3\text{D}^o$ channel, the $^3\text{P}^o$ channel is barely visible in Figure 5.13.

In order to estimate the storage time evolution of the metastable state contribution, the previous fit was applied to storage time cuts of the distribution given in Figure 5.13. The parameters $f_1(t)$ and $f_2(t)$ and their uncertainties were obtained from the fits, while the conditions for the ground state $f_3 = 0.48$ and $f_4 = 1$ are not changing with storage time. The following approach allows to extract the three parameters τ_m, $P_m(t = 0)$ and $\frac{\sigma_0}{\sigma_m}$:

The storage-time-dependent metastable $C_m(t)$ and ground state $C_0(t)$ contribution to the 2D distance distributions, measured in number of fragmentation events, are on

the one hand given by

$$\begin{aligned} C_\mathrm{m}(t) &= I_0(t)(f_1(t) + f_2(t)) \\ C_0(t) &= I_0(t)(f_3 + f_4) \end{aligned} \tag{5.32}$$

On the other hand, they are proportional to the number of ions in the respective states N_m and N_0 as well as to the cross sections σ_m and σ_0:

$$\begin{aligned} C_\mathrm{m}(t) &= K N_\mathrm{m}(t)\sigma_\mathrm{m} \\ C_0(t) &= K N_0(t)\sigma_0 \end{aligned} \tag{5.33}$$

with a proportionality factor K that includes, e. g., the detection efficiency and electron density. A ratio of the latter quantities is independent of K:

$$R(t) = \frac{C_\mathrm{m}(t)}{C_0(t)} = \frac{N_\mathrm{m}(t)\sigma_\mathrm{m}}{N_0(t)\sigma_0} \tag{5.34}$$

While the total number of ions in CSR ($N_\mathrm{tot}(t) = N_\mathrm{m}(t) + N_0(t)$) can be assumed to decay exponentially with storage time, characterized by the lifetime τ_s, the metastable ions additionally decay with their intrinsic lifetime

$$N_\mathrm{tot}(t) = N_\mathrm{tot}(t=0)e^{-t/\tau_\mathrm{s}} \tag{5.35}$$

$$N_\mathrm{m}(t) = P_\mathrm{m}(t=0)N_\mathrm{tot}(t=0)e^{-t/\tau_\mathrm{s}}e^{-t/\tau_\mathrm{m}} \tag{5.36}$$

$$N_0(t) = N_\mathrm{tot}(t) - N_\mathrm{m}(t) = N_\mathrm{tot}(t=0)e^{-t/\tau_\mathrm{s}}\left(1 - P_\mathrm{m}(t=0)e^{-t/\tau_\mathrm{m}}\right) \tag{5.37}$$

where $P_\mathrm{m}(t) = \frac{N_\mathrm{m}(t)}{N_\mathrm{tot}(t)}$ is the metastable relative population. By inserting equations 5.36 and 5.37 into equation 5.34, one obtains

$$R(t) = \frac{f_1(t) + f_2(t)}{f_3 + f_4} = \frac{\sigma_\mathrm{m}}{\sigma_0}\frac{1}{e^{t/\tau_\mathrm{m}}/P_\mathrm{m}(t=0) - 1} \tag{5.38}$$

The values for $R(t)$ were inferred from time-dependent fits of the 2D distance distributions and are presented in Figure 5.14 a). For long storage times equation 5.38 expects an exponential decay that is visible in the figure until 20 s. However, for even longer storage times, the data are deviating from a pure exponential. As the 2D distance distribution for the last time interval (Figure 5.14 b)) demonstrates, the metastable signal does converge to a non-zero constant.

An explanation for the remaining fraction can be found in the preceding discussion about the metastable state decay mechanism in chapter 2.2.1. As a consequence of the theoretical treatment of the decay in Hechtfischer et al. 2007, the $a^3\Pi(v=0, J=0, f)$ substate (*dark state*) was proposed to have a significantly higher lifetime than τ_m. Hechtfischer et al. 2007 estimated a $\approx 1\%$ fraction of the initial metastables to end up in this dark state, which is on the same order as the metastable signal in Figure 5.14. Thus, the measured signal can be interpreted as an experimental observation of this dark state. It underlines the importance of a fine structure treatment of CH^+ states for electronic transitions and strengthens the characterization of the metastable $a^3\Pi$

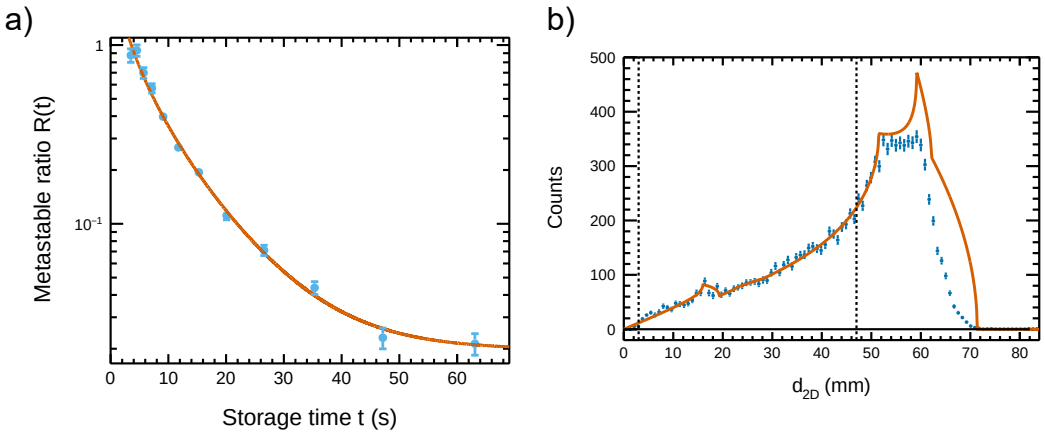

Figure 5.14: Metastable state characterization by 2D imaging. a): Metastable contribution ratio $R(t)$ (see equations 5.34 and 5.38) as function of storage time. The data points are fitted by equation 5.40. b): 2D distance distribution of the last storage time interval $[53.9\,\mathrm{s}, 72.2\,\mathrm{s}]$ showing a small remaining signal from the metastable state.

structure in Hechtfischer et al. 2007. With optimized cryogenic and storage conditions, it might even be possible to measure its lifetime in CSR if it lies below a few thousands of seconds.

In order to account for the metastable dark state in this analysis, the population evolution of the metastable state was corrected to

$$P(t) = P_{\mathrm{m,nd}}(t=0)e^{-t/\tau_\mathrm{m}} + P_{\mathrm{m,d}} \tag{5.39}$$

where $P_{\mathrm{m,d}}$ is the population of the dark state and $P_{\mathrm{m,nd}}(t=0)$ the initial population of all other metastable substates. The renewed assumption for the metastable population can be propagated through equations 5.34-5.38 in order to obtain a corrected value for $R(t)$. Furthermore, the storage times of interest for later analysis are located beyond 21 s such that the metastable decay is slightly reformulated, resulting in

$$R(t) = \frac{f_1(t)+f_2(t)}{f_3+f_4} = \frac{\sigma_\mathrm{m}}{\sigma_0}\frac{P_{\mathrm{m,nd}}(t=21\,\mathrm{s})e^{-(t-21\,\mathrm{s})/\tau_\mathrm{m}} + P_{\mathrm{m,d}}}{1 - P_{\mathrm{m,nd}}(t=21\,\mathrm{s})e^{-(t-21\,\mathrm{s})/\tau_\mathrm{m}} - P_{\mathrm{m,d}}} \tag{5.40}$$

A fit of the data with equation 5.40 is added in Figure 5.14 a), describing the evolution quite well. The following parameters can be obtained from the fit:

$$\begin{aligned} \tau_\mathrm{m} &= 10.1(10)\,\mathrm{s} \\ P_{\mathrm{m,nd}}(t=21\,\mathrm{s}) &= 9.8(33)\,\% \\ P_{\mathrm{m,d}} &= 2.49(70)\,\% \\ \frac{\sigma_0}{\sigma_\mathrm{m}} &= 1.26(43) \end{aligned} \tag{5.41}$$

The obtained lifetime is on the same order as the one in equation 2.27 but still differs significantly compared to the statistical uncertainties. This can be attributed to the fact

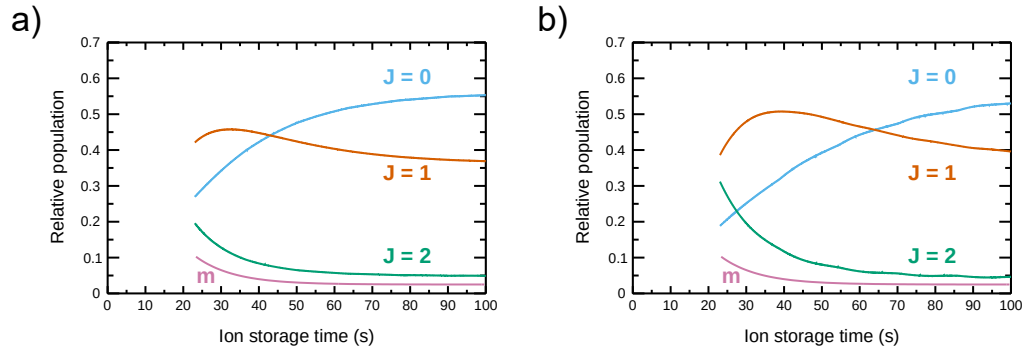

Figure 5.15: Rotational and metastable state populations for high and low electron density. The metastable population was calculated with equation 5.42. The relative rotational populations Figure 5.11 c) were scaled according to equation 5.43. a): high-density model for conditions of run set 4-5 in Table B.4. b): low-density model for conditions of run set 7-9 in Table B.5.

that the dark state was not included in the analysis by Amitay et al. 1996. Furthermore, the cross section ratio differs significantly from TSR, indicating either a mismatching 0 eV ground state or metastable state rate coefficient (see chapter 6.1). With the given fit parameters, a metastable state population of 12.3% at $t = 21\,\mathrm{s}$ is expected. One of the reasons why all following DR measurements include an initial electron cooling phase of $t = 21\,\mathrm{s}$, is to reduce the metastable state contribution to this level.

Comparing the metastable state decay to the ground state rotational population evolution in Figure 5.11, it can be concluded that the relative metastable state population is, in fact, only a factor of two smaller than the $J = 2$ rotational level population. Since the final rotational state of the electronic metastable decay is unknown, it is assumed here that it does not affect the relative rotational populations shown in the previous section. For further modeling the metastable population is set to the most likely fit results (equation 5.41)

$$P_\mathrm{m}(t) = 0.098e^{-(t-21\,\mathrm{s})/10.1\,\mathrm{s}} + 0.025 \tag{5.42}$$

and the rotational populations obtained in the previous section are scaled down to still satisfy the required unity sum:

$$P'_J(t) = P_J(t)(1 - P_\mathrm{m}(t)) \tag{5.43}$$

The resulting population evolution of all four states is presented in Figure 5.15, for high and low electron density separately. The metastable population reveals to be at least twice as low as $P_{J=2}$. Unfortunately, the lifetime of the metastable and $J = 2$ state is similar, which complicates to differentiate between their individual effects on the DR rate coefficient. Nevertheless, the here presented populations can be used for estimating rotational state effects of the $J = 0$ and $J = 1$ DR in chapter 6.4.

5.7 Summary of measurement parameters, runs and rate coefficient analysis

The CH^+ DR measurements were conducted with the NICE detector (chapter 3.3) and the CSR electron cooler (chapter 3.2) with parameters given in section 5.2. The general measurement scheme was discussed in section 4.4. In this section a summary of rate and imaging measurements will be provided together with comments on the rate coefficient analysis procedure.

MBRC spectra were obtained by scanning the electron beam detuning energy E_d and by measuring DR count rates on the detector. As discussed in section 5.2, the whole measurement campaign was divided into the *high-density* and the *low-density* campaign. Further details about the used measurement parameters, run settings and the scanning of electron energies for obtaining the MBRC spectrum, are given in appendix B.1. In both, the high- and low-density campaign, the MBRC was probed in an energy range of $E_\mathrm{d} = 0 - 1.3\,\mathrm{eV}$ and for storage times in CSR of $t = 21 - 95\,\mathrm{s}$. The measurements at different storage times allow to observe dependencies of the DR rate coefficient on the CH^+ rotational state populations (section 5.5).

The determination of the rate coefficient spectrum from the measured count rates involves several analysis steps. First, the detector *dark count rate* (see chapter 3.3) has to be determined. Second, the relative rate coefficient is obtained for each individual run and scaled to a common reference via pressure normalization (see chapter 4.4.1). Finally, an absolute ion current measurement (chapter 4.1) is conducted simultaneously to the relative MBRC measurement in order scale the data to absolute MBRCs. All previously mentioned steps are discussed in detail in appendix C.1, where a focus was put on providing a comprehensive list for the absolute rate coefficient uncertainty budget (Table C.2). In summary, it results in an absolute scaling uncertainty for the high-density data of

$$\frac{\Delta\alpha_\mathrm{mb}}{\alpha_\mathrm{mb}} = 17\% \tag{5.44}$$

The low-density data were scaled to the high-density data with an additional uncertainty of 3.3%, which can be neglected compared to the value above. Chapter 6 presents the results of the CH^+ DR rate coefficient measurements.

Additionally to the rate measurements, imaging measurements were conducted to determine DR final channels and infer dissociation dynamics. They are based on detecting fragment distances and differences of fragment arrival times, as shown in chapter 4.4.2. Here, four different detuning energies out of the complete MBRC spectrum were observed: $E_\mathrm{d} = 0\,\mathrm{meV}$, $8\,\mathrm{meV}$, $70\,\mathrm{meV}$ and $320\,\mathrm{meV}$. Details about the specific measurement schemes and conditions are given in appendix B.2, while chapter 7 presents the results of the CH^+ DR imaging measurements.

Chapter 6

Recombination rate coefficient results

A key element for understanding the Dissociative Recombination (DR) process of a molecule is to study the collision energy dependence of its cross section. The cross section, as a theoretical quantity, is understood for a single and exactly known collision energy. As described previously, the CSR merged-beams setup allows a realization of a quasi-monochromatic electron beam with a tunable average collision energy, coming close to a situation where the precise energy dependence of the cross section can be determined. However, the measured quantity, denoted as Merged-Beams Rate Coefficient (MBRC), represents an average over the narrow electron velocity distribution (chapter 4.2.2). Based on the detailed description and characterization of the CSR electron-ion merged-beams setup in the previous chapters and the analysis steps for the CH^+ beamtime, this chapter presents the results of this measurement campaign.

The object of astrophysical interest is mainly the related *plasma rate coefficient* that expresses reaction probabilities in a plasma at collisional thermal equilibrium. As explained in chapter 1, the Interstellar Medium (ISM) can be often approximated by such an environment. For modeling of the low-temperature ISM, plasma rate coefficients of internally (vibrationally and rotationally) cold ions are desired. Hence, the derivation of such plasma rate coefficients from the measured MBRC will be discussed.

At TSR the MBRC of *vibrationally* cold CH^+ ions was measured in a room temperature storage ring and it was demonstrated that the results differ from previous single-pass experiments with vibrationally excited ions (see chapter 2.3). This measurement served as a benchmark for theory and experiment for more than 20 years. The results of this chapter aim to improve those data by obtaining rate coefficients for CH^+ ions, which are additionally in their lowest *rotational* states, and to reveal any possible rotational dependence of the CH^+ DR process. Furthermore, the astrophysically-relevant low collision energies can be studied with much higher accuracy, owing to an order-of-magnitude improvement of the electron energy spread (see chapter 4.2.2). Thus, the first three scientifically open questions presented in chapter 2.4 can be addressed here.

While the energy- and storage-time-dependent MBRC results are presented in section 6.1 and 6.2, section 6.3 is concerned with a comparison of the data for different electron densities, i. e., rotational cooling behaviors. The rotational state dependence of the rate coefficient is studied in section 6.4. From the MBRC data the plasma rate coefficient for cold CH^+ ions is calculated in section 6.5, where also an estimate of the pure $J = 0$ plasma rate coefficient is provided. Those results are followed by a discussion of their astrophysical relevance in section 6.6. At the end of the chapter (section 6.7), the experimental results are compared to recent calculations of the rotational-state-specific CH^+ DR cross section.

6.1 Energy dependence

A major result of the DR rate analysis is the energy dependence of the absolute rate coefficient, which cannot only be used as a benchmark for theoretical cross section calculations, but also to determine the plasma rate coefficient. For presentation of the results in this section, the statistically better low-density data are chosen in the storage time window of $60 - 80\,\mathrm{s}$ (see section 5.7 for the set of probed storage times). In this benchmarking time interval, inelastic electron collisions already caused an almost equilibrated rotational population ensemble and the best possible internal cooling of CH^+ ions in CSR is reached, as shown in chapter 5.5. Data for later storage times suffer from statistical point of view compared to this set and are anyhow not expected to differ much from the $60 - 80\,\mathrm{s}$ time window, as Figure 5.11 indicates.

Figure 6.1 a) shows the MBRC in this storage time window. The rate coefficient is characterized by a rich structure of resonances for energies above $E_\mathrm{d} = 30\,\mathrm{meV}$, together with a very pronounced increase by two orders of magnitude towards $E_\mathrm{d} = 0\,\mathrm{eV}$. Below $E_\mathrm{d} \approx 1\,\mathrm{meV}$ the rate flattens out because of the finite electron cooler energy resolution (Figure 4.5). As a *direct* DR process (see chapter 2.1.3) would be represented by a $\sim E_\mathrm{d}^{-0.5}$ dependence in the rate coefficient and the increase towards lower E_d occurs with a much higher exponent of E_d, the $E_\mathrm{d} = 0\,\mathrm{eV}$ feature can be attributed to a strong resonance. This can either be a constructive cross section resonance close to $E = 0\,\mathrm{eV}$ or a broad, destructive window resonance at higher E, extending into the 0.1 eV regime. An interpretation of the structures and comparison to theory will be provided in section 6.7.

An extreme test of rotational state effects on the DR rate coefficient is possible by comparing the measured data with room-temperature experiments. As discussed in chapter 2.2.2, in a 300 K environment a variety of rotational states is populated, while for the late storage times in CSR only $J = 0 - 2$ are present. In Figure 6.1 a) a comparison to the TSR room-temperature results (see chapter 2.3) is shown. Relative rotational state populations are presented in subfigures b) and c) for both experiments,

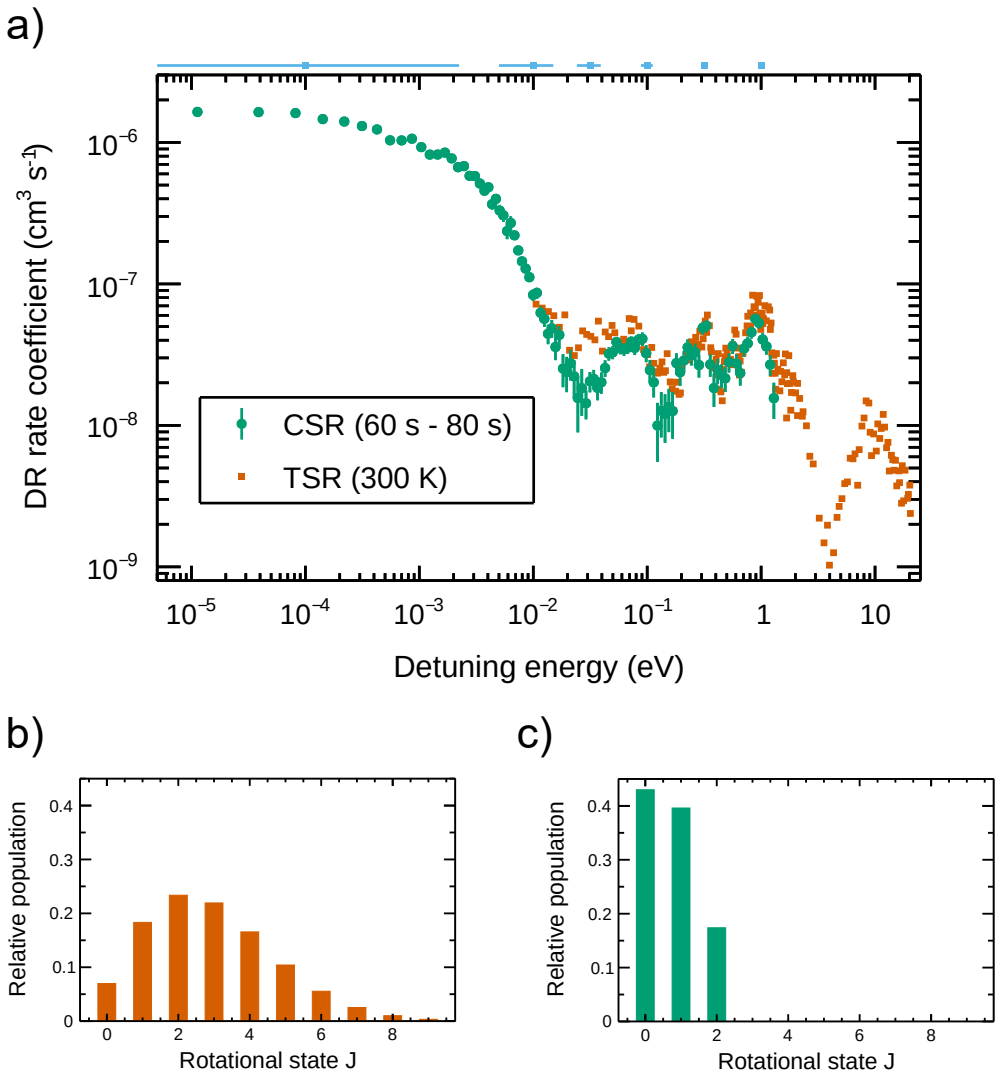

Figure 6.1: DR rate coefficient for rotationally cold CH^+ ions, including a comparison to room-temperature data. a): CSR data for $t = 60 - 80$ s. The included error bars are solely of statistical nature, while the absolute uncertainty of all data points together amounts to 17%. The markers and lines on top of the graph indicate the CSR electron cooler FWHM energy resolution. The CSR data are compared to digitized data from TSR (Amitay et al. 1996). Their energy-averaged cross sections were multiplied by the electron velocity $v = \sqrt{\frac{2E_d}{m_e}}$ to obtain a rate coefficient. b): Relative J-state populations at TSR (Figure 2.5). c): Measured relative J-state populations for CSR at $t = 60 - 80$ s (Figure 5.11 b)).

with CSR populations derived from the laser-based measurement discussed in chapter 5.5. It should be mentioned at this point that of the populations in TSR should still somewhat deviate from the radiative equilibrium populations at 300 K (subfigure b)) because of inelastic electron collisions. Still, the 300 K blackbody radiation dominates the rotational populations at room temperature.

At detuning energies above $E_d = 40$ meV, both data sets match quite well, except for a difference in scaling. This can be explained by the absolute rate coefficient uncertainty of both measurements (TSR: ±50%, this work: ±17%). Due to the relatively better residual gas background conditions at TSR, they were able to measure up to 20 eV, including the high energy peak that was assigned in Amitay et al. 1996 to a *direct* DR process. Here, no rotational state effects are expected. Those data will be used to complement the CSR cross section in the plasma rate coefficient determination in section 6.5.

Because of the limited energy resolution at TSR ($T_\parallel = 0.5$ meV, $T_\perp = 17$ meV), no reliable data below $E_d = 20$ meV could be obtained. Here, the CSR electron cooler demonstrates the advantage of a photocathode-based high-resolution collision target. The enormous DR rate coefficient increase in the meV range could not be revealed by the TSR experiment. Moreover, the dip at $E_d = 20$ meV is smeared out in their data.

The comparison to room-temperature measurements does not show any rotational state effects above $E_d = 100$ meV. Even the $E_d = 30 - 100$ meV resonance is compatible within the TSR energy resolution. Below $E_d = 30$ meV the TSR data are not able to provide further information about rotational state effects. It should still be mentioned, that both data sets do not strictly exclude rotational-state-dependent DR in any energy range as the possibility exists that both ion ensembles (Figure 6.1 b) and c)), by chance, lead to the same combined cross section.

Up to the point of this work, the strong rate coefficient increase in the meV range has not been expected. This energy region is of special interest for astrophysical application in the ISM because of the enhanced meV collision energies in this cold ($T < 100$ K) environment (see chapter 1). The strong resonance detected here will propagate into the plasma rate analysis (section 6.5) and influence the astrophysically-relevant temperature regime of electron recombination.

6.2 Storage time evolution

Rotational state effects on the DR rate coefficient can be detected by observing its storage time evolution. Figure 5.11 already showed that for the low-electron-density data the relative population of the $J = 0$ state increases to twice the value of its initial population during the measurement, while the $J = 2$ state decreases to less than half. Thus, any strongly J-dependent DR resonances are expected to be visible in storage

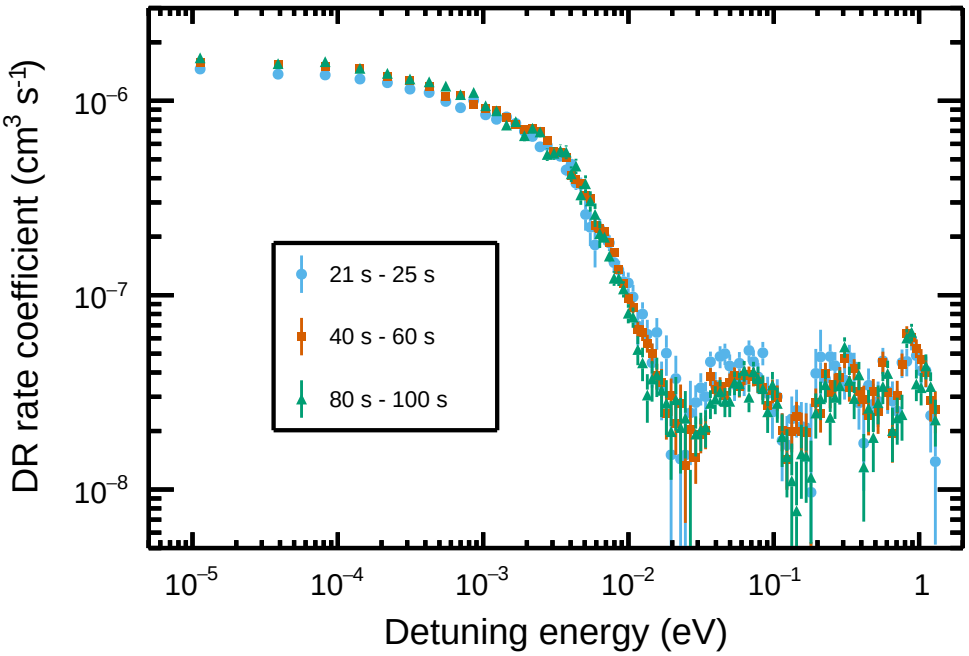

Figure 6.2: Storage time dependence of the CH^+ DR rate coefficient. Data for the first, the middle and the last measured storage time interval are compared to each other.

time cuts. A possible storage-time-dependent rate contribution of the metastable $a^3\Pi$ state has been minimized by obtaining data only after $t = 21\,s$, which corresponds to twice of its intrinsic lifetime (chapter 5.6). Furthermore, any contribution from the ion collection effect (see Figure 5.6) could be excluded in the given time intervals by proving that the projection of the ion beam profile on the fragment imaging detector stays constant.

Figure 6.2 presents the DR rate coefficient for the first, the middle and the last measured storage time window. The comparison does not reveal any appearing or vanishing resonances, as could be found for the HeH^+ ion (see chapter 1). Consequently, the rotational state dependence of the CH^+ DR process seems to be considerably weaker than in the HeH^+ case studied before. This is further underlined by the good match of the here presented results to the TSR data, as emphasized in the previous section.

In order to detect possible storage time effects, Figures 6.3-6.5 zoom into individual energy ranges of Figure 6.2 with a linear y-axis. In the low-energy region (Figure 6.3) a slight and continuous increase of the rate coefficient on the order of 10% becomes visible. Since the low-energy range could be studied with great statistics, a detailed analysis of J-state specific rate coefficients at $E_d = 0\,eV$ will be presented in section 6.4.

While the intermediate-energy region (Figure 6.4) does not reveal any significant difference, another feature, visible in the high-energy region (Figure 6.5), is the high-

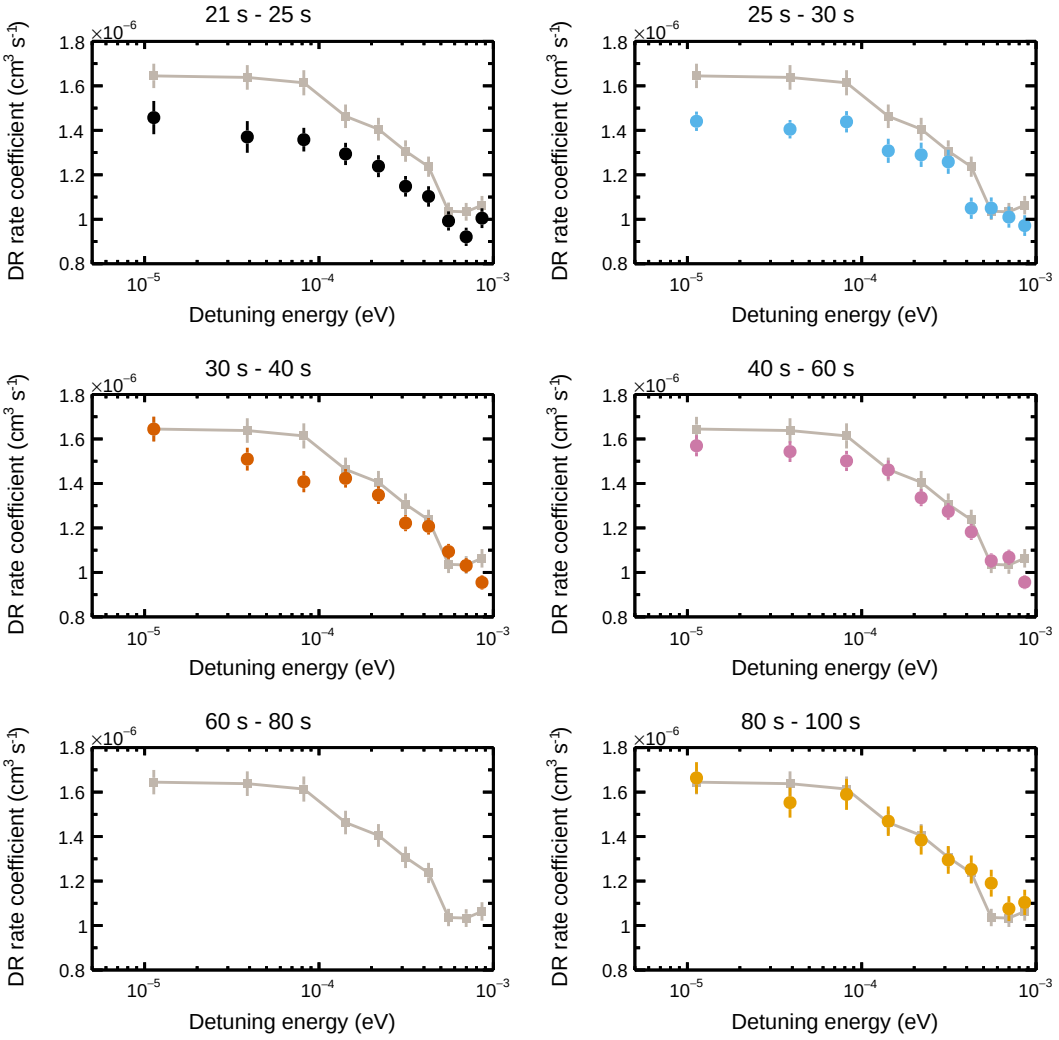

Figure 6.3: DR rate coefficient - low-energy storage time comparison. Each panel shows the data up to $E_\mathrm{d} = 1\,\mathrm{meV}$ for a different storage time window, compared to the result for $t = 60 - 80\,\mathrm{s}$ represented by gray squares and a connecting full line.

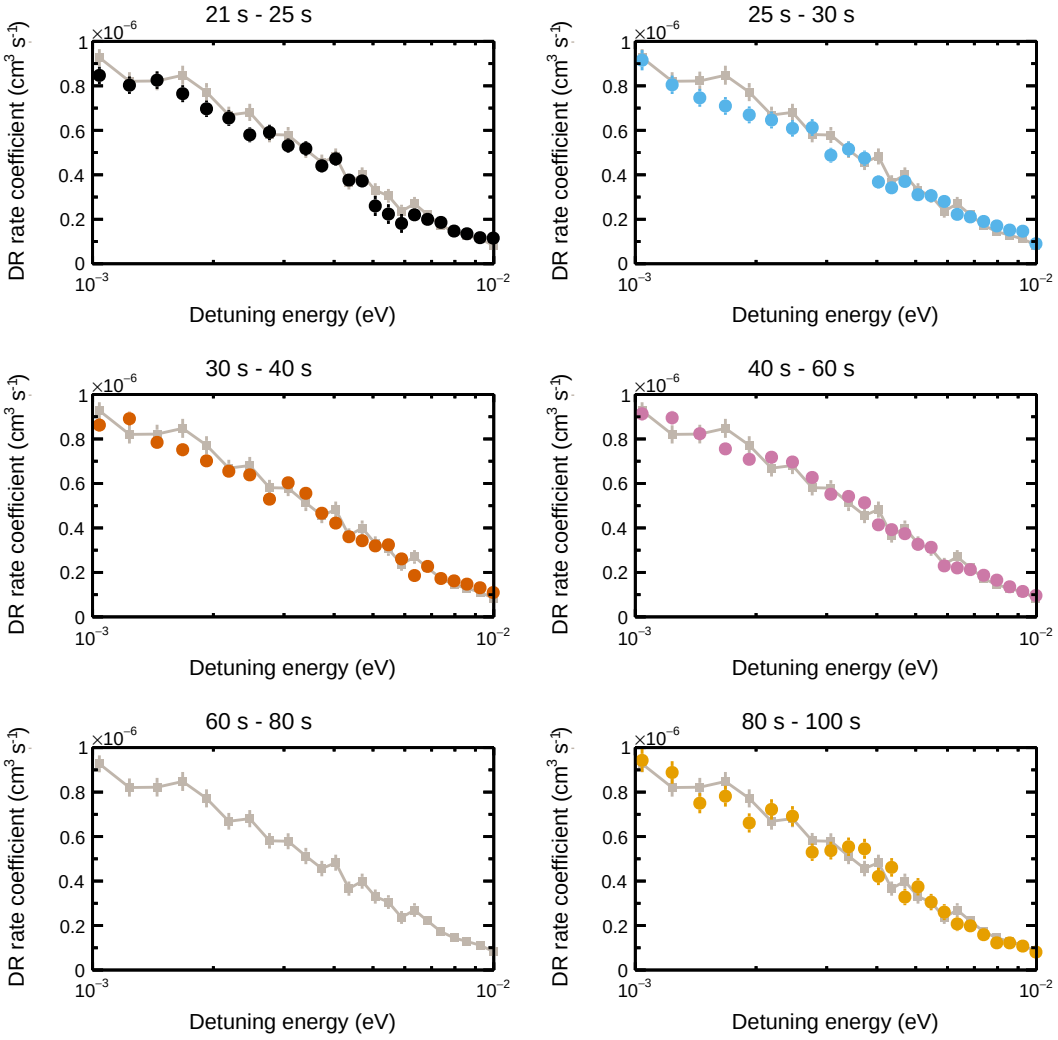

Figure 6.4: DR rate coefficient - intermediate-energy storage time comparison. Each panel shows the data in the range $E_d = 1 - 10$ meV for a different storage time window, compared to the result for $t = 60 - 80$ s represented by gray squares and a connecting full line.

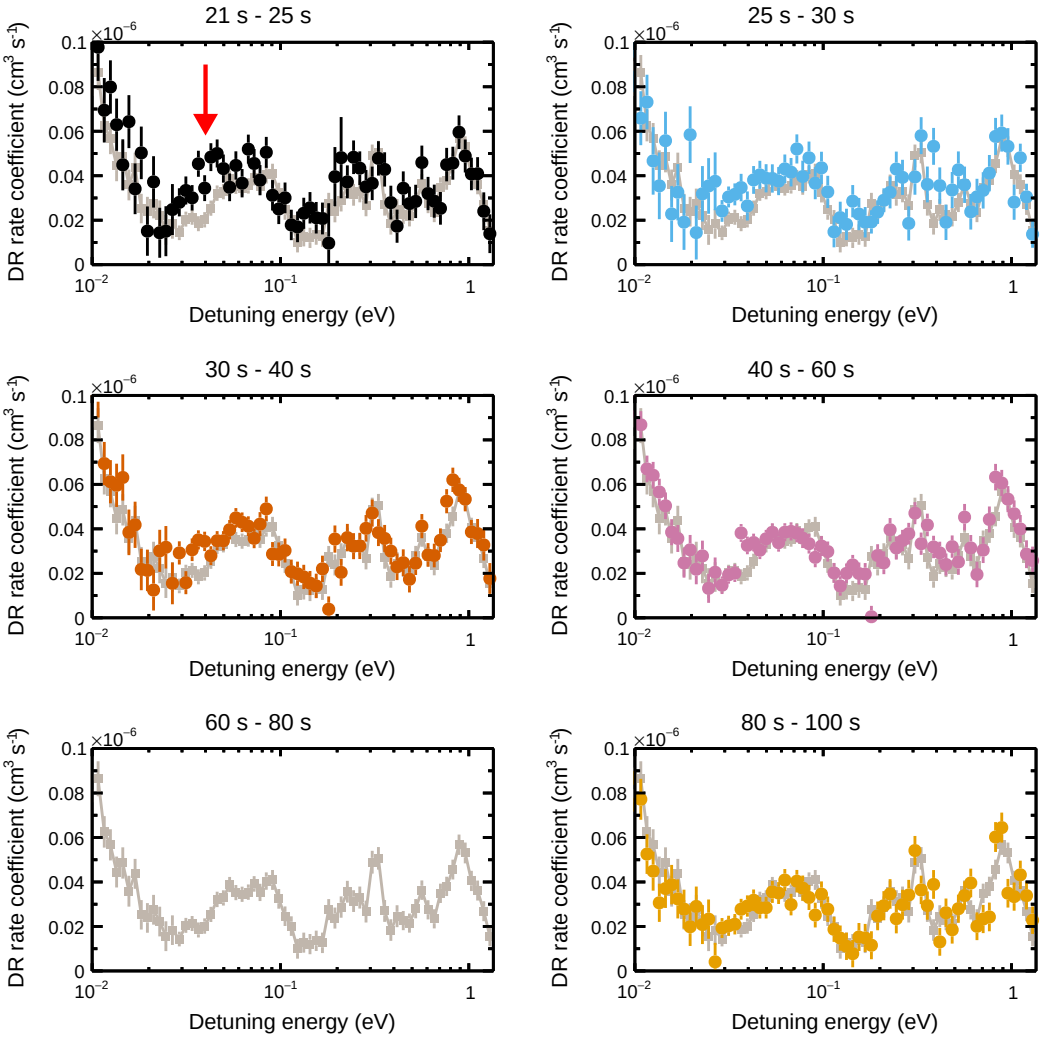

Figure 6.5: DR rate coefficient - high-energy storage time comparison. Each panel shows the data above $E_\mathrm{d} = 10\,\mathrm{meV}$ for a different storage time window, compared to the result for $t = 60 - 80\,\mathrm{s}$ represented by gray squares and a connecting full line. The region around $E_\mathrm{d} = 40\,\mathrm{meV}$, highlighted in the first panel, shows a small enhancement at early storage times.

lighted occurrence of a certain resonant enhancement at earlier storage times around $E_d = 40\,\text{meV}$. More information about this decay will be obtained in section 6.4.

6.3 Electron density comparison

For the CH^+ ion, inelastic electron collisions at densities in the $10^5 - 10^6\,\text{cm}^{-3}$ regime have been found in the laser probing measurement to significantly influence rotational cooling, both theoretically and experimentally (see chapter 5.5). Since the DR rate coefficient for a given ionic state is of course independent of electron density, obtaining MBRC data at different densities can reveal rotational state effects.

In this work two electron densities were studied (see appendix B.1). The results for the factor two different low and high density are compared in Figures 6.6-6.8 for different detuning energy and storage time intervals. Due to the fact that fast detector switching has not been implemented for the high-density data, its statistical quality, especially for high energies, is worse than for the low-density data. In this respect, no significant deviation of both data sets at energies beyond 10 meV (Figure 6.8) is visible.

In contrast to that, the low-energy region (Figure 6.6) shows a reduction on the order of the statistical uncertainty of the rate coefficient at high electron densities. As the low-energy regime also revealed storage time dependencies in Figure 6.3, the observed slight density dependence is not surprising. In the different time intervals the high-density rate coefficient lies constantly but only slightly below the low-density value. An exception is given for the $80 - 100\,\text{s}$ time slice, where the difference becomes significantly higher. If the deviations between both data sets were caused by their different rotational state populations (see Figure 5.11), it would be expected to shrink for later storage times, as the populations for both densities approach each other. This is not the case and raises questions about the here presented results. However, on the considered 10% scale there are other systematic effects, which might cause a constant scaling factor between both data sets:

- In appendix C.1.4 the low-density data were scaled to the high-density data at high detuning energies, resulting in an uncertainty of 3.3%. This is the fundamental limit for comparisons.
- Any uncertainty introduced by the pressure normalization (appendix C.1.2) is not included in the rate coefficient uncertainties, as it does not affect neighboring energy bins but appears as a scaling uncertainty of certain energy and storage time ranges. Since the low-density data use different pressure proxies for high and low energies, an additional scaling uncertainty seems likely.
- Changes in the electron-ion beam overlap can influence the MBRC. Since the electron-cooling-induced ion collection effect (Figure 5.6) was not discovered be-

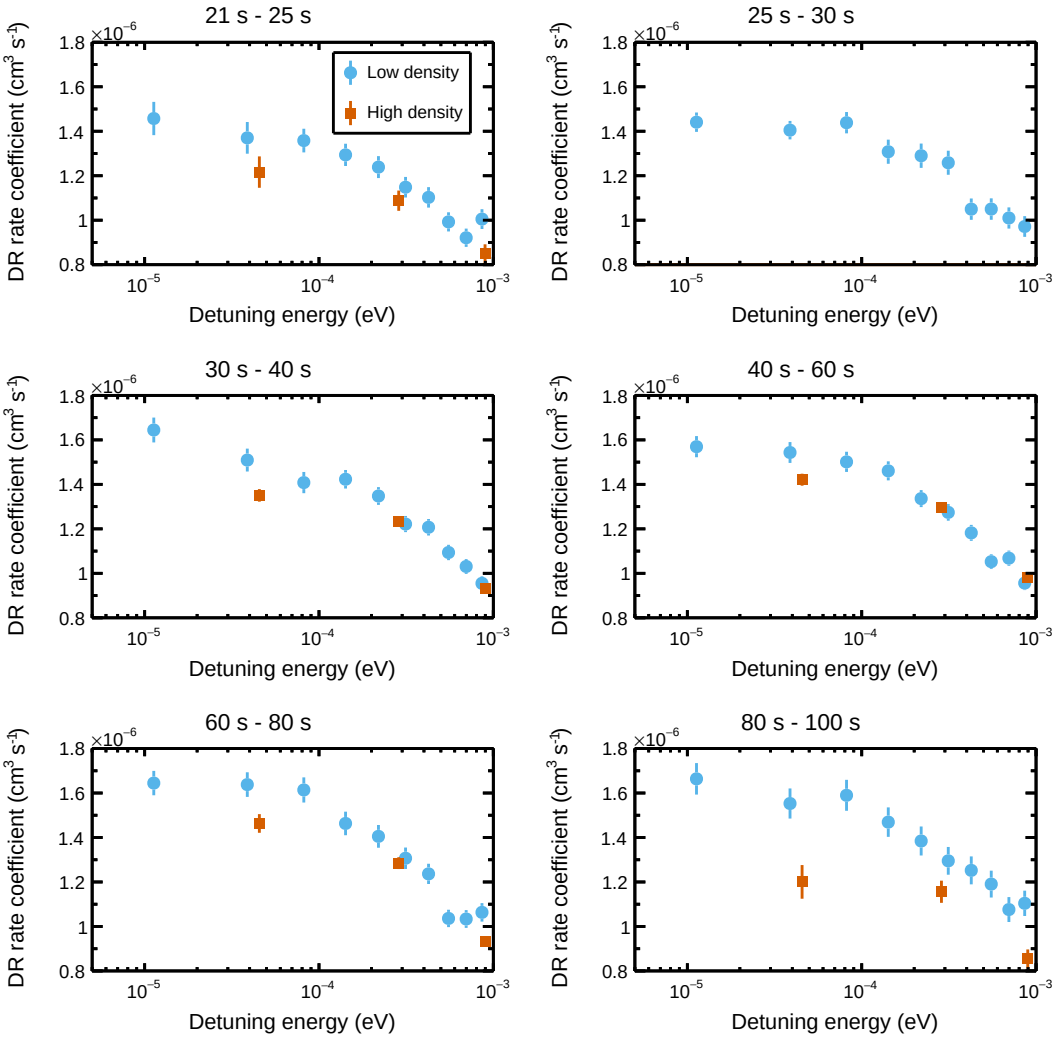

Figure 6.6: DR rate coefficient - electron density comparison at low energies. Each panel compares the $E_\mathrm{d} < 1\,\mathrm{meV}$ results for a different storage time window. The low density data ($n_\mathrm{e} = 3.4 \times 10^5\,\mathrm{cm}^{-3}$) are drawn as blue circles, the high-density data ($n_\mathrm{e} = 6.6 \times 10^5\,\mathrm{cm}^{-3}$) as orange squares. No high-density data were obtained for this energy range in the second time window.

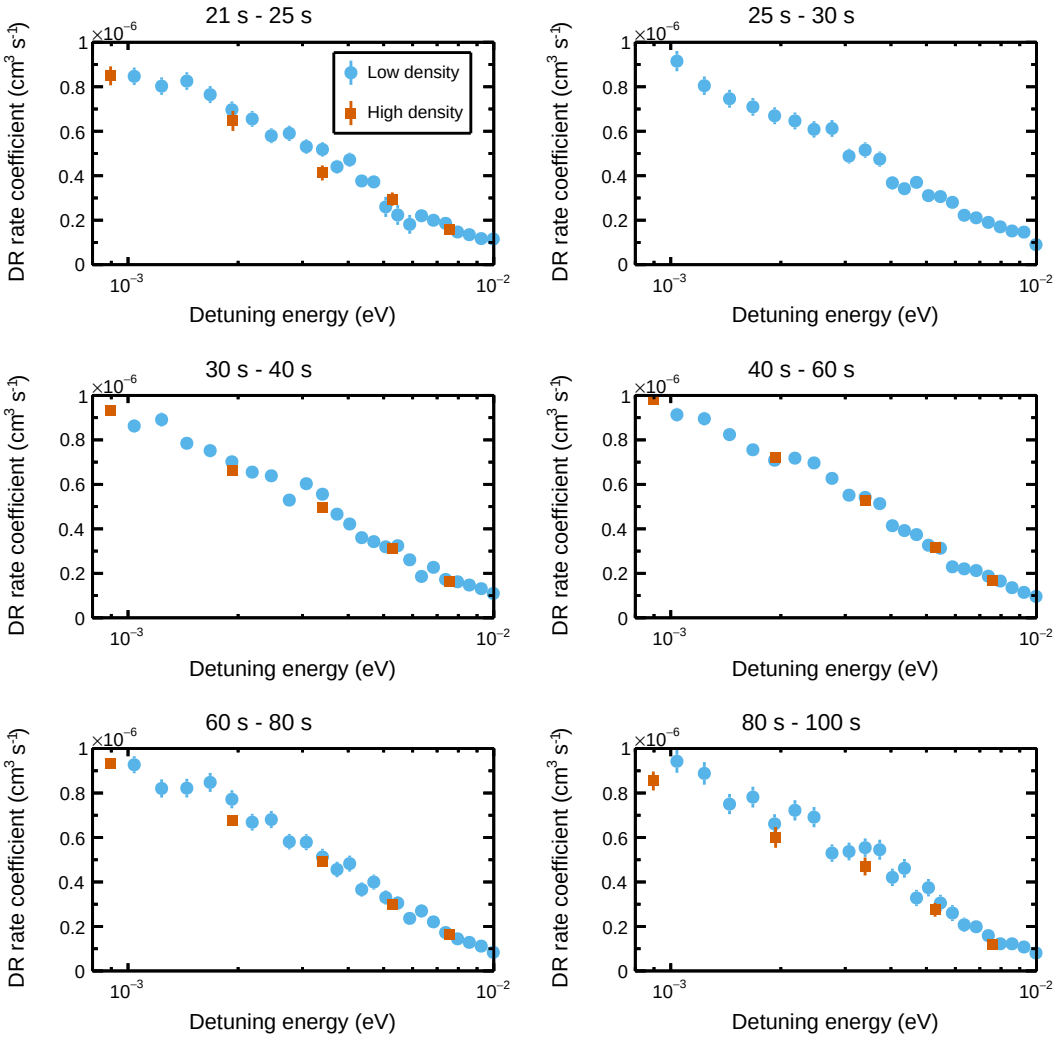

Figure 6.7: DR rate coefficient - electron density comparison at intermediate energies. Each panel compares the $E_\mathrm{d} = 1 - 10\,\mathrm{meV}$ results for a different storage time window. The low-density data ($n_\mathrm{e} = 3.4 \times 10^5\,\mathrm{cm}^{-3}$) are drawn as blue circles, the high density data ($n_\mathrm{e} = 6.6 \times 10^5\,\mathrm{cm}^{-3}$) as orange squares. No high-density data were obtained for this energy range in the second time window.

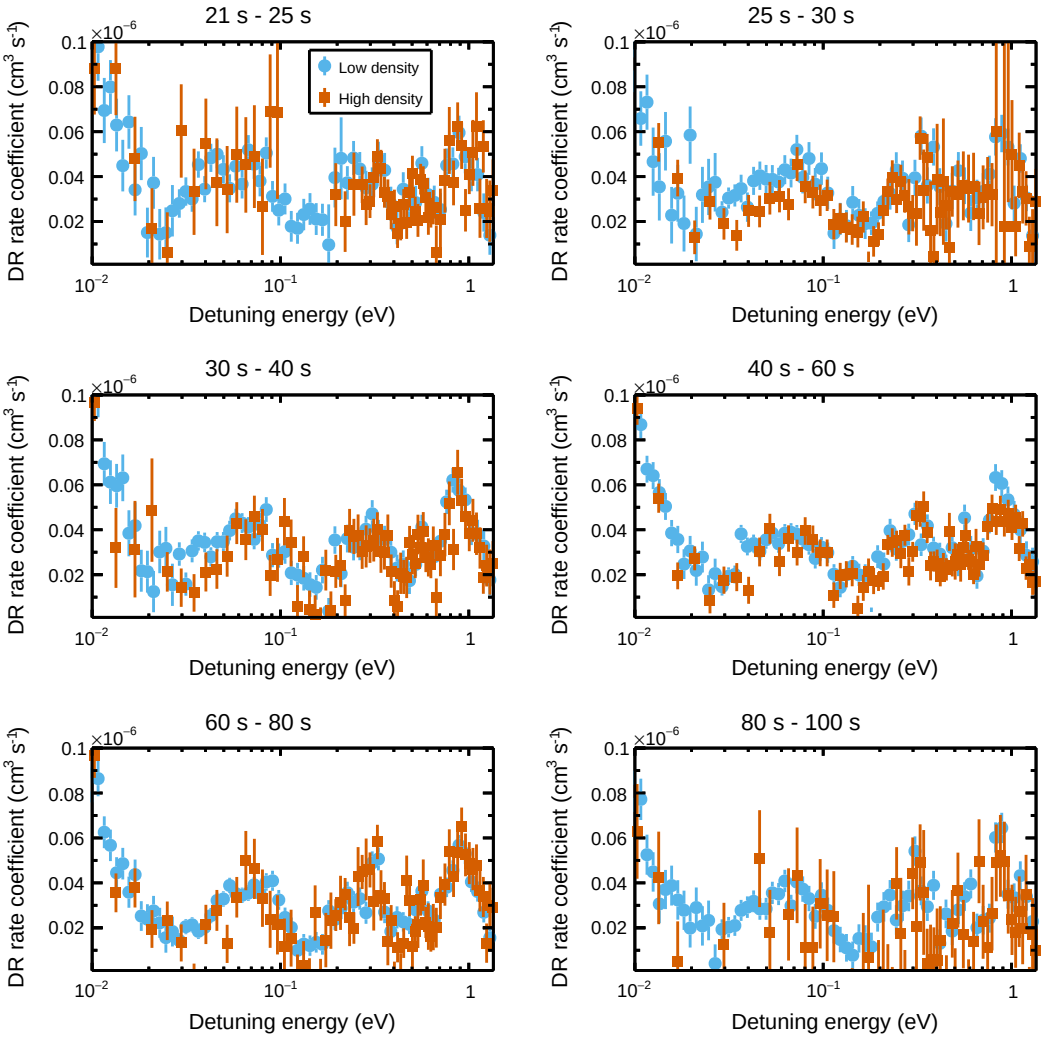

Figure 6.8: DR rate coefficient - electron density comparison at high energies. Each panel compares the $E_\mathrm{d} = 0.01 - 1.3\,\mathrm{eV}$ results for a different storage time window. The low-density data ($n_\mathrm{e} = 3.4 \times 10^5\,\mathrm{cm}^{-3}$) are drawn as blue circles, the high-density data ($n_\mathrm{e} = 6.6 \times 10^5\,\mathrm{cm}^{-3}$) as orange squares.

fore obtaining the high-density data, the electron beam could have been detuned from the optimal cooling energy by tens of meV in the lab frame. Due to ion beam dragging, the set electron energy is still expected to match the ion beam velocity after electron cooling and should not change the energy scale of the rate coefficient measurements. However, a different electron-ion beam overlap could be the result, leading to a lower rate coefficient for the high-density data.

- The transverse electron temperature $T_\perp$ predominantly determines the energy resolution and, thus, the amplitude of the 0 eV resonance. It is expected to be constant for both data sets, but no studies of its density dependence could be performed up to now. Such a dependence could introduce deviations between both data sets.

Considering all of these points, no conclusion about precise rotational-state-dependent effects can be drawn from the comparison of low- and high-density data. Nevertheless, the fact that both data sets deviate from each other by not more than 10% confirms the weak J-dependence indicated in the previous sections and could, otherwise, reflect a systematic uncertainty on the order of 10% as a combined effect of the above mentioned points. The storage time dependence of the 0 eV resonance can be analyzed in detail when observing a single DR measurement run, where all of the above mentioned systematics do not appear. This is a major subject of the following section.

6.4 *J*-specific merged-beams rate coefficients

The MBRC data presented in section 6.2 for the low-density measurement series, with little variation of systematic uncertainties, revealed an increasing rate coefficient for higher storage times in CSR, i. e., for internally cold CH^+ ions, at meV detuning energies. As the low-energy regime is of special interest for astrophysical studies of the ISM (chapter 1), a quantitative analysis is targeted in this section. Comparison of low- and high-density data in section 6.3 gave rather inconclusive results, which were mainly attributed to systematic effects between different measurement runs. Here, only a single high-density run with excellent statistics at $E_\mathrm{d} = 0\,\mathrm{eV}$ is analyzed in order to explicitly study the rotational state dependence of the low-energy resonance.

Equation 4.65 introduced a method to determine J-state-specific rate coefficients. However, in this beamtime a small fraction of the metastable $a^3\Pi$ ions needs to be included for modeling the storage-time-dependent rate coefficient $\alpha_\mathrm{mb}(t)$. In Figure 5.15 a) the storage-time-dependent state populations $P_{J=0}(t)$, $P_{J=1}(t)$, $P_{J=2}(t)$ and $P_\mathrm{m}(t)$ have been summarized for the high-density data. They can be used for the modification of equation 4.65:

$$\alpha_\mathrm{mb}(t) = \alpha_{J=0} P_{J=0}(t) + \alpha_{J=1} P_{J=1}(t) + \alpha_{J=2} P_{J=2}(t) + \alpha_\mathrm{m} P_\mathrm{m}(t) \tag{6.1}$$

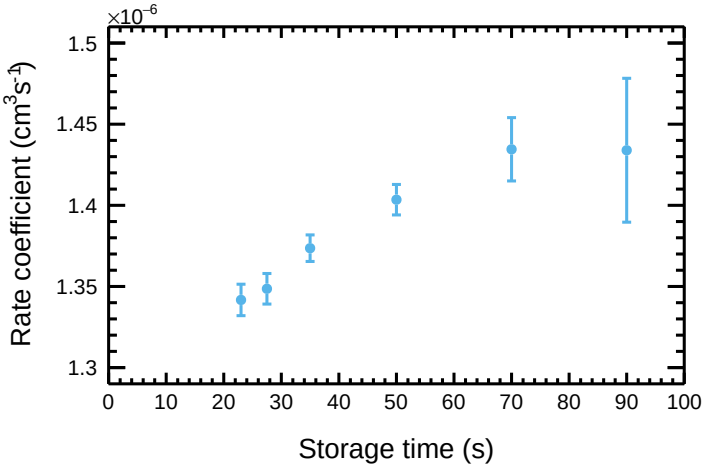

Figure 6.9: Storage time dependence of the $E_\mathrm{d} = 0\,\mathrm{eV}$ rate coefficient.

In the latter equation it is assumed that the rotational substates of the metastable state can be described by a single rate coefficient α_m, which does not need to be the case. Nevertheless, the total metastable population is small enough to apply this approximation and use α_m as an effective, averaged rate coefficient.

For $E_\mathrm{d} = 0\,\mathrm{eV}$ the storage time dependence of the rate coefficient is visualized in Figure 6.9. A clearly significant, continuous increase on the order of 10% is visible and confirms the observations in section 6.2. In principle, the data can be fitted with equation 6.1 through a least-squares minimization procedure of χ^2 with

$$\chi^2 = \sum_{i=1}^{6} \left(\frac{\alpha_\mathrm{mb}(t_i) - \alpha_{J=0} P_{J=0}(t_i) - \alpha_{J=1} P_{J=1}(t_i) - \alpha_{J=2} P_{J=2}(t_i) - \alpha_\mathrm{m} P_\mathrm{m}(t_i)}{\Delta\alpha_\mathrm{mb}(t_i)} \right)^2 \tag{6.2}$$

where $\alpha_\mathrm{mb}(t_i)$ and $\Delta\alpha_\mathrm{mb}(t_i)$ correspond to the data points and error bars in Figure 6.9. This approach, however, leads to strongly anti-correlated values for $\alpha_{J=2}$ and α_m with huge uncertainties on the level of $1 \times 10^5\,\mathrm{cm^3 s^{-1}}$. Both facts together result in a situation, in which a large fraction of the allowed parameter space is governed by such combinations $\alpha_{J=2}$ and α_m where one of the two rate coefficients is negative. Thus, in the following the aim is to carry out a model fit where parameter bounds are introduced to limit all rate coefficients to positive values. Consequently, the problem becomes non-linear and can only be solved numerically.

In order to solve the χ^2 minimization problem and to obtain probability distributions for the parameters $\alpha_{J=0}$, $\alpha_{J=1}$, $\alpha_{J=2}$ and α_m, a Markov Chain Monte Carlo (MCMC) (Hogg and Foreman-Mackey 2018) method was applied. It is based on the Bayesian inference principle, where the probability distribution of parameters $p(\alpha|D)$ given the data D (*posterior*) can be calculated from the known marginal-likelihood distribution $p(D|\alpha)$ and from an initial assumption about the parameter distributions $p(\alpha)$ (*prior*)

by

$$p(\alpha|D) = \frac{1}{Z} p(D|\alpha)p(\alpha) \tag{6.3}$$

with Z being a proportionality constant. For χ^2 minimization the marginal-likelihood function is given by

$$p(D|\alpha) = e^{-\chi^2/2} \tag{6.4}$$

MCMC algorithms use a Markov chain to sample the likelihood function. Instead of a uniform sampling of the parameter space, MCMC algorithms are able to scan predominantly the relevant region around the maximum likelihood and are especially suited for high-dimensional problems.

As a specific implementation of a MCMC solver, the Python-based *emcee* package was used (Foreman-Mackey et al. 2013). In addition to the state populations and the measured rate coefficients, the restriction $\alpha > 0$ was used as an input for the model. A broad uniform distribution $\alpha \in [0, 1 \times 10^5\,\mathrm{cm^3 s^{-1}}]$ was defined as a prior. After around 50 iterations the Markov chain converged to a dynamic equilibrium. From all further steps the posterior distribution can be inferred, which is much better confined than the prior in all dimensions.

The probability distributions $p(\alpha|D)$ for all four state-specific rate coefficients, resulting from the MCMC routine, are displayed in Figure 6.10. Due to the weak population of the $J = 2$ and metastable state, the model accepts a broad range of values for these rate coefficients, which is, however, consistent with the physical situation. Only an upper limit can be defined for $\alpha_{J=2}$ and α_m. In contrast to that, $\alpha_{J=0}$ and $\alpha_{J=1}$ can be well confined from both sides. Despite a small overlap of the distributions, the mean value for $\alpha_{J=0}$ is clearly shifted towards higher rate coefficients, indicating a higher cross section of the lowest rotational state.

By evaluating the histograms in Figure 6.10 quantitatively, most probable values for $\alpha_{J=0}$ and $\alpha_{J=1}$ can be extracted as mean values of the histogram and their 1σ uncertainties as the standard deviations of the histograms. The other two rate coefficients are described by the upper limits of the full distributions, such that

$$\begin{aligned}
\alpha_{J=0}(0\,\mathrm{eV}) &= 1.649(98) \times 10^{-6}\,\mathrm{cm^3 s^{-1}} \\
\alpha_{J=1}(0\,\mathrm{eV}) &= 1.16(13) \times 10^{-6}\,\mathrm{cm^3 s^{-1}} \\
\alpha_{J=2}(0\,\mathrm{eV}) &< 2.5 \times 10^{-6}\,\mathrm{cm^3 s^{-1}} \\
\alpha_{\mathrm{m}}(0\,\mathrm{eV}) &< 4.5 \times 10^{-6}\,\mathrm{cm^3 s^{-1}}
\end{aligned} \tag{6.5}$$

Here, the upper limit for $\alpha_{J=2}$ and α_m corresponds to the maximum values found in the distributions. Clearly, all of the results in equation 6.5 are affected by the absolute scaling uncertainty of 17%. Furthermore, it should be noted that $\alpha_{J=0}$ and $\alpha_{J=1}$ turn out to be almost fully anti-correlated. Hence, their sum is known with lower relative uncertainty than that of the individual values.

Equation 6.5 indicates a significantly higher $\alpha_{J=0}$ rate coefficient at $E_\mathrm{d} = 0\,\mathrm{eV}$. Thus, the increasing storage-time-dependent rate coefficient in Figure 6.9 can be explained

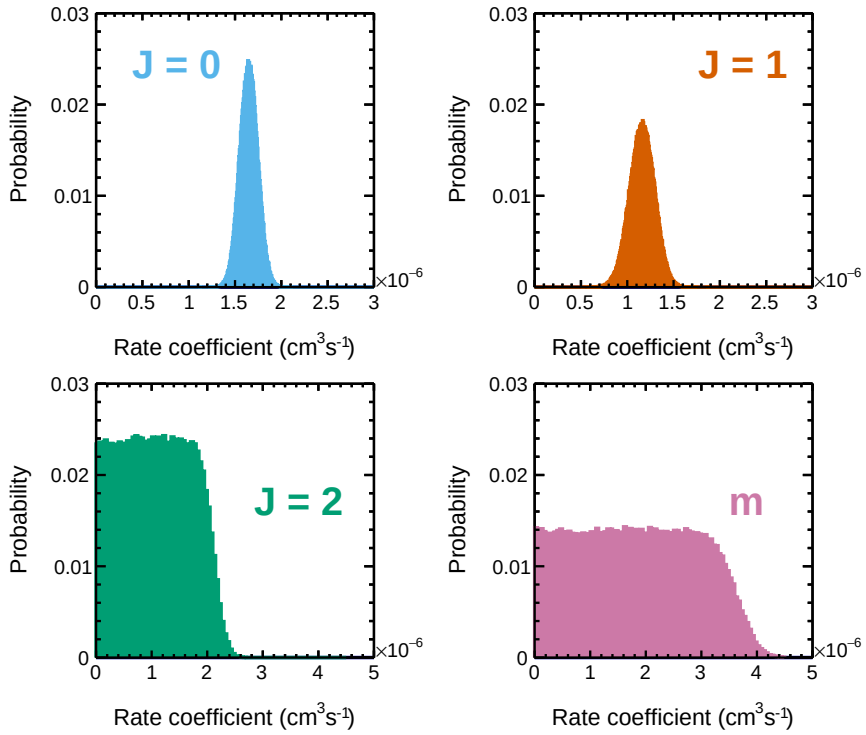

Figure 6.10: J-specific DR rate coefficients at $E_\mathrm{d} = 0\,\mathrm{eV}$. The four histograms represent probability distributions for α_J and α_m according to the MCMC analysis described in the text.

by the increasing population of $J = 0$. Furthermore, in the $t = 60 - 80\,\mathrm{s}$ storage time window, which has been chosen for presentation, the populations of the two higher states are limited by $P_{J=2} < 6.5\%$ and $P_\mathrm{m} < 3.0\%$. Even when assuming the maximum possible rate coefficients from equation 6.5, those two states can only slightly ($< 15\%$) contribute to the total rate coefficient, which is dominated by $\alpha_{J=0}$ and $\alpha_{J=1}$.

J-specific rate coefficient for $E_\mathrm{d} > 0$

An analysis similar to that for the previously presented case of $E_\mathrm{d} = 0\,\mathrm{eV}$ can be applied to non-zero detuning energies and, in principle, be extended over the whole rate coefficient spectrum in Figure 6.1. However, the statistical quality of the measured rate coefficient is reduced significantly beyond $E_\mathrm{d} = 10\,\mathrm{meV}$ and the results are expected to lose predictive power. Nevertheless, any constraint of $\alpha_{J=0}(E_\mathrm{d})$ is helpful to draw more solid astrophysical conclusions. A simple example for such a constraint, valid over the whole energy range, follows from the fact that $P_{J=0} \approx 50\%$ in the $t_\mathrm{r} = 60 - 80\,\mathrm{s}$ storage times interval. It can be concluded that $\alpha_{J=0}(E_\mathrm{d}) < 2\alpha_\mathrm{mb}(E_\mathrm{d}, t_\mathrm{r})$.

In order to increase statistics for a $E_\mathrm{d} > 0\,\mathrm{eV}$ analysis, the fact is made use of that any rotational state effect in the data can occur only over a range of energies corresponding to the energy resolution of the electron cooler. Energy distributions similar to Figure 4.5

were determined for different detuning energies and are represented by their FWHM values $\Delta E(E_\mathrm{d})$. For the whole MBRC spectrum (Figure 6.1) a running average in the energy domain was calculated, including all rate coefficient values in the range $E_\mathrm{d} - \Delta E(E_\mathrm{d}) < E_\mathrm{d} < E_\mathrm{d} + \Delta E(E_\mathrm{d})$ at a single energy E_d. The storage time dependence of each averaged value was later on analyzed in a similar MCMC procedure as discussed for the $E_\mathrm{d} = 0\,\mathrm{eV}$ case. The only difference in this analysis is that the rotational populations expected for the low-electron-density data set (Figure 5.15 b)) were used. Even though these populations were modeled from data for a single measured run set, it is assumed here that they are also applicable to the other run sets. Despite of their different electron energies and, consequently, inelastic collisions properties, their rotational cooling behaviors are dominated by the common electron cooling step (see appendix B.1), which justifies this assumption.

Figure 6.11 shows a set of selected rate coefficient probability distributions for certain detuning energies. Instead of the absolute rate coefficients in Figure 6.10, here, relative deviations between the J-specific rate coefficients and the $t = 60 - 80\,\mathrm{s}$ data are displayed, which were calculated as

$$x_{\mathrm{rel},J} = \frac{\alpha_J(E_\mathrm{d}) - \alpha_\mathrm{mb}(E_\mathrm{d}, t = 60 - 80\,\mathrm{s})}{\alpha_\mathrm{mb}(E_\mathrm{d}, t = 60 - 80\,\mathrm{s})} \tag{6.6}$$

In this respect, a deviation of $x_{\mathrm{rel},J} = 0$ indicates that the J-specific result matches the measured data, while it is twice as high for $x_{\mathrm{rel},J} = 1$ and vanishes for $x_{\mathrm{rel},J} = -1$.

The presented histograms indicate an interesting energy trend. For $E_\mathrm{d} = 2.5\,\mathrm{meV}$ the energies are still close to $E_\mathrm{d} = 0\,\mathrm{eV}$. Thus, similar to the previous results $\alpha_{J=0}$ is observed to be slightly higher than the measured data and $\alpha_{J=1}$ to be slightly lower, with both distributions having a certain overlap. At $E_\mathrm{d} = 12\,\mathrm{meV}$, $\alpha_{J=0}$ is reduced by about 70% compared to the data and the rate coefficient is dominated by $\alpha_{J=1}$. For energies above $E_\mathrm{d} = 100\,\mathrm{meV}$, the distributions become quite broad. This can be attributed to the lower statistical data quality and the fact that less data points for averaging are available. The resulting distributions cannot exclude variations of the J-specific rate coefficients within about a factor of 2, but no systematic rotational dependencies are observable.

A complete set of histograms similar to Figure 6.11 allows for summarizing the energy dependence of J-specific effects as mean values and standard deviations. The corresponding energy dependence is presented in Figure 6.12 for the $J = 0$ and $J = 1$ state. The results for $J = 2$ and the metastable state do not yield any information and are therefore not shown. The figure confirms the slightly enhanced $J = 0$ rate coefficient around $E_\mathrm{d} = 0\,\mathrm{eV}$ as well as the previously discussed, almost vanishing rate coefficient around $E_\mathrm{d} = 12\,\mathrm{meV}$. Beyond $E_\mathrm{d} = 20\,\mathrm{meV}$ the 1σ error bands amount to $\approx 40\%$ and no further conclusion about J-specific effects compared to the simple estimate before can be drawn from the data. Since at $t = 60 - 80\,\mathrm{s}$ the $J = 0$ and $J = 1$ states contribute with similar populations, the behavior of $\alpha_{J=0}(E_\mathrm{d})$ has to be counteracted by $\alpha_{J=1}(E_\mathrm{d})$, which becomes obvious by comparing both subfigures.

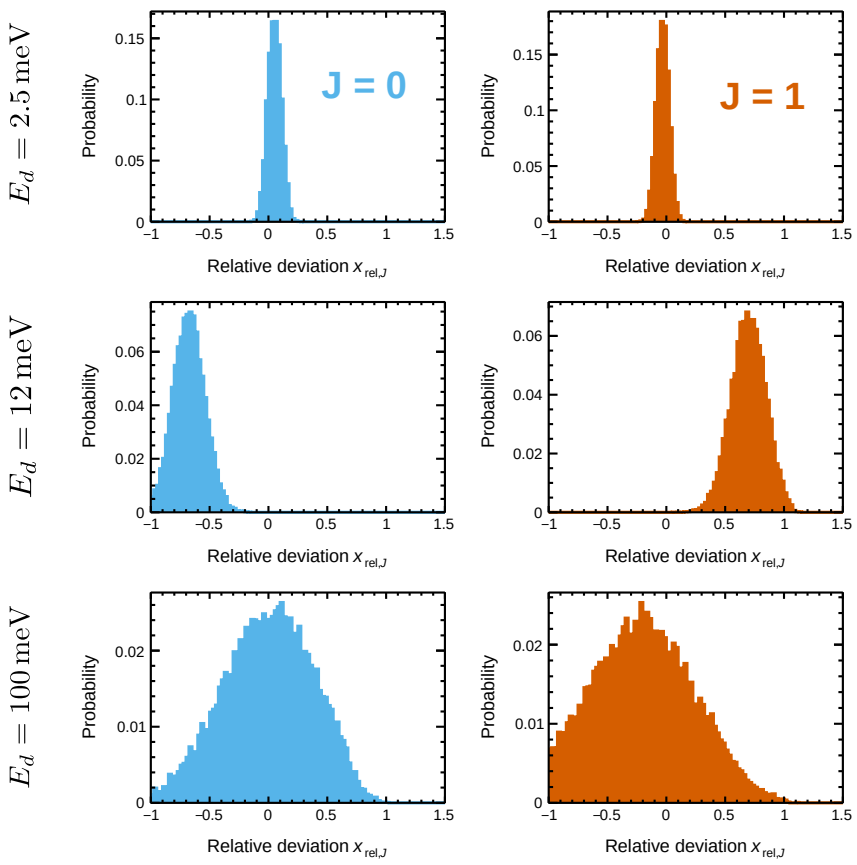

Figure 6.11: Relative J-specific DR rate coefficients for selected $E_\mathrm{d} > 0$. The probability distributions for $\alpha_{J=0}$ and $\alpha_{J=1}$ are evaluated similarly to Figure 6.10 but with rate coefficients averaged over the electron cooler energy resolution. Instead of absolute values, the relative deviation $x_{\mathrm{rel},J}$ (equation 6.6) to the measured $t = 60 - 80\,\mathrm{s}$ data (Figure 6.1) is shown. $\alpha_{J=2}$ and α_m suffer from extremely broad distributions and are therefore not included.

As a conclusion of this section, the analysis of J-specific effects helps to constrain the astrophysically-relevant $J = 0$ DR rate coefficient of CH^+ quite well up to $E_\mathrm{d} = 20\,\mathrm{meV}$. Since especially this energy range is important for collisions in low-temperature environments and, moreover, contributes the highest cross section for the DR process, such a constraint is valuable and will be used in section 6.5 to give limits for the $J = 0$ plasma rate coefficient.

An interesting observation made in this section is that the $J = 0$ rate coefficient is slightly lower than the measured MBRC in the range $E_\mathrm{d} = 10 - 100\,\mathrm{meV}$. Since the $J = 0$ population is increasing with storage time, this observation coincides with the storage time trend seen at $E_\mathrm{d} = 40\,\mathrm{meV}$ in Figure 6.5. Moreover, the fact that $\alpha_{J=0}$ almost vanishes around $E_\mathrm{d} = 12\,\mathrm{meV}$ could not be observed as storage time trend in

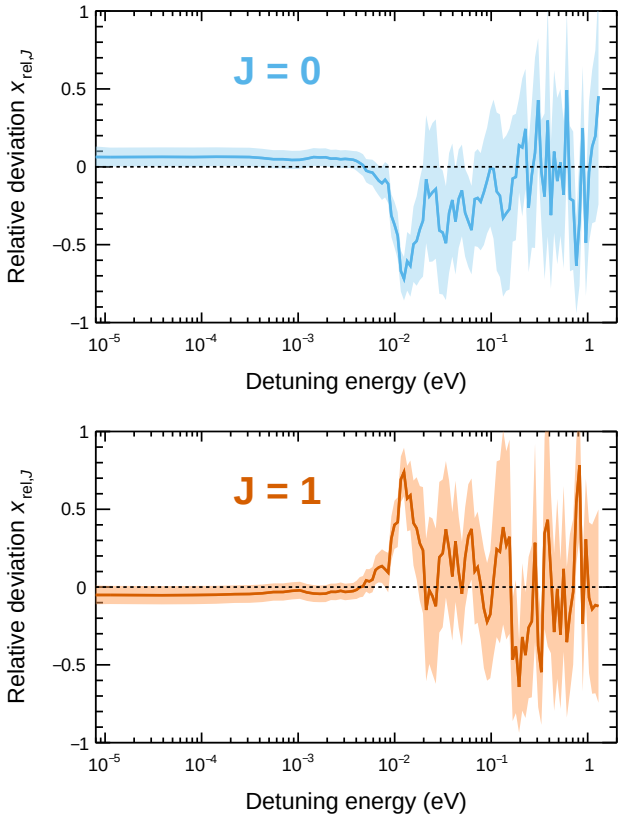

Figure 6.12: Energy dependence of J-specific DR effects. The two figures show the relative deviation $x_{\mathrm{rel},J}$ to the measured $t = 60 - 80\,\mathrm{s}$ data (Figure 6.1) for all resolution-averaged detuning energies (see text). The thick lines represent the mean value of probability distributions (Figure 6.11), while the error bands are extracted from their standard deviations.

Figure 6.4. Only the energy-resolution averaging conducted in this section could infer this J-dependent effect from the data. However, since the feature is rather narrow and corresponds to a small measured rate coefficient, its impact on the plasma rates, discussed in the following section, is almost negligible.

6.5 Plasma rate coefficient for DR of rotationally cold ions

In the Interstellar Medium (ISM) the motion of particles in the gas can be normally described by a Maxwell-Boltzmann distribution f_{pl} defined by the kinetic temperature T_{pl}, often called *plasma temperature*. The internal excitation of molecules, however, might be attributed to a different temperature T_{ex}. E. g., without collisional excitation the molecules can radiatively cool to equilibrium with the radiation field, i. e., to the cosmic microwave background at $\approx 2.7\,\mathrm{K}$. In contrast to that, the kinetic and internal gas temperatures can get in equilibrium ($T_{\mathrm{pl}} = T_{\mathrm{ex}}$) if collisional excitation exceeds radiative cooling (McGuire 2018). Such conditions, also referred to as Local Thermodynamic Equilibrium (LTE), are reached at particle densities higher than the so called *critical density* n_{crit}.

In CH^+ relevant regions, like diffuse clouds or Photon Dominated Regions (PDRs), gas densities below $n = 1 \times 10^4\,\mathrm{cm}^{-3} \lesssim n_{\mathrm{crit}}$ lead to a subthermal internal excitation for most molecular species, often populating only the rotational ground state. Thus, for proper modeling of chemical networks in such environments, the reaction rate coefficients entering the calculations need to be differentiated for various kinetic plasma temperatures and, independently, for the lowest rotational states (see Faure et al. 2017). For the CH^+ ion, in particular, absorption line spectroscopy was already done in the 1930s (see chapter 1). As an unfortunate coincidence, no relevance was attributed to the observed excitation temperature $T_{\mathrm{ex}} = 2.3\,\mathrm{K}$ (Herzberg 1950), even though it was, in fact, the first measurement of the cosmic microwave background temperature. The excellent match of the CH^+ excitation temperature with the cosmic microwave background confirms that predominantly the CH^+ $J = 0$ state is populated in the ISM.

In this section the CH^+ DR plasma rate coefficient is evaluated for lowest rotational states with relative populations close to $\approx 50\%$ for $J = 0$ and $J = 1$, each, as populated in the CSR experiment at long storage times ($t = 60 - 80\,\mathrm{s}$). Furthermore, a constraint for the pure $J = 0$ rate coefficient is provided.

6.5.1 Plasma rate calculation and uncertainties

The MBRC spectra presented in section 6.2 can be converted to plasma rate coefficients α_{pl} using the procedure described in chapter 4.3. α_{pl} is determined in a temperature range $T_{\mathrm{pl}} = 10 - 40000\,\mathrm{K}$. For the highest temperatures the convolution using $f_{\mathrm{pl}}(E)$ requires the inclusion of collision energies beyond the 1.3 eV upper limit of the measured MBRC data. From the previous TSR data (Figure 6.1 a)) one can observe that the rate coefficient at energies $E_{\mathrm{d}} > 1.3\,\mathrm{eV}$ drops significantly and, thus, no strong contribution from higher collision energies is expected - even at the highest T_{pl} covered in the above mentioned range. Nevertheless, to include even minor contributions from higher collision energies, the TSR data are used as an extension of the CSR MBRC spectrum in the energy range $E_{\mathrm{d}} = 1.3 - 20\,\mathrm{eV}$. At these high energies, the major contribution to the plasma rate stems from the peak around $E_{\mathrm{d}} = 10\,\mathrm{eV}$ (Figure 6.1 a))

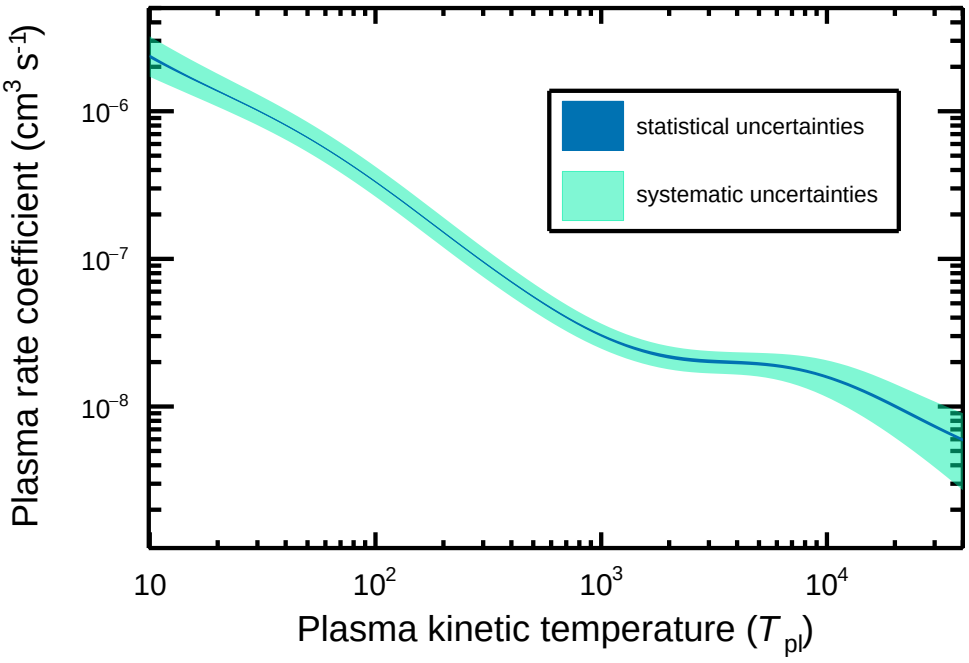

Figure 6.13: CH^+ DR plasma rate coefficient for the lowest rotational states, calculated from the $t = 60 - 80$ s MBRC data (Figure 6.1). Statistical uncertainties correspond to the narrow blue band, which almost appears as a line in the plot. The asymmetric green error band shows the total systematic uncertainties derived from the individual systematic uncertainties of absolute scaling (17% global uncertainty, see chapter 5.7), room temperature extension of cross section data at high energies, and electron beam temperatures ($T_\parallel$, $T_\perp$).

that has been attributed to a non-resonant *direct* DR process (section 6.1) and is, thus, independent of rotational excitation. On the other hand, the experimental energy resolutions differ strongly for both measurements. In order to correct for this effect, TSR data were deconvolved with the procedure in chapter 4.3 and using the corresponding experimental energy resolution. Afterwards, the resulting cross section data were reconvolved with the CSR energy distribution (chapter 4.2.2) to a MBRC and used to extend the CSR data at high energies. The systematic uncertainty introduced by the TSR data extension is further discussed below.

The plasma rate conversion is accompanied by a few systematic uncertainties. Figure 6.13 includes those systematics as green error band for the comparative storage time window of $t = 60 - 80$ s and compares them to the statistical uncertainties (blue error band). The systematic error band was calculated from the squared sum of all systematic uncertainties, as discussed below. First, the absolute scaling of the MBRC leads to a global uncertainty of 17% (chapter 5.7), which dominates the total uncertainty at temperatures from 400 K to 7000 K. Furthermore, the uncertainties on the transverse and longitudinal temperature ($T_\perp$, $T_\parallel$) of the electron beam were propagated through

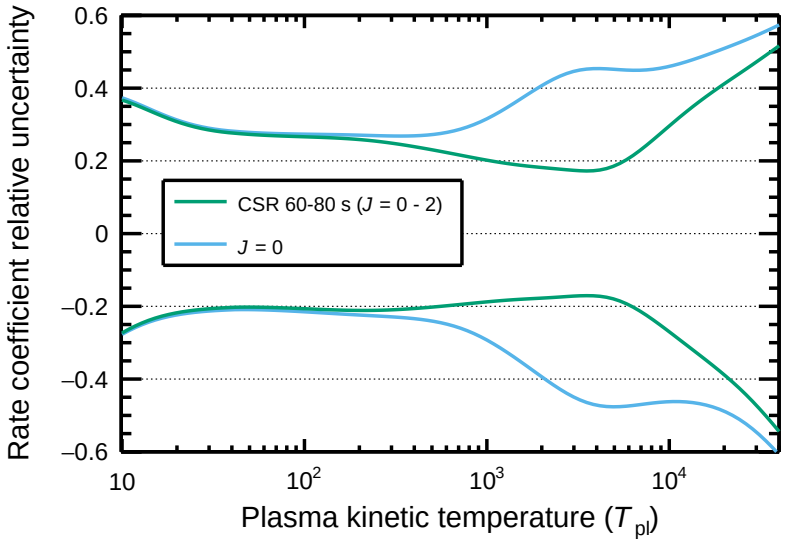

Figure 6.14: Total relative systematic plasma rate coefficient uncertainties. The figure compares the uncertainties of the measured CSR data at $t = 60 - 80\,\mathrm{s}$ (Figure 6.13) with a constraint of the pure $J = 0$ rate coefficient, which is calculated from the latter (see text).

the deconvolution procedure. Here, extreme values for the transverse temperatures of $k_\mathrm{B}T_\perp = 1.5\,\mathrm{meV}$ and 3 meV were used to quantify the corresponding uncertainty range in α_pl. Similarly, electronic noise contribution values of $\Delta U = 50\,\mathrm{mV}$ and 150 mV were propagated, which influence the longitudinal temperature predominantly (see chapter 4.2.2). Both effects affect the low plasma temperatures ($T_\mathrm{pl} \lesssim 1000\,\mathrm{K}$).

For temperatures above 7000 K, the plasma rate is also influenced by the inclusion of the TSR data at high detuning energies. The uncertainty from this extension is dominated by the low absolute scaling quality of the TSR data. To estimate the effect, the TSR data were scaled by factors of 0, 0.5 and 1.0, where best amplitude-match with CSR is reached for the factor 0.5 (compare Figure 6.1 a)). As expected, despite of the strong scaling factors, the contribution to the error band stays moderate because the plasma rate is mostly influenced by the detuning energies below 1.3 eV, which are included in the CSR data. The resulting total relative systematic uncertainty is similar for α_pl in all storage times and exceeds statistical uncertainties by far (compare the error bands in Figure 6.13). Its dependence on T_pl is plotted in Figure 6.14 as green curve. Due to the low influence of statistical uncertainties, they will be neglected for further plots, unless stated differently.

Out of all acquired CH^+ DR data, the previously presented data from the $t = 60 - 80\,\mathrm{s}$ storage time window give the DR rate coefficient for mostly relaxed CH^+ ions, where only the lowest three rotational states and a slight contribution of the metastable $a^3\Pi$ state remained with laser-probed populations of $P_{J=0} = 47\%$, $P_{J=1} = 44\%$, $P_{J=2} = 6\%$ and $P_\mathrm{m} = 3\%$ (Figure 5.15 b)). For astrophysical applica-

tions the plasma rate coefficient for pure ground state ($J = 0$) ions is of even higher importance. Due to the already high contribution of the $J = 0$ state in the CSR data, the corresponding rate coefficient can be derived. Section 6.4 was already dedicated to constraining the $J = 0$ MBRC, which is possible with a good precision especially in the low-energy region at $E_\mathrm{d} < 20\,\mathrm{meV}$.

Starting from the relative deviation $x_{\mathrm{rel},J}$ of the $J = 0$ MBRC in Figure 6.12, the most probable MBRC $\alpha_{J=0}(E_\mathrm{d})$ was calculated as well as its upper and lower 1σ limit described by the error band. All three curves were converted into a plasma rate coefficient for pure $J = 0$ with a systematic uncertainty band. This systematic uncertainty was added in square with all previously described systematic uncertainties (green curve in Figure 6.14). The resulting relative uncertainty is represented by the blue lines in Figure 6.14. Up to $T_\mathrm{pl} \approx 300\,\mathrm{K}$ the systematic uncertainty introduced by the $J = 0$ confinement is negligible compared to the other uncertainty sources. It rises with increasing temperatures and even dominates the total uncertainty between $T_\mathrm{pl} \approx 800\,\mathrm{K}$ and $T_\mathrm{pl} \approx 10\,000\,\mathrm{K}$. At even higher temperatures the uncertainty introduced by the TSR extension becomes the dominant contribution.

6.5.2 Results

In order to characterize rotational excitation effects on the plasma rate coefficient, Figure 6.15 presents the plasma rate coefficient derived from the MBRC data acquired at several storage time windows in CSR, with corresponding populations listed in Table 6.1. In this comparison only statistical uncertainties were propagated from the MBRC data, as systematic uncertainties are expected to affect all storage time windows equally. The plasma rate coefficient reveals increasing values with storage time for low temperatures ($10 - 50\,\mathrm{K}$) and a decreasing trend for high temperatures ($700 - 5000\,\mathrm{K}$). Those tendencies can be attributed directly to the storage time dependence of the 0 eV (Figure 6.3) and 40 meV region (Figure 6.5) in the MBRC. In total, the differences between the curves are small when comparing to the extent of systematic uncertainties (Figure 6.13). Thus, the plasma rate dependence on the rotational state excitation reveals to be especially weak.

The overall shape of the plasma rate curve as a function of T_pl is approximately described by a hyperbola-like function ($\alpha_\mathrm{pl} \sim 1/\sqrt{T_\mathrm{pl}}$), which has been added to Figure 6.15, with additionally enhanced rates at low temperatures ($T_\mathrm{pl} \lesssim 800\,\mathrm{K}$) and high temperatures ($T_\mathrm{pl} \gtrsim 3000\,\mathrm{K}$). Those enhanced rates arise from the strong $E_\mathrm{d} = 0\,\mathrm{eV}$ resonance ($T_\mathrm{pl} \lesssim 800\,\mathrm{K}$) and from the various resonances in the range $E_\mathrm{d} = 0.04 - 1.3\,\mathrm{eV}$ of the MBRC ($T_\mathrm{pl} \gtrsim 3000\,\mathrm{K}$), see Figure 6.1 a). In contrast to the MBRC, however, the plasma rate curve is significantly smoothed out due to the broad Maxwell-Boltzmann energy distribution (f_pl) used for the convolution. A plasma rate coefficient associated with a hyperbola, as described above, would be expected for a pure *direct* DR process (see chapter 2.1.3). The comparison of the measured data to this hyperbola function further emphasizes the strongly enhanced rate at low temperatures.

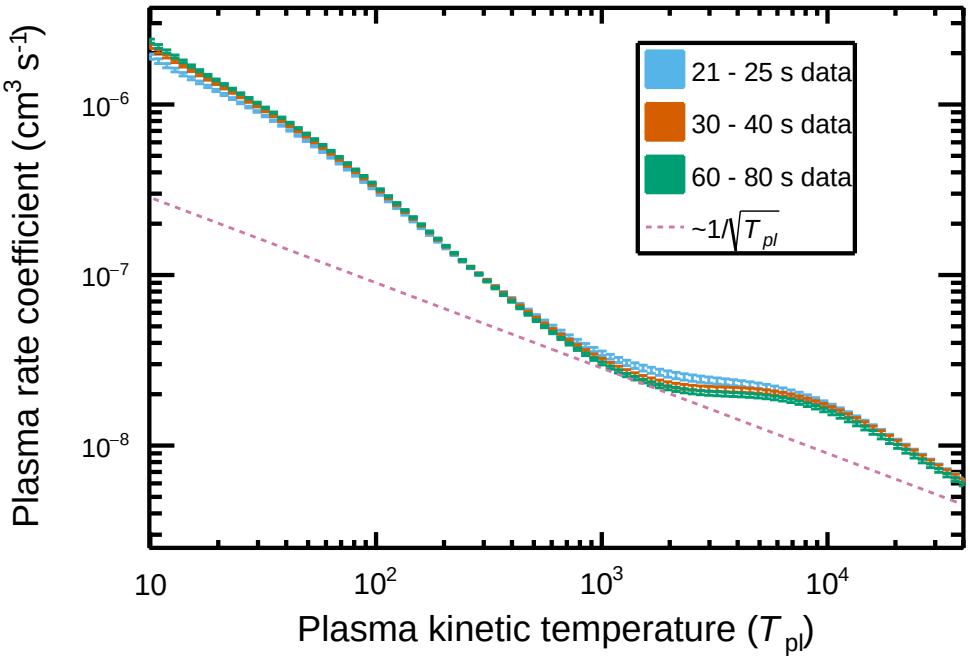

Figure 6.15: Temperature-dependent CH^+ DR plasma rate coefficient for various storage times in CSR. The state-dependent populations in the different storage time windows correspond to the values in Table 6.1. Statistical uncertainties are indicated by the error bars, while systematic uncertainties were neglected in this plot. A $\alpha_{\mathrm{pl}} \sim 1/\sqrt{T_{\mathrm{pl}}}$ line was added to the figure, which represents the temperature dependence of a *direct* DR process.

Table 6.1: State-dependent populations in CSR for different storage times. The values are extracted from Figure 5.15 b) and include the lowest three rotational states as well as the metastable $a^3\Pi$ state. The storage time windows correspond to the ones shown in Figure 6.15.

Storage time	$P_{J=0}$	$P_{J=1}$	$P_{J=2}$	P_{m}
$21-25\,\mathrm{s}$	19%	38%	32%	11%
$30-40\,\mathrm{s}$	29%	50%	16%	5%
$60-80\,\mathrm{s}$	47%	44%	6%	3%

The preceding derivation of the ISM-relevant DR plasma rate coefficient of cold molecular CH^+ ions in section 6.5.1 leads to a twofold result: First, a plasma rate coefficient for rotational state ensemble close to a $J = 0$ and $J = 1$ mixture with 50% relative population each is obtained directly from the measured MBRC. This result is applicable for models of astrophysical environments with slightly excited rotational populations due to either collisional excitation or caused by the interstellar radiation field. Second, the pure $J = 0$ plasma rate coefficient was calculated from storage time dependencies in the measured DR rates. This result typically represents the diffuse ISM best, where collisions are rare and CH^+ radiatively cools down to its rotational ground state.

Figure 6.16 summarizes and compares both results. The deviation of the central lines in subfigures a) and b) is visualized in subfigure c) and shows a match better than 11% over the whole temperature range, which is within the systematic uncertainty bands (also included in the figure). This reflects the finding of rather small rotational state effects for the DR of CH^+ (compare Figure 6.15). Moreover, also the uncertainty bands show similar relative values up to $T_{\mathrm{pl}} \approx 300\,\mathrm{K}$, as already presented in Figure 6.14. While the uncertainty stays moderate in subfigure a), the pure $J = 0$ uncertainty increases significantly at higher kinetic temperatures.

In astrophysical databases plasma rate coefficients are typically provided in a parameterized, functional form. For this sake a function chosen by Novotný et al. 2013 is used also the purpose of this work:

$$\alpha_{\mathrm{pl}}(T_{\mathrm{pl}})[\mathrm{cm^3 s^{-1}}] = A \left(\frac{300}{T_{\mathrm{pl}}[\mathrm{K}]} \right)^n + T_{\mathrm{pl}}[\mathrm{K}]^{-1.5} \sum_{i=1}^{4} c_i \exp\left(-\frac{T_i}{T_{\mathrm{pl}}[\mathrm{K}]} \right) \tag{6.7}$$

The data for the central line, upper and lower error band boundaries for both results in Figure 6.16 were fitted by this functional dependence. The obtained fit parameters are summarized in Table 6.2 for the plasma rate coefficient of the $J = 0 - 2$ mixture and in Table 6.3 for the pure $J = 0$ plasma rate coefficient. Depending on the specific astrophysical conditions, either of the two might be included in future chemical network simulations. The maximum deviation between database fit function and the data for the central line does not exceed 3.2% in both cases, which is far below the respective uncertainties.

The results presented in this section represent the closest experimental approach to ISM conditions ever achieved in a laboratory collision experiment. Thus, they shed light onto the previously unexplored DR of internally cold CH^+ ions. Their impact on astrophysical databases as well as an updated view onto the important astrochemical reaction chains relevant for the diffuse ISM is discussed in the following section.

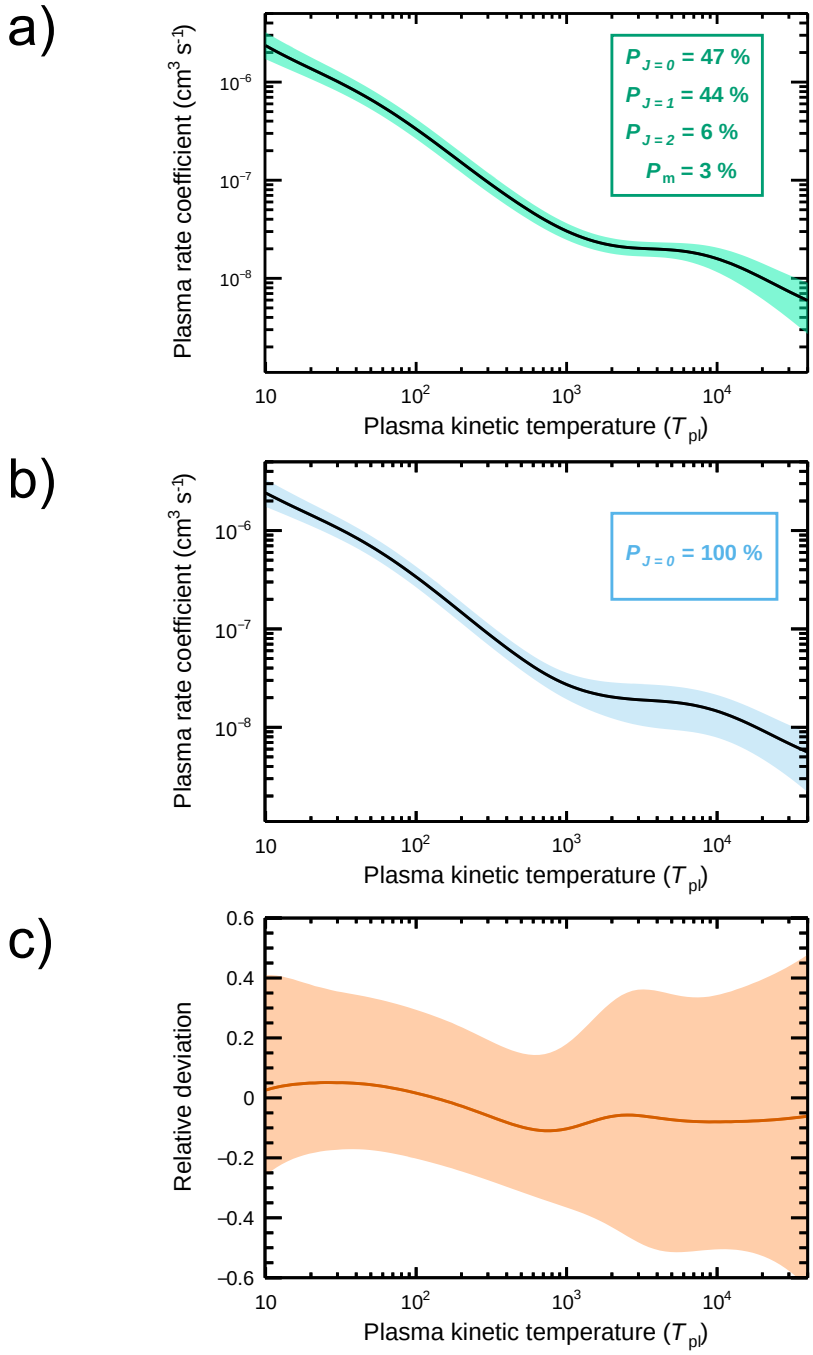

Figure 6.16: DR plasma rate coefficient for rotationally cold CH^+ ions. The error bands represents the total 1σ uncertainties shown in Figure 6.14. a): Plasma rate coefficient for a population ensemble of $J = 0 - 2$ and metastable state m, as present in the CSR measurement. The relative populations are indicated in the figure. b): $J = 0$ plasma rate coefficient calculated from the $J = 0$ MBRC data (Figure 6.12). c): Relative deviation of the $J = 0$ central line (b) to the $J = 0 - 2$ mixture central line (a). The error band reflects the relative uncertainty of the $J = 0$ rate coefficient.

Table 6.2: CH^+ DR plasma rate coefficient fit parameters for a $J = 0-2$ mixture: $P_{J=0} = 47\%$, $P_{J=1} = 44\%$, $P_{J=2} = 6\%$ - with a small metastable state contribution $P_m = 3\%$. The parameters were obtained by fitting the curves in Figure 6.16 a) with equation 6.7 for the central line, lower and upper error band, respectively. Maximum relative deviations between fit functions and the data amount to 2.9% (central line), 6.7% (lower error band) and 7.8% (upper error band) and are located at $T_{pl} = 40\,000\,K$.

Parameter	Central line value	Lower error band value	Upper error band value
A	1.58×10^{-7}	8.61×10^{-8}	1.48×10^{-7}
n	0.744	0.872	0.895
c_1	2.04×10^{-2}	1.68×10^{-2}	6.49×10^{-2}
c_2	-1.61×10^{-3}	-3.30×10^{-4}	2.49×10^{-2}
c_3	-7.67×10^{-4}	9.60×10^{-5}	-7.36×10^{-4}
c_4	3.49×10^{-5}	-4.56×10^{-6}	6.90×10^{-5}
T_1	11 670	8060	28 020
T_2	1120	267	8590
T_3	263	36.8	364
T_4	12.9	24.8	34.8

Table 6.3: CH^+ DR plasma rate fit parameters for the $J = 0$ state. See Table 6.2 for further explanations. Maximum relative deviations between fit functions and the data (Figure 6.16 b)) amount to 3.2% (central line), 4.8% (lower error band) and 5.8% (upper error band) and are located at $T_{pl} = 22\,300\,K$, $T_{pl} = 40\,000\,K$ and $T_{pl} = 40\,000\,K$, respectively.

Parameter	Central line value	Lower error band value	Upper error band value
A	1.60×10^{-7}	1.95×10^{-8}	2.10×10^{-7}
n	0.748	0.684	0.810
c_1	1.81×10^{-2}	1.52×10^{-2}	4.25×10^{-2}
c_2	-1.70×10^{-3}	1.46×10^{-3}	1.87×10^{-2}
c_3	-8.30×10^{-4}	1.67×10^{-4}	-1.41×10^{-3}
c_4	4.35×10^{-5}	1.29×10^{-4}	-1.17×10^{-3}
T_1	11 880	12 110	27 440
T_2	1060	3110	8060
T_3	256	50.7	1010
T_4	14.3	10.1	275

6.6 Astrophysical implications

Plasma rate coefficients are of essential knowledge for modeling ion chemistry in astrophysical environments. For simulations of chemical networks, these rate coefficients are typically taken from astrophysical databases, which collect the rate coefficient from various sources, generally in a form of plasma rate coefficients. While many of the database entries are based on coarse estimates and simplified calculations, experiments are the most valued source of data. However, many of the experiments stem from laboratory measurements performed at room temperature, where, as discussed in section 6.5, the rotational excitation of molecules is usually far higher than expected in cold astrophysical environments.

The CH^+ DR results presented in the previous section provide the rare opportunity for using a pure $J = 0$ plasma rate coefficient as an input for astrochemistry calculations. In the following subsections the new values are compared to existing entries in astrophysical databases. Furthermore, the impact of the new DR results for the comparably simple CH^+ chemistry in the diffuse ISM and outer Photon Dominated Regions (PDRs) is discussed, followed by a general conclusion on astrophysical implications.

6.6.1 Comparison to astrochemical databases

In Figure 6.17 the pure $J = 0$ DR plasma rate coefficient for CH^+ ions is compared to values stored in astrophysical databases, currently used for astrochemical models, and to data from the room-temperature TSR experiment (Amitay et al. 1996), representing the best experimental benchmark for the CH^+ DR up to the point of this work.

For the database comparison CH^+ plasma rate coefficients listed in the Kinetic Database for Astrochemistry (KIDA)[1] and University of Manchester Institute of Science and Technology (UMIST)[2] database were included. The UMIST database values are based on a simplified approximation of data from the single-pass merged-beams experiment of Mitchell and McGowan 1978 (see chapter 2.3), where vibrationally and electronically excited CH^+ ions may have been involved. It is therefore not expected to be applicable for the cold ISM conditions. The plasma rate curve from the KIDA database is referred to as 'estimated' in the respective database entry, with a rate coefficient of $\alpha_{\mathrm{pl}} = 7 \times 10^{-8}\,\mathrm{cm^3 s^{-1}}$ at 300 K. Both databases assume a simple power law dependence of the plasma rate coefficient and miss the additional kinetic-temperature-dependent features of the CSR results. While KIDA matches the new CSR data at high temperatures, it underestimates the low-temperature rates by factor of six. In contrast to that, UMIST is closer to the CSR data at low temperatures, with only a factor of four difference at 10 K, but overestimates the high temperature plasma rate.

The published TSR MBRC data were processed analog to the CSR data by deconvolving into a collision-energy-dependent cross section, which was further convolved to

[1] http://kida.astrophy.u-bordeaux.fr/reaction/1312/CH+_+_e-.html (22.01.2021)
[2] http://udfa.ajmarkwick.net/index.php?reaction=3180 (22.01.2021)

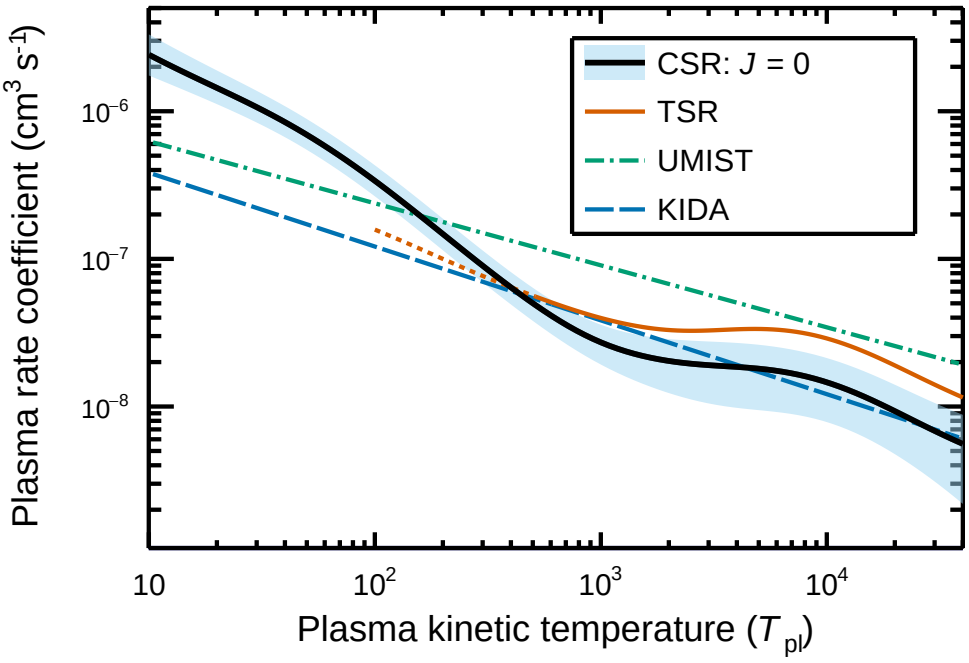

Figure 6.17: CSR $J = 0$ plasma rate coefficient compared to the room-temperature TSR experiment and astrochemical databases. TSR plasma rates were obtained from the data shown in Figure 6.1 a), UMIST and KIDA from the respective database entries. See text for further information.

the temperature dependent plasma rate (chapter 4.3). Within its scaling uncertainty of 50%, the TSR plasma rates at high temperatures match the CSR data. At temperatures below $T_{\mathrm{pl}} = 500\,\mathrm{K}$, both measurements begin to deviate. This can be attributed to the now ≈ 10 times improved energy resolution at CSR, which made a detection of the strong 0 eV resonance possible (compare Figure 6.1). Moreover, the published TSR data only include energies above 10 meV, causing unreliable plasma rate values at lowest temperatures. Therefore, the TSR data at $T_{\mathrm{pl}} = 100 - 500\,\mathrm{K}$ are plotted by a dashed line only.

In summary, the database values in use so far differ strongly from the new CSR $J = 0$ data, especially at the astrophysically interesting temperatures between $T_{\mathrm{pl}} = 10\,\mathrm{K}$ and $T_{\mathrm{pl}} = 100\,\mathrm{K}$ (see chapter 1). At these T_{pl} the DR rates presented here are significantly higher than previously assumed. Thus, the destruction of CH^+ ions by electron collisions in the ISM turns out to be more relevant than used in current chemical models. Implications for the ISM chemistry will be further discussed in the following section.

6.6.2 Impact on chemistry of the diffuse ISM

For the comparably simple CH^+ ISM chemistry in diffuse interstellar clouds and outer PDR regions, only few reactions are considered to be of importance. As discussed in chapter 1, the only efficient CH^+ production mechanism at low temperatures is based on

$$C^+ + H_2 \longrightarrow CH^+ + H. \tag{6.8}$$

On the contrary, the CH^+ ion is frequently destroyed by reactions with the most abundant species, namely hydrogen atoms or molecules (Myers, McKee, and Li 2015) via

$$CH^+ + H \longrightarrow C^+ + H_2 \tag{6.9}$$

$$CH^+ + H_2 \longrightarrow {CH_2}^+ + H \tag{6.10}$$

The rate coefficients for both reactions are listed in the UMIST database[3,4] as

$$k_H(T_{pl}) = 9.1 \times 10^{-10}\,cm^3s^{-1} \left(\frac{T_{pl}[K]}{300}\right)^{-0.37} \exp\left(\frac{-29.1}{T_{pl}[K]}\right) \tag{6.11}$$

$$k_{H_2} = 1.2 \times 10^{-9}\,cm^3s^{-1} \tag{6.12}$$

respectively, and are extracted from experimental studies of Plasil et al. 2011 and a compilation of experimental studies in McEwan et al. 1999. It should be noted that Plasil et al. 2011 give a function for the fully thermal ($T_{ex} = T_{pl}$) rate coefficient only for temperatures $T_{pl} = 100 - 1000\,K$. The equation 6.11 used by the UMIST database is different and attempts to fit the data of Plasil et al. 2011 also at lower temperatures. Still, it should be emphasized that the function only matches the data of Plasil et al. 2011 down to $T_{pl} \approx 70\,K$ and overestimates the data significantly towards lower temperatures.

Plasil et al. 2011 do not provide a functional form of the fully thermal rate coefficient for $T_{pl} = 10 - 100\,K$. However, their publication includes an approach for extracting J-state-selective rate coefficients for temperatures of $T_{pl} = 10 - 60\,K$. They were able to control the CH^+ and H temperatures separately, mimicking the difference between internal and kinetic temperature. As a result, they provide an empirical functional dependence for the rate coefficient $k_{H,J=0}$ of the lowest rotational CH^+ state:

$$k_{H,J=0}(T_{pl}) = 1 \times 10^{-9}\,cm^3s^{-1} \left(0.05 + 0.1(T_{pl} - 9\,K)/50\,K\right) \tag{6.13}$$

Both, equation 6.11 and 6.13, will be used further for quantifying the atomic hydrogen destruction process.

The rate coefficient for the molecular hydrogen destruction reaction (equation 6.12) was measured at room temperature and does not include any temperature trend. Even though it seems to be too simplified for ISM conditions, there are no better data available for this reaction.

[3] http://udfa.ajmarkwick.net/index.php?reaction=435 (27.01.2021)
[4] http://udfa.ajmarkwick.net/index.php?reaction=523 (27.01.2021)

Dissociative recombination with electrons

$$\mathrm{CH^+ + e \longrightarrow C + H} \tag{6.14}$$

with a plasma rate coefficient $\alpha_{\mathrm{pl}}(T_{\mathrm{pl}})$ determined in the previous section, is another $\mathrm{CH^+}$ destruction channel competing with the two hydrogen destruction reactions 6.9 and 6.10.

The respective destruction rates by the three mechanisms are given by

$$\frac{\mathrm{d}n_{\mathrm{CH^+}}}{\mathrm{d}t}(\mathrm{H}) = -n_{\mathrm{CH^+}} n_{\mathrm{H}} k_{\mathrm{H}}(T_{\mathrm{pl}}) \tag{6.15}$$

$$\frac{\mathrm{d}n_{\mathrm{CH^+}}}{\mathrm{d}t}(\mathrm{H_2}) = -n_{\mathrm{CH^+}} n_{\mathrm{H_2}} k_{\mathrm{H_2}} \tag{6.16}$$

$$\frac{\mathrm{d}n_{\mathrm{CH^+}}}{\mathrm{d}t}(\mathrm{e}) = -n_{\mathrm{CH^+}} n_{\mathrm{e}} \alpha_{\mathrm{pl}}(T_{\mathrm{pl}}) \tag{6.17}$$

where n_x denotes the particle number density of species x. Clearly, a high relative electron density compared to the hydrogen density increases the relative importance of $\mathrm{CH^+}$ destruction by DR. For the two extreme cases of a fully atomic ($n_{\mathrm{H_2}} = 0$) or a fully molecular ($n_{\mathrm{H}} = 0$) hydrogen environment, the DR and hydrogen-induced destruction channels become equal for density ratios of

$$\chi_{\mathrm{e}} \equiv \frac{n_{\mathrm{e}}}{n_{\mathrm{H}}} = \frac{k_{\mathrm{H}}(T_{\mathrm{pl}})}{\alpha_{\mathrm{pl}}(T_{\mathrm{pl}})} \tag{6.18}$$

$$\chi_{\mathrm{e}} \equiv \frac{n_{\mathrm{e}}}{2n_{\mathrm{H_2}}} = \frac{k_{\mathrm{H_2}}(T_{\mathrm{pl}})}{2\alpha_{\mathrm{pl}}(T_{\mathrm{pl}})} \tag{6.19}$$

respectively. Here, χ_{e} denotes the fractional ionization of the plasma environment. Assuming that χ_{e} is known for the given environment, the last two equations can be reordered to determine a critical DR rate coefficient for fully atomic and fully molecular environments

$$\alpha_{\mathrm{crit,H}}(T_{\mathrm{pl}}) = \frac{k_{\mathrm{H}}}{\chi_{\mathrm{e}}} \tag{6.20}$$

$$\alpha_{\mathrm{crit,H_2}}(T_{\mathrm{pl}}) = \frac{k_{\mathrm{H_2}}}{2\chi_{\mathrm{e}}} \tag{6.21}$$

If the DR rate coefficient exceeds the critical value, then DR is the dominant destruction process in the medium.

In a recent astrophysical publication (Myers, McKee, and Li 2015) a fractional ionization of $\chi_{\mathrm{e}} = 1.6 \times 10^{-4}$ is given as 'standard parameter' in the ISM. Assuming this value and the hydrogen destruction rate coefficients from equations 6.11 and 6.13 for fully atomic environment as well as from equation 6.12 for fully molecular environment, allows to calculate $\alpha_{\mathrm{crit,H}}(T_{\mathrm{pl}})$ and $\alpha_{\mathrm{crit,H_2}}(T_{\mathrm{pl}})$, respectively. The temperature dependencies of both values are visualized in Figure 6.18 as solid color lines and labeled by the corresponding environment condition. The lighter areas above each line indicate the

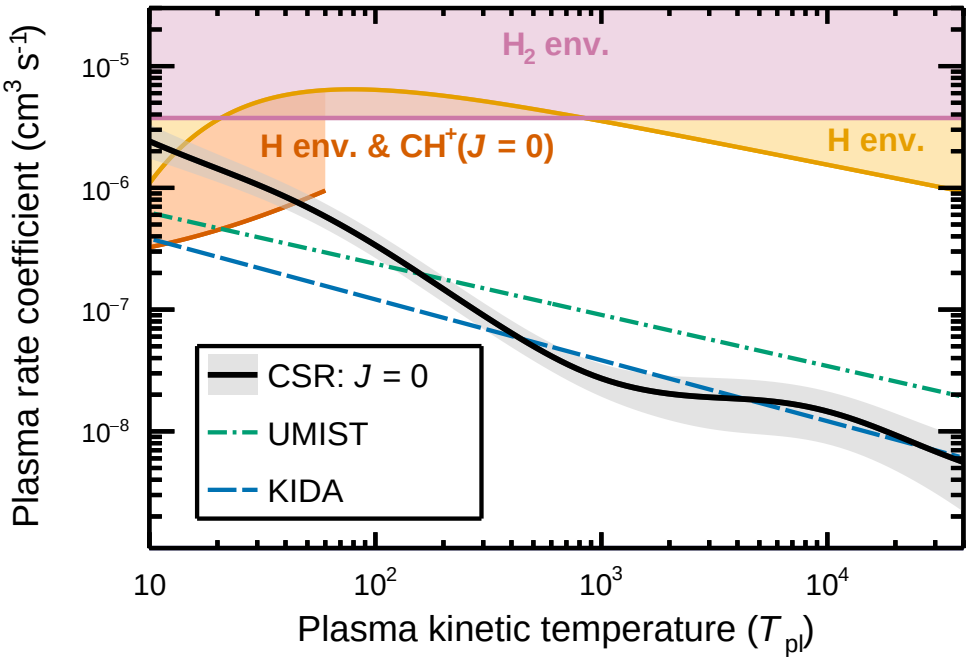

Figure 6.18: Relevant CH^+ DR rate coefficient regimes for the diffuse ISM. The $J = 0$ DR plasma rate coefficient measured in this work (full line) is shown together with the presently assumed database values (dashed and dash-dotted lines), similar to Figure 6.17. The colored areas above the other full lines represent the regimes where the DR rate exceeds hydrogen-based destruction processes for different environments, assuming an ionization fraction of $\chi_e = 1.6 \times 10^{-4}$ (Myers, McKee, and Li 2015). The lower boundaries of the areas correspond to the critical DR rates (equations 6.20 and 6.21). Pink: fully molecular (H_2) environment, light orange: fully atomic (H) environment, assuming the UMIST hydrogen destruction rate coefficient given in equation 6.11, dark orange: fully atomic environment with CH^+ ions in the $J = 0$ state, assuming the hydrogen destruction rate coefficient given by equation 6.13.

region where DR exceeds the respective hydrogen-based destruction mechanism and is the dominant destruction process for CH^+.

Since no temperature dependence of the hydrogen destruction rate coefficient (equation 6.12) is known, the area boundary for the fully molecular environment is a horizontal line. In contrast to that, the thermal rate coefficient for hydrogen-induced CH^+ destruction in fully atomic environment (equation 6.11) defines a critical DR rate ($\alpha_{\mathrm{crit,H}}(T_{\mathrm{pl}})$), which decreases below temperatures of $T_{\mathrm{pl}} = 70\,\mathrm{K}$ because of reduced hydrogen destruction in cold environment. As discussed above, equation 6.11 only fits to experimental data down to $T_{\mathrm{pl}} = 70\,\mathrm{K}$. At lower temperatures the rate coefficient from equation 6.13 is suited better and, in addition, considers also reactions with CH^+ ions in the $J = 0$ state. The corresponding line for $\alpha_{\mathrm{crit,H}}(T_{\mathrm{pl}})$ in Figure 6.18 is displayed in dark orange and is located remarkably lower than the other two lines.

As Plasil et al. 2011 discuss in their publication, the hydrogen destruction rate of the $J = 0$ state revealed to be lower than for higher excited states, which is one reason for the high deviation.

In order to estimate the relevance of DR for the CH^+ chemistry in the ISM, the newly measured CSR rate coefficient is compared to the colored areas. At high temperatures ($T_{pl} > 100\,K$), DR is weaker than both hydrogen destruction processes and can be neglected. However, in the ISM-relevant low-temperature ($T_{pl} = 10 - 100\,K$) regime, the strong increase of the DR plasma rate coefficient enhances the relevance of DR in comparison to the rather flat or even decreasing temperature-dependencies of the hydrogen processes.

In fully molecular environments the CH^+ destruction by DR reaches up to $\approx 50\%$ of the molecular hydrogen destruction rate at the lowest temperatures around 10 K, but it can be neglected at higher temperatures. It should be still noted again that the rate coefficient of the molecular hydrogen destruction reaction (equation 6.12) was determined at room temperature (McEwan et al. 1999). The temperature dependence of this reaction has not been studied yet and a future investigation in cold environment using state-selected reactants may change the critical DR rate coefficient for molecular environments.

In case of a fully atomic environment and for temperatures below $T_{pl} = 70\,K$, the CSR results should be compared to critical rate based on the CH^+ $J = 0$ destruction rate coefficient (equation 6.13). The comparison in Figure 6.18 reveals that DR becomes the dominant destruction process below $T_{pl} = 45\,K$. At even lower temperatures, the relevance increases towards $T_{pl} = 10\,K$, where DR exceeds atomic hydrogen destruction at an almost order-of-magnitude higher rate. Thus, a considerable fraction of the ISM-relevant temperature range ($T_{pl} = 10 - 100\,K$) is governed by DR being the main CH^+ destruction mechanism.

The previous conclusion about the DR relevance at low temperatures could only be revealed by the new CSR results and is a consequence of the remarkably increased rate coefficient at low temperatures compared to the database values (UMIST and KIDA in Figure 6.18). Concluding from the database values alone, i. e., comparing the dashed and dash-dotted curve with the 'H env.' area, one would have erroneously declared CH^+ DR as negligible in the whole temperature range, as it is also done in Myers, McKee, and Li 2015. The previously underestimated relevance of DR in atomic environments of the ISM manifests the importance for state-selective and also high-resolution laboratory collision studies for astrophysical purposes, as presented in this work. Both are essential requirements to address the astrophysically-relevant low-temperature regime.

6.6.3 Concluding remarks

In the previous section the CH^+ DR plasma rate coefficient for the rotational ground state $J = 0$ was determined experimentally from the CSR merged-beams collision rates. At low temperatures ($T_{pl} \lesssim 100\,K$) the CSR-based data exceed strongly the rate coefficients currently used in astrophysical models and databases. This increase corresponds to a strongly enhanced destruction rate of CH^+ in the astrophysically-relevant low-temperature regime, which might affect chemical models in various environments. More specifically, in the diffuse ISM DR becomes the dominant destruction mechanism in fully atomic environments at temperatures below $T_{pl} = 45\,K$. This is in contrast to the previous assumptions that the CH^+ DR can be neglected in the diffuse ISM for all regimes (Myers, McKee, and Li 2015).

The unexpectedly high abundance of the CH^+ molecule in the ISM (chapter 1) can obviously not be explained by the updated DR rate coefficient. On the contrary, the increased DR rate tends to even decrease the CH^+ abundance in very cold environments. Nevertheless, the new CSR DR data obtained at ISM-equivalent conditions lower significantly the uncertainty in the astrochemical models and better constrain the potential sources of discrepancy between the observed and modeled CH^+ abundances. E. g., the destruction rate via molecular hydrogen (equation 6.12) was measured only at 300 K and its unknown temperature- and rotational-excitation dependence acts as a strong uncertainty source. Moreover, other, more complex processes for CH^+ production have been considered, mostly involving non-equilibrium energy sources like shocks and turbulences (see chapter 1), or reactions with multiply charged ions (Plašil et al. 2021). To date, however, none of these alternative attempts could fully explain the observed CH^+ abundances in the diffuse ISM. Estimating the effect of the new CH^+ DR data on these non-equilibrium models is beyond the scope of this work.

While above CH^+ was discussed only in the context of the diffuse ISM, it was found also in other environments, e. g., in dense clouds (see chapter 1) or star forming regions (Benz et al. 2013), where the particle number densities exceed those in the diffuse ISM by far. Moreover, the CH^+ chemistry in environments with a high amount of free electrons as potential reaction partners, like the Galactic center and supernovae remnants, might be particularly affected by the DR rates found in this work (Wolfire and Neufeld 2020).

6.7 Comparison to theory

In chapter 2.2.3 the most recent theory of Mezei et al. 2019 on the CH^+ DR process was discussed in detail. They provided the calculated rotational-state-dependent cross sections (Figure 2.7) in digitized form for the sake of an experimental comparison in this work. The cross section data were convolved with the energy distribution function of the CSR electron cooler (chapter 4.2.2) in order to obtain J-state-specific MBRCs (see chapter 4.3 for convolution process).

The convolved theory rate coefficients are compared to the experimental data ($t = 60 - 80\,\mathrm{s}$) in Figure 6.19. Due to the applied experimental energy resolution, the manifold of rotational resonances in Figure 2.7 is mostly averaged out, resulting in broader structures in the rate coefficient. Up to $E_\mathrm{d} = 3\,\mathrm{meV}$ the $J = 0$ rate coefficient exceeds the other J slightly - a difference, which is not easily visible in the cross section domain. The higher non-resonant part or the average of all rotational resonances below 3 meV in Figure 2.7 cause this feature. Around $E_\mathrm{d} = 20\,\mathrm{meV}$ the $J = 0$ rate is significantly lower than the other two, which can be unambiguously attributed to the 20 meV resonance in the cross section. The remaining energy ranges in the MBRC are almost J-independent. In total, the calculated rotational state dependence in Figure 6.19 appears to be rather weak and causes differences between pure J-states of at most $\pm 25\%$.

The theoretical MBRC data differ strongly from the CSR experimental results, both quantitatively and qualitatively. The main difference can be observed at the 0 eV resonance, which is underestimated by at least a factor of five. Moreover, the resonance positions are not correctly predicted by the calculations. Since theory in the low-energy regime relies on exact Potential Energy Curves (PECs), which are often not precise on the meV level, a shift between theoretical and experimental resonance energies could cause the observed discrepancies. With a shift of 30 meV towards higher energies, the theory rate coefficient would match the experimentally observed resonances much better. As a consequence, amplitude variations of the resonances are also expected, which are especially crucial for the 0 eV rate (Singh 2020). At energies above 200 meV, DR pathways via core-excited Rydberg states become the dominant process, as shown in Figure 2.8. The calculations by Mezei et al. 2019 neglect these pathways and, thus, become inaccurate at high energies.

Despite of the overall rather poor match of both rate coefficients, it should be noticed that the theoretical J-dependence at $E_\mathrm{d} = 0\,\mathrm{eV}$ qualitatively matches the experimental results in Figure 6.10. While the calculated $J = 0$ rate exceeds the $J = 1$ rate by 15%, the experimental data of this work indicate a 42% enhancement.

Since the rotational state populations $P_J(t)$ in CSR are known (Figure 5.11 b)), equation 4.65 can be used to calculate theoretical rate coefficients for population ensembles equivalent to any storage time window in the CSR experiment. Such storage-time-dependent theory rate coefficients are compared to experimental ones in Figure 6.20. This procedure seems more robust than comparing the less precise $J = 0$ experimental

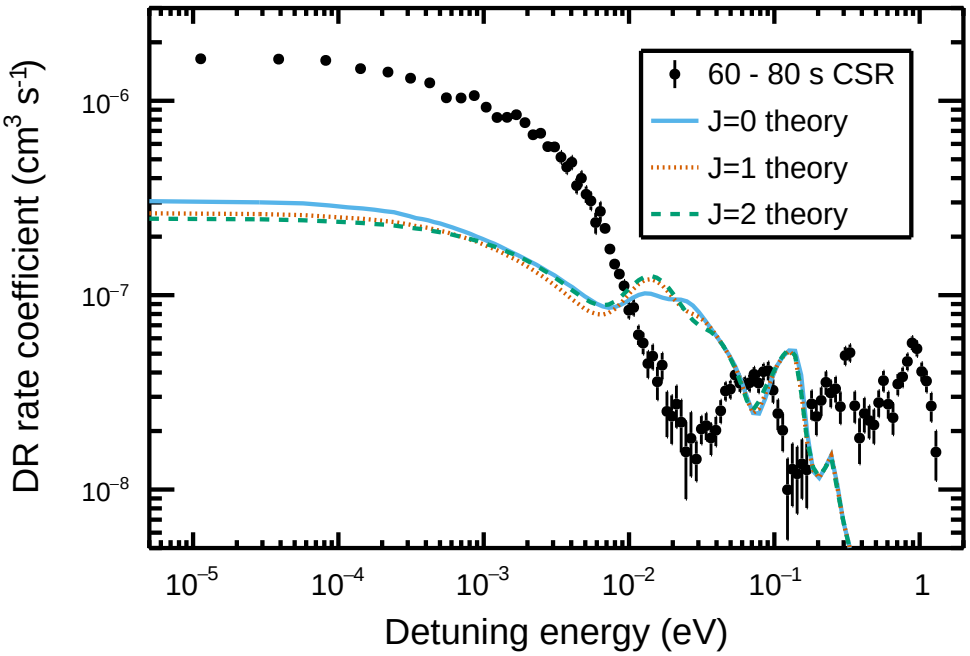

Figure 6.19: CH^+ DR rate coefficient (MBRC) comparison to J-state specific theory (Mezei et al. 2019). The cross sections from Figure 2.7 were convolved with the electron cooler energy distribution to obtain theoretical rate coefficients.

rate coefficient (section 6.4). Because of the minimal J-state dependence of theoretical rate coefficients, it is not surprising that the resulting storage time effects are weak. The most pronounced deviations are of about $\pm 4\%$ at $E_\mathrm{d} = 0\,\mathrm{eV}$ and $E_\mathrm{d} \approx 15\,\mathrm{meV}$, following a similar trend as the previously discussed J-dependencies.

For comparing experimental to theoretical plasma rate coefficients the same cross section data from Figure 2.7 were convolved with equation 4.63. The resulting theoretical plasma rate coefficients for individual rotational states have already been published earlier in Faure et al. 2017. Here, they were further weighted by the rotational state populations for $t = 60 - 80\,\mathrm{s}$ in CSR. Despite of the fact that the $J = 0$ plasma rate coefficient is of higher astrophysical interest, Figure 6.16 showed that its difference to the rate coefficient for the population ensemble in CSR is minimal. Thus, a theory comparison on the level of the rotational populations in the CSR experiment seems reasonable. The theoretical result for the $J = 0 - 2$ state mixture in CSR is compared to the experimental result in Figure 6.21. It shows a remarkable deviation to CSR data and underestimates the low- and high-temperature rates by far. As discussed above, for reliable estimates at high temperatures, theory would need to be extended by the core-excited DR process. At low temperatures the deviation is explained by the pronounced 0 eV resonance, whose extent is underestimated by theory (see Figure 6.19).

All in all, the rate coefficient data obtained in this work reveal a necessity of refining the rotationally-resolved MQDT calculations in Mezei et al. 2019. From the consider-

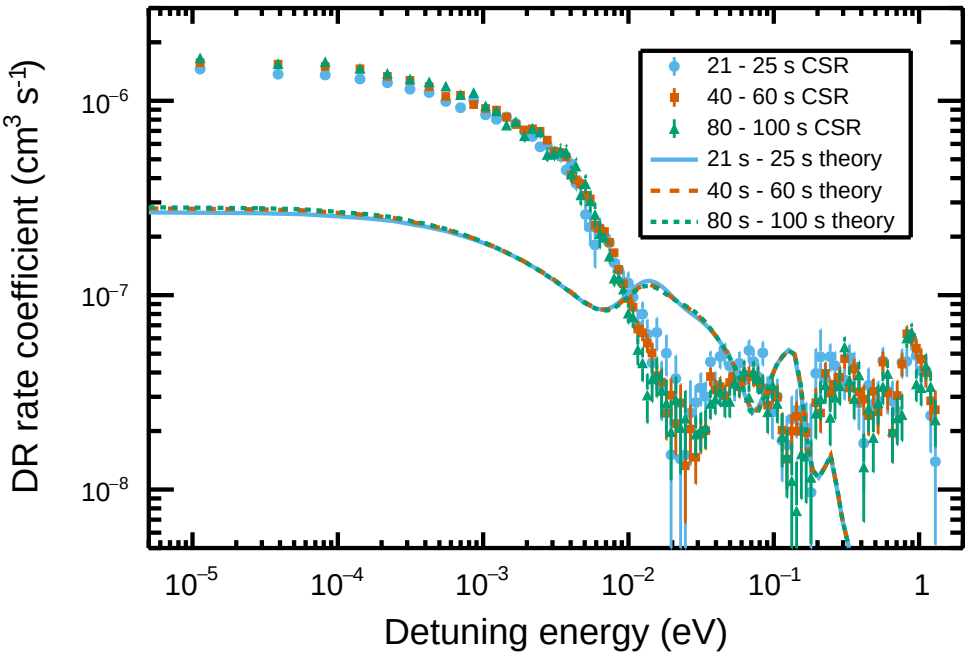

Figure 6.20: CH^+ DR rate coefficient (MBRC) - storage time and theory comparison. J-specific theory DR rates from Figure 6.19 are weighted by the laser-probed J-state populations in CSR (Figure 5.11 b)) and compared to experimental data.

ations in this section, two ways for future theoretical improvements seem reasonable.

On the one hand, a shift between the ionic and neutral potential curves on the order of 30 meV could be applied. This would shift theoretical resonance positions close to the experimental ones. However, it is unclear whether new resonances are introduced or existing ones are dampened by such a shift, which in the end might change the resonance behavior quite significantly. More generally, the new, more accurate and state-rich R-matrix molecular structure data computed by Chakrabarti, Ghosh, and Choudhury 2019 are about to be included in exploratory calculations based on the same method already employed in Mezei et al. 2019 (Schneider and Kokoouline 2021).

On the other hand, the calculations in Mezei et al. 2019 did not include DR pathways via core-excited Rydberg states. As this is most likely the reason for deviations at high energies, core-excited calculations without rotational state effects in Chakrabarti et al. 2018 also result in low-energy resonances (see Figure 2.8). Thus, interference of those core-excited channels with rovibrationally excited ground state ion core channels could also affect the rates in the meV collision energy regime. A computationally cumbersome inclusion of both, rovibrational and core-excited states, is currently under investigation in theoretical studies (Schneider and Kokoouline 2021).

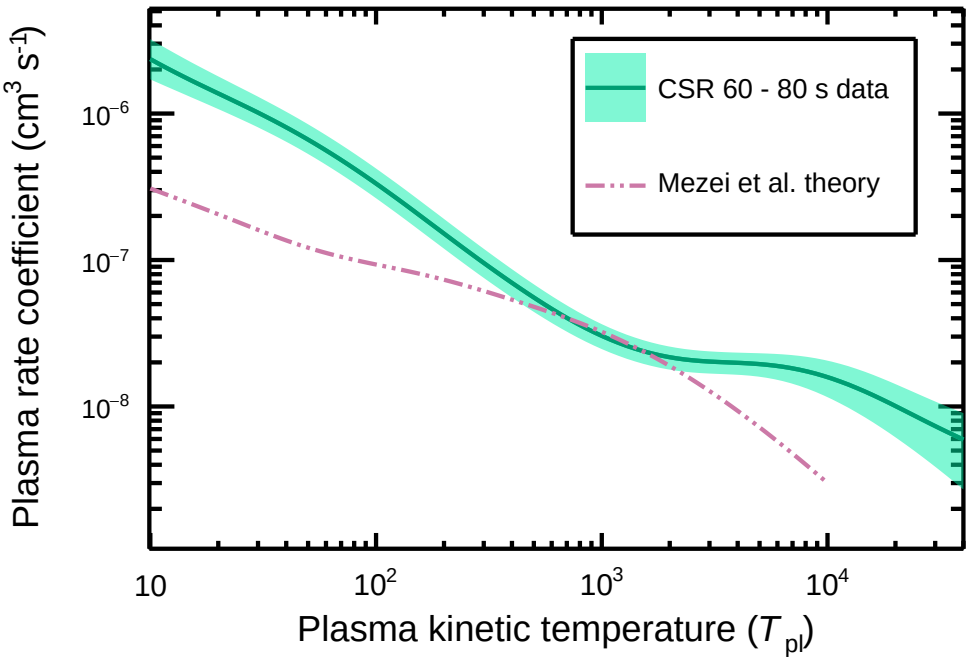

Figure 6.21: CH^+ DR plasma rate coefficient: experiment vs. theory. The theory curve was obtained from convolution of the cross sections in Mezei et al. 2019 and weighting the J-specific rates by the measured rotational populations in Figure 5.11 b).

Chapter 7

Results on DR final states and dissociative state symmetries

With the determination of the absolute DR cross section for internally cold CH^+ ions, the main questions concerning its astrophysical interest could be answered. Nevertheless, these results are not able to characterize the dissociation dynamics, which are essential to understand the process from a fundamental point of view. Especially chapter 6.7 revealed the necessity for improved theoretical calculations on the reaction to match the observed rate coefficient.

As presented in chapter 4.4.2, 3D imaging information can be used to obtain Kinetic Energy Releases (KERs), final state branching ratios and angular fragment distributions in a clean manner. While the KER is directly linked to the molecular initial state and atomic final state energies, the branching ratios give rise to participating dissociation channels. Finally, from angular distributions the symmetries of dissociative states can be inferred, as discussed in chapter 2.1.3. All information together serve as additional information for theoretical understanding of the reaction and might indicate insufficient descriptions.

For the CH^+ system, in particular, previous literature raised questions about the final state branching ratios, which were formulated as the last two points in chapter 2.4. Here, the $C(^1S)+H(1\,s)$ final state contribution, introduced as an explanation of the 2D fragment imaging distributions observed at the TSR (Amitay et al. 1996), could not be explained theoretically and this interpretation was later criticized (Guberman 2005). The main interest of this chapter is focused on the clarification of this $C(^1S) + H(1\,s)$ puzzle by means of 3D imaging.

A 3D imaging technique is implemented at the NICE detector (chapter 3.3), which allows to simultaneously observe DR fragment positions and arrival times with a ≈ns resolution. A few calibration steps used for data analysis have been presented in chapter 4.5 and the data properties were characterized in chapter 5.3. Furthermore, appendix

B.2 gives an overview of data sets and discusses the background subtraction procedure. It results in the electron-induced signal S_i, which is commonly used for plots in this chapter. In order to detect possible electron energy dependencies, the dissociation properties were studied by fragment imaging at four different detuning energies: 0 meV, 8 meV, 70 meV and 320 meV.

Since 3D imaging at CSR is for the first time applied to DR data in the course of this work, an insight into the original detector data will be provided in section 7.1. The detector limitations in combination with the specific measurement conditions at the low ion beam energies of CSR require to include data filters, which are explicitly discussed in section 7.2. Effective-KER distributions can consequently be analyzed in section 7.3, enabling to derive the CH^+ ground state dissociation energy. Section 7.4 is concerned with the modeling of angular distributions, while final state branching ratios are calculated in section 7.5. The chapter concludes with an interpretation of all the results, unambiguously confirming the existence of the $C(^1S) + H(1\,s)$ final channel and conclusions about the intermediate molecular potential curves of the dissociative molecule. This includes evidence for a dissociative route involving $^2\Sigma^+$ molecular states, which still awaits theoretical confirmation.

7.1 First insights into imaging results

CH^+ DR at low electron energies is characterized by comparatively high KERs of ≈ 5 eV (see Table 2.4). On the one hand, this property complicates the measurements due to the fact that fragments partly gain so much transverse velocity that they do not hit the detector surface anymore (see chapter 5.3). On the other hand, for events where both fragments reach the detector surface, their arrival time difference can become large enough to be conveniently measured at the $\gtrsim 15$ ns separation time limit of the detector. The latter fact paves the way for 3D imaging analysis of DR fragments. This section compares the experimental results for fragment distance distributions with ideally expected ones that were presented in chapter 4.4.2. The data shown here are solely for the $E_d = 0$ meV measurement, as those could be measured with high statistics thanks to the high DR rate at very low collision energies (compare Figure 6.1).

Figure 7.1 b) presents the unfiltered distribution of 3D events, showing combined transverse (d_{2D}) and longitudinal ($d_\parallel$) fragment distances. The latter were obtained by multiplication of time differences with the ion velocity, derived from the revolution frequency (equation 5.1) and the CSR circumference (chapter 3.1). With help of the mass assignment and COBRA algorithms (see chapters 4.5.2 and 4.5.3), the events with C atom arriving first and H atom arriving first can be distinguished, leading to $d_\parallel > 0$ and $d_\parallel < 0$, respectively.

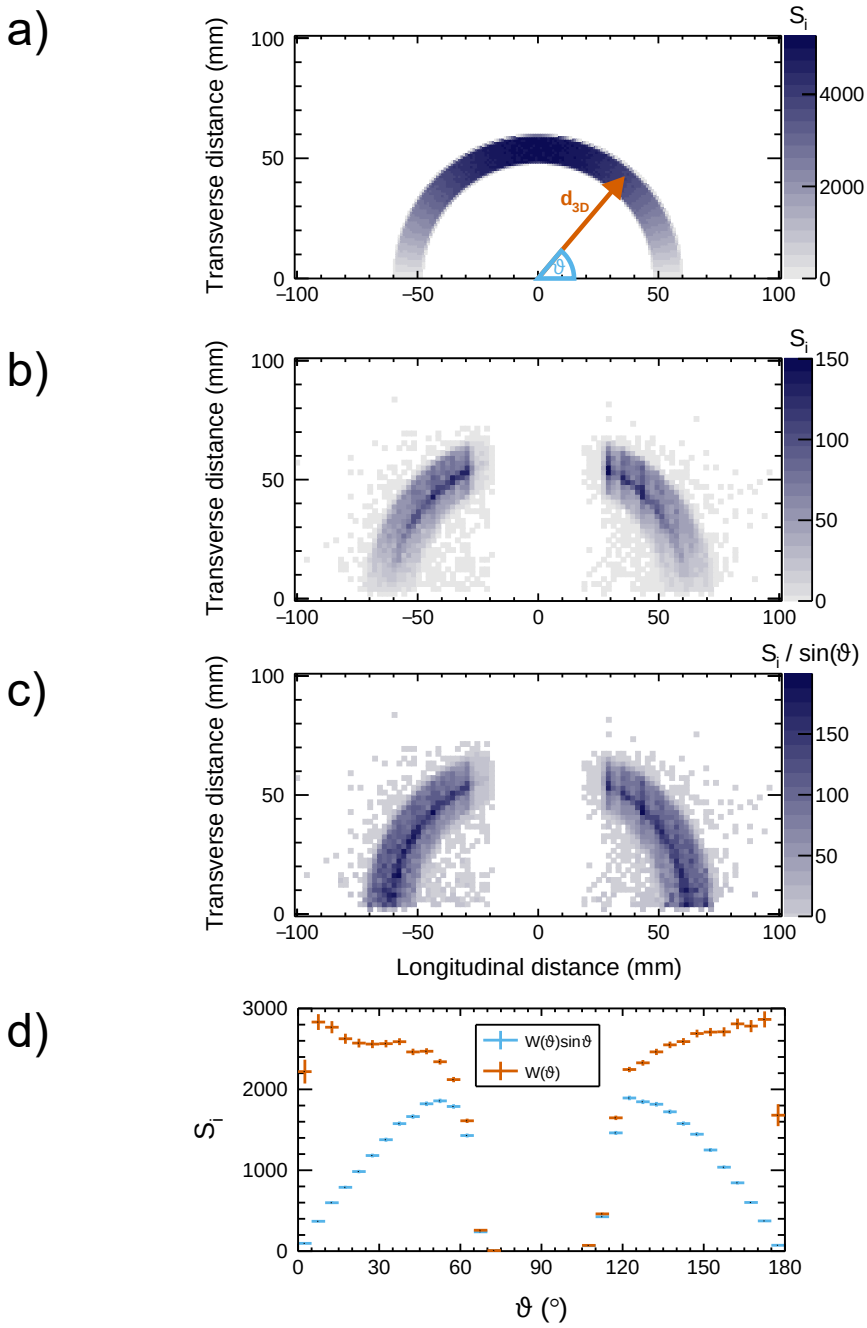

Figure 7.1: Combined CH^+ DR fragment distance and angular distribution for $E_d = 0\,eV$, without specific data cuts. $d_{2D} > 0$ and $\vartheta < 90°$ represent events where the C atom impinges the detector first. In the other cases, H atoms are arriving first. a): Ideal combined distance distribution from Figure 4.11 a), re-plotted for comparison. b): Combined distance distribution for background-subtracted, electron-induced signal S_i. c): Distribution b) normalized by $1/\sin(\vartheta)$ to eliminate the spherical Jacobian weighting factor (see section 4.4.2). d): Angular distribution for the unweighted data b) and weighted data c), resembling the measured $W_{meas}(\vartheta) = W(\vartheta)\sin(\vartheta)$ and real $W(\vartheta)$ angular fragment distribution, respectively.

The resulting figure can be compared to the ideal distribution (Figure 4.11 a)), which has been plotted again for comparison in Figure 7.1 a). The expected circular arc is clearly visible in the experimental distribution, underlining the correctness of the detector calibration. A faint signal can be spotted outside and inside of the arcs. This signal can be assigned to statistically imperfect background subtraction. On the circular arc a small line with high intensity is visible, which is discussed below. In general, no clear differences between the left and right half of the distribution are visible, indicating not too strong *forward-backward asymmetries* (see chapter 4.4.2) in the DR rate coefficient data at $E_\mathrm{d} = 0\,\mathrm{meV}$.

The most obvious deviation between the experimental and the ideal distribution is the missing data in the center of the plot. This cutoff is not caused by any data filter but due to the limited arrival time detection possibilities of NICE (see Figure 5.7 b) and discussion around). It is related to the minimum pulse separation time and has to be considered for further analysis. A similar but horizontal cutoff becomes visible at low transverse distances close to $d_\mathrm{2D} = 0$, where two spots on the phosphor screen cannot be distinguished any more. This cutoff, however, only affects a minor fraction of the data.

On the circular arc of Figure 7.1 b) the signal intensity drops towards $\vartheta = 0°$ and $\vartheta = 180°$, where ϑ is defined as shown in subfigure a). Reduced intensity regions are expected, even in the ideal case, because of the Jacobian factor $\sin(\vartheta)$ (see chapter 4.4.2), influencing the measured angular distribution $W_\mathrm{meas}(\vartheta) = W(\vartheta)\sin\vartheta$. In subfigure c) the distribution was normalized by $\frac{1}{\sin\vartheta}$ in order to remove this trend and visualize the real angular fragment distribution $W(\vartheta)$. In this figure the intensity appears quite homogeneous over the arc.

The real angular fragment distribution $W(\vartheta)$ is identical with the event distribution along ϑ in subfigure c) and is explicitly drawn in Figure 7.1 d), together with the measured angular distribution $W(\vartheta)\sin\vartheta$ of the non-normalized subfigure b). The data indicate a falling intensity towards $\vartheta = 90°$ on both sides. Here, the intensity first decreases slightly up to $\vartheta = 55°$ and down to $\vartheta = 125°$ with a transition to a fast intensity loss towards 0 at $\vartheta = 70°$ and $\vartheta = 110°$. At the latter point, the time difference detection limits prevent any data acquisition. Furthermore, the first and the last bin are affected by the transverse detection limit. Both effects have to be considered for further analysis.

The first impression of the combined distance distributions might lead to the conclusion that the circular arc well represents a single DR final channel. A detailed analysis of final channels can be done with the 3D distance (d_3D) distribution, the radial distribution of Figure 7.1 b). In ideal case, a box function is expected for a single channel (Figure 4.11 b)), which has been drawn in Figure 7.2 a) for a KER of $E_\mathrm{KER} = 5.92\,\mathrm{eV}$. The experimental distribution in subfigure c) appears much more complex than a simple box function. Furthermore, sub-distributions are presented, where C atom and H atoms, respectively, first impinge on the detector. An significant shift between the two sub-distributions becomes visible.

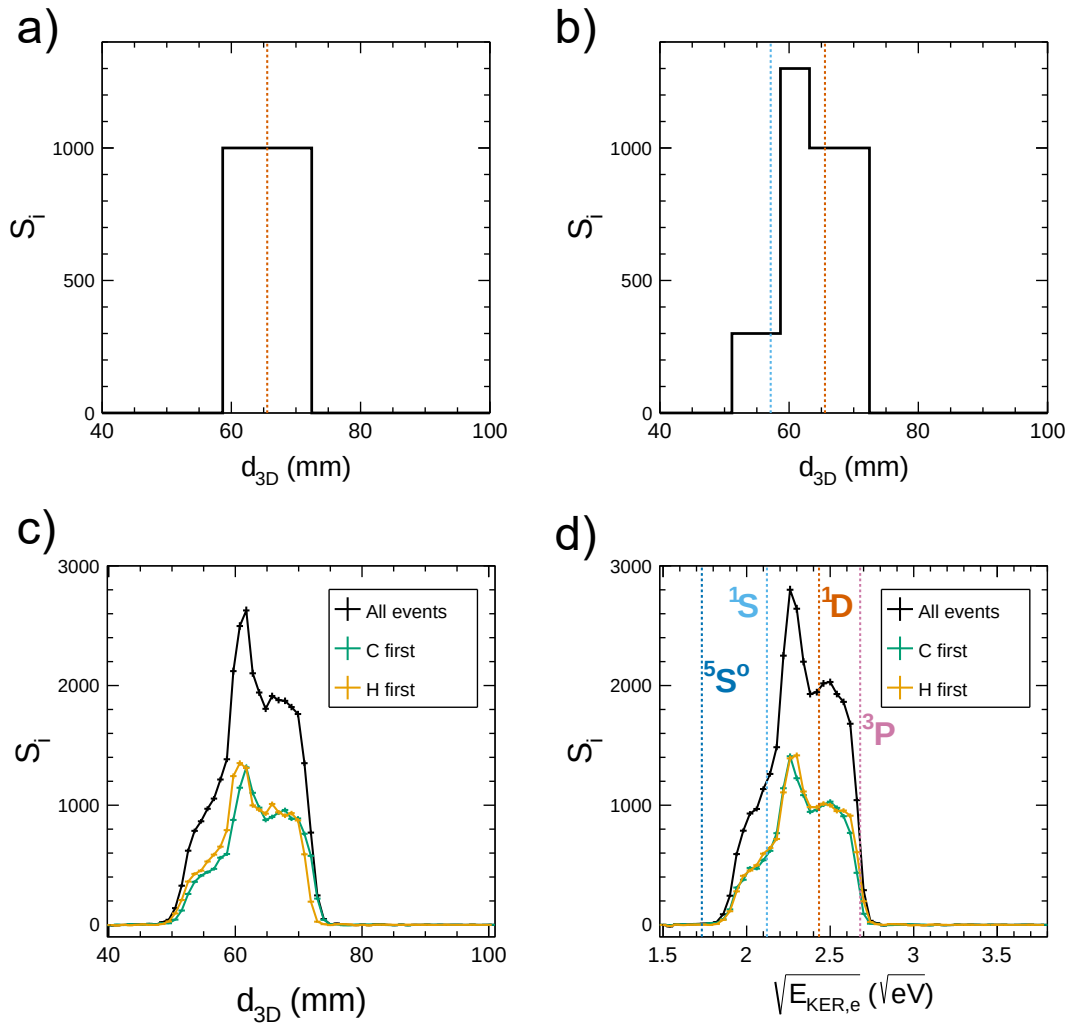

Figure 7.2: 3D distance and effective-KER distribution for $E_d = 0\,eV$ - compared to ideal distributions. The error bars of the last two (experimental) plots are of statistical nature and were propagated from counting errors. The contribution of events with C atoms or H atoms arriving first is highlighted in those two subfigures. a): Ideal distribution neglecting fragment recoil effects, as shown in Figure 4.11 b). The center position (orange dashed line) corresponds to a KER of $E_{KER} = 5.92\,eV$ for the presented experimental conditions. b): Ideal distribution arising from a superposition of two channels with $E_{KER} = 4.50\,eV$ and $E_{KER} = 5.92\,eV$. c): Experimental 3D distance distribution. d): Experimental effective-KER distribution using the fragment recoil correction (chapter 4.4.2). The position of different final channel energies measured at TSR is indicated (compare Table 2.4 and Figure 2.4).

In chapter 4.4.2 effort was put into the characterization of and correction for the fragment recoil, which predominantly becomes important for high fragment mass differences and high KERs, as in the case of CH^+. The there presented results indicate that the C-atom-first distribution should be shifted towards higher distances compared to the H-atom-first distribution (see Figure 4.12 b)). This is indeed visible in the here presented data. Thus, the formalism for obtaining the effective-KER distribution (equation 4.92), which includes the recoil correction, was applied and the result is shown in Figure 7.2 d). Here, the shift between both sub-distributions is significantly reduced, underlining the validity and importance of considering fragment recoils at CSR. Moreover, the distribution edges appear sharper than in the 3D distance distribution.

The here presented fragment recoil correction is the first application of this method to fragment imaging data from a storage ring merged-beams experiment and will be used for all results shown in section 7.3 and further on.

For an interpretation of the still quite complex distribution, the expected values for $\sqrt{E_{\mathrm{KER}}}$ of three DR channels with the highest KERs (see Table 2.4) have been included in subfigure d) as dashed lines. Additionally, the $\sqrt{E_{\mathrm{KER}}}$ value for the energetically next higher dissociation channel $\mathrm{C}(^5\mathrm{S}^o)[2s2p^3]+\mathrm{H}[1s]$ was calculated by comparing the atomic final levels (see Figure 2.4) and added to the figure. Considering the superimposed box distributions for the various KERs, the major intensity is centered around the $\mathrm{C}(^1\mathrm{D})$ channel, which is expected to be the dominant channel also from the measurements at TSR. The peak towards lower $\sqrt{E_{\mathrm{KER,e}}}$ as well as the left flank can be attributed to an additional contribution of the $\mathrm{C}(^1\mathrm{S})$ channel. Below 2.1 $\sqrt{\mathrm{eV}}$ the signal is solely caused by the $\mathrm{C}(^1\mathrm{S})$ channel. The total distribution can be interpreted as a sum of two box functions for the $\mathrm{C}(^1\mathrm{D})$ and $\mathrm{C}(^1\mathrm{S})$ channel (ideal picture in Figure 7.2 b)), which qualitatively explains the peak and both flatter regions. The $\mathrm{C}(^3\mathrm{P})$ channel, corresponding to the carbon ground state, does not show any detectable contribution. If so, a signal at higher energies than 2.8 $\sqrt{\mathrm{eV}}$ would be expected, which is not seen in Figure 7.2 d). Similarly, the $\mathrm{C}(^5\mathrm{S}^o)$ channel can be excluded. A quantitative modeling of the total distribution will follow in section 7.3.

Already at this point it can be concluded from the shape of the effective-KER distribution that the low-energy CH^+ DR *does* have a partial cross section into the $\mathrm{C}(^1\mathrm{S})$ final channel. This result confirms the previous interpretation of Amitay et al. 1996 of the TSR experiment and answers the fourth scientific question in chapter 2.4. In a second step, the inability to explain the existence of this channel from theoretical considerations (chapter 2.3) raises the question which dissociative molecular potential curves contribute to the observed $\mathrm{C}(^1\mathrm{S})$ final state. Further considerations on this topic are given in section 7.6. In contrast to the TSR results, the here presented detection via 3D imaging is unambiguous since the angular and effective-KER distribution are decoupled from each other.

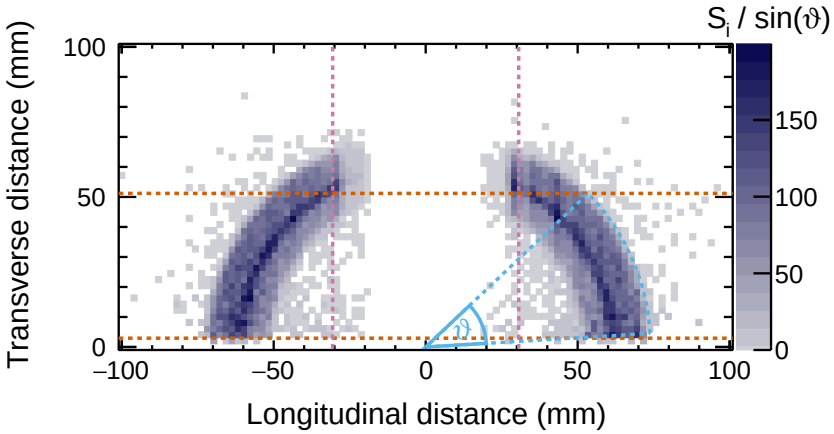

Figure 7.3: Visualization of angular data filters on the combined distance distribution from Figure 7.1 b). The dashed lines define the borders of the undisturbed regime in both coordinates. Lower orange line: separation limit of two camera spots, upper orange line: geometric detector limit, pink lines: arrival time separation limit. Altogether, they define a range of valid angles ϑ, indicated in blue, which can be translated similarly to negative longitudinal distances. See text for more information.

7.2 Data filters, modeling and systematic uncertainties

From the unfiltered 3D imaging data presented in the last section, already preliminary qualitative conclusions could be drawn. A quantitative analysis of observed KERs, angular distributions and branching ratios, however, requires to consider several systematic effects that have been already pointed out previously. In this section these systematics are addressed by including data filters and effective modeling of the data.

Figure 7.3 is based on the data shown in Figure 7.1 b) and summarizes most systematics to be discussed in the following. The horizontal orange lines in the figure represent the borders where transverse distances become unreliable. At *small* distances camera spots cannot be distinguished any more. The online peak search algorithm used for the camera data in the CH^+ beamtime integrated intensities over several neighboring pixels such that the minimum possible distance is $d_{2D,min} = 2.94\,mm \mathrel{\widehat{=}} 7\,Pix$, corresponding to the lower limit in Figure 7.3. At *large* transverse distances, hydrogen fragments can miss the detector surface, leading to a smooth reduction of the signal, which starts at $d_{2D,max} = 51.2\,mm \mathrel{\widehat{=}} 122\,Pix$ (see chapter 5.3).

Regarding longitudinal distances, an obvious limitation is the minimum arrival time difference that can be detected. As discussed in chapter 5.3, a minimum time of $\Delta t = 15\,ns$ is chosen for this analysis, resulting in a minimum distance of $d_{\parallel,min} = 30.6\,mm$. This limit was added to Figure 7.3 as the vertical pink dashed line.

In order to prevent the above mentioned effects from affecting the data quality, data filters were introduced. Any filter on d_{2D} and $d_{\parallel}$, however, would artificially alter the

shape of the important angular and effective-KER distributions. Thus, data filters have to be defined in the coordinates ϑ and $\sqrt{E_{\mathrm{KER,e}}}$, which, as a result of the fragment recoil correction, are nearly orthogonal. The most reasonable choice is to filter on the angle ϑ. In that case, the effective-KER distribution is not affected at all, while the angular distribution can only be interpreted in the filtered region. The three criteria corresponding to the limits of d_{2D} and $d_{\parallel}$ can be formulated as

$$\vartheta > \arcsin\left(\frac{d_{\mathrm{2D,min}}}{d_{\mathrm{3D,min}}}\right) \tag{7.1}$$

$$\vartheta < \arcsin\left(\frac{d_{\mathrm{2D,max}}}{d_{\mathrm{3D,max}}}\right) \tag{7.2}$$

$$\vartheta < \arccos\left(\frac{d_{\parallel,\mathrm{min}}}{d_{\mathrm{3D,min}}}\right) \tag{7.3}$$

where $d_{\mathrm{3D,min}}$ and $d_{\mathrm{3D,max}}$ are the minimum and maximum 3D distance observed in Figure 7.2 c). For the $E_{\mathrm{d}} = 0\,\mathrm{eV}$ data, $d_{\mathrm{3D,min}} = 48\,\mathrm{mm}$ and $d_{\mathrm{3D,max}} = 74\,\mathrm{mm}$ were chosen. Those values have to be adapted for higher electron energies as the distribution is shifting towards higher distances, leading to slightly different angular filters. It should be noted that the unfiltered 3D distance distributions have to be used to determine the limits $d_{\mathrm{3D,min}}$ and $d_{\mathrm{3D,max}}$, beyond which no DR events are visible any more. Thus, the values listed above are not a generally applicable filter but are specifically suited for the CH^+ system. Nevertheless, equations 7.1 - 7.3 can be used in a system-independent manner with adapted values for $d_{\mathrm{3D,min}}$ and $d_{\mathrm{3D,max}}$.

A visualization of the remaining angular range after the data filter is added to Figure 7.3 as the segment limited by the blue dashed lines and is applied symmetrically for the other half of the distribution. The filter removes part of the data that visually do not differ much from the allowed region. However, for higher angles the smooth transverse detection limit starts to already affect the high 3D distances, i. e., the high effective KERs in the respective distributions, which hence are filtered out. Unfortunately, due to the Jacobian $\sin\vartheta$ weighting factor, exactly these data carry the highest signal (see Figure 7.1 b)), such that the statistical data quality is substantially reduced by the filter.

For completeness, it should be mentioned that a common angular filter on the azimuthal angle $155° < \varphi < 210°$ has been introduced in chapter 5.3 in order to eliminate the cutout visible in Figure 5.7 a). Due to almost ideal cylindrical symmetry of the collision process, which is only violated regarding a small signal contribution from the toroid region of the electron cooler (see chapter 5.3), this filter is not expected to affect any distribution presented in this chapter.

A quantitative evaluation of the remaining data is possible by modeling the angular and effective-KER distributions. Since angular distributions, after the $\frac{1}{\sin(\vartheta)}$ normalization, are expected to follow Legendre polynomials (see equation 4.79), the following fit

function is used

$$W(\vartheta) = a_0 \left(1 + a_1 \cos\vartheta + \frac{a_2}{2}(3\cos^2\vartheta - 1)\right) \tag{7.4}$$

where a_0 is an additionally introduced scaling parameter to match the observed intensities.

Effective-KER ($\sqrt{E_{\mathrm{KER,e}}}$) distributions, resulting from the fragment recoil correction approach, can, in principle, be described by a simple box function for each channel (equation 4.94). However, Figure 7.2 d) revealed that the experimental distributions do not posses sharp but rather smoothed out edges. This can be attributed to a scatter in the detected event arrival times, as discussed in chapter 5.3. Moreover, the interaction zone is not sharply limited, but the electron energy is adjusted to the desired value in the transition region at entrance and exit of the drift-tubes (see chapter 3.2.2 and Figure 4.5). In these transition regions, the energy-dependence of the DR cross section leads to different, typically lower, reaction rates, thus smoothing out the observed effective KER distributions.

Quantitative description of the above mentioned effects would require a cumbersome full detector simulation as well as calculating the spatial dependence of reaction rates inside the electron cooler. Instead, an empirical approach for modeling the effective-KER distribution is chosen. The ideal box function (equation 4.94) is convolved with a Gaussian distribution of standard deviation σ, resulting in

$$\begin{aligned} P\left(\sqrt{E_{\mathrm{KER,e}}}\right) = & \frac{I L_0}{2\Delta L\sqrt{E_{\mathrm{KER}}}} \left[\mathrm{erf}\left(\frac{\sqrt{E_{\mathrm{KER,e}}} - \sqrt{E_{\mathrm{KER}}} + \Delta L\sqrt{E_{\mathrm{KER}}}/(2L_0)}{\sqrt{2}\sigma} \right) - \right. \\ & \left. \mathrm{erf}\left(\frac{\sqrt{E_{\mathrm{KER,e}}} - \sqrt{E_{\mathrm{KER}}} - \Delta L\sqrt{E_{\mathrm{KER}}}/(2L_0)}{\sqrt{2}\sigma} \right) \right] \end{aligned} \tag{7.5}$$

where $L_0 = 3807\,\mathrm{mm}$ is the detector distance from the interaction zone center, ΔL the interaction length, I the function integral and E_{KER} the KER of the specific DR channel. Multiple channels are modeled by a sum of n terms following equation 7.5 with different values of I and E_{KER}, leading to I_n and $E_{\mathrm{KER},n}$.

All of the considerations above rely on the correct determination of d_{2D} and $d_{\parallel}$. While the ion velocity, necessary for obtaining $d_{\parallel}$, is known with high precision, the calculation of d_{2D} depends on the camera calibration, which transforms pixel coordinates into real length units. This calibration was done in chapter 4.5.1 and resulted in a value of

$$C_{\mathrm{pix}} = 0.4196(65)\,\mathrm{mm/pix} \tag{7.6}$$

For the following analyses the influence of its uncertainty on the results was characterized by obtaining and modeling distributions for the center and both limits of the pixel to millimeter calibration factor C_{pix}. The biggest deviation between fit parameters, corresponding to the different factors, is declared as systematic uncertainty.

7.3 Kinetic energy releases and CH^+ dissociation energy

The Kinetic Energy Release (KER) resulting from the DR reaction is directly connected to molecular properties. A precise measurement of the KER, together with the electron energy ϵ allows to infer the dissociation energy of the CH^+ molecule in the vibrational ground state D_0, as shown in chapter 2.1.3. The present study focuses on the dependence of the effective-KER spectra, arising from the fragment recoil correction, on the detuning energy E_d between electron and ion beam. Hence, the contributions of the various DR product channels are probed as a function of the electron collision energy, which can be approximated by $\epsilon \approx E_\mathrm{d}$. Consequently, the highest reachable precision is given by the electron beam energy resolution and is on the order of 2 meV. In this section effective-KER distributions for all measured values of E_d are presented. According to section 7.2, data filters were applied to update the distribution in Figure 7.2 d).

Figure 7.4 a) presents the filtered effective-KER distributions for the four detuning energies. The energy positions in the rate coefficient spectrum (Figure 6.1) are indicated in subfigure b). Here, the $E_\mathrm{d} = 0$ meV data stem from the highest signal. For $E_\mathrm{d} = 8$ meV the energy was set to the falling slope of the rate coefficient. $E_\mathrm{d} = 70$ meV and $E_\mathrm{d} = 320$ meV probe two different resonance maxima. For modeling of the data in subfigure a), a two channel fit function was chosen:

$$P_\mathrm{tot}\left(\sqrt{E_\mathrm{KER,e}}\right) = \sum_{n=1}^{2} P\left(\sqrt{E_\mathrm{KER,e}}, I_n, E_{\mathrm{KER},n}\right) \tag{7.7}$$

where $P\left(\sqrt{E_\mathrm{KER,e}}, I_n, E_{\mathrm{KER},n}\right)$ corresponds to equation 7.5 with different integrals and KERs for the two channels.

The $E_\mathrm{d} = 0$ meV data are well reproduced by the fit, with a major contribution from the C(^{1}D) and a somewhat contributing C(^{1}S) channel, as already discussed in section 7.1. Within the statistical uncertainties also the $E_\mathrm{d} = 70$ meV data are described well by the superposition of the two distributions. From $E_\mathrm{d} = 0$ meV to $E_\mathrm{d} = 70$ meV the C(^{1}S) integral continuously decreases, indicating a changing branching ratio.

A less good match of data and model is given for the $E_\mathrm{d} = 8$ meV case. In contrast to the other distributions, this data set shows a pronounced signal increase at the left and (to some degree) also the right edges of the ideal flat top boxes. Especially the region $2.4 - 2.6\sqrt{\mathrm{eV}}$ seems to deviate significantly from a flat top. This observation raises the question about possible differences between the $E_\mathrm{d} = 8$ meV measurement and the other data sets.

In the rate coefficient spectrum, $E_\mathrm{d} = 8$ meV is located on a steep slope (subfigure b)), where small energy changes can cause big differences in the detected rates. As a possible reason for the observed deviations, a slightly imperfect spatial match between electron and ion beam can lead to collisions at different values of the electron beam space-charge field, through which the lab-frame energy varies by maximum 0.2 eV from

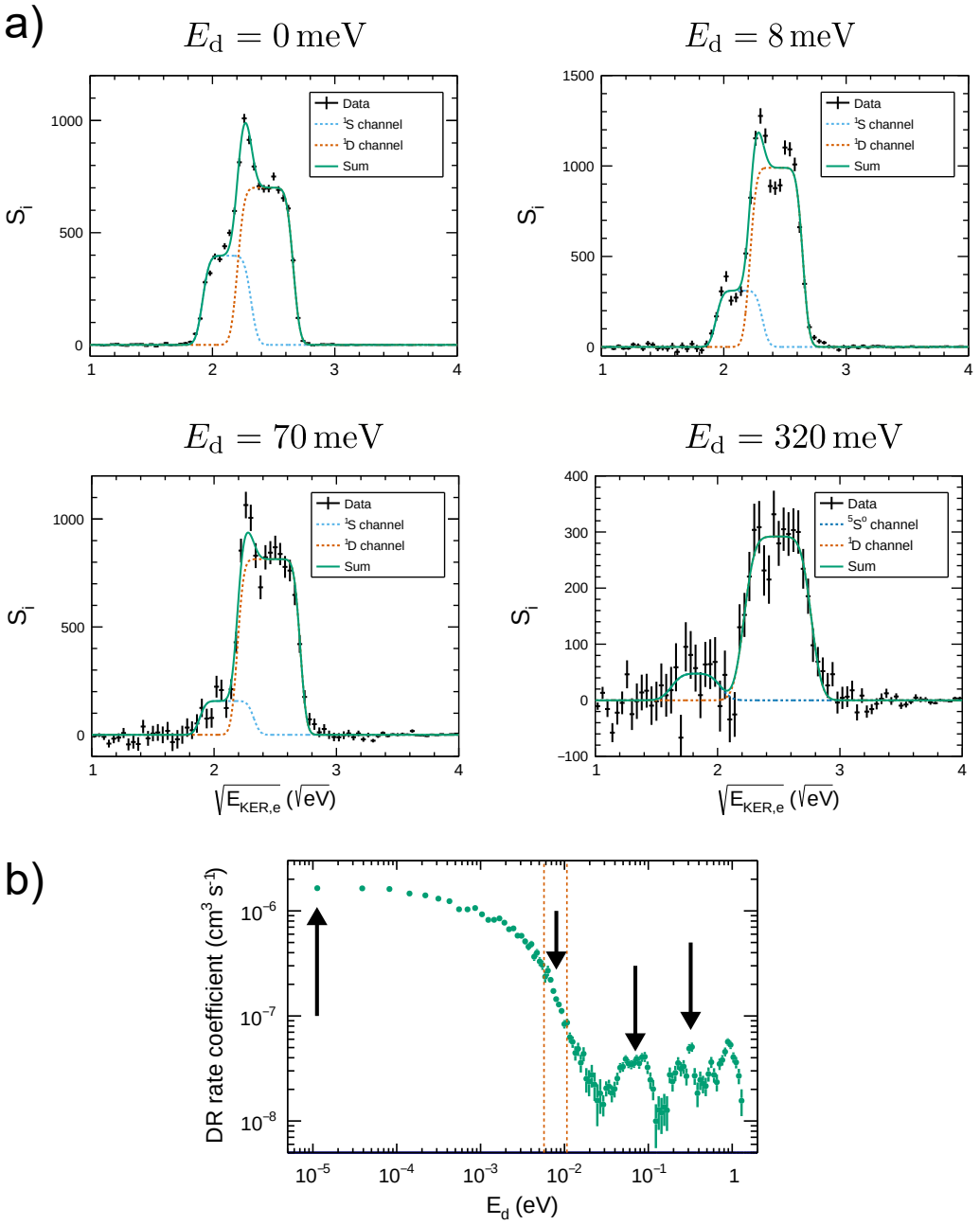

Figure 7.4: Modeling of effective-KER distributions for different detuning energies. a): All effective-KER distributions are fitted with equation 7.7, resulting in the green full lines. Individual final channels are indicated as dashed lines (light blue: C(^{1}S) + H(1 s), orange: C(^{1}D) + H(1 s), dark blue: C(^{5}S^o) + H(1 s) - see Figure 2.4). b): Position of the four detuning energies in the rate coefficient spectrum. For presentation purposes $E_d = 0$ meV was shifted to slightly positive energies. The dashed, orange lines indicate a collision energy shift induced by a lab-frame electron beam energy shift of ± 0.1 eV for $E_d = 8$ meV (see text).

center to boundary of the electron beam. Figure 7.4 b) includes two orange dashed lines, which show the effect for collision energies when shifting the electron lab-frame energy by ±0.1 eV. At these positions the steep slope of the rate coefficient implies a DR rate different by factor of ≈ 2 compared to that at $E_\mathrm{d} = 8\,\mathrm{meV}$. The observed fluctuations over the distribution in subfigure a) are about 20% and, thus, could be explained by an even smaller effect than estimated above. The total effect on the effective-KER distribution is not yet fully understood. 3D imaging experiments on a steep slope of the rate coefficient seem to be influenced more heavily, as subfigure a) implies. Despite of this discrepancy, the integrals and positions of the two channels in the $E_\mathrm{d} = 8\,\mathrm{meV}$ distribution are still reasonably well described by the fit, which averages out the discussed features.

A very interesting observation can be found in the $E_\mathrm{d} = 320\,\mathrm{meV}$ distribution. Here, the first channel is shifted towards lower energies and does not coincide with the C(^{1}S) position any more. Instead, the signal can be interpreted to arise from the C($^5S^o$) channel, which is expected to be centered around $1.8\,\sqrt{\mathrm{eV}}$, slightly higher than in Figure 7.2 d) due to the additional electron energy. In this distribution no significant contribution of the C(^{1}S) can be found any more, underlining the decrease of its branching ratio with increasing electron energy. The detection of the C($^5S^o$) final state with electron configuration ($2s2p^3$) is surprising, considering the high spin of this state ($S = 2$) for the carbon atom in comparison to the singlet ($S_+ = 0$) CH^+ ground state and $s = 1/2$ spin of the incoming electron. Further discussion about possible reaction dynamics involved in producing this final atomic state can be found in section 7.6. Apparently, because of its small size, this contribution could not be detected in the earlier 2D imaging data from TSR (Amitay et al. 1996).

The resulting fit parameters and their uncertainties are listed in Table 7.1. Here, the statistical and systematic uncertainties are given separately to estimate the influence of the detector position calibration (see section 7.2). For the extracted KERs this systematic uncertainty amounts to ≈ 0.8% and limits the precision of all measurements. For the high statistics data ($E_\mathrm{d} = 0\,\mathrm{eV}$) it acts as dominant uncertainty, opposing the low statistical quality cases of the C(^{1}S) and C($^5S^o$) channels for the high detuning energies. A similar trend can be observed for the channel integrals. In contrast to the KERs, however, the systematic uncertainty does not exceed the statistical one for high statistics measurements but is rather comparable.

A from technical aspect interesting quantity is the effective cooler length ΔL. It is expected to be close to the geometric drift-tube length of 800 mm but varies significantly for the different detuning energies. At $E_\mathrm{d} = 0\,\mathrm{eV}$ it is lower than the geometric length, indicating that the potential from the region outside the drift-tubes partly penetrates the interaction zone. In the transition region, the detected rates are much lower such that the effective value ΔL decreases. For $E_\mathrm{d} = 8\,\mathrm{meV}$ the cooler length is even lower. As discussed previously, at this energy effects of the transition region are expected to be most dominant. The steeply decreasing rate coefficient suppresses signal from higher energies such that the distribution becomes narrower and ΔL decreases. For the higher

Table 7.1: Fit parameters obtained from effective-KER distributions in Figure 7.4. The two values given in parenthesis indicate statistical (first) and systematic (second) uncertainties. The latter were determined from fitting distributions generated with a different detector position calibration factor (see section 7.2).

	$E_d = 0\,meV$	$E_d = 8\,meV$	$E_d = 70\,meV$	$E_d = 320\,meV$
$E_{KER}[^5S^o]$ (eV)	-	-	-	3.33(19)(2)
$E_{KER}[^1S]$ (eV)	4.482(8)(33)	4.521(23)(28)	4.424(61)(33)	-
$E_{KER}[^1D]$ (eV)	5.918(7)(47)	5.905(9)(46)	5.990(16)(45)	6.206(42)(51)
$I[^5S^o]$	-	-	-	19.2(60)(4)
$I[^1S]$	157.2(23)(32)	117.5(46)(28)	69.1(84)(17)	-
$I[^1D]$	318.8(28)(69)	427.4(61)(70)	418(9)(11)	161.0(69)(39)
ΔL (mm)	711.7(49)(54)	676.3(67)(22)	798(11)(3)	843(32)(8)
σ ($\sqrt{eV}$)	0.0437(67)(10)	0.0414(19)(21)	0.0407(44)(17)	0.068(14)(3)

two energies the lengths are compatible with the geometric length. Here, the electron-induced rates do not depend so sensitively on energy changes and the transition field contributes similarly to the interaction zone.

According to equation 2.6, the dissociation energy of the CH^+ molecule can be obtained from the fitted KERs of the $C(^1S)$ channel by

$$D_0 = E[H(1\,s) + C^+(^2P^o)] - E[H(1\,s) + C(^1S)] - (E_{KER}[^1S] - E_d) \tag{7.8}$$

The difference of the atomic level energies can be inferred from the well known ionization and excitation energies of carbon and the excitation energies of C^+ (see section 2.2.1) such that

$$D_0 = 8.576\,eV - (E_{KER}[^1S] - E_d) \tag{7.9}$$

The same holds for the $C(^1D)$ channel with the adjusted carbon excitation energy:

$$D_0 = 9.996\,eV - (E_{KER}[^1D] - E_d) \tag{7.10}$$

In order to extract a value for D_0 from last two equations, Figure 7.5 combines the different measurements by plotting the resulting KERs against E_d, for the $C(^1S)$ and $C(^1D)$ channel separately. It should be noted that only statistical uncertainties were propagated to the figure because the systematic uncertainty shifts all points in a common manner and is therefore treated later on. Since the KER is expected to increase linearly with E_d, a line with slope 1 was fitted to both data sets. The $C(^1D)$ results are well reproduced by the line. In contrast to that the $C(^1S)$ results are described worse but are still compatible within the experimental uncertainties. Here, the $E_d = 70\,meV$ result deviates about 2σ from the fit. Especially for this energy the low $C(^1S)$ contribution in Figure 7.4 a) might be influenced by drift-tube boundary effects from the much

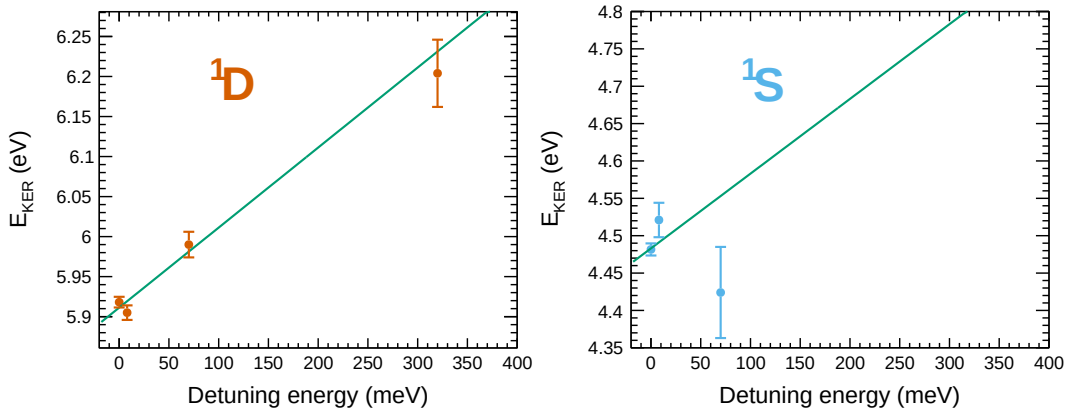

Figure 7.5: KER dependence on detuning energy for the C(^{1}D) and C(^{1}S) channel. The data from Table 7.1 (only statistical uncertainties) were fitted by a linear function with unity slope for determining the dissociation energy of the CH^+ ion (see text).

higher C(^{1}D) signal. Unfortunately, no significant contribution of the C(^{1}S) channel for $E_d = 320\,\text{meV}$ could be observed, which would complement this data set.

The line fit results in a value and uncertainty of the offset $(E_{KER} - E_d)$, which can be directly propagated to the dissociation energy. Here, the systematic uncertainty from the detector calibration has to be implemented. Its magnitude was derived from Table 7.1, for the C(^{1}S) and C(^{1}D) channel separately. The resulting dissociation energies are

$$D_0[^1\text{S}] = 4.093(8)_{\text{stat}}(31)_{\text{sys}}\,\text{eV} \tag{7.11}$$

$$D_0[^1\text{D}] = 4.085(5)_{\text{stat}}(48)_{\text{sys}}\,\text{eV} \tag{7.12}$$

Since both values were determined with the same detector calibration, they should agree within the lower statistical uncertainty, which is indeed the case. The absolute value, however, bares a 4-10 times higher uncertainty, arising from the detector calibration. Since the statistical uncertainty is almost negligible compared to that, the C(^{1}S) analysis results in a lower uncertainty, despite being the minor contribution in the distributions. The constant relative calibration uncertainty leads to a lower absolute KER uncertainty for the C(^{1}S) channel with a smaller KER. Hence, smaller KERs are advantageous for the determination of D_0. For future beamtimes the here presented results motivate the clarification of the discrepancies between the horizontal and vertical position calibration that were discussed in chapter 4.5.1. Otherwise, the fundamental precision limit for KER measurements stays around $\approx 0.8\%$.

The determination of the CH^+ dissociation energy within a sub-percent precision demonstrates the possibilities of 3D imaging experiments at CSR. Aiming for measurements of channels with lower KER even reduces the uncertainty of D_0. Nevertheless, for the CH^+ system this precision cannot compete with results from sophisticated spectroscopy experiments. By laser spectroscopy at TSR Hechtfischer et al. 2002 obtained

a value of $D_0 = 4.084\,87(14)\,\mathrm{eV}$. The analysis of their room-temperature storage ring experiment involved the cumbersome simultaneous modeling of over 50 rovibrational transitions. All of the above presented results agree well with the literature value and underline the robustness of 3D imaging experiments.

The here presented analysis was performed with an ensemble of the lowest three rotational states of CH^+ (see Figure 5.11). Rotational energies were neglected, which at maximum amount to 10 meV for $J = 2$ (Table 2.3) and are on the order of the statistical uncertainty. Despite of this and the above described precision limits, the determination of dissociation energetics as a byproduct of DR measurements turns out to be very effective. Moreover, the CSR radiation field reduces the complexity of rovibrationally excited states significantly. In this environment not only DR but also spectroscopic experiments become much easier to analyze. As presented here, DR experiments can also be used to infer static molecular properties. With a lower precision compared to spectroscopy (if available), they provide another experimental technique that can be applied for a variety of molecular cations.

An interesting point to note is that the CH^+ metastable $a^3\Pi$ state (see chapters 2.2.1 and 5.6) cannot be easily probed by spectroscopy of the $X^1\Sigma$ ground state due to the fact that the two states have a different spin configuration. By photodissociation spectroscopy of the two states, independently, Hechtfischer et al. 2007 determined the excitation energy of the $a^3\Pi$ state to $T_\mathrm{e} = 1.1816(62)\,\mathrm{eV}$, which is the most precisely known literature value. The relative uncertainty of this value is 0.5% and close to the uncertainties achieved for the dissociation energies in this section. A determination of T_e from the DR measurements in this work is possible by evaluating

$$T_\mathrm{e} = D_0 - D_{0,\mathrm{m}} = 0.7709\,\mathrm{eV} + E_{\mathrm{KER,m}}[^3\mathrm{D}^o] - E_\mathrm{d} \tag{7.13}$$

where the right hand side was simplified by inserting the well-known ground state dissociation energy D_0 (see above) and by substituting the metastable dissociation energy $D_{0,\mathrm{m}}$ by a value obtained from the level energy of the dominant metastable $^3\mathrm{D}^o$ DR atomic limit. A measurement of the KER for the $^3\mathrm{D}^o$ channel $E_{\mathrm{KER,m}}[^3\mathrm{D}^o]$ (signal at low distances in Figure 5.13), thus, allows for the determination of T_e. The fact that this KER value is about 0.4 eV (see Table 2.5) even promotes a precise measurement, as discussed previously. Unfortunately, the fragment time separation limit of 15 ns does not allow for 3D imaging measurements of this channel with the current CSR setup. Instead, as shown in Figure 5.13, 2D imaging can be used to determine $E_{\mathrm{KER,m}}[^3\mathrm{D}^o]$ and, hence, also T_e. The derived value is compatible with the literature value of Hechtfischer et al. 2007, however, the systematic uncertainties are higher by more than a factor of two. This is due to the higher influence of the detector position calibration uncertainty when only the position information is used, as in 2D imaging. Nevertheless, an upgrade is planned for the NICE detector, which will be discussed in the following sections. With this upgrade the metastable $^3\mathrm{D}^o$ channel might become accessible by 3D imaging, which could possibly lead to a new, more precise experimental value of the metastable excitation energy.

7.4 Angular fragmentation characteristics

The observation and the modeling of angular fragment distributions is a versatile method to obtain information about DR partial waves and the symmetry of contributing dissociative states. Connections between these properties have been pointed out in Table 2.1 and the discussion in chapter 2.1.3 serves as basis for the discussions in this section. The here presented results involve studies at detuning energies of $E_\mathrm{d} = 0\,\mathrm{meV}$ and $E_\mathrm{d} = 8\,\mathrm{meV}$. At $E_\mathrm{d} = 0\,\mathrm{meV}$ purely isotropic distributions are expected due to the fact that nearly symmetric collision properties are present in the center of mass system (see discussion in chapter 4.4.2). For $E_\mathrm{d} = 8\,\mathrm{meV}$ the collision energy exceeds both, the longitudinal ($T_\parallel \approx 0.2\,\mathrm{meV}$) and transverse ($T_\perp \approx 2\,\mathrm{meV}$) electron beam temperature and the electrons define a clear reference direction. Here, the observed angular distributions can be directly related to DR partial waves.

Figure 7.6 presents the angular fragment distributions $W(\vartheta)$ of the C(^{1}S) and C(^{1}D) channel for $E_\mathrm{d} = 0\,\mathrm{meV}$ and $E_\mathrm{d} = 8\,\mathrm{meV}$. In order to distinguish between the channels, the shown data were filtered for certain regions in the effective-KER distributions (Figure 7.4) that can be predominantly attributed to one of the two channels. Thus, the peaks in the distributions, occurring through the overlapping of both contributions, were excluded to prevent mixing the results for both channels. The further data filters presented in section 7.2 were applied, leading to small remaining angular ranges of $\vartheta = 5° - 45°$ and $\vartheta = 135° - 175°$. The statistical quality of the $E_\mathrm{d} = 70\,\mathrm{meV}$ and $E_\mathrm{d} = 320\,\mathrm{meV}$ data do not allow to draw conclusions about angular symmetries and they are not shown here.

The distributions in the figure were fitted with equation 7.4 and the resulting fit parameters are listed in Table 7.2. a_0 is spared out since it is only an overall scaling factor. In analogy to Table 7.1 statistical and systematic (detector calibration) uncertainties were distinguished.

The parameter a_1 indicates possible preferences for the electron to be captured when hitting the carbon or hydrogen part of the molecule and has been denoted as *forward-backward asymmetry* in chapter 4.4.2. As expected from theory, this parameter is close to 0 for all distributions but deviates from 0 by more than 2σ for the two $E_\mathrm{d} = 8\,\mathrm{meV}$ values.

Technical uncertainties might influence the measured values of a_1: First, it is known from pulse height distributions that carbon atoms, on average, result in higher pulses. Thus, a difference in detection efficiencies for carbon and hydrogen atoms first events is expected. In this case, a negative a_1 parameter can be explained. However, a quantitative estimate revealed that an event fraction of less than 10^{-3} should be affected, which far too low to explain the negative a_1 value. Second, filters on the effective-KER distribution were included to distinguish the two channels. Figure 7.2 d) revealed that on the right flank of the C(^{1}D) channel the carbon and hydrogen first distribution do not completely agree. Even such a small difference might explain the slightly positive value of a_1 for the C(^{1}S) channel. Therefore, the small but non-zero values for a_1 should not

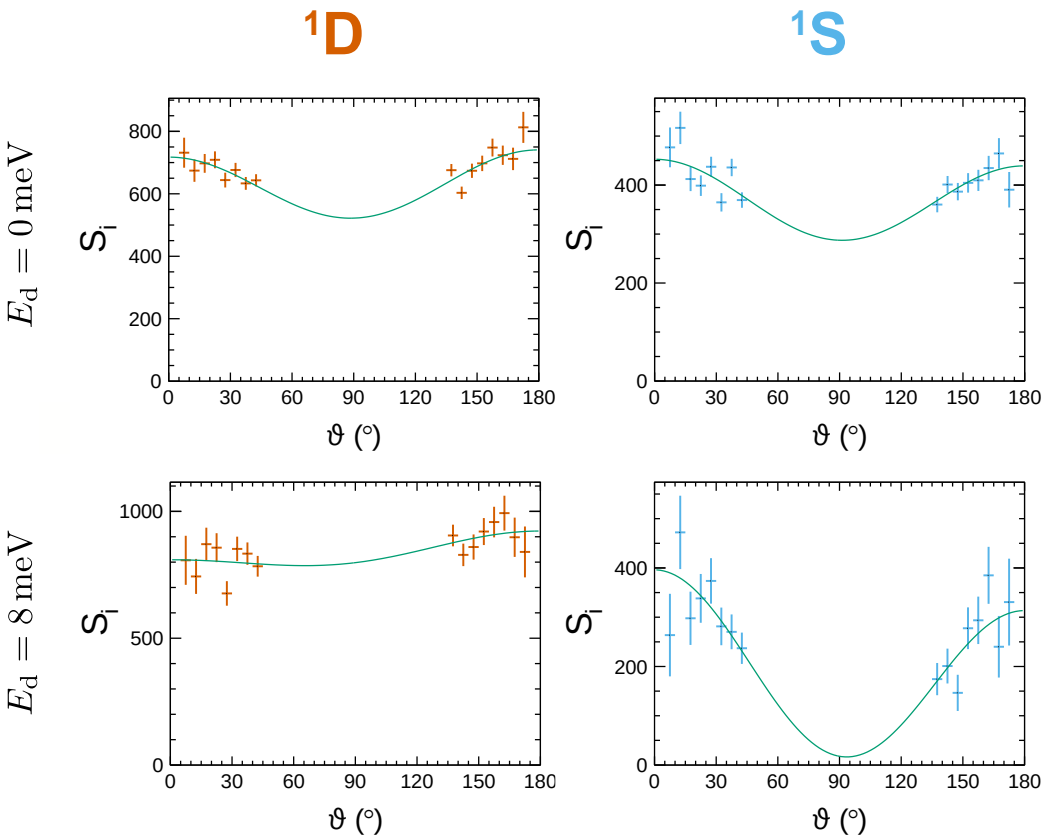

Figure 7.6: Angular fragment distributions for the C(^{1}D) and C(^{1}S) final channels. Distributions for $E_d = 0$ meV and $E_d = 8$ meV are presented and fitted by equation 7.4 to obtain anisotropy parameters a_1 and a_2.

Table 7.2: Angular anisotropy parameters for the C(^{1}D) and C(^{1}S) final channel. Values were obtained from the fits in Figure 7.6. The two values given in parenthesis indicate statistical (first) and systematic (second) uncertainties, where the latter were determined from fitting distributions generated with a different detector position calibration factor (see section 7.2).

	$a_1[^1\mathrm{S}]$	$a_1[^1\mathrm{D}]$	$a_2[^1\mathrm{S}]$	$a_2[^1\mathrm{D}]$
$E_d = 0$ meV	0.020(18)(6)	−0.020(13)(4)	0.31(9)(11)	0.23(6)(10)
$E_d = 8$ meV	0.31(13)(6)	−0.069(20)(9)	1.73(83)(61)	0.06(8)(12)

directly be interpreted as detected *forward-backward asymmetry* but motivate further systematic checks of the detection system.

In addition, the parameter a_2 characterizes asymmetries between longitudinal and transverse breakup. For $E_\mathrm{d} = 0\,\mathrm{meV}$ there is no preferred direction in the collision process and, thus, $a_2 = 0$ is expected. The measurements, however, show slightly positive values, favoring longitudinal fragmentation. Two explanations for this observation are possible: An imperfect match of the electron beam energy or angle to the ion beam may cause a preferred direction. In that case, it would be expected that the value rises strongly towards $E_\mathrm{d} = 8\,\mathrm{meV}$, which is observed for the C(^{1}S) channel but excluded for C(^{1}D). Consequently, the most likely explanation for finding $a_2 \neq 0$ at $E_\mathrm{d} = 0\,\mathrm{meV}$ is a systematic uncertainty, which might arise from the timing detection. In chapter 5.3 the pattern observed in the time difference distribution indicated uncertainties on the order of $\Delta t = 1\,\mathrm{ns}$. Any systematic shift of the time difference, attributed, e. g., to cross talk between the pulses, would affect the longitudinal distances and, by that, also the angular distribution. It could be proven that such an influence systematically shifts the parameter a_2 on a level comparable to the observed positive values.

The obtained anisotropy parameters lead to some minor discrepancies, which are slightly higher than the listed uncertainties in Table 7.2. Since these could arise from the fundamental detection principle, the effects cannot be quantified by further data analysis. More experimental studies are needed to discover systematic dependencies of the anisotropy parameters. A detection system with better time resolution, based on a silicon photomultiplier array, has meanwhile been developed to overcome the time detection resolution limit and might possibly resolve the uncertainties in the time domain.

In total, however, very important conclusions can drawn from Table 7.2: As discussed in the beginning of this section, $a_1 = a_2 = 0$ is expected for $E_\mathrm{d} = 0\,\mathrm{meV}$. The measured values are close to 0 and the deviation can be attributed to the level of not yet fully understood systematic uncertainties. At $E_\mathrm{d} = 8\,\mathrm{meV}$ also $a_1 = 0$ is expected and the observed *forward-backward asymmetry* is indeed small. The much more interesting case is the a_2 value, which can be directly related to DR partial waves. For the C(^{1}D) channel $a_2 \approx 0$ and the distribution is isotropic. According to Table 2.1, this corresponds to a $s\sigma$ partial wave. As the CH^+ ground state is of Σ^+ symmetry, the neutral dissociative state converging to the C(^{1}D) state seems to be also of Σ^+ symmetry. In contrast to that, the C(^{1}S) channel at $E_\mathrm{d} = 8\,\mathrm{meV}$ is associated with a strong anisotropy value *close to the upper physical limit* of $a_2 = 2$. This indicates a strong preference for longitudinal fragmentation of the C(^{1}S) channel, compatible with a $3\cos^2\vartheta$ distribution. Following Table 2.1 as before, the dissociation dynamics for the C(^{1}S) channel are dominated by a $p\sigma$ partial wave and also correspond to a dissociative state of Σ^+ symmetry. A detailed interpretation of these results will follow in section 7.6.

7.5 Final state branching ratios

The major advantage of the 3D imaging technique consists in a clear separation of effective KER and angular distributions. The intensities for individual channels detected in the former distribution can be used to infer branching ratios B_n. Any dependence of B_n on the electron beam energy is an indication for changing dynamics in the dissociation process. This section is dedicated to the analysis (section 7.5.1) and interpretation (section 7.5.2) of branching ratios for the DR of CH^+ ions at low collision energies. At energies beyond 1 eV it is known from TSR experiments that low-energy channels are favored (Table 2.4), which cannot be detected with 3D imaging due to the low time differences between fragments, corresponding to the data gap in Figure 7.3.

7.5.1 Branching ratio calculation and corrections

From the fits of the effective-KER distributions in Figure 7.4, integrals of the C(^{1}D), C(^{1}S) and C($^5S^o$) channel were extracted to Table 7.1. In principle, the ratio of these integrals can be trivially used to infer branching ratios. However, two things have to be considered as a correction to the so determined branching ratios: First, only a limited angular range could be observed in the distributions of Figure 7.4 due to the necessary angular filters in section 7.2. Consequently, the measured intensities have to be upwards-corrected by extrapolating the measured angular distributions in section 7.4 to the full range. The correction is solely dependent on the anisotropy parameter a_2 and its uncertainty, where high values lead to a small upwards-correction of intensities and vice versa. Second, at $E_\mathrm{d} = 320\,\mathrm{meV}$ the C($^3P^o$) channel (compare Figure 2.4) is expected to be energetically accessible but cannot be seen in 3D imaging measurements, owing its low KER. 2D imaging has to be applied to measure its DR contribution and determine all branching ratios for the $E_\mathrm{d} = 320\,\mathrm{meV}$ case.

Both previously discussed corrections are followed in detail in appendix C.2. The uncorrected and resulting corrected branching ratios of the C(^{1}S) channel are exemplary visualized in Figure 7.7. For $E_\mathrm{d} = 0\,\mathrm{meV}$ and $E_\mathrm{d} = 8\,\mathrm{meV}$ the uncertainties increased by more than a factor two because of the uncertainty of the a_2 values. Furthermore, the branching ratio for the $E_\mathrm{d} = 8\,\mathrm{meV}$ case was corrected downwards due to the high a_2 parameter of the C(^{1}S) channel (see Table 7.2). At $E_\mathrm{d} = 70\,\mathrm{meV}$ the correction results in an enormous uncertainty because no limitation of a_2 can be drawn from the measurement of the C(^{1}S) channel. Here, the error bar exceeds the uncorrected one by far and more represents hard limits for the branching ratio than Gaussian uncertainties. For $E_\mathrm{d} = 320\,\mathrm{meV}$ the upper detection limit was adjusted such that the worst case scenario of a_2 combinations is still included. It can be also interpreted as a hard limit.

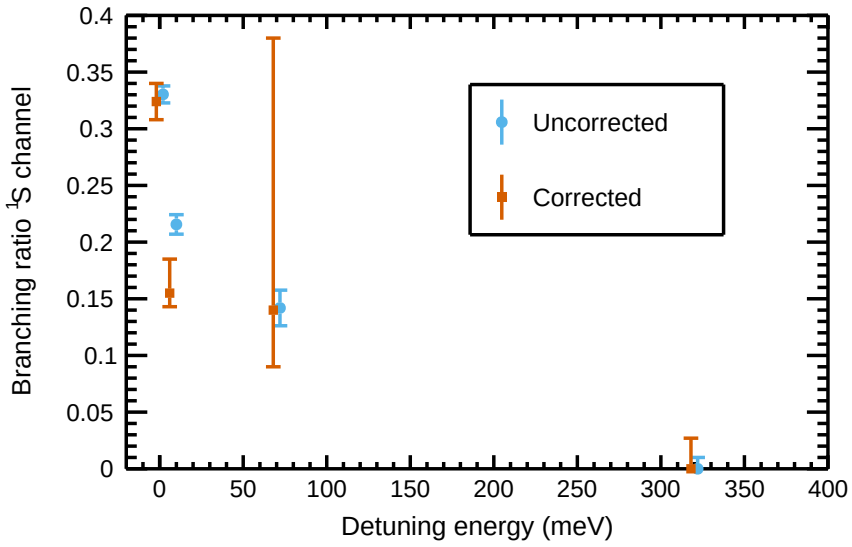

Figure 7.7: Branching ratio of the C(^{1}S) channel for different detuning energies. The uncorrected values (blue circles) correspond to the fitted channel integrals in Table 7.1. These data were corrected for angular data cuts to obtain the orange squares (see text). For the sake of visualization the blue/orange points were shifted by 2 meV to higher/lower energies.

7.5.2 Results

Table 7.3 summarizes the branching ratios of all observed channels for the four different detuning energies. The results for $E_\mathrm{d} = 0\,\mathrm{meV}$ and $E_\mathrm{d} = 8\,\mathrm{meV}$ underlie moderate uncertainties. Here, the previously explained branching ratio correction could be conducted with known anisotropy coefficients. In contrast to that, the higher detuning energies bear high uncertainties, which can be attributed to the full range of anisotropy parameters to be considered in the correction. These uncertainties reflect hard limits instead of Gaussian error bars, as described previously. The central value was arbitrarily chosen as $a_2 = 0$ for the undetermined anisotropies. In total, the high error bars underline the importance of measuring the total angular range, which has not been possible in this case due to the required data filters (see section 7.2).

An interesting observation of the branching ratios is the strong decay of the C(^{1}S) channel contribution from $E_\mathrm{d} = 0\,\mathrm{meV}$ to $E_\mathrm{d} = 8\,\mathrm{meV}$, which has already been visualized in Figure 7.7. Despite the very low energy added to the system, the DR dynamics are affected quite significantly, indicating an energy-sensitive resonant process around $E_\mathrm{d} = 0\,\mathrm{meV}$. This result will be used for further interpretation in the following section.

While no further conclusion can be drawn from the $E_\mathrm{d} = 70\,\mathrm{meV}$ measurement, the branching ratios at $E_\mathrm{d} = 320\,\mathrm{meV}$ undergo a drastic change. The C(^{1}S) channel is not visible any more. In contrast to that, the C($^5\mathrm{S}^o$) channel can be observed, which has not been detected at TSR. Moreover, the by $\approx 300\,\mathrm{meV}$ endothermic C($^3\mathrm{P}^o$) channel opens up and takes over a significant part of the branching ratio. The prominent increase seen

Table 7.3: Branching ratios of CH^+ DR final channels. The values were calculated from the intensities in Table 7.1. Uncertainties were obtained by adding up systematic and statistical uncertainties in square and, additionally, considering the correction for angular cuts. The latter as well as the separate treatment of the $E_d = 320\,\text{meV}$ case are explained in appendix C.2.

	$B[^3P^o]$ (%)	$B[^5S^o]$ (%)	$B[^1S]$ (%)	$B[^1D]$ (%)
$E_d = 0\,\text{meV}$	-	$0^{+2.8}_{-0}$ [a]	32.4 ± 1.6	67.6 ± 1.6
$E_d = 8\,\text{meV}$	-	$0^{+2.7}_{-0}$ [a]	$15.5^{+3.0}_{-1.2}$	$84.5^{+1.2}_{-3.0}$
$E_d = 70\,\text{meV}$	-	$0^{+3.2}_{-0}$ [a]	14^{+24}_{-5} [a]	86^{+5}_{-24} [a]
$E_d = 320\,\text{meV}$	37.0 ± 7.0	5^{+10}_{-3} [a]	$0^{+2.7}_{-0}$ [a]	58^{+7}_{-16} [a]

[a] Instead of a 1σ interval the given uncertainties represent a hard limit, taking into account all possible angular distribution shapes. This effect dominates the uncertainty.

in the rate coefficient around $E_d = 320\,\text{meV}$ (see Figure 7.4 b)) can be attributed to the opening of this channel. Following the TSR measurement (Table 2.4), the $C(^3P^o)$ and other low-energy channels take over the full branching ratio from the high-energy channels up to $E_d = 1\,\text{eV}$. It is interesting to note that this branching ratio takeover does not immediately happen when the $C(^3P^o)$ channel is accessible but follows an energy-dependent, few step or even continuous process.

The results presented in this section underline the sensitivity of 3D imaging experiments. The puzzle about the tentatively detected $C(^1S)$ channel (chapter 2.4) could finally be answered by an unambiguous detection in this chapter. Furthermore, a significant contribution of the $C(^5S^o)$ channel was discovered, a result that could have not been concluded from 2D imaging measurements alone (compare Figure 7.4 a) and Figure C.4).

7.6 Summary and interpretation - indications for a dissociative Σ-state

In this chapter 3D imaging measurements were analyzed for the low-energy DR of the CH^+ molecule. The event-by-event detection principle is based on the statistical evaluation of fragment impact positions and impact time differences on the NICE imaging detector. The here presented results, in form of effective-KER and angular fragment distributions, are the first systematically analyzed 3D imaging studies at CSR.

The low energies of ions stored in CSR, in combination with the high KERs for the CH^+ DR, led to a strong separation of the two fragments from interaction zone to the detector. Consequently, the lighter hydrogen fragment could not be always detected, as it missed the detector in a full transverse fragmentation process. Nevertheless, 3D imaging allowed for a full analysis of KERs, branching ratios and angular fragment distributions, which could not have been achieved by 2D imaging alone. The probed angular range was limited from $\vartheta = 5°$ to $\vartheta \approx 45°$ and reconstruction of the missing events could be achieved from the angular distribution shapes.

Another feature arising from the low ion energies at CSR and, previously been neglected at high-energy storage rings, is the velocity change of the fragments induced by the additional kinetic energy gained in the DR process. This *recoil effect* was mathematically treated in chapter 4.4.2 and resulted in a transformation of the coordinate space (d_{3D}, ϑ) into $(\sqrt{E_{KER,e}}, \vartheta)$. The latter benefits from a better orthogonality of the two coordinates such that KERs and angular distributions can be analyzed almost independently. It can be seen as an higher order correction of the typically used analysis procedure and, to identify the fragments, requires the application of the COBRA algorithm beforehand (chapter 4.5.3).

For the evaluation of DR rate measurements in chapter 6, 2D imaging was used to characterize the contribution of the metastable $a^3\Pi$ state (see also chapter 5.6). The extracted storage time dependence of its population in CSR could be included in the state-resolved DR rate analysis of chapter 6.4. Especially for molecular ions possessing metastable excited states, such as the CH^+ ion, an imaging characterization of final states is required for extracting the rate coefficient of the electronic ground state, as typically desired.

An unfortunate limitation for most of the results presented in this chapter is the inaccessible angular range discussed in section 7.2. It does not only limit the precision of angular anisotropy factors (Figure 7.6) but also appears as a (sometimes huge) uncertainty in the measured branching ratios (Table 7.3). There exists an obvious interest in accessing angles around $\vartheta = 90°$ in Figure 7.3, which would even allow to obtain higher statistics in the region where the Jacobian $\sin\vartheta$ factor is maximized. In order to extend the angular detection range, an upgrade for the current detection system has been developed, allowing to reach the desired low fragment arrival time differences. It combines the current system with a silicon photomultiplier array and

has been constructed and recently implemented in the work of Jäger 2021. In this unit transversally-spaced DR fragments are detected on separate pixels and no fundamental limit for a minimal separation time exists. In an ideal situation the time resolution of the technology was measured to 230 ps and would allow to observe longitudinal distances with an uncertainty of 0.5 mm for CH^+. However, studying the CH^+ system at CSR underlies a second restriction, namely the high transverse distances, which exceed the geometric detector size. Since this restriction is even stronger, an improved time separation limit is not able to extend the angular range for this particular system but becomes essential for ions with lower KERs, which is often the case.

In addition to the technical aspects mentioned above, results regarding the low-energy DR process of the CH^+ ion could be obtained. The following points collect the results achieved in this chapter and will be used for an interpretation of the DR process further below. Additionally to the nomenclature used previously in this chapter, atomic carbon final states will be labeled by their outer shell configuration.

I The effective-KER distribution at $E_\mathrm{d} = 0\,\mathrm{meV}$ (Figure 7.4 a)) confirms the existence of the $\mathrm{C}(^1\mathrm{S})[2s^2 2p^2]+\mathrm{H}[1s]$ atomic final state with a branching ratio of about $\approx 30\%$. This result resolves a discussion (Guberman 2005) about the assignment in the previous TSR experiment (Amitay et al. 1996) and, thus, answers the fourth open question formulated in chapter 2.4.

II At $E_\mathrm{d} = 8\,\mathrm{meV}$ the strongly directed electron beam introduces a reference axis to the collision process. Under the assumption of a fast dissociation process, where the orientation of the molecule is preserved during fragmentation (axial recoil approximation), the angular dependence of the DR cross section is measured. The results of section 7.4 revealed remarkably different angular characteristics, i. e., partial wave contributions, between the $\mathrm{C}(^1\mathrm{D})[2s^2 2p^2] + \mathrm{H}[1s]$ and $\mathrm{C}(^1\mathrm{S})[2s^2 2p^2] + \mathrm{H}[1s]$ final states. For the $\mathrm{C}(^1\mathrm{D})$ channel an almost isotropic distribution was observed, which is compatible with a $s\sigma$ partial wave but can be also interpreted as an incoherent superposition of other partial waves (see interpretation below). On the other hand, a strong preference for longitudinal fragmentation was observed for the $\mathrm{C}(^1\mathrm{S})$ channel, arising from a pure $p\sigma$ partial wave (see Table 2.1).

III The branching ratio of the $\mathrm{C}(^1\mathrm{S})[2s^2 2p^2]+\mathrm{H}[1s]$ channel revealed a high sensitivity on the collision energy (Figure 7.7). From $E_\mathrm{d} = 0\,\mathrm{meV}$ to $E_\mathrm{d} = 8\,\mathrm{meV}$ the $\mathrm{C}(^1\mathrm{S})$ contribution reduces by a factor of two.

IV At $E_\mathrm{d} = 320\,\mathrm{meV}$ the $\mathrm{C}(^3\mathrm{P}^o)[2s^2 2p3s] + \mathrm{H}[1s]$ final state was observed with a very low KER of 20(10) meV with 2D imaging (Figure C.4). Furthermore, by 3D imaging a small contribution ($\approx 5\%$) of the $\mathrm{C}(^5\mathrm{S}^o)[2s2p^3] + \mathrm{H}[1s]$ channel was detected (Figure 7.4 a)).

V Branching ratios for all observed channels and the four collision energies $E_\mathrm{d} = 0\,\mathrm{meV}$, $8\,\mathrm{meV}$, $70\,\mathrm{meV}$ and $320\,\mathrm{meV}$ are summarized in Table 7.3 and reveal that the $\mathrm{C}(^1\mathrm{D})[2s^2 2p^2] + \mathrm{H}[1s]$ channel is the dominant DR final channel at

low collision energies. The results answer the question about the energy dependence of the branching ratios, as formulated in chapter 2.4.

VI A measurement of the CH^+ ground state dissociation energy was conducted in section 7.3. It is consistent with the currently most precise literature value obtained from spectroscopic information. The results motivate 3D imaging measurements of the metastable $a^3\Pi$ KERs, which might improve the current knowledge about its excitation energy T_e. An upgrade of the NICE detector is required to access the low metastable KERs with 3D imaging and is currently in progress.

An interpretation of these findings is attempted in the following, based on the Potential Energy Curves (PECs) of the CH^+ and CH molecule. Figure 7.8 contains the relevant curves for interpretation. In comparison to Figure 2.4 two states have been added to discuss especially the $E_d = 320\,\text{meV}$ branching ratio results. According to the convention in chapter 2.2.1, most of the shown potential curves are of adiabatic nature, i. e., underlying the Born-Oppenheimer approximation. Ionic potential curves are represented by solid lines. Neutral potential curves with different symmetries are indicated by different lines styles. Since the fast dissociation step in the DR process is better described by a diabatic PEC, two such curves have been included with dashed line styles and marked with an apostrophe in the legend: the $2\ ^2\Pi'$ state (light blue) and the $3\ ^2\Pi'$ state (dark blue).

As discussed in chapter 2.3, all theoretical efforts to describe the CH^+ DR process, to this date, solely considered the diabatic $2\ ^2\Pi'$ state as dissociative curve. The electron inducing the DR process is expected to be either captured directly into this state (*direct* process) or to be first captured in an intermediate bound Rydberg state and, afterwards, to follow the same $2\ ^2\Pi'$ dissociation route (*indirect* process). Since the $2\ ^2\Pi'$ state crosses the CH^+ ground state close to $v = 0$, it supports the direct as well as the normal and *core-excited* Rydberg state indirect processes quite efficiently. Rotational coupling of the $2\ ^2\Pi'$ state to states of other symmetry (Σ, Δ) has been found to be small (chapter 2.3) and, thus, all current theoretical calculations imply that the CH^+ DR process, including the involved Rydberg states, takes place exclusively in the space of PECs with $^2\Pi$ symmetry. Since the $2\ ^2\Pi'$ state converges to the $C(^1D)$ atomic limit (see Figure 7.8), no other final channel is expected from theoretical side. It should be emphasized that this stands in clear contrast to the observations presented above. An interpretation of the observed final atomic states and possible dissociation routes is provided below, and propagates along each final state, individually.

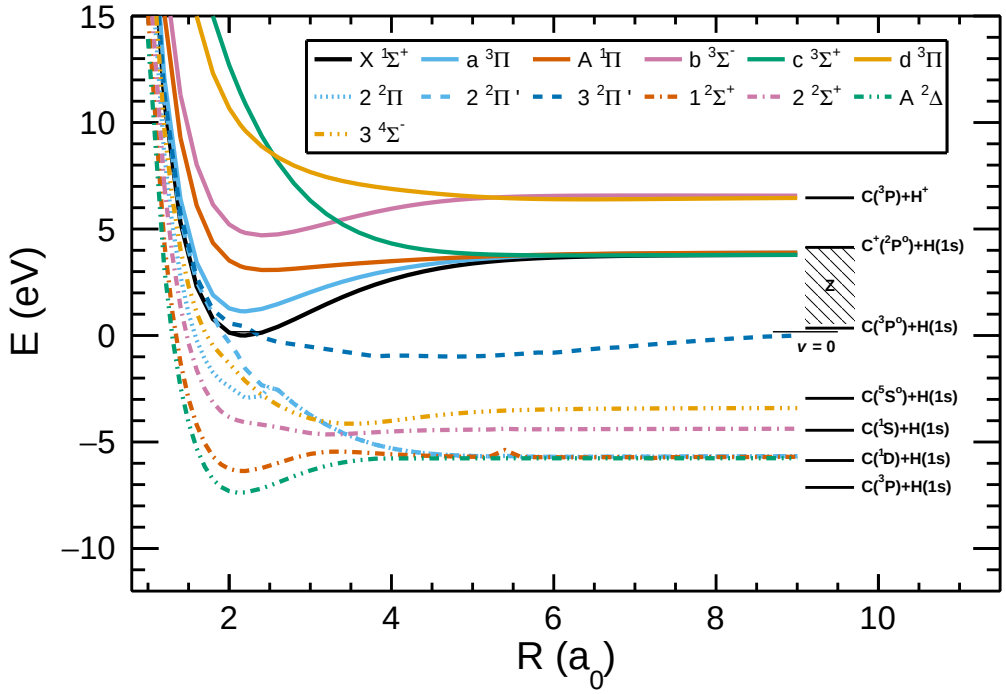

Figure 7.8: CH^+ and CH Potential Energy Curves for interpretation of the DR process. The curves are identical to Figure 2.4. In addition, the adiabatic 3 $^4\Sigma^-$ (Figure A.5) and diabatic 3 $^2\Pi'$ (Figure A.2 a)) states were added for interpretation of the $E_d = 320$ meV case.

$C(^3P^o)[2s^22p3s] + H[1s]$ final channel

The $C(^3P^o)[2s^22p3s]+H[1s]$ final channel has been discovered already in the TSR room-temperature storage ring measurement (Amitay et al. 1996) for energies of $E_d = 1.18$ eV and above. Due to the fact that one electron in this configuration occupies the $3s$ shell, it is located more than 5 eV above the $C(^1D)+H[1s]$ channel (see Figure 7.8). Moreover, its energy exceeds the CH^+ $X^1\Sigma^+$ ground state, thus being a closed channel at electron energies $E_d \leq 280$ meV (see Table 2.4).

As a result of this chapter, the $C(^3P^o)$ channel was found at $E_d = 320$ meV in coexistence with the $C(^1D)$ channel with a low KER of 20(10) meV (result IV). This implies that the threshold for observing this DR final channel is located at $E_P = 300(10)$ meV, which is compatible with the TSR findings.

The dissociation process into the $C(^3P^o)$ channel cannot be driven by the 2 $^2\Pi'$ dissociative curve but requires another diabatic state. Due to the low excess energy in this channel at $E_d = 320$ meV, this state has to be extremely flat. One possible candidate is the 3 $^2\Pi'$ state, which (motivated by the present measurement) has been calculated for the first time very recently in Chakrabarti, Ghosh, and Choudhury 2019. It even crosses the $v = 0$ CH^+ ground state close to its right-hand turning point and might allow for *direct* and *indirect* processes. An interesting feature of this dissociative

curve is the potential minimum around $4\,a_0$. If the electron energy is not sufficient to overcome this minimum in the predissociation process, i. e., for $E_d < 290\,meV$, the intermediate compound molecule might instead undergo a transition to the $2\ ^2\Pi'$ curve or be autoionized again.

The opening of the $C(^3P^o)$ channel results in a factor-of-two increase in the rate coefficient at $E_d \approx 300\,meV$ (Figure 6.1). As discussed before, for energies above $E_d = 1\,eV$, the TSR measurement results show that the $C(^3P^o)$ and other channels with final states in the region 'Z' dominate the CH^+ DR, much exceeding the contribution of the four higher-KER channels ($C(^5S^o)$ to $C(^3P)$). The here presented results support the importance of including the $3\ ^2\Pi'$ state in DR calculations for energies above 290 meV.

$C(^5S^o)[2s2p^3] + H[1s]$ final channel

An interesting observation of this chapter is the detected $C(^5S^o)[2s2p^3] + H[1s]$ channel at $E_d = 320\,meV$ (result IV). Compared to the carbon ground state, in this carbon configuration one electron from the $2s$ shell is lifted into the $2p$ shell. All spins of the four outer electrons are aligned, leading to a total spin of $S = 2$, i. e., a quintet state. Since the single hydrogen electron only carries a spin of $s = 1/2$, the corresponding dissociative molecular CH state must have a spin of $S = 3/2$ or $S = 5/2$, i. e., be a quartet or even sextet state. Any DR process driven by a sextet dissociative state is very unlikely because it would require a double excitation of the CH^+ ground state configuration $1\sigma^2 2\sigma^2 3\sigma^2$ during electron capture. Therefore, a dissociative quartet state is the most likely explanation.

In Figure 7.8 the only adiabatic PEC converging to the $C(^5S^o)$ atomic limit belongs to the $3\ ^4\Sigma^-$ state. No other adiabatic, neither any diabatic state converging to this limit is known from the literature (compare figures in appendix A.2). Thus, in order to explain the existence of the $C(^5S^o)$ atomic limit, a dissociative quartet state has to be found first. Due to the fact that both, the carbon and hydrogen fragment, in this final channel do not carry orbital angular momentum, the dissociative state, additionally, needs to be of Σ symmetry, as also the previously discussed adiabatic $3\ ^4\Sigma^-$ state, and is therefore denoted as $^4\Sigma'$.

A possible dissociation route into the $C(^5S^o)$ channel is given by a single-state dissociation pathway via the proposed $^4\Sigma'$ curve. Because of the high spin of the $^4\Sigma'$ state, only *indirect* DR processes are supported from the singlet ground state ($X\,^1\Sigma^+$) to the $^4\Sigma'$ state. Here, a spin-orbit coupling between a bound doublet and quartet Rydberg state is required to enable the spin transition. Typically, the probability for spin-orbit coupling is low, which might be the cause for the small branching ratio of the $C(^5S^o)$ channel. Nevertheless, the fact that this channel was detected is somewhat surprising. Despite of the low branching ratio, further theoretical studies of this channel seem to be worthwhile from a fundamental point of view.

On the experimental side, there is also a motivation to probe the energy dependence

of the C(^{5}S^o) channel further. In this chapter it could not be observed for $E_\mathrm{d} = 70\,\mathrm{meV}$ or lower energies. One could suspect that for the C(^{5}S^o) and C(^{3}P^o) channels there might be a common dissociation route that distinguishes between the two in the predissociation step. Further measurements just below the threshold of the C(^{3}P^o) state ($E_\mathrm{d} \lesssim 300\,\mathrm{meV}$) could test this hypothesis.

C(^{1}S)[$2s^2 2p^2$] + H[$1s$] final channel

The initial motivation for the presented imaging results in this chapter was the confirmation and characterization of the C(^{1}S)[$2s^2 2p^2$] + H[$1s$] channel. Indeed, a significant branching ratio of this channel has been unambiguously confirmed at $E_\mathrm{d} = 0 - 70\,\mathrm{meV}$ (result I). The corresponding carbon configuration is given by $2s^2 2p^2$ and is similar to the carbon ground state configuration, except for the orbital angular momentum coupling of the valence electrons ($L = 0$).

The angular dependence of its DR cross section revealed that the C(^{1}S) channel is driven by a $p\sigma$ partial wave (result II), which (following Table 2.1) is related to a dissociative state of Σ^+ symmetry. No diabatic state of this symmetry is known in literature. However, the adiabatic 2 $^2\Sigma^+$ state in Figure 7.8 converges to the C(^{1}S) limit. It is reasonable to assume that this 2 $^2\Sigma^+$ state belongs to a series of $^2\Sigma^+$ states building a diabatic dissociation pathway of same symmetry. This postulated dissociative state is further on referred to as $^2\Sigma^{+\prime}$.

One might consider that the $^2\Sigma^{+\prime}$ state is accessed by an initial capture into the well known 2 $^2\Pi'$ diabatic state. Since the 2 $^2\Pi'$ state crosses the adiabatic 2 $^2\Sigma^+$ state at $3.4\,a_0$, a transition to the diabatic $^2\Sigma^{+\prime}$ state via rotational coupling could occur. Finally, it could converge to the C(^{1}S) limit. However, as discussed in chapter 2.3, the rotational coupling probability has been calculated theoretically and cannot explain the observed branching ratio of the C(^{1}S) channel. Furthermore, the observed $p\sigma$ partial wave for this channel (result II) *excludes* an initial capture into the 2 $^2\Pi'$ state.

A much more likely explanation is given by an initial capture into the $^2\Sigma^{+\prime}$ state, either by a *direct* or through an *indirect* DR process. A manifold of $^2\Sigma^+$ Rydberg states converging to the CH^+ ground state ($X^1\Sigma^+$) is available (compare Figure A.2 b)), which could drive the indirect process. In order to compete in the capture process with the 2 $^2\Pi'$ curve, the $^2\Sigma^{+\prime}$ PEC must be located close to the 2 $^2\Pi'$ one around the CH^+ ground state. In *indirect* processes even a few meV might distinguish between the resonant capture into Rydberg states, whose symmetry is either $^2\Pi$ or $^2\Sigma^+$. This argument would explain the strong energy sensitivity of the C(^{1}S) state branching ratio (result III).

Even earlier literature contains a hint for a diabatic $^2\Sigma^{+\prime}$ state. Figure 7.9 a) is extracted from the calculations of Chakrabarti, Ghosh, and Choudhury 2019 and summarizes the evolution of effective principal quantum numbers ν, which can be calculated from the quantum defects (see chapter 2.1.3), with internuclear distance for the adiabatic $^2\Sigma^+$ states in Figure A.2 b). In the range $2 - 3\,a_0$ the ν values for most states

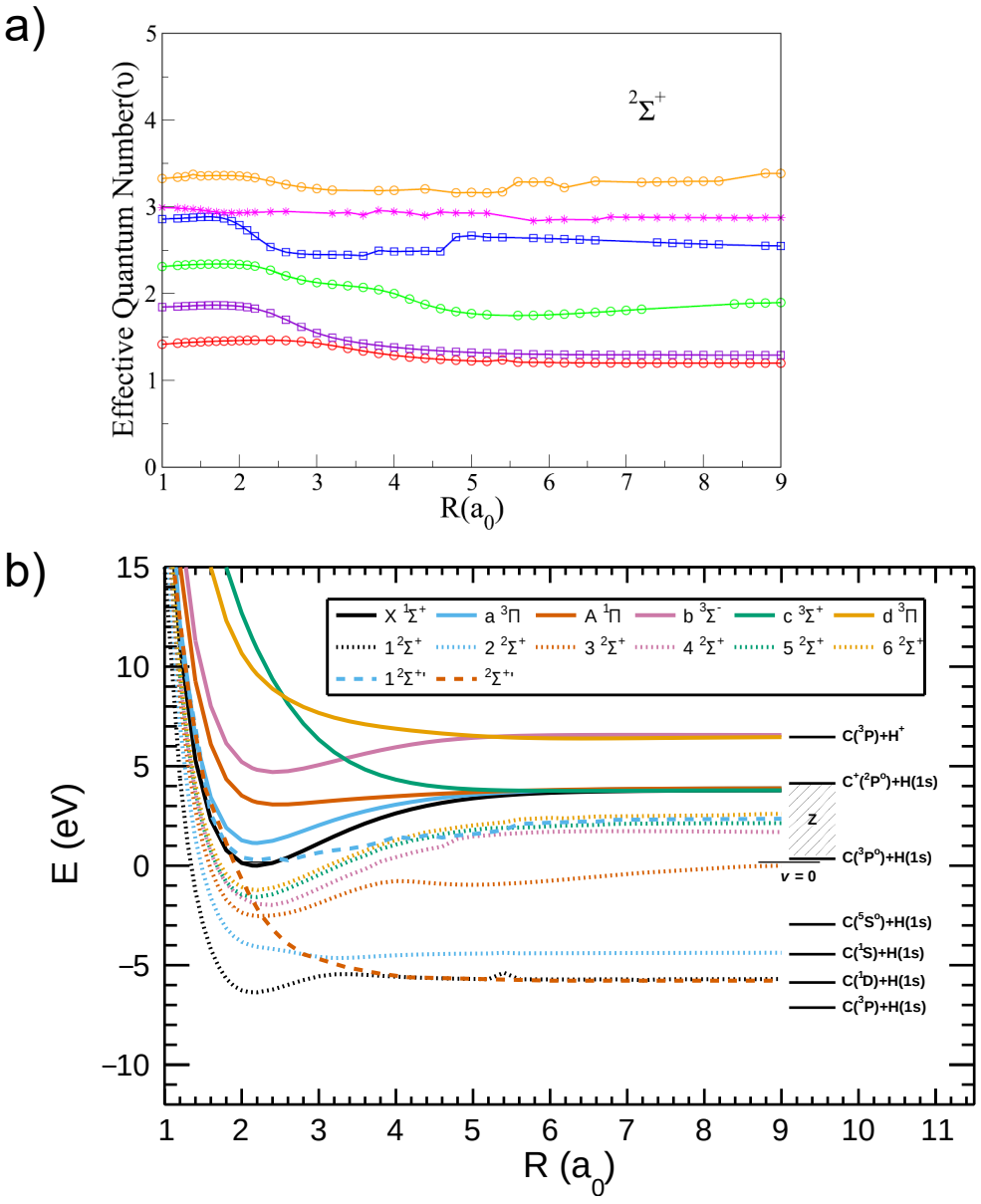

Figure 7.9: Possible interpretation of DR results with a new dissociative Σ state. a): Effective quantum numbers of calculated adiabatic $^2\Sigma^+$ states, extracted from Chakrabarti, Ghosh, and Choudhury 2019. From bottom to top the lines correspond to the dotted CH PECs in b) in a similar order. The region $2-3\,a_0$ indicates non-adiabatic effects. b): CH^+ PECs and $^2\Sigma^+$ CH PECs. The Figure is similar to Figure A.2 b). A diabatic $^2\Sigma^{+\prime}$ curve (orange dashed line) has been constructed manually and might qualitatively explain the findings of this chapter (see text).

undergo a transition from the hitherto flat curve towards the ν value of the next lower state. These changes in the quantum defect indicate non-adiabatic effects and are another argument for the existence of the proposed $^2\Sigma^{+\prime}$ state.

Figure 7.9 b) is used to qualitatively visualize a possible PEC for the proposed $^2\Sigma^{+\prime}$ state, together with the adiabatic $^2\Sigma^+$ states. As discussed above, it is expected to cross the CH^+ ground state close to its $v = 0$ level (similar to the 2 $^2\Pi'$ state). In the range of $2 - 3\,a_0$, where the diabatic effects have been observed in subfigure a), it crosses most adiabatic states. At $3.2\,a_0$ an avoided crossing between the adiabatic $1^2\Sigma^+$ and $2^2\Sigma^+$ state occurs. Here, the diabatic curve can, in principle follow both pathways, resulting in a probability p_S to end up in the C(^{1}S) and $p_D = 1 - p_S$ for converging to the C(^{1}D) atomic limit. In subfigure b) the convergence limit has been chosen for visualization.

C(^{1}D)[$2s^2 2p^2$] + H[$1s$] final channel

The only one of the four observed final channels in this chapter that can be explained by the 2 $^2\Pi'$ dissociative PEC used for DR calculations so far is the C(^{1}D)[$2s^2 2p^2$] + H[$1s$] channel. Here, the carbon atom possesses a similar electron configuration to the C(^{1}S) state but differs in the total angular momentum ($L = 2$). For already more than 30 years the 2 $^2\Pi'$ diabatic state serves as main dissociation route converging to the C(^{1}D) channel in DR calculations. Since the 2 $^2\Pi'$ state crosses the CH^+ ground state close to $v = 0$, it supports the *direct* as well as normal and core-excited Rydberg state *indirect* process quite efficiently.

The results in this work allow cast doubt about on the exclusive importance of the 2 $^2\Pi'$ state for the C(^{1}D) final state. If it was the dominant dissociation route, one should expect the DR process to be dominated by a $p\pi$ partial wave. However, the experimentally observed angular cross section dependence at $E_d = 8\,meV$ is close to isotropic (result II). For only a single contributing dissociation pathway this would indicate a $s\sigma$ partial wave and would then require a Σ^+ dissociative state, similar to the C(^{1}S) channel (Table 2.1). Assuming the C(^{1}D) channel to be exclusively driven by the same $^2\Sigma^{+\prime}$ state as discussed for the C(^{1}S) channel (Figure 7.9) would lead to a constant branching ratio between C(^{1}S) and C(^{1}D) because the final state would be only determined by the probabilities p_D and p_S discussed above. This is a contradiction to the energy dependence of the C(^{1}S) branching ratio (result III).

The most likely explanation for resolving this contradiction is to assume that the C(^{1}D) channel is driven by both, the 2 $^2\Pi'$ and the $^2\Sigma^{+\prime}$ dissociative state. In this case, the varying branching ratio could be explained as in the previous C(^{1}S) discussion. Furthermore, with a similar contribution of both states, a sum of $p\pi$ and $p\sigma$ partial waves is expected with angular cross section dependencies of $\sigma(\vartheta) \sim \sin^2\vartheta$ and $\sigma(\vartheta) \sim \cos^2\vartheta$, respectively. The sum of the two partial waves can, in fact, result in a total angular dependence that is approximately isotropic, as observed in the experiment. Thus, in contrast to the currently used theory, the here presented results indicate a similar contribution of the 2 $^2\Pi'$ and $^2\Sigma^{+\prime}$ dissociative states in the population of the

C(^{1}D) final channel.

Conclusion

As a result of the previous discussion, it turns out that the current understanding of the CH^+ DR process is significantly limited by the knowledge about participating dissociative states. Aside of the impossibility to describe the C(^{1}S) final channel with currently known states, even the angular data for dissociation into the most dominant final channel C(^{1}D) revealed discrepancies that call for a search of new dissociative states.

It is instructive to review once more the rate coefficient results in Figure 6.1, which have been compared to current DR theory in Figure 6.19. The most prominent difference in this comparison was the high rate coefficient at $E_\mathrm{d} = 0\,\mathrm{eV}$ measured in this work. Especially here, the contribution of the C(^{1}S) channel is found to be the highest in the imaging data. The proposed $^2\Sigma^{+\prime}$ state seems to be driving this channel and is currently not included in the theory. Therefore, 30% of the DR signal, corresponding to the C(^{1}S) branching ratio, cannot be explained by the known 2 $^2\Pi'$ state but might be driven by the dissociative $^2\Sigma^{+\prime}$ state. Furthermore, $\approx 50\%$ of the C(^{1}D) signal seem to be caused by the $^2\Sigma^{+\prime}$ state as well, such that about 65% of the total DR signal can be attributed to the $^2\Sigma^{+\prime}$ state. Therefore, the strongly underestimated theory cross section at low energies could largely arise from the missing inclusion of such a dissociative Σ state.

Putting together the observations of this chapter and previous literature on the CH^+ DR leads to five arguments for proposing the existence of a yet undiscovered dissociative Σ state: the existence of the C(^{1}S) channel, its energy-sensitive branching ratio and anisotropic angular distribution, a negligible rotational coupling of the 2 $^2\Pi'$ state with the $^2\Sigma^+$ state, and the non-adiabatic effects in the $^2\Sigma^+$ quantum defects. As a conclusion, the recommendation for further theoretical work is to search for diabatic states of $^2\Sigma^+$ symmetry and to include these states in future DR MQDT calculations. This strategy might help to close the gap between current experimental and theoretical results on the CH^+ DR process.

Chapter 8

Summary and outlook

In this work the Dissociative Recombination (DR) process of vibrationally and rotationally cold CH^+ ions was studied experimentally with the electron cooler of the CSR facility. The main results were split into two parts: the determination of high-resolution absolute merged-beams and plasma rate coefficients as well as the characterization of DR final states and dissociation dynamics via 3D fragment imaging.

In the course of the experimental work and data analysis a few technical aspects in the description of the CSR electron cooler and collision experiments were observed. Since the electron beam experiences multiple acceleration and deceleration processes, its longitudinal temperature varies over the trajectory. A formalism has been developed to quantify the effect and include electronic noise in the acceleration step. It has been used for simulating collision energy distributions for the CH^+ beamtime and can be applied to any other electron-ion collision experiment. The resulting distributions revealed that electronic noise is crucial for the experimental energy resolution. Noise filters were developed to suppress this effect and already proved to result in narrower rate coefficient features and increase electron-cooled ion beam lifetimes in an OH^+ beamtime. For the near future it is planned to verify the simulated distributions by means of scanning a strong and narrow DR cross section resonance.

For previous 3D imaging experiments in high-energy storage rings an approximate formalism for the evaluation of Kinetic Energy Releases (KERs) was used. Detailed analytic calculations on the fragmentation kinematics revealed that the approximation is violated for the low ion energies used at CSR and the next higher order correction (recoil effect) was calculated. The new approach results in an effective-KER distribution, which is recommended to use instead of the 3D distance distribution. This could be underlined by experimental findings in chapter 7.

Electron cooling of CH^+ ions turned out to be more difficult than for previously cooled, lighter ions, an effect that was attributed to dispersive electron cooling. Mean-

while, CSR is typically operated in a dispersion-less (*achromat*) mode to cancel this effect. First cooling tests on other molecules already indicated more stable storage conditions in this new storage ring mode.

In addition to the technical aspects, results on the CH^+ structure and DR collision process could be obtained. As a side-aspect of the metastable $a^3\Pi$ state characterization, an indication for a long-lived substate was found. It could be attributed to the $a^3\Pi(v = 0, J = 0, f)$ component, which decays only via magnetic dipole interaction, as proposed by Hechtfischer et al. 2007. Optimized storage conditions in CSR might provide the unique opportunity to determine an upper limit or even a value for the lifetime of this state in the future.

The main focus was directed to the evaluation of the Merged-Beams Rate Coefficient (MBRC) for the CH^+ DR process. Here, the high resolution of the CSR electron cooler allowed to study collision energies down to the meV regime. An exceptionally high DR rate could be discovered for this system at very low collision energies, which has been neither predicted theoretically, nor accessible for previous experiments.

Following the storage time evolution of the MBRC and comparing it to room-temperature results of Amitay et al. 1996, rotational state effects in the CH^+ DR appeared rather weak, in clear contrast to the HeH^+ system previously studied at the CSR (see chapter 1). Since this is the second system to be ever directly probed for rotational state effects in DR, no conclusion about general behaviors can be drawn yet. Nevertheless, a small increase of the $J = 0$ rate coefficient at collision energies near 0 eV and a stronger rate coefficient reduction at 12 meV were found.

In astrophysical environments like the Interstellar Medium (ISM) the effect of DR processes is described by the plasma rate coefficient. It was obtained for an ensemble close to a 50:50 distribution of $J = 0$ and $J = 1$. Furthermore, an estimate of the pure $J = 0$ plasma rate coefficient, which is most relevant for cold environments in space, was obtained with an uncertainty of $\approx 30\%$ for $T = 10 - 500$ K. The plasma rate results revealed a higher destruction rate of CH^+ by DR in the ISM than previously assumed. A simple model for diffuse clouds was used to determine the impact of these new results onto the ISM CH^+ chemistry. For fully atomic environments it turned out that the previously neglected DR process becomes, in fact, the dominant CH^+ destruction mechanism for temperatures below 45 K. Similarly, the implementation of the new CSR results into astrophysical databases might be a key step for understanding the CH^+ chemistry in other, more complex environments.

This work can be seen as a proof of principle for the feasibility of a full-loop laboratory astrophysics approach at CSR: an astrophysical question motivates a laboratory experiment, which provides new results to be used for an improved astrophysical model.

Regarding the collision dynamics of the CH^+ DR process, the first 3D imaging experiments at CSR presented in this work revealed interesting properties. Effective-KER distributions were studied in order to determine KER values and branching ratios of

final atomic states. Here, the C(^{1}S) final channel, assigned at TSR and later been critically discussed, could be clearly confirmed. The branching ratio was measured to be $\approx 30\%$ at lowest collision energies near 0 eV. Additionally, a new channel (C(^{5}S^o)) was discovered. The existence of both DR final states is not explained by current DR theory. Furthermore, angular fragment distributions were measured, yielding the angular dependencies of the DR cross section for the various final-state channels. Here, even for the theoretically predicted C(^{1}D) channel the angular characteristics revealed discrepancies regarding the symmetry of the driving dissociative CH state.

In sum, the 3D imaging results indicate the existence of a new dissociative $^2\Sigma^+$ state, which would not only explain the existence of the C(^{1}S) channel but also the observed angular dependence of the DR cross section. Final channel branching ratios manifest its relevance at low collision energies. Thus, searching for this dissociative $^2\Sigma^+$ state could be an important step to resolve discrepancies between theoretical and experimental DR cross sections, especially at the above mentioned, strong 0 eV resonance. The experimentally obtained rate coefficient in this work can serve as a benchmark for improved theory calculations in future, which are currently actively been developed.

For further electron-ion collision experiments at CSR several improvements are foreseen that have been partly addressed and motivated in the course of this work. The laser-probing of rotational states has proven to be a powerful tool for J-specific rate coefficient analyses. Even for ions with strong inelastic collisions, where calculation of rotational populations requires sophisticated theory, independent results can be obtained experimentally. In this work, however, the statistical quality of the laser results calls for improvement. Thus, an upgrade for the laser system of CSR is planned to increase the laser-ion overlap almost to the length of a full straight section in the storage ring.

A strong restriction in the CH^+ beamtime was given by the instable CSR temperatures, affecting mainly the background collision rate, which complicates experimental conditions. It has been observed that the electron cooler operation partly leads to a temperature increase in CSR. In order to compensate for this, a hardware upgrade is planned, which includes cooling via additional cold heads. This upgrade might even reduce the contribution of the 300 K blackbody radiation field introduced by the room-temperature parts of the electron cooler and lead to rotationally colder ion beam ensembles in CSR.

Despite the successful use of the 3D imaging technique in the course of this work, the range of molecular systems that can be studied has limitations, mainly due to the restricted time resolution of the detector. A NICE detector upgrade by a silicon photomultiplier array was already implemented recently and provided encouraging results for accessing low fragment time differences (Jäger 2021).

Another limitation for the current detection setup is the mass assignment of multi-fragment DR processes. The indirect assignment algorithm is based on the fragment

positions on the detector and loses reliability for a high number of DR fragments. In future, the position-sensitive micro-calorimeter detector MOCCA (Gamer et al. 2016, Novotný et al. 2015) shall be implemented into CSR. It will be additionally capable of measuring fragment masses directly and will be used for DR experiments on polyatomic system, where various possibilities for final atomic and molecular fragments exist.

To this point, the CSR has proven to be a valuable window into astrophysically-relevant molecular processes. Regarding DR, the first two studied systems already revealed that revisiting room-temperature collision studies in cryogenic environment can lead to different results and conclusions. With the above mentioned upgrades, a manifold of new molecular systems will be accessible and CSR experiments might help to solve some of the puzzle related to molecular abundances in space.

Appendix A

Potential energy curves

This appendix includes a collection of Potential Energy Curves (PECs) for the ionic CH^+ and neutral CH system, extracted from Chakrabarti et al. 2017 and Chakrabarti, Ghosh, and Choudhury 2019. The procedure for obtaining the curves and additional information in the following plots is given in chapter 2.2.1. The important PECs for considerations in this work are condensed in Figure 2.4.

A.1 CH^+ curves

In this section adiabatic CH^+ PECs are presented. Figure A.1 a) is a collection of singlet states, while Figure A.1 b) summarizes triplet states. State symmetries (Λ) are indicated by the lines style of the corresponding curves.

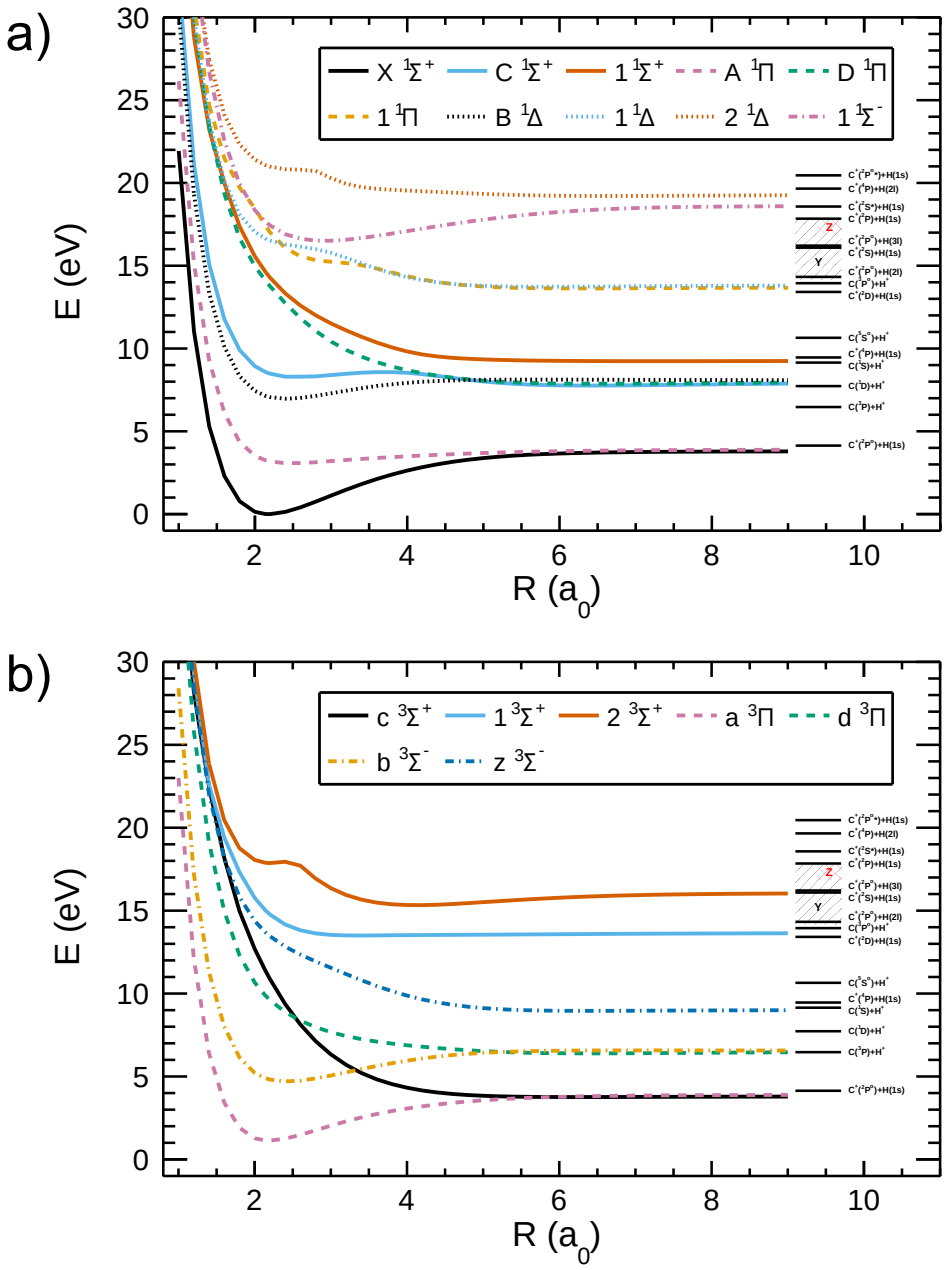

Figure A.1: Adiabatic Potential Energy Curves of the CH^+ ion. The curves are based on the data in Chakrabarti et al. 2017. States of same Λ quantum numbers are drawn with the same line style. Atomic dissociation limits were added as black lines. Here, the regions 'Y' and 'Z' contain a variety of channels corresponding to the $C^+(^2P) + H(n)$ and $C(n) + H^+$ Rydberg series, respectively. a): singlet states, b): triplet states. (For better visibility of final state labels: see electronic version)

A.2 CH curves

In this section adiabatic and diabatic CH PECs are presented. The different figures represent different spin state and symmetry combinations ($^{2S+1}\Lambda$). In each figure the lowest six ionic CH^+ states (see previous section) are drawn as solid lines for comparison. Adiabatic CH states are represented by dotted lines. Diabatic states, where available, are indicated by dashed lines and are important for the interpretation of DR pathways.

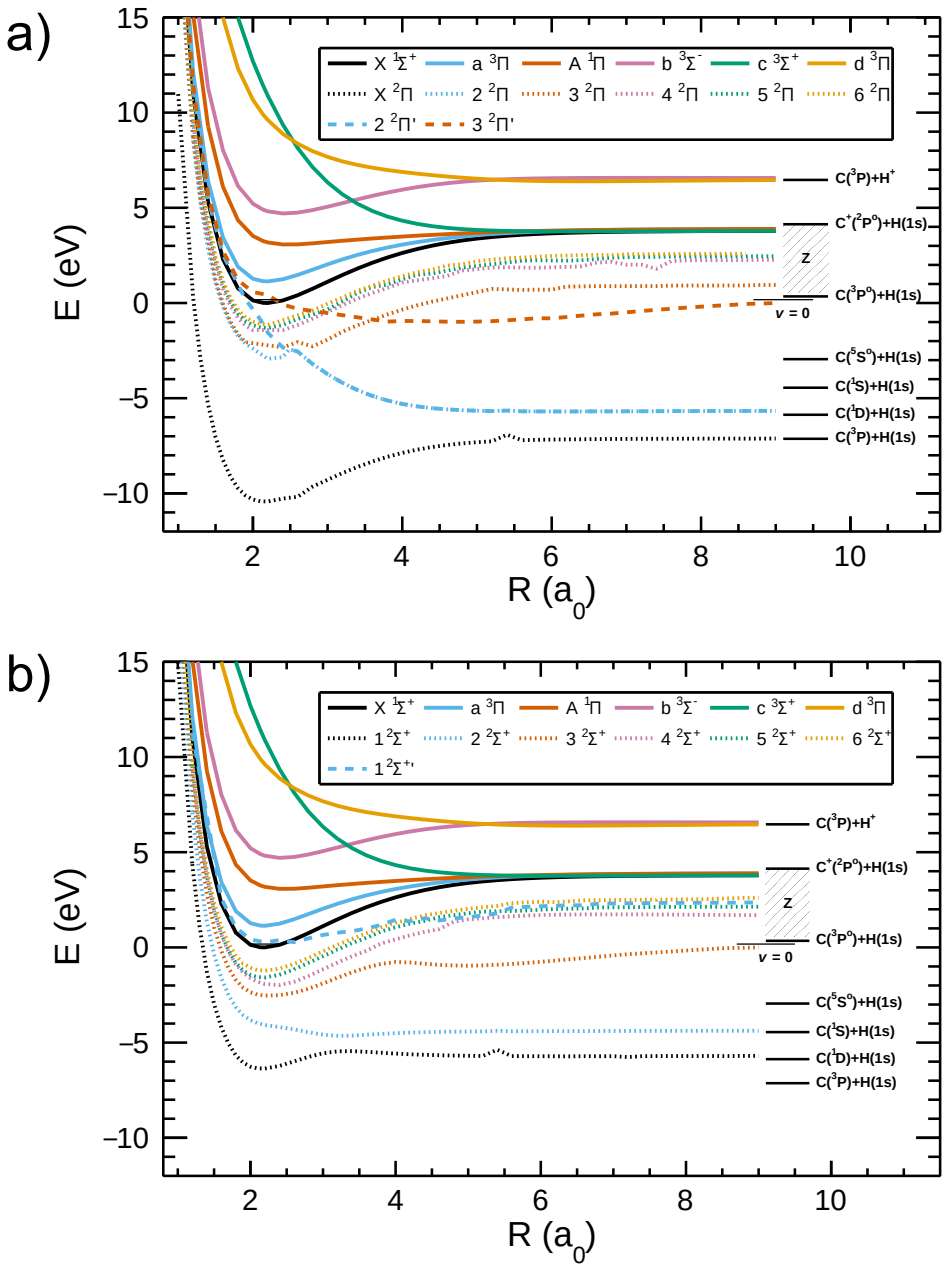

Figure A.2: Potential Energy Curves of the CH molecule - collection I. The curves are based on the data in Chakrabarti, Ghosh, and Choudhury 2019. Adiabatic states are drawn as dotted lines and diabatic states (labeled by apostrophes in the legend) as dashed lines. A few CH^+ PECs from Figure A.1 are added as solid lines. Atomic dissociation limits are indicated as black lines. Here, the region 'Z' contains a variety of channels corresponding to the C(n) + H(1s) Rydberg series. a): $^2\Pi$ states, b): $^2\Sigma^+$ states.

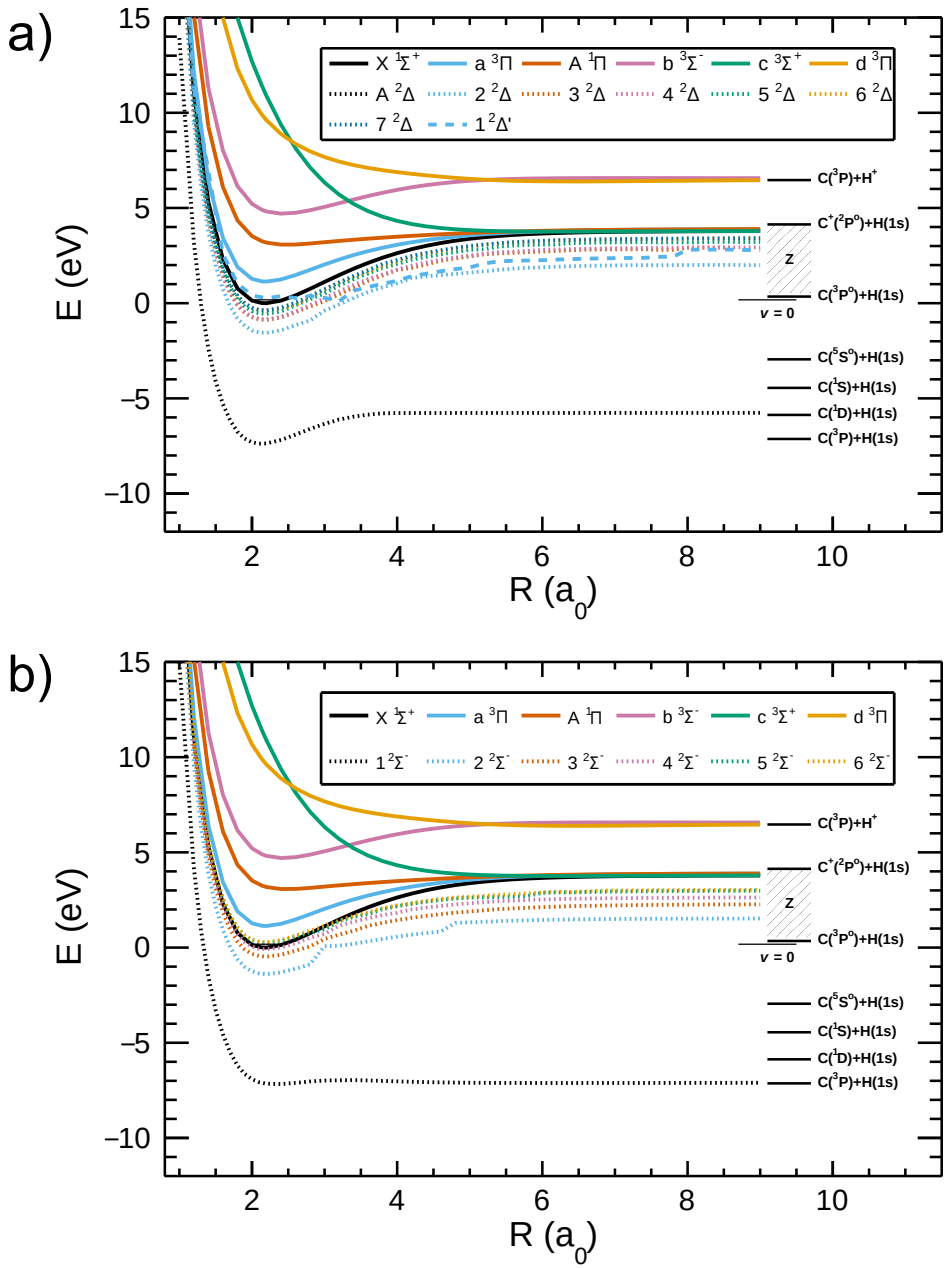

Figure A.3: Potential Energy Curves of the CH molecule - collection II. For details see caption of Figure A.2. a): $^2\Delta$ states, b): $^2\Sigma^-$ states.

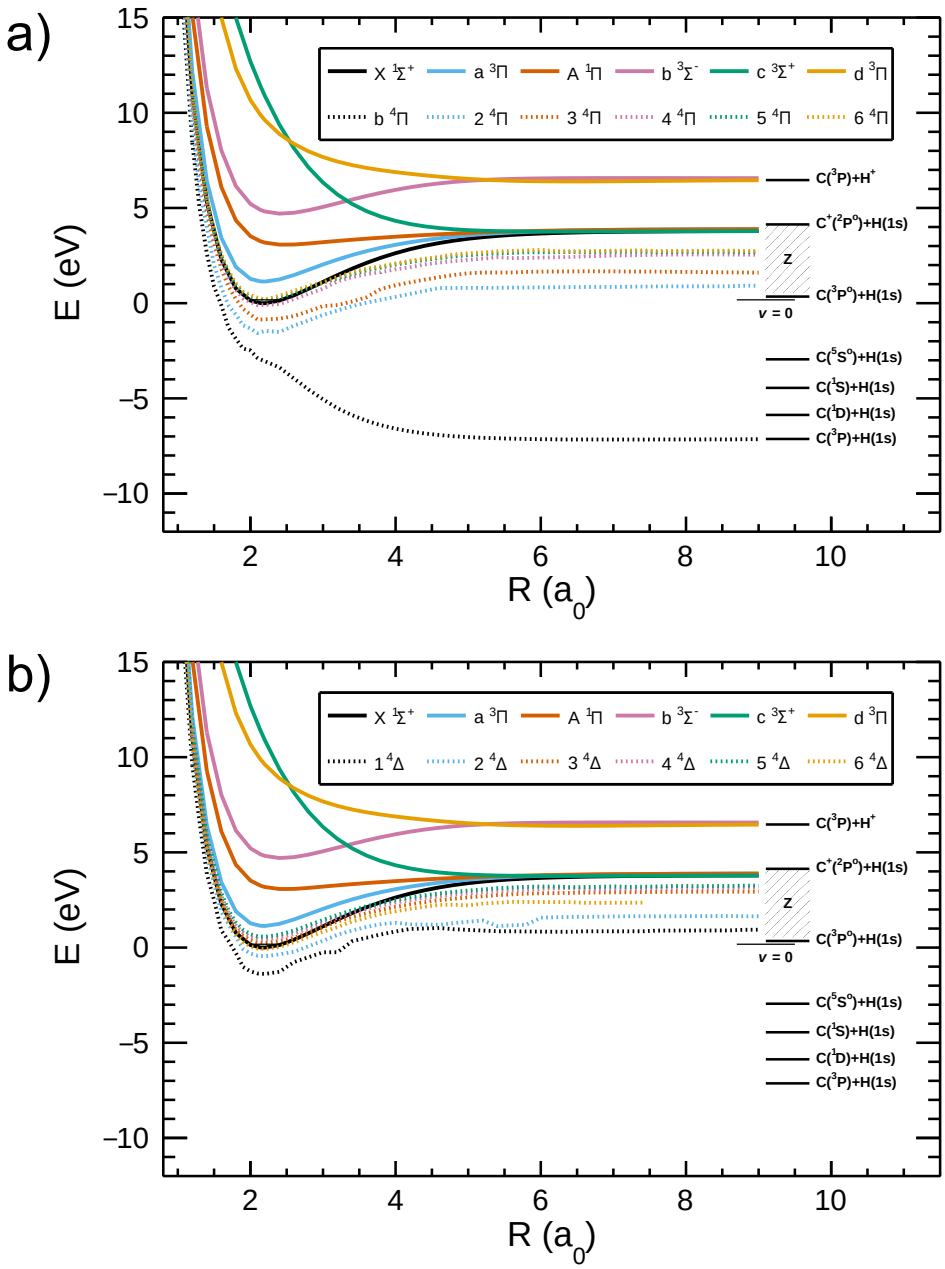

Figure A.4: Potential Energy Curves of the CH molecule - collection III. For details see caption of Figure A.2. a): $^4\Pi$ states, b): $^4\Delta$ states.

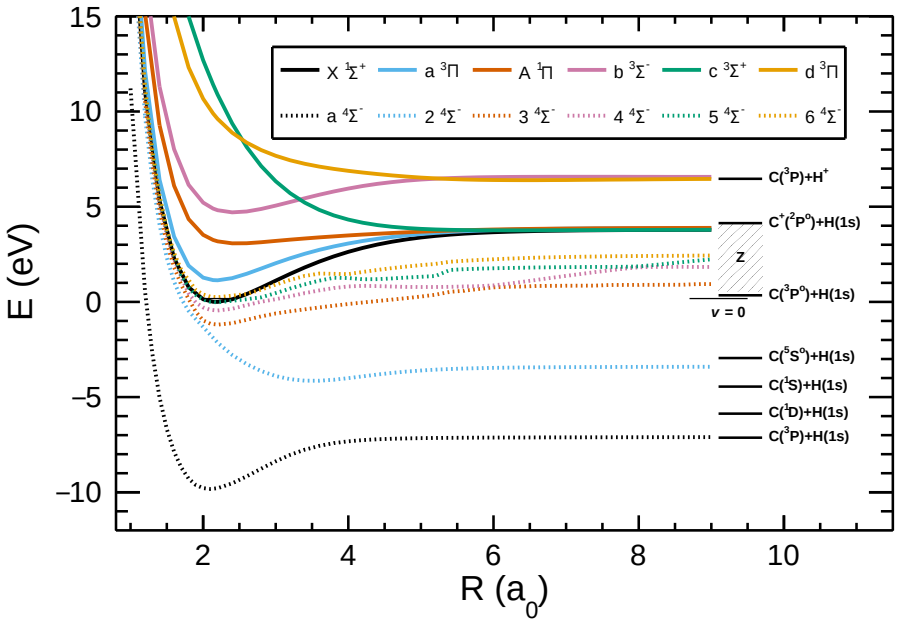

Figure A.5: Potential Energy Curves of the CH molecule - collection IV. For details see caption of Figure A.2. The figure shows $^4\Sigma^-$ states.

Appendix B

Measurement schemes and parameters

This appendix includes detailed information about the measurement conditions used for rate and imaging measurements on the CH^+ DR process in this work. Section B.1 is concerned with the rate measurements, where results are presented in chapter 6. In section B.2 imaging measurement are discussed, which were used for the results in chapter 7.

B.1 Rate coefficient measurements

This section contains information about the conditions in the Merged-Beams Rate Coefficient (MBRC) measurements. These measurements were conducted with the NICE detector (chapter 3.3) and the CSR electron cooler (chapter 3.2). The electron cooler settings are similar to the ones discussed in section 5.2. The whole campaign was split into two parts using different electron densities in the interaction zone, which are referred to a *high-density* and *low-density* campaign.

Regarding the NICE detector, voltages applied to the MCP front (U_{front}) and back (U_{back}) as well as to the phosphor screen (U_{phosphor}) for both CH^+ campaigns are given in Table B.1. Previous experiments indicated that a grounded MCP back and, correspondingly, high negative potential of the front can cause a second, delayed signal for detected particles that was attributed to either ionized gas or sputtered and ionized MCP material, attracted by the negative high-voltage. Therefore, in this work U_{front} was operated at a low negative potential. Additionally, a high-voltage switch was used for grounding U_{front} on a timescale of nanoseconds, which is helpful for turning off the detector in case of laser experiments (section 5.5) and for avoiding high electron-induced count rates at specific detuning energies (section 4.4). The reason for choosing different

Table B.1: NICE detector voltages for high- and low-density campaigns.

Voltages	U_{front} (V)	U_{back} (V)	U_{phosphor} (V)
High-density campaign	-568	1200	11000
Low-density campaign	-668	1050	10900

settings in the two campaigns is the optimization for the COBRA analysis (see chapter 4.5.3), which was followed between the high-density and low-density campaigns.

The timing and steps of the general rate measurement scheme (chapter 4.4) were adapted to the CH^+ conditions. As Figure 5.5 indicates, $\approx 20\,\text{s}$ are needed to reach a stable size of the ion beam. Considering also the metastable state decay time (Figure 5.14), the initial cooling scheme was followed for a duration of 21 s. In the subsequent measurement scheme, a timing of 100 ms cooling, 25 ms DR measurement and 25 ms residual gas background measurement was chosen with a waiting time between steps of 5 ms.

As the switching of electron current reduced the ion beam lifetime significantly in this beamtime, the residual gas background was obtained with electron beam set to a detuning energy of $E_\text{d} = 4\,\text{eV}$, where a minimum of the DR rate coefficient is expected according to Amitay et al. 1996. Comparing to the results of chapter 6.1, the rate coefficient value at this energy is about an order of magnitude lower than the approximate detection limit in the presented experimental configuration, thus, the electron induced DR signal can be neglected. As a tentative result of section 5.3, residual-gas-collision induced background events are predominantly caused by the process

$$\text{CH}^+ + \text{H}_2 \longrightarrow \text{C} + \text{H}^+ + \text{X} \tag{B.1}$$

For further analysis it is assumed that the corresponding background cross section, especially at high collision energies of 280 keV, does not depend on the CH^+ rotational state and, thus, is storage time independent.

The measurement parameters for $n_{\text{e,int,high}} = 6.6 \times 10^5\,\text{cm}^{-3}$ (high density) and $n_{\text{e,int,low}} = 3.4 \times 10^5\,\text{cm}^{-3}$ (low density) are comprehensively summarized in Table B.2 and Table B.3, respectively. While parameters like the ion mass m_{ion}, ion energy E_{ion}, cooling energy E_{cool} and expansion α_{int} were constant within both campaigns, the effective cathode radius r_{cath}, electron current I_e and cooling voltage U_{cool} can slightly vary from run to run and were measured several times over the beamtime.

From the given parameters, all information necessary for the analysis is calculated for each run. First, the contact potential can be calculated by reordering equation 3.4 for cooling conditions:

$$(W_{\text{int}} - W_{\text{cath}}) = eU_{\text{cool}} - e|U_{\text{sc}}| - E_{\text{cool}} \tag{B.2}$$

where $e|U_{\text{sc}}|$ is given by equation 3.5 with $r_{\text{beam}} = r_{\text{cath}}\sqrt{\alpha_{\text{int}}}$. Tuning the electron beam energy is reached by changing the drift-tube voltage U_{int}. For a given value, the lab

Table B.2: Measurement parameters for the high-electron-density campaign ($n_{\mathrm{e,int,high}} = 6.6 \times 10^5\,\mathrm{cm}^{-3}$). Parameters without uncertainties are assumed to be known accurate enough such that their uncertainty does not enter the analysis.

m_{ion}(u)	f_{rev}(Hz)	E_{ion}(keV)	E_{cool}(eV)	r_{cath}(mm)	I_{e}(μA)	U_{cool}(V)	α_{int}
13.00727	57986.5	279.55(80)	11.790(34)	1.135(50)	18.5(1)	14.87	20.000(12)

Table B.3: Measurement parameters for the low-electron-density campaign ($n_{\mathrm{e,int,low}} = 3.4 \times 10^5\,\mathrm{cm}^{-3}$). Parameters without uncertainties are assumed to be known accurate enough such that their uncertainty does not enter the analysis.

m_{ion}(u)	f_{rev}(Hz)	E_{ion}(keV)	E_{cool}(eV)	r_{cath}(mm)	I_{e}(μA)	U_{cool}(V)	α_{int}
13.00727	57973.75	279.43(80)	11.785(34)	1.088(50)	8.3(1)	14.58	20.000(12)

energy can be calculated with equations 3.4, 3.5 and 3.6 in an iterative way. Once E_{lab} is obtained, the detuning energy E_{d}, corresponding to U_{int}, is evaluated with equation 3.13.

Tables B.4 and B.5 provide the detuning energy and storage time intervals measured for several sets of runs for the high- and low-density campaign, respectively. In the choice of intervals it was intended to cover the full range of detuning energies between 0 eV and 1.3 eV at storage times of $21 - 95$ s with certain overlaps for neighboring intervals.

Especially for high detuning energies ($E_{\mathrm{d}} > 40$ meV), measurements were challenging due to orders of magnitude lower count rates compared to the cooling step. For the low-density data sets a separate technique was used to increase statistics. A higher number of ions was injected to still achieve reasonable count rates in the measurement steps. In the cooling step the corresponding signal would saturate the NICE detector with count rates beyond 10 kHz. Therefore, the detector was switched off always in

Table B.4: Measurement sets for high electron density ($n_{\mathrm{e,int,high}} = 6.6 \times 10^5\,\mathrm{cm}^{-3}$).

Run set	Detuning energies	Storage time intervals
1	$0 - 0.6$ eV	$21 - 95$ s
2	$0 - 0.6$ eV	$44 - 95$ s
3	$0 - 3$ eV	$21 - 95$ s
4	$0.2 - 2$ eV	$21 - 95$ s
5	$0.2 - 2$ eV	$44 - 95$ s
6	$1 - 2$ eV	$21 - 95$ s

Table B.5: Measurement sets for low electron density ($n_{\mathrm{e,int,low}} = 3.4 \times 10^5\,\mathrm{cm}^{-3}$).

Run set	Detuning energies	Storage time intervals
1	$0 - 0.04\,\mathrm{eV}$	$21 - 50\,\mathrm{s}$
2	$0 - 0.04\,\mathrm{eV}$	$40 - 80\,\mathrm{s}$
3	$0 - 0.04\,\mathrm{eV}$	$70 - 100\,\mathrm{s}$
4	$0.007 - 0.07\,\mathrm{eV}$	$21 - 50\,\mathrm{s}$
5	$0.007 - 0.07\,\mathrm{eV}$	$40 - 80\,\mathrm{s}$
6	$0.007 - 0.07\,\mathrm{eV}$	$70 - 100\,\mathrm{s}$
7	$0.03 - 1.3\,\mathrm{eV}$	$21 - 50\,\mathrm{s}$
8	$0.03 - 1.3\,\mathrm{eV}$	$40 - 83\,\mathrm{s}$
9	$0.03 - 1.3\,\mathrm{eV}$	$60 - 104\,\mathrm{s}$

the cooling step and switched on for the measurement and reference step again. The detector switching occurred between the steps on a microsecond time scale and did not affect the measurement itself. Moreover, for measurements at later storage times, the detector was switched off before the listed time intervals in both campaigns to handle a higher ion number at injection.

Table B.6: Measurement runs for imaging data. The cycle timing describes the duration of the cooling, measurement and reference step. The saturation scaling factor C_{sat} and signal to background ratio R_{sb} give information about the measurement conditions (see text).

Run number	Detuning energies	Storage time intervals	Cycle timing (ms)	C_{sat}	R_{sb}
326	0 meV	0 − 110 s	100 + 0 + 25	0.384	28.9
366	8 meV	21 − 50 s	100 + 50 + 50	1.22	2.73
367	70 meV/320 meV	21 − 50 s	100 + 50 + 50	2.12/2.10	0.559/0.234

B.2 Imaging measurements

This section is concerned with the measurement scheme and parameters used for the CH^+ DR imaging measurements, where results are presented in chapter 7. Furthermore, information about subtraction of residual gas background is given.

All imaging measurements were conducted with similar conditions and parameters to the high-density rate measurements (see appendix B.1). In contrast to those, here, only one to two fixed detuning energies per run were addressed in order to account for the relatively higher statistics needed for imaging analyses. As the goal of imaging measurements is to characterize the contribution of different DR final channels, detuning energies were chosen on the maximum of resonances in the rate coefficient spectrum, which is presented in chapter 6.1.

A summary of the different imaging runs is given in Table B.6. For run 326 no measurement step was included and the data in the cooling step ($E_{\mathrm{d}} = 0\,\mathrm{eV}$) is analyzed. All other runs made use of the detector switching technique in the cooling step (see section B.1) such that a higher number of ions could be stored for the sake of increased measurement statistics.

In order to characterize measurement conditions and for further analysis, two more parameters were added to Table B.6. The saturation scaling factor C_{sat} has already been defined in section 5.4 to account for differences in acquisition times between the measurement and reference step and for a less efficient camera detection in the measurement step (see equation 5.26). For run 326 the scaling factor is much higher than the measurement time ratio (0.25), indicating a high electron induced count rate. In run 366 it is closer to the time ratio (1.0), while for the high energies in run 367 the deviation from the time ratio (2.0) is only about 5%. In total, the trend of C_{sat} follows the decreasing DR cross section for higher energies (see Figure 2.7).

Evaluation of imaging data is done on the basis of counting detector events in the electron on (N_{on}) and off (N_{off}) steps and binning the events into distance, angular and effective-KER distributions (see chapter 4.4.2). Generated histograms are background subtracted by applying

$$S_i = C_{\mathrm{sat}} N_{\mathrm{on},i} - N_{\mathrm{off},i} \tag{B.3}$$

for each bin i to obtain a signal histogram S_i. Afterwards, the data can be modeled by any expected distribution.

For further comparison of runs, the signal to background ratio can be defined as

$$R_{\mathrm{sb}} = \frac{\sum_i S_i}{\sum_i N_{\mathrm{off},i}} \tag{B.4}$$

It is listed for the different runs in Table B.6. While run 326 is almost background free, background subtraction becomes important for run 366. In run 367 the residual gas induced counts even dominate the electron induced signal such that the statistical quality of these data is significantly worse than for the other two runs. The previously explained trend for C_{sat} matches the observations for R_{sb}, as electron induced signal rapidly decays with increasing detuning energies.

With the previous considerations the imaging analysis is straightforward and the results are presented in chapter 7.1. Further treatment of the data, especially the introduction of and reasoning for data cuts, will be discussed in chapter 7.2.

Appendix C

Analysis steps

This appendix includes analysis steps that were applied over the course of this work. Section C.1 is dedicated to the analysis of the absolute CH^+ DR Merged-Beams Rate Coefficients (MBRCs) shown in chapter 6. Section C.2 presents an intermediate analysis step used in chapter 7.5.1, where DR final state branching ratios are corrected for the missing angular detection range and further information from 2D imaging results is incorporated.

C.1 Rate coefficient analysis

This section intends to explain relevant analysis steps for extracting the CH^+ Merged-Beams Rate Coefficient (MBRC) from detector rates, where a general procedure was already presented in chapter 4.4.1 and the same variable definitions are used here. A first step towards the absolute MBRC is the relative rate coefficient (identical to equation 4.71):

$$\alpha_{\mathrm{mb,rel}}(E_\mathrm{d}, t) = \frac{P_i}{\eta(E_\mathrm{d}) n_\mathrm{e}(E_\mathrm{d}) l_\mathrm{e} / C_0} \frac{R_\mathrm{meas}(E_\mathrm{d}, t) - R_\mathrm{ref}(t)}{R_\mathrm{ref}(t) - R_\mathrm{dark}} \tag{C.1}$$

Its connection to the absolute rate coefficient is given by the determination of the ion current. Since the number of ions during measurements in CSR cannot always be probed, relative rates are calculated first for each run and afterwards scaled to a single absolute ion number measurement via

$$\alpha_\mathrm{mb}(E_\mathrm{d}, t) = \frac{R_\mathrm{meas}(E_\mathrm{d}, t) - R_\mathrm{ref}(t)}{\eta(E_\mathrm{d}) l_\mathrm{e} / C_0 N_\mathrm{ion} n_\mathrm{e}(E_\mathrm{d})} \tag{C.2}$$

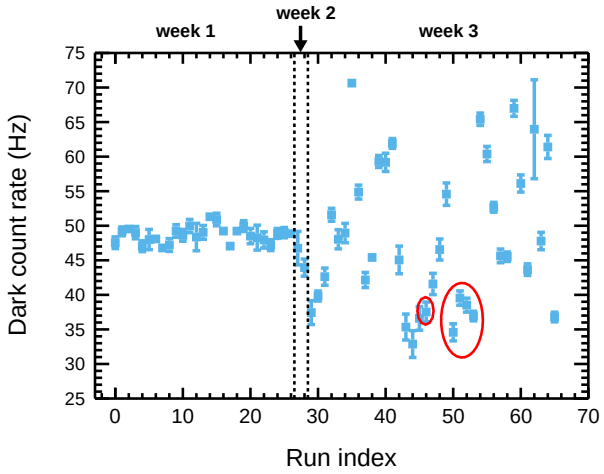

Figure C.1: Dark count rate measurements for all DR runs. The vertical, dotted lines symbolized the borders between the three measurement weeks. The highlighted points in week 3 were measured with an additional ion beam aperture before the storage ring.

While the values for the detection efficiency $\eta(E_\mathrm{d})$ (chapter 5.4) and electron density in the interaction zone $n_\mathrm{e}(E_\mathrm{d})$ (equations 3.4-3.6) are determined independently, the other quantities are obtained from rate measurements (see chapter 4.4.1 and section B.1). In the next subsections a special emphasis is put on the determination of the dark count rate R_dark and pressure proxies P_i as well as on the absolute scaling of relative rate coefficients.

C.1.1 Dark count rate

One property of the NICE detector is its *dark count rate*, a continuous rate, homogeneously distributed among the MCP aperture (see chapter 5.3). It typically amounts to $\approx 50\,\mathrm{Hz}$ and can slightly vary due to temperature or voltage changes. Thus, the dark count rate is measured always at the end of an ion beam injection cycle after the ions were removed from the storage ring, as explained in chapter 4.4.

In Figure C.1 dark count rates for all runs in the CH^+ beamtime are evaluated. The first beamtime week shows a rather stable rate for all runs and stays slightly below 50 Hz. In week three the dark count rate reaches lower minimum values, which can be explained by the slightly lower detector voltage used in the low-density campaign (see Table B.1). However, especially in the third week, the values are also fluctuating by a factor of two. Further analysis of the dark count rate dependence on other parameters as well as analysis of imaging data, revealed that the measured dark count rate scales with the ion number during the measurement phase. Moreover, a broad, but enhanced signal of spots on the lower half of the detector screen could be observed.

Both effects led to the conclusion that this signal is caused by real ions propagating to detector, even though the electrostatic chopper (chapter 3.1) should dump the beam already in the transfer beamline. Obviously, its functionality is limited and a low amount

of ions leaks through the chopper. In the ion-beam-off phase the first 6° deflector in CSR is grounded and allows the current leaking through the chopper to advance to the detector. Due to the non-negligible chopper deflection, the resulting signal is focused far off the detector center. During the measurement phase, the 6° deflector is on voltage and leakage current cannot be stored, as proven in a simulation by Dr. Manfred Grieser. Hence, the measured dark count rate in Figure C.1 does not reflect the real dark count rate, nor the constant rate offset of the detector.

Fortunately, for five runs in the third measurement week (highlighted with red circles in Figure C.1), additional apertures in the transfer beamline were inserted to limit the ion number. In those runs leakage current cannot pass the transfer line because of its different trajectory compared to the main beam. Consequently, for those runs low dark count rate were measured, which can be used to estimate the dark count rate for other runs in that week. Their average amounts to

$$R_{\mathrm{dark},3} = 37.0(36)\,\mathrm{Hz} \tag{C.3}$$

C.1.2 Pressure normalization

For relative normalization of different DR runs, the count rate measured in the reference step, which is caused by residual gas collisions, is typically used as a proxy for the number of stored ions. Assuming a constant pressure in CSR, the reference rate is only depending on the number of stored ions. On the contrary, for fluctuating pressures a determination of the relative ion number is impossible without measuring the relative pressure between runs. As explained in chapter 5.1 the comparatively high and unstable CSR-chamber temperatures during the beamtime are expected to cause pressure fluctuations. Therefore, a method for obtaining relative pressures (*pressure proxies*) is presented in this section.

Equation 4.71 can be solved for the pressure proxy:

$$P_i = \alpha_{\mathrm{mb,rel}}(E_\mathrm{d}, t)\eta(E_\mathrm{d})\frac{l_\mathrm{e}}{C_0}n_\mathrm{e}(E_\mathrm{d})\frac{R_\mathrm{ref}(t) - R_\mathrm{dark}}{R_\mathrm{meas}(E_\mathrm{d}, t) - R_\mathrm{ref}(t)} \tag{C.4}$$

In a fixed detuning energy and storage time interval, all runs must provide a constant rate coefficient. Therefore, all run-independent quantities can be neglected in the determination of the pressure proxy by summarizing them in a factor
$k = \alpha_{\mathrm{mb,rel}}(E_\mathrm{d}, t)\eta(E_\mathrm{d})\frac{l_\mathrm{e}}{C_0}$ such that

$$p_i(E_\mathrm{d}, t) = \frac{P_i(E_\mathrm{d}, t)}{k} = n_\mathrm{e}(E_\mathrm{d})\frac{R_\mathrm{ref}(t) - R_\mathrm{dark}}{R_\mathrm{meas}(E_\mathrm{d}, t) - R_\mathrm{ref}(t)} \tag{C.5}$$

defines a pressure proxy that can be directly determined for each run. The fact that such a proxy can only be compared within a certain storage time and detuning energy interval is highlighted in the previous equation.

In principle, the simplest approach for pressure normalization is to measure a common energy and time interval for each run. This was facilitated in the high-density data set

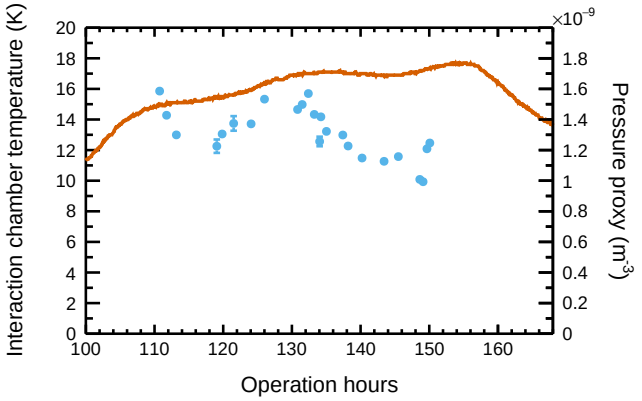

Figure C.2: Pressure proxies for high-density data. The relative pressure proxy development (blue data) is compared to the time evolution of the electron cooler interaction chamber temperature, shown in orange (see also Figure 5.1). The temperature is measured by a PT-1000 sensor, which is not calibrated absolutely at these conditions.

(Table B.4), where all runs included rate measurements in the cooling step ($E_\mathrm{d} = 0\,\mathrm{eV}$) with excellent statistics. A single pressure proxy

$$p_{0,j,\mathrm{high}}(E_\mathrm{d} = 0\,\mathrm{eV}, t = [45\,\mathrm{s}, 55\,\mathrm{s}]) \tag{C.6}$$

is sufficient for the normalization of all runs j. In Figure C.2 the values for $p_{0,j,\mathrm{high}}$ are presented and compared to the temperature development in the electron cooler interaction zone (see sensor 'Vacuum interaction zone' of Figure 5.1). As the used PT-1000 sensor is not calibrated in the given low-temperature range, both quantities should only be interpreted as relative values. Maxima and minima seem to be correlated, which indicates that gas evaporation from the inner chamber walls at high temperatures leads to increased pressures. In case of falling temperature, the gas is adsorbed to the walls again, resulting in decreasing pressure. The slight shift between both evolutions might be explained by heat capacities in the system if the sensor position is not identical with the point of most intense gas evaporation. Despite the qualitative match of pressure proxies and temperature, some jumps between neighboring data points can be discovered. Those jumps indicate the precision limit of the pressure normalization procedure.

Previous considerations indicate that the pressure proxies are a reasonable estimate of the residual gas density in CSR and can be used for pressure normalization. In contrast to the high-density measurements, for the low-density data no common detuning energy and storage time interval was measured. In order to optimize rate statistics, the detector was switched off during the cooling step (section B.1). Still, a normalization of the low-density data can be obtained by using several pressure proxies for different storage time and detuning energy intervals, as long as there are overlaps in both quantities between the measurement sets.

Table C.1: Pressure proxies for low-density data. The run set number of anchoring runs is given in parenthesis. The parameters of listed run sets are identical to Table B.5.

Proxy nr.	Detuning energies (eV)	Storage times (s)	Run set nr.	Anchoring run [set nr.]
1	0-0.002	40-49	1,2	442 [2]
2	0-0.002	70-80	3	442 [2]
3	0.007-0.01	40-49	4,5	442 [2]
4	0.007-0.01	70-80	6	442 [2]
5	0.03-0.07	40-49	7,8	450 [5]
6	0.03-0.07	70-80	9	450 [5]

Table C.1 shows the definition of pressure proxies for the low-density data sets defined earlier in Table B.5. At first, an anchoring run has to be defined that acts as reference for normalization. In this case, run 442 from set 2 was chosen, whose pressure proxy $p_{1,442}$ is evaluated. All runs j in set 1 and 2 can be normalized by the determination of

$$S_j = \frac{p_{1,j}}{p_{1,442}} \tag{C.7}$$

in the listed storage time and detuning energy range for proxy 1, where S_j is the scaling factor for the relative MBRC in run j. Runs k, belonging to other proxies i with anchoring run 442, are normalized by evaluating

$$S_k = \frac{p_{i,k}}{p_{i,442}} \tag{C.8}$$

With this procedure all runs in sets 1-6 can be scaled, including the next anchoring run for sets 7-9 (run 450). In accordance with the previous equations, runs l in those sets are scaled by

$$S_l = S_{450} \frac{p_{i,l}(E_\mathrm{d}, t)}{p_{i,450}(E_\mathrm{d}, t)} \tag{C.9}$$

The explained procedure defines a recursive algorithm for pressure normalization of all runs to the first anchoring run (442), which can be applied also for other beamtimes. While for the high-density data scaling equation 4.71 can be used with

$$\alpha_{\mathrm{mb,rel},j,\mathrm{high}}(E_\mathrm{d}, t) = \frac{p_{0,j,\mathrm{high}}}{\eta(E_\mathrm{d}) n_\mathrm{e}(E_\mathrm{d}) l_\mathrm{e} / C_0} \frac{R_\mathrm{meas}(E_\mathrm{d}, t) - R_\mathrm{ref}(t)}{R_\mathrm{ref}(t) - R_\mathrm{dark}} \tag{C.10}$$

the pressure proxy is replaced by the scaling factors S_j in the more complex low-density normalization, leading to

$$\alpha_{\mathrm{mb,rel},j,\mathrm{low}}(E_\mathrm{d}, t) = \frac{S_j}{\eta(E_\mathrm{d}) n_\mathrm{e}(E_\mathrm{d}) l_\mathrm{e} / C_0} \frac{R_\mathrm{meas}(E_\mathrm{d}, t) - R_\mathrm{ref}(t)}{R_\mathrm{ref}(t) - R_\mathrm{dark}} \tag{C.11}$$

C.1.3 Combining data sets

After pressure normalization relative MBRCs for each run j

$$\alpha_{\mathrm{mb,rel},j}(E_\mathrm{d}, t) \tag{C.12}$$

are available. For the sake of combining the statistics of different runs, their data can be merged. The rate coefficient data are first binned into six storage time intervals (t_m) with bin edges

$$t = \{21\,\mathrm{s}, 25\,\mathrm{s}, 30\,\mathrm{s}, 40\,\mathrm{s}, 60\,\mathrm{s}, 80\,\mathrm{s}, 100\,\mathrm{s}\} \tag{C.13}$$

Furthermore, the data are binned into detuning energies ($E_{\mathrm{d},n}$) such that each bin exactly contains one measured energy. Since the drift-tube voltage U_int was chosen always the same for different runs in a run set but the measurement parameters (I_e, n_e, $W_\mathrm{int} - W_\mathrm{cath}$) are changing slightly, a small shift in detuning energies between different runs is expected. It could be proven, however, that this shift is below the bin size and does not influence the averaging procedure. By labeling the binned relative rate coefficient of a run j as

$$\alpha_{\mathrm{mb,rel},j}(E_{\mathrm{d},n}, t_m) \pm \sigma_j(E_{\mathrm{d},n}, t_m) \tag{C.14}$$

with a statistical uncertainty $\sigma_j(E_{\mathrm{d},n}, t_m)$, arising from the rate measurements, the run-averaged rate coefficient is given by an uncertainty weighted mean value

$$\alpha_{\mathrm{mb,rel}}(E_{\mathrm{d},n}, t_m) = \frac{\sum_j \alpha_{\mathrm{mb,rel},j}(E_{\mathrm{d},n}, t_m)\sigma_j^{-2}(E_{\mathrm{d},n}, t_m)}{\sum_j \sigma_j^{-2}(E_{\mathrm{d},n}, t_m)} \tag{C.15}$$

and its uncertainty is calculated as

$$\sigma(E_{\mathrm{d},n}, t_m) = \sqrt{\frac{1}{\sum_j \sigma_j^{-2}(E_{\mathrm{d},n}, t_m)}} \tag{C.16}$$

The latter two equations are used to create a merged histogram, where the MBRC is plotted against E_d, for each time interval t_m.

C.1.4 Absolute scaling

Absolute scaling of the MBRC requires an experimental determination of the ion current in CSR. In chapter 4.1 a general measurement method with help of the current pickup was already explained and shall be applied here to the CH^+ beamtime. A concern of this work is to list a detailed uncertainty budget for the absolute scaling, which can, qualitatively, be adapted for further beamtimes.

As the ion number is only measured at a single storage time, the absolute MBRC equation 4.69 shall be restructured first for a time-independent scaling. The MBRC in this case is evaluated for $E_\mathrm{d} = 0\,\mathrm{eV}$ and $t = 21 - 40\,\mathrm{s}$ for a single run at high electron density:

$$\alpha_\mathrm{mb}(0\,\mathrm{eV}, t) = \frac{R_\mathrm{meas}(0\,\mathrm{eV}, t) - R_\mathrm{ref}(t)}{\eta(0\,\mathrm{eV}) l_\mathrm{e}/C_0 N_\mathrm{ion}(t) n_\mathrm{e}(0\,\mathrm{eV})} \tag{C.17}$$

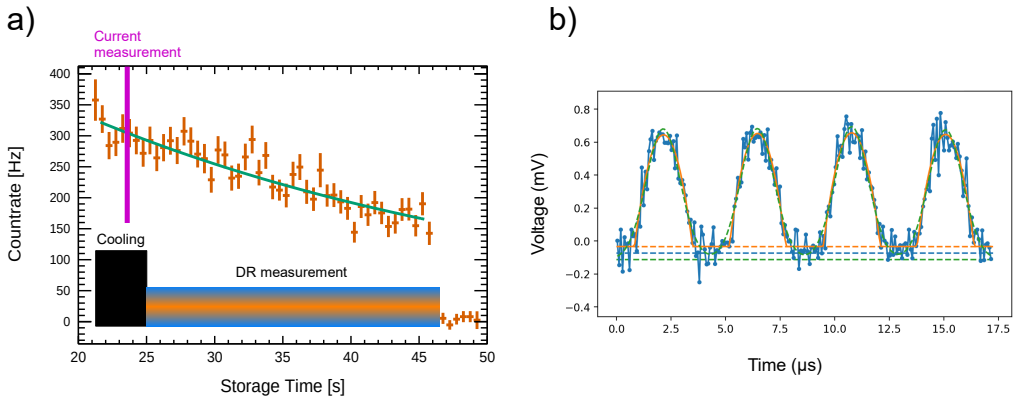

Figure C.3: Absolute rate coefficient scaling measurement. a): Schematic description of the measurement scheme. The ion beam is electron-cooled until 21 s where the DR measurement starts. Here, the residual gas induced count rate $R_{\mathrm{ref}}(t) - R_{\mathrm{dark}}$ (orange data) is acquired and can be extrapolated by an exponential fit (green) towards the current measurement time around 19 s. b): Voltage induced by the $h = 4$ ion bunches in CSR. The signal (blue) is averaged over ≈ 8500 revolutions and fitted by a Gaussian (green) and parabolic (orange) model for determination of its integral (see text). The dashed lines of similar color symbolize the fitted offset, while the blue dashed line represents the mean value of the two models.

For a constant pressure the ion number is proportional to the residual gas collision rate $N_{\mathrm{ion}}(t) = S(R_{\mathrm{ref}}(t) - R_{\mathrm{dark}})$. Thus, the whole storage time dependence can be isolated into a measured rate term by

$$\alpha_{\mathrm{mb}}(0\,\mathrm{eV}, t) = \frac{1}{\eta(0\,\mathrm{eV}) l_{\mathrm{e}}/C_0 S n_{\mathrm{e}}(0\,\mathrm{eV})} \frac{R_{\mathrm{meas}}(0\,\mathrm{eV}, t) - R_{\mathrm{ref}}(t)}{R_{\mathrm{ref}}(t) - R_{\mathrm{dark}}} \tag{C.18}$$

Due to technical restrictions, the calibration of residual gas induced rate and ion number via the scaling factor S could not be done simultaneously to the rate coefficient measurement but was instead done at $t \approx 19\,\mathrm{s}$.

The number of ions was determined on the capacitive current pickup in a time interval of $t = 19.1 - 19.25\,\mathrm{s}$. A precise detection of the induced voltage is only possible for a RF-bunched ion beam, while rate coefficient measurements and electron cooling are typically done with a coasting beam. Hence, the electron beam was injected without the RF voltage and a coasting beam was electron cooled for $t_1 = 19\,\mathrm{s}$. At this time, the RF voltage was ramped up and reached its nominal value at $t_2 = 19.1\,\mathrm{s}$. Between t_2 and $t_3 = 19.25\,\mathrm{s}$ the ion number was measured. Finally, the RF voltage was ramped down until $t_4 = 19.35\,\mathrm{s}$ and the DR rate measurement was initiated with a coasting beam at $t_5 = 21\,\mathrm{s}$. A schematic description of the measurement is presented in Figure C.3 a), together with the residual gas induced collision rate $R_{\mathrm{ref}}(t) - R_{\mathrm{dark}}$.

Figure C.3 b) shows the measured voltage signal of the $h = 4$ ion bunches in CSR. Here, equation 4.1 gives the connection between ion number and the waveform integral.

For evaluation of that integral, two different models were used to fit the data: a Gaussian and a parabolic model. Since the current pickup is a floating device, the baseline is undefined and has to be determined by the fits, leading to a significant model-dependence of the integral value. The waveform evaluation and modeling analysis was done by Dr. Ábel Kálosi, who provided the results for the measured ion number.

Ion number scaling factor

The evaluation of the waveform integral yields

$$\begin{aligned} Q = \int_0^{T_0} U_\mathrm{p}(t)\,\mathrm{d}t = 3.53 \times 10^{-9}\,\mathrm{Vs} \\ \frac{\Delta Q}{Q} = 11.9\% \end{aligned} \tag{C.19}$$

where the relative uncertainty is chosen such that it includes the results of both models, Gaussian and parabolic, and Q is their average. With equation 4.1 and the parameters $z = 1$, $f_\mathrm{rev} = 57.9738\,\mathrm{kHz}$, C_0, C_p and L_0 as given in chapter 4.1, the ion number can be calculated. The amplifier gain of $G = 851$ was measured separately and its uncertainty is estimated to 5% such that

$$\begin{aligned} N_\mathrm{ion,meas} &= 168900 \\ \frac{\Delta N_\mathrm{ion,meas}}{N_\mathrm{ion,meas}} &= 13.9\% \end{aligned} \tag{C.20}$$

Two corrections were applied to this result: First, the bunching quality was inferred from the time structure caused by residual gas collisions with respect to the bunching frequency on the NICE detector. Fitting the resulting bunch structure revealed that $f_\mathrm{b} = 97.3 \pm 2.7\%$ of the ions in the beam are definitely within the bunches and only the remaining fraction could contribute to the baseline in Figure C.3 b), such that the real number of ions in the ring is higher than the measured one by a factor $\frac{1}{f_\mathrm{b}}$. Second, calculations with a Gaussian shaped ion beam, whose size can be inferred from its projection on the detector (see Figure 5.5), and an electron beam with a flat top profile of radius $r_\mathrm{cath}\sqrt{\alpha_\mathrm{int}}$ revealed that the electron beam does not cover the whole ion beam but only a fraction of $f_\mathrm{a} = 97.5 \pm 2.5\%$. The missing fraction does not contribute to a DR signal, which can be compensated by scaling down the measured ion number by f_a. Both corrections together result in a slightly different estimate for the number of ions

$$\begin{aligned} N_\mathrm{ion} &= 169200 \\ \frac{\Delta N_\mathrm{ion}}{N_\mathrm{ion}} &= 14.4\% \end{aligned} \tag{C.21}$$

As a second input parameter for the ion number scaling factor, the residual gas induced rate is determined from Figure C.3 a). The data for $R_\mathrm{ref}(t) - R_\mathrm{dark}$ were fitted by an exponential decay to extrapolate its value to $t = 19.175\,\mathrm{s}$, the center of the ion

current measurement. It corresponds to a value and statistical uncertainty of

$$\begin{aligned} R_{\mathrm{ref}} - R_{\mathrm{dark}} &= 344.8\,\mathrm{Hz} \\ \frac{\Delta(R_{\mathrm{ref}} - R_{\mathrm{dark}})}{R_{\mathrm{ref}} - R_{\mathrm{dark}}} &= 2.6\% \end{aligned} \tag{C.22}$$

leading to a scaling factor of

$$\begin{aligned} S &= 2.037 \times 10^{-3}\,\mathrm{Hz} \\ \frac{\Delta S}{S} &= 14.6\% \end{aligned} \tag{C.23}$$

Detected rates

The rate ratio

$$\rho(t) = \frac{R_{\mathrm{meas}}(0\,\mathrm{eV}, t) - R_{\mathrm{ref}}(t)}{R_{\mathrm{ref}}(t) - R_{\mathrm{dark}}} \tag{C.24}$$

contains all storage time dependent observables and was evaluated in the storage time interval $t = [21\,\mathrm{s}, 40\,\mathrm{s}]$ to obtain the absolute rate coefficient in this time window. It amounts to

$$\begin{aligned} \rho(t) &= 7.012 \\ \frac{\Delta\rho(t)}{\rho(t)} &= 1.7\% \end{aligned} \tag{C.25}$$

Electron density

Equations 3.6, 4.3 and 5.6 enable to calculate the electron density by

$$n_{\mathrm{e}} = \frac{I_{\mathrm{e}}}{e\pi r_{\mathrm{cath}}^2 \alpha_{\mathrm{int}} \sqrt{2E_{\mathrm{cool}}/m_{\mathrm{e}}}} \tag{C.26}$$

While the electron current ($I_{\mathrm{e}} = 18.9(1)\,\mu\mathrm{A}$) was monitored accurately for the absolute calibration run, the effective cathode radius was measured separately to $r_{\mathrm{cath}} = 1.187\,\mathrm{mm}$ with an assumed uncertainty of $0.05\,\mathrm{mm}$. It dominates the electron density uncertainty with

$$\begin{aligned} n_{\mathrm{e}} &= 6.54 \times 10^{5}\,\mathrm{cm}^{-3} \\ \frac{\Delta n_{\mathrm{e}}}{n_{\mathrm{e}}} &= 8.2\% \end{aligned} \tag{C.27}$$

Detection efficiency

A detailed derivation of the NICE detection efficiency as a function of detuning energy ($\eta(E_{\mathrm{d}})$) was already followed in chapter 5.4. Due to the fact, that the value $\eta(0\,\mathrm{eV})$ was measured explicitly, no additional systematic uncertainties from energy interpolation have to be included and

$$\begin{aligned} \eta(0\,\mathrm{eV}) &= 0.7931 \\ \frac{\Delta\eta(0\,\mathrm{eV})}{\eta(0\,\mathrm{eV})} &= 1.1\% \end{aligned} \tag{C.28}$$

Relative cooler length

Ideally, an electron target provides an electron-ion overlap at fixed collision energy over a length l_e, while before and after the interaction region no collisions are possible. For realistic overlap geometries the desired collision energy is reached only after a certain overlap length and the effective cooler length lies below the geometric one. In the work of Saurabh 2019, a method was developed to estimate the full overlap length of electrons and ions, which already starts in the merging region of the electron cooler. For the parameters used in this beamtime, it is estimated to

$$L_{\text{full}} = 1.136(14)\,\text{m} \tag{C.29}$$

from the simulations done by Saurabh 2019.

According to chapter 4.3 the effective cooler length can be derived from the full overlap length and the collision energy distribution in Figure 4.5:

$$l_e = L_{\text{full}} \frac{\max\{f_{\text{mb}}(E, E_d = 0\,\text{eV})\}}{\max\{f^*_{\text{mb}}(E, E_d = 0\,\text{eV})\}} = 0.7263\,\text{m} \tag{C.30}$$

Normalization to the CSR circumference leads to

$$\begin{aligned} \frac{l_e}{C_0} &= 0.02067 \\ \frac{\Delta l_e / C_0}{l_e / C_0} &= 1.5\% \end{aligned} \tag{C.31}$$

Absolute rate coefficient at 0 eV

Inserting all previously derived quantities into equation C.18 yields the absolute rate coefficient at cooling energy for a storage time interval of $21 - 40\,\text{s}$:

$$\begin{aligned} \alpha_{\text{mb}}(0\,\text{eV}, 21 - 40\,\text{s}) &= 1.35 \times 10^{-6}\,\text{cm}^3\text{s}^{-1} \\ \frac{\Delta\alpha_{\text{mb}}(0\,\text{eV}, 21 - 40\,\text{s})}{\alpha_{\text{mb}}(0\,\text{eV}, 21 - 40\,\text{s})} &= 17\% \end{aligned} \tag{C.32}$$

The uncertainty budget for the calculation is listed in Table C.2. The major contribution arises from the model uncertainty in the determination of the integrated ion beam induced voltage. In order to minimize this uncertainty, the signal-to-noise ratio of the measured voltage needs to be improved. The noise is mainly caused by the current pickup cryogenic preamplifier, which is known to be in a worse condition compared to other beamtimes. Because of the limited availability of low-noise cryogenic amplifiers, a lot of effort was put into purchasing and selecting the optimal ones for CSR measurements. The absolute scaling results in this section underline the importance of such improvements. Furthermore, the ion beam signal could be improved, depending on the ion species, by injecting the maximum number of ions and calibrating the DR rates under these conditions. For the CH^+ beamtime, however, the ion source did not provide as many ions as can be stored in CSR and such an option did not exist.

Table C.2: Absolute MBRC scaling uncertainty budget. See text for definition of the individual uncertainties.

Uncertainty origin	Variable	Uncertainty type	Relative value (%)
model for pickup voltage integral	Q	sys	11.9
electron density	n_e	sys	8.2
current pickup system capacity	C_p	sys	5.0
pickup amplifier gain	G	sys	5.0
imperfect bunching	f_b	sys	2.7
residual gas induced rate	$R_\mathrm{ref} - R_\mathrm{dark}$	stat	2.6
ion-electron beam overlap	f_a	sys	2.5
electron induced relative rate	ρ	stat	1.7
effective cooler length	l_e	sys	1.5
NICE detection efficiency	η	stat	1.1
total uncertainty	α_mb		17

The second most important contribution stems from the determination of the electron density, resulting from the effective cathode radius uncertainty. As discussed in chapter 4.2.1, the deviation between two independent measurements at different Faraday cups is the origin of this estimated uncertainty. For absolute rate coefficient measurements it seems worthwhile to follow these discrepancies. Moreover, the assumption of a constant density electron beam is not completely valid (see chapter 4.2.1). Here, an optimization of the electron beam properties by the adjustment of the electron gun electrodes provides a possible improvement option.

Even though the pickup system capacity uncertainty seems to be almost negligible compared to the latter two, it should be mentioned that the uncertainty estimate here is quite vague. The capacity was measured already four years ago and is expected to change in cryogenic conditions. In future, a more reliable estimate could be obtained by measuring the system capacity always when the CSR is warmed up to room temperature. Furthermore, relative changes of the capacity, e. g., when cooling down the storage ring, can be followed in a resonance circuit measurement, which is planned for future beamtimes.

Despite its negligible influence on the uncertainty budget for the rate coefficient at $E_\mathrm{d} = 0\,\mathrm{eV}$, a special role is dedicated to the detection efficiency η. It was measured precisely for a few detuning energies in chapter 5.4 and was interpolated to the full range of E_d. In principle, $\eta(E_\mathrm{d})$ may scatter in the interpolated regions (Figure 5.9) due to changes in final DR channel branching ratios. However, considering the fact that $0.6174 < \eta < 0.8536$ (see chapter 5.4) are the extreme limits, the deviations between its real value and the interpolated curve are expected to be below 10%. Due to the complex nature of this uncertainty, it is not included in results for the measured rate

coefficient in chapter 6. Even when propagating the conservative uncertainty limit of 10% globally into the total rate coefficient uncertainty $\alpha_{\mathrm{mb}}(E_{\mathrm{d}})$, the latter would not exceed 20%.

Scaling of relative rate coefficients

Following the previous considerations, the absolute scaling procedure for the high density data is straight-forward. The relative rate coefficient, obtained with the procedure described in section C.1.3, is scaled such that its value in the same storage time and detuning energy interval $\alpha_{\mathrm{mb}}(0\,\mathrm{eV}, 21-40\,\mathrm{s})$ is similar to the absolute calibration run. The statistical uncertainty of this scaling amounts only to 0.1% and can be neglected.

For the low-density data, the 0 eV rate coefficient at similar storage times can deviate from the high-density data because of its different rotational state composition, resulting from inelastic electron collisions (chapter 5.5). Thus, a different approach was chosen for absolute scaling. At high detuning energies ($E_{\mathrm{d}} \approx 1\,\mathrm{eV}$), exceeding rotational energies by far, DR resonances are typically broad and result from electronic couplings to *core-excited states* (chapter 2.1.3). Here, the cross section can be assumed to be independent of rotational states and a scaling of the low-density to the high-density data is justified.

For the sake of increasing statistics, an average over all storage times was built for both data sets. The low-density data were scaled such that both integrals in the detuning energy interval $E_{\mathrm{d}} = 0.67 - 1.23\,\mathrm{eV}$ match. The relative statistical uncertainty, arising from the both integrals, amounts to 3.3%. Error propagation into the absolute scaling uncertainty of 17% only affects the result on the third digit and can therefore be neglected.

C.2 Final state branching ratio correction for angular data cuts and 2D imaging extension

The here presented analysis steps are needed for the determination of DR final channel branching ratios in chapter 7.5.1. As introduced there, two corrections need to be applied to the measured intensities: An intensity correction by the angular range that could not be detected and the determination of the C(^{3}P^o) channel branching ratio for $E_\mathrm{d} = 320\,\mathrm{meV}$ by 2D imaging.

For the calculation of branching ratios, the C(^{1}S) and C(^{5}S^o) intensities are simplified in the variable I_S and the C(^{1}D) intensity is denoted as I_D. This is justified because in all distributions either the C(^{1}S) or the C(^{5}S^o) channel has been observed, resulting in a two-channel system. First, the systematic and statistical uncertainties are added in square to derive the total uncertainties ΔI_S and ΔI_D. The ratio of both intensities is given by

$$R = \frac{I_\mathrm{S}}{I_\mathrm{D}} \tag{C.33}$$

$$\frac{\Delta R}{R} = \sqrt{\left(\frac{\Delta I_\mathrm{S}}{I_\mathrm{S}}\right)^2 + \left(\frac{\Delta I_\mathrm{D}}{I_\mathrm{D}}\right)^2} \tag{C.34}$$

and the branching ratios of the two channels can be trivially calculated as

$$B_\mathrm{S} = \frac{1}{1 + R^{-1}} \tag{C.35}$$

$$\Delta B_\mathrm{S} = \frac{\Delta R}{R}\frac{R}{(1+R)^2} \tag{C.36}$$

$$B_\mathrm{D} = 1 - B_\mathrm{S} \tag{C.37}$$

$$\Delta B_\mathrm{D} = \Delta B_\mathrm{S} \tag{C.38}$$

The resulting branching ratios for the C(^{1}S) channel are presented in Figure 7.7 as blue points. Here, the detection limit of the 320 meV point was estimated to 1%.

A major complication to be considered at this point is that the intensities were derived from the effective-KER distributions, which are filtered on certain angular ranges (see section 7.2). Since different channels can, in principle, underlie quite different angular distributions, the angular filters might artificially enhance or suppress the intensity of certain channels relative to the others. Assuming an angular distribution according to equation 7.4, the fraction remaining after the angular filter $([\vartheta_0, \vartheta_1] \cup [180° - \vartheta_1, 180° - \vartheta_0])$ can be calculated to

$$\begin{aligned} I_\mathrm{rel}(\vartheta_0, \vartheta_1, a_2) = &\frac{1}{\pi(1 + a_2/4)}\Bigg(2\vartheta_1 - 2\vartheta_0 \\ &+ \frac{a_2}{2}(\vartheta_1 - \vartheta_0 + 3\sin\vartheta_1\cos\vartheta_1 - 3\sin\vartheta_0\cos\vartheta_0)\Bigg) \end{aligned} \tag{C.39}$$

This relative intensity does not depend on a_1 because the corresponding terms are averaged out by symmetrically integrating over both halves of the angular distribution. However, for the angular ranges used in chapter 7, the dependence on a_2 is quite strong. Especially low values of $a_2 = -1$ result in about 83% of the signal hidden in the filtered out part of the angular distribution, while it is only around 30% for $a_2 = 2$. Thus, for precise derivation of the branching ratios, knowledge about the a_2 parameter for both channels is required and the measured integral ratio has to be corrected by:

$$R_{\mathrm{corr}} = \frac{I_{\mathrm{S}} C_{\mathrm{S}}}{I_{\mathrm{D}} C_{\mathrm{D}}} \tag{C.40}$$

where $C_{\mathrm{S}} = 1/I_{\mathrm{rel,S}}$ and $C_{\mathrm{D}} = 1/I_{\mathrm{rel,D}}$ for the respective channels.

The correction factors C_{S} and C_{D} and their uncertainties can be evaluated for $E_{\mathrm{d}} = 0\,\mathrm{meV}$ and $E_{\mathrm{d}} = 8\,\mathrm{meV}$ from the a_2 values in Table 7.2. However, for the two higher energies only the C(^{1}D) anisotropy parameter can be limited by the measurement, while for the secondary channels the full span $-1 < a_2 < 2$ has to be considered. $a_2 = 0$ was chosen as most probable value. With equation C.39 the most probable values C_n and their upper and lower uncertainties $\Delta_{\mathrm{high}} C_n$ and $\Delta_{\mathrm{low}} C_n$ were obtained and can be propagated to the uncertainty of R_{corr} by:

$$\frac{\Delta_{\mathrm{high}} R_{\mathrm{corr}}}{R_{\mathrm{corr}}} = \sqrt{\left(\frac{\Delta I_{\mathrm{S}}}{I_{\mathrm{S}}}\right)^2 + \left(\frac{\Delta I_{\mathrm{D}}}{I_{\mathrm{D}}}\right)^2 + \left(\frac{\Delta_{\mathrm{high}} C_{\mathrm{S}}}{I_{\mathrm{S}}}\right)^2 + \left(\frac{\Delta_{\mathrm{low}} C_{\mathrm{D}}}{I_{\mathrm{D}}}\right)^2} \tag{C.41}$$

$$\frac{\Delta_{\mathrm{low}} R_{\mathrm{corr}}}{R_{\mathrm{corr}}} = \sqrt{\left(\frac{\Delta I_{\mathrm{S}}}{I_{\mathrm{S}}}\right)^2 + \left(\frac{\Delta I_{\mathrm{D}}}{I_{\mathrm{D}}}\right)^2 + \left(\frac{\Delta_{\mathrm{low}} C_{\mathrm{S}}}{I_{\mathrm{S}}}\right)^2 + \left(\frac{\Delta_{\mathrm{high}} C_{\mathrm{D}}}{I_{\mathrm{D}}}\right)^2} \tag{C.42}$$

With equations C.35-C.38 the corrected branching ratio $B_{n,\mathrm{corr}}$ and its upper and lower uncertainty can be calculated by replacing R by R_{corr}.

The second correction to be applied is only relevant for the $E_{\mathrm{d}} = 320\,\mathrm{meV}$ case. The TSR experiment (see Table 2.4) did not observe any other final channels than C(^{1}S), C(^{1}D) and C(^{3}P) for detuning energies up to 280 meV. However, the slightly higher energy addressed here might open up new channels already, which have been detected at TSR only at $\approx 1\,\mathrm{eV}$. Judging by the measured KERs in the table, the next higher C(^{3}P^o) channels should become accessible at $E_{\mathrm{d}} = 300\,\mathrm{meV}$. Since 3D imaging is not able to detect correspondingly low KERs at $E_{\mathrm{d}} = 320\,\mathrm{meV}$, 2D imaging (see chapter 4.4.2) has to be used as complementary method to clarify the branching ratio of the C(^{3}P^o) channel.

The 2D distance distribution for $E_{\mathrm{d}} = 320\,\mathrm{meV}$ is presented in Figure C.4. Here, a clear signal at distances up to 6 mm becomes visible that can be attributed to the C(^{3}P^o) channel. The broad signal peaking at high distances around 60 mm is arising from the combined C(^{1}D) and C(^{5}S^o) channel. On the first sight, the signal visible at 12 mm seems puzzling because no channel is expected between the C(^{5}S^o) and C(^{3}P^o) channels (see Figure 2.4). Considering the fact that a small population of the metastable

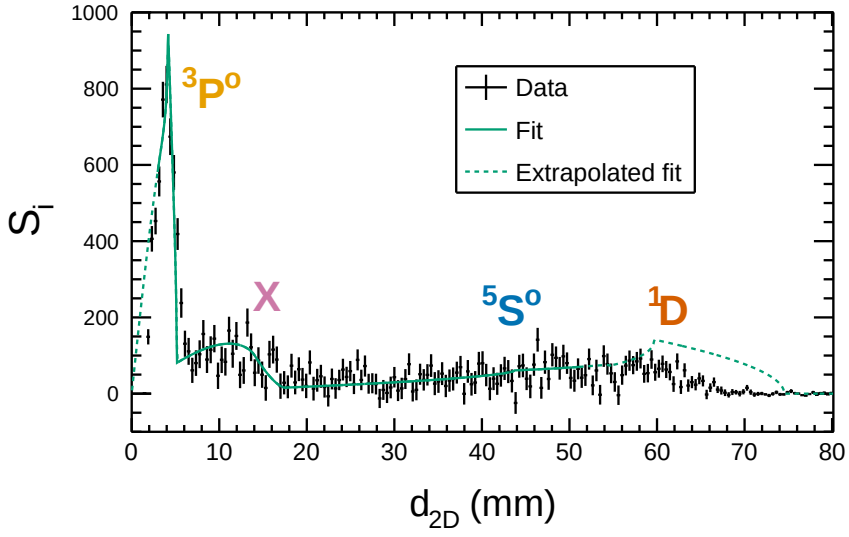

Figure C.4: Fitted 2D distance distribution for $E_d = 320\,\text{meV}$. Four channels were included in the fit, corresponding to the carbon state dissociation limits indicated at the peak positions. Here, the KER values of the C($^5S^o$) and C(^1D) channels were fixed to the fit results in Figure 7.4 a). The channel labeled as 'X' can be attributed to the metastable state and the signal from the region outside the drift-tube (see text) and is not considered further on. The dashed part of the fit function was not used in the fit because it is influenced by detector effects (see Figure 7.3).

$a^3\Pi$ state is expected (see chapter 5.6), this signal can be attributed to metastable DR. The position coincides with the TSR measurement of the C($^3D^o$) channel in Table 2.5.

Moreover, the electron detuning energy outside the drift-tube section was set to $E_d \approx 1.1\,\text{eV}$. In contrast to the high rate at $E_d = 0\,\text{meV}$, at $E_d = 320\,\text{meV}$ the recombination cross section outside the drift-tubes is comparably high to the interaction zone (see Figure 7.4 b)). The higher electron energy in this region shifts the C($^3P^o$) and other channels, which are closed at $E_d = 320\,\text{meV}$, towards higher distances. Hence, the signal at 12 mm (labeled as 'X') might be attributed to both, metastable DR and contributions from outside the drift-tubes. For completeness, it should be mentioned that the latter also influences the rate coefficient results in chapter 6 but is considered in the deconvolution procedure and, thus, does neither distort the intermediately calculated cross section nor the final plasma rate coefficient results.

In order to estimate the branching ratio into the C($^3P^o$) channel from Figure C.4, the experimental data were modeled by a four channel fit function, where the individual channels are described by equation 4.80. The result is drawn into the figure as green line, where the regions outside the chosen fit range (see Figure 7.3) are marked as dashed line. For the fit, the integral ratio of the C($^5S^o$) and the C(^1D) channel was fixed to possible values of R_{corr} from the previous 3D imaging analysis. Furthermore, the anisotropy parameters of those channels were fixed. Fits for different values of a_2

and R_{corr} for the two high energy channels allow to obtain uncertainty estimates.

The main result of the fit is the parameter R_{P}, which describes the integral ratio of the C(^{3}P^o) to the C(^{1}D) channel. It can be trivially propagated into the C(^{3}P^o) branching ratio

$$B_{\mathrm{P}} = \frac{R_{\mathrm{P}}}{1 + R_{\mathrm{P}} + R_{\mathrm{corr}}} \tag{C.43}$$

Its uncertainty is dominated by the different values of the above mentioned, fixed input parameters. Altogether, the branching ratio is given by

$$B_{\mathrm{P}} = 0.37 \pm 0.07 \tag{C.44}$$

Figure C.4 reveals that the C(^{3}P^o) peak is rather poorly described by the fit. Especially the right edge of the fit function is much sharper than the data indicate. At these low KERs of around 20 meV, the finite electron energy resolution is expected to broaden the peak. Moreover, rotational energies are on the same order as the observed KER and lead to a similar effect. An inclusion of both effects is possible and has been applied for precision measurements on the DR of TiO^+ ions in Jain 2020. However, the required analysis steps fall out of the scope of this work. In case of the $E_{\mathrm{d}} = 320$ meV C(^{3}P^o) branching ratio, the introduced uncertainty by the less precise fit in Figure C.4 can be neglected compared to the uncertainties arising from the choice of fixed input parameters.

With the knowledge of B_{P}, the remaining branching ratio has to be split among the C(^{5}S^o) and C(^{1}D) channel such that their ratio R_{corr} from the 3D imaging analysis remains. This is done via

$$B_{\mathrm{S}} = \frac{R_{\mathrm{corr}}}{1 + R_{\mathrm{corr}}}(1 - B_{\mathrm{P}}) \tag{C.45}$$

$$B_{\mathrm{D}} = \frac{1}{1 + R_{\mathrm{corr}}}(1 - B_{\mathrm{P}}) \tag{C.46}$$

Hereby, the uncertainty of B_{P} and asymmetric uncertainty from R_{corr} were propagated to the branching ratio results (Table 7.3).

Bibliography

Alman, D. A., D. N. Ruzic, and J. N. Brooks (2000). 'A hydrocarbon reaction model for low temperature hydrogen plasmas and an application to the Joint European Torus.' In: *Physics of Plasmas* 7 (5), pp. 1421–1432. DOI: 10.1063/1.873960.

Amitay, Z., D. Zajfman, P. Forck, U. Hechtfischer, M. Grieser, D. Habs, D. Schwalm, and A. Wolf (1997). 'Electron impact dissociation of cold CH^+: Cross sections and branching ratios.' In: *AIP Conference Proceedings* 392 (1), pp. 51–54. DOI: 10.1063/1.52513.

Amitay, Z., D. Zajfman, P. Forck, U. Hechtfischer, B. Seidel, M. Grieser, D. Habs, R. Repnow, D. Schwalm, and A. Wolf (1996). 'Dissociative recombination of CH^+: Cross section and final states.' In: *Physical Review A* 54 (5), pp. 4032–4050. DOI: 10.1103/PhysRevA.54.4032.

Bates, D. R. (1950). 'Dissociative Recombination.' In: *Physical Review* 78 (4), pp. 492–493. DOI: 10.1103/PhysRev.78.492.

Becker, A. (2016). 'Imaging of Neutral Fragmentation Products from Fast Molecular Ion Beams: Paving the Way for Reaction Studies in Cryogenic Environment.' PhD thesis. Ruprecht-Karls-Universität Heidelberg. DOI: 10.11588/heidok.00020213.

Benz, A. O., S. Bruderer, E. F. van Dishoeck, P. Stäuber, and S. F. Wampfler (2013). 'Neutral and Ionized Hydrides in Star-Forming Regions. Observations with Herschel/HIFI.' In: *The Journal of Physical Chemistry A* 117 (39), pp. 9840–9847. DOI: 10.1021/jp312813a.

Beutelspacher, M., M. Grieser, K. Noda, D. Schwalm, and A. Wolf (2003). 'Dispersive electron cooling experiments at the heavy ion storage ring TSR.' In: *Nuclear Instruments and Methods in Physics Research Section A: Accelerators, Spectrometers, Detectors and Associated Equipment* 512 (3), pp. 459–469. DOI: 10.1016/S0168-9002(03)01976-4.

Bishop, D. M. and S.-k. Shih (1976). 'An effective Schrödinger equation for the rovibronic energies of H_2 and D_2.' In: *The Journal of Chemical Physics* 64 (1), pp. 162–169. DOI: 10.1063/1.431967.

Budker, G. I. (1967). 'An effective method of damping particle oscillations in proton and antiproton storage rings.' In: *Soviet Atomic Energy* 22, pp. 438–440. DOI: 10.1007/BF01175204.

Carata, L., A. E. Orel, M. Raoult, I. F. Schneider, and A. Suzor-Weiner (2000). 'Core-excited resonances in the dissociative recombination of CH^+ and CD^+.' In: *Physical Review A* 62 (5), p. 052711. DOI: 10.1103/PhysRevA.62.052711.

Chakrabarti, K., A. Dora, R. Ghosh, B. S. Choudhury, and J. Tennyson (2017). 'R-matrix study of electron impact excitation and dissociation of CH^+ ions.' In: *Journal of Physics B: Atomic, Molecular and Optical Physics* 50 (17), p. 175202. DOI: 10.1088/1361-6455/aa8377.

Chakrabarti, K., R. Ghosh, and B. S. Choudhury (2019). 'R-matrix calculation of bound and continuum states of CH.' In: *Journal of Physics B: Atomic, Molecular and Optical Physics* 52 (10), p. 105205. DOI: 10.1088/1361-6455/ab121f.

Chakrabarti, K., J. Z. Mezei, O. Motapon, A. Faure, O. Dulieu, K. Hassouni, and I. F. Schneider (2018). 'Dissociative recombination of the CH^+ molecular ion at low energy.' In: *Journal of Physics B: Atomic, Molecular and Optical Physics* 51 (10), p. 104002. DOI: 10.1088/1361-6455/aab937.

Cheng, M., J. M. Brown, P. Rosmus, R. Linguerri, N. Komiha, and E. G. Myers (2007). 'Dipole moments and orientation polarizabilities of diatomic molecular ions for precision atomic mass measurement.' In: *Physical Review A* 75 (1), p. 012502. DOI: 10.1103/PhysRevA.75.012502.

Child, C. D. (1911). 'Discharge From Hot CaO.' In: *Physical Review (Series I)* 32 (5), pp. 492–511. DOI: 10.1103/PhysRevSeriesI.32.492.

Čurík, R., D. Hvizdoš, and C. H. Greene (2020). 'Dissociative Recombination of Cold HeH^+ Ions.' In: *Physical Review Letters* 124 (4), p. 043401. DOI: 10.1103/PhysRevLett.124.043401.

Davies, J. A., R. E. Continetti, D. W. Chandler, and C. C. Hayden (2000). 'Femtosecond Time-Resolved Photoelectron Angular Distributions Probed during Photodissociation of NO_2.' In: *Physical Review Letters* 84 (26), pp. 5983–5986. DOI: 10.1103/PhysRevLett.84.5983.

Dikansky, N. S., V. I. Kudelainen, V. A. Lebedev, I. N. Meshkov, V. V. Parkhomchuk, A. A. Sery, A. N. Skrinsky, and B. N. Sukhina (1988). *Ultimate possibilities of electron cooling*. Tech. rep. 88-61. Budker INP.

Doménech, J. L., P. Jusko, S. Schlemmer, and O. Asvany (2018). 'The First Laboratory Detection of Vibration-rotation Transitions of $^{12}CH^+$ and $^{13}CH^+$ and Improved Measurement of Their Rotational Transition Frequencies.' In: *The Astrophysical Journal* 857 (1), p. 61. DOI: 10.3847/1538-4357/aab36a.

Douglas, A. E. and G. Herzberg (1941). 'Note on CH^+ in Interstellar Space and in the Laboratory.' In: *The Astrophysical Journal* 94, p. 381. DOI: 10.1086/144342.

Draine, B. T. and N. Katz (1986). 'Magnetohydrodynamic Shocks in Diffuse Clouds. II. Production of CH^+, OH, CH, and Other Species.' In: *The Astrophysical Journal* 310, p. 392. DOI: 10.1086/164693.

Dunham, T. (1937). 'Interstellar Neutral Potassium and Neutral Calcium.' In: *The Astronomical Society of the Pacific* 49 (287), pp. 26–28. DOI: 10.1086/124759.

Dunn, G. H. (1962). 'Anisotropies in Angular Distributions of Molecular Dissociation Products.' In: *Physical Review Letters* 8 (2), pp. 62–64. DOI: 10.1103/PhysRevLett.8.62.

Fadil, H., M. Grieser, D. Orlov, and A. Wolf (2006). 'Design of a low energy electron cooler for the Heidelberg CSR.' In: *Conference Proceedings C* 060626, pp. 1630–1632.

Faure, A., V. Kokoouline, C. H. Greene, and J. Tennyson (2006). 'Near-threshold rotational excitation of molecular ions by electron impact.' In: *Journal of Physics B: Atomic, Molecular and Optical Physics* 39 (20), pp. 4261–4273. DOI: 10.1088/0953-4075/39/20/023.

Faure, A. et al. (2017). 'State-to-state chemistry and rotational excitation of CH^+ in photon-dominated regions.' In: *Monthly Notices of the Royal Astronomical Society* 469 (1), pp. 612–620. DOI: 10.1093/mnras/stx892.

Florescu-Mitchell, A. I. and J. B. A. Mitchell (2006). 'Dissociative recombination.' In: *Physics Reports* 430 (5), pp. 277–374. DOI: 10.1016/j.physrep.2006.04.002.

Forck, P., M. Grieser, D. Habs, A. Lampert, R. Repnow, D. Schwalm, A. Wolf, and D. Zajfman (1993). 'Dissociative recombination of cold HD^+ at the Test Storage Ring.' In: *Physical Review Letters* 70 (4), pp. 426–429. DOI: 10.1103/PhysRevLett.70.426.

Foreman-Mackey, D., D. W. Hogg, D. Lang, and J. Goodman (2013). 'emcee: The MCMC Hammer.' In: *Publications of the Astronomical Society of the Pacific* 125 (925), pp. 306–312. DOI: 10.1086/670067.

Fraser, G. W., J. F. Pearson, and J. E. Lees (1987). 'Dark noise in microchannel plate X-ray detectors.' In: *Nuclear Instruments and Methods in Physics Research Section A: Accelerators, Spectrometers, Detectors and Associated Equipment* 254 (2), pp. 447–462. DOI: 10.1016/0168-9002(87)90699-1.

Gamer, L., D. Schulz, C. Enss, A. Fleischmann, L. Gastaldo, S. Kempf, C. Krantz, O. Novotný, D. Schwalm, and A. Wolf (2016). 'MOCCA: A 4k-Pixel Molecule Camera for the Position- and Energy-Resolving Detection of Neutral Molecule Fragments at CSR.' In: *Journal of Low Temperature Physics* 184 (3), pp. 839–844. DOI: 10.1007/s10909-015-1453-0.

Gao, H. and C. H. Greene (1990). 'Alternative vibrational frame transformation for electron-molecule scattering.' In: *Physical Review A* 42 (11), pp. 6946–6949. DOI: 10.1103/PhysRevA.42.6946.

Gaspard, D. (2018). 'Connection formulas between Coulomb wave functions.' In: *Journal of Mathematical Physics* 59 (11), p. 112104. DOI: 10.1063/1.5054368.

Gerlich, D., R. Disch, and S. Scherbarth (1987). '$C^+ + H_2(j) \rightarrow CH^+ + H$: The effect of reagent rotation on the integral cross section in the threshold region.' In: *The Journal of Chemical Physics* 87 (1), pp. 350–359. DOI: 10.1063/1.453580.

Giusti-Suzor, A., J. N. Bardsley, and C. Derkits (1983). 'Dissociative recombination in low-energy e-H_2^+ collisions.' In: *Physical Review A* 28 (2), pp. 682–691. DOI: 10.1103/PhysRevA.28.682.

Grussie, F. (2016). 'Experimental studies of ion-neutral reactions under astrophysical conditions.' PhD thesis. Ruprecht-Karls-Universität Heidelberg. DOI: 10.11588/heidok.00021435.

Guberman, S. L. (2004). 'Product angular distributions in dissociative recombination.' In: *The Journal of Chemical Physics* 120 (20), pp. 9509–9513. DOI: 10.1063/1.1698648.

Guberman, S. L. (2005). 'Dissociative recombination angular distributions.' In: *Journal of Physics: Conference Series* 4 (008), pp. 58–65. DOI: 10.1088/1742-6596/4/1/008.

Hakalla, R., R. Kepa, W. Szajna, and M. Zachwieja (2006). 'New analysis of the Douglas-Herzberg system ($A^1\Pi$-$X^1\Sigma^+$) in the CH^+ ion radical.' In: *The European Physical Journal D - Atomic, Molecular, Optical and Plasma Physics* 38 (3), pp. 481–488. DOI: 10.1140/epjd/e2006-00063-9.

Haken, H. and H. C. Wolf (1992). *Molekülphysik und Quantenchemie*. 5th ed. Springer-Verlag. DOI: 10.1002/bbpc.19930971248.

Hamilton, J. R., A. Faure, and J. Tennyson (2015). 'Electron-impact excitation of diatomic hydride cations – I. HeH^+, CH^+, ArH^+.' In: *Monthly Notices of the Royal Astronomical Society* 455 (3), pp. 3281–3287. DOI: 10.1093/mnras/stv2429.

Hechtfischer, U., J. Rostas, M. Lange, J. Linkemann, D. Schwalm, R. Wester, A. Wolf, and D. Zajfman (2007). 'Photodissociation spectroscopy of stored CH^+ and CD^+ ions: Analysis of the $b^3\Sigma^-$-$a^3\Pi$ system.' In: *The Journal of Chemical Physics* 127 (20), p. 204304. DOI: 10.1063/1.2800004.

Hechtfischer, U., C. J. Williams, M. Lange, J. Linkemann, D. Schwalm, R. Wester, A. Wolf, and D. Zajfman (2002). 'Photodissociation spectroscopy of stored CH^+ ions: Detection, assignment, and close-coupled modeling of near-threshold Feshbach resonances.' In: *The Journal of Chemical Physics* 117 (19), pp. 8754–8777. DOI: 10.1063/1.1513459.

Herzberg, G. (1950). *Spectra of Diatomic Molecules*. 2nd ed. Van Nostrand Company.

Hilborn, R. C. (1982). 'Einstein coefficients, cross sections, f values, dipole moments, and all that.' In: *American Journal of Physics* 50 (11), pp. 982–986. DOI: 10.1119/1.12937.

Hinterberger, F. (2008). *Physik der Teilchenbeschleuniger und Ionenoptik*. 2nd ed. Springer. DOI: 10.1007/978-3-540-75282-0.

Hogg, D. W. and D. Foreman-Mackey (2018). 'Data Analysis Recipes: Using Markov Chain Monte Carlo.' In: *The Astrophysical Journal Supplement Series* 236 (1), p. 11. DOI: 10.3847/1538-4365/aab76e.

Hunt, J. R., J. Resta-López, C. P. Welsch, C. Carli, B. Dupuy, and D. Gamba (2020). 'Novel transverse emittance measurements for electron cooling characterization.'

In: *Physical Review Accelerators and Beams* 23 (3), p. 032802. DOI: 10.1103/PhysRevAccelBeams.23.032802.

Hvizdoš, D., C. H. Greene, and R. Čurík (2020). 'Backpropagated frame transformation theory: A reformulation.' In: *Physical Review A* 101 (1), p. 012709. DOI: 10.1103/PhysRevA.101.012709.

Jäger, J. (2021). 'Implementation of a new setup for improved 3D imaging of neutral fragments at the Cryogenic Storage Ring.' Preliminary title - in preparation. MA thesis. Ruprecht-Karls-Universität Heidelberg.

Jain, N. (2020). 'Electron Recombination Studies on Titanium Oxide Ions in the Cryogenic Storage Ring at the Max Planck Institute for Nuclear Physics, Heidelberg.' MA thesis. Indian Institute of Space Science and Technology, Thiruvananthapuram, India.

Jansen, G. H. (1990). *Coulomb interactions in particle beams*. Boston: Acedemic Press.

Kálosi, Á. et al. (2021). 'Laser probing of rotational cooling by inelastic electron collisions with molecular ions.' In preparation.

Krantz, C. (2009). 'Intense Electron Beams from GaAs Photocathodes as a Tool for Molecular and Atomic Physics.' PhD thesis. Ruprecht-Karls-Universität Heidelberg. DOI: 10.11588/heidok.00010009.

Kudelainen, V. I., V. A. Lebedev, I. N. Meshkov, V. V. Parkhomochuk, and B. N. Sukhina (1982). 'Temperature relaxation in a magnetized electron beam.' In: *Soviet Physics JETP* 56 (6), pp. 1191–1196.

Larsson, M. (2005). 'Molecular ion recombination in merged beams: experimental results on small systems and future perspectives.' In: *Journal of Physics: Conference Series* 4 (007), pp. 50–57. DOI: 10.1088/1742-6596/4/1/007.

Lepp, S., P. C. Stancil, and A. Dalgarno (2002). 'Atomic and molecular processes in the early Universe.' In: *Journal of Physics B: Atomic, Molecular and Optical Physics* 35 (10), R57–R80. DOI: 10.1088/0953-4075/35/10/201.

Lion, J. (2015). 'Das mit Flüssigneon gekühlte supraleitende Magnetsystem des Elektronenkühlers am kryogenen Ionen-Speicherring CSR.' BA Thesis. Ruprecht-Karls-Universität Heidelberg.

Lippmann, B. A. and J. Schwinger (1950). 'Variational Principles for Scattering Processes. I.' In: *Physical Review* 79 (3), pp. 469–480. DOI: 10.1103/PhysRev.79.469.

Lohmann, S. (2015). 'Beam diagnostics and collector for the electron cooler of the cryogenic storage ring CSR.' MA thesis. Ruprecht-Karls-Universität Heidelberg.

McCall, B. J. (2001). 'Spectroscopy of H_3^+ in Laboratory and Astrophysical Plasmas.' PhD thesis. The University of Chicago.

McEwan, M. J., G. B. I. Scott, N. G. Adams, L. M. Babcock, R. Terzieva, and E. Herbst (1999). 'New H and H_2 Reactions with Small Hydrocarbon Ions and Their Roles in Benzene Synthesis in Dense Interstellar Clouds.' In: *The Astrophysical Journal* 513 (1), pp. 287–293. DOI: 10.1086/306861.

McGuire, B. A. (2018). '2018 Census of Interstellar, Circumstellar, Extragalactic, Protoplanetary Disk, and Exoplanetary Molecules.' In: *The Astrophysical Journal Supplement Series* 239 (2), p. 17. DOI: 10.3847/1538-4365/aae5d2.

Meyer, C. (2018). 'The lowest rotational quantum states of the hydroxyl anions probed by electron photodetachment in a cryogenic storage ring.' PhD thesis. Ruprecht-Karls-Universität Heidelberg. DOI: 10.11588/heidok.00024388.

Meyer, C. et al. (2017). 'Radiative Rotational Lifetimes and State-Resolved Relative Detachment Cross Sections from Photodetachment Thermometry of Molecular Anions in a Cryogenic Storage Ring.' In: *Physical Review Letters* 119 (2), p. 023202. DOI: 10.1103/PhysRevLett.119.023202.

Mezei, Z. J., M. D. Epée Epée, O. Motapon, and I. F. Schneider (2019). 'Dissociative Recombination of CH^+ Molecular Ion Induced by Very Low Energy Electrons.' In: *Atoms* 7 (3), p. 82. DOI: 10.3390/atoms7030082.

Mitchell, J. B. A. and J. W. McGowan (1978). 'The Dissociative Recombination of CH^+ $X^1\Sigma^+(v = 0)$.' In: *The Astrophysical Journal Letters* 222, p. L77. DOI: 10.1086/182696.

Mul, P. M., J. B. A. Mitchell, V. S. D'Angelo, P. Defrance, J. W. McGowan, and H. R. Froelich (1981). 'Merged electron-ion beam experiments. IV. Dissociative recombination for the methane group CH^+,...,CH^{5+}.' In: *Journal of Physics B: Atomic and Molecular Physics* 14 (8), pp. 1353–1361. DOI: 10.1088/0022-3700/14/8/020.

Myers, A. T., C. F. McKee, and P. S. Li (2015). 'The CH^+ abundance in turbulent, diffuse molecular clouds.' In: *Monthly Notices of the Royal Astronomical Society* 453 (3), pp. 2747–2758. DOI: 10.1093/mnras/stv1782.

Novotny, S. (2004). 'Fast-beam molecular fragmentation imaging using a high-speed gated camera system.' Diploma thesis. Ruprecht-Karls-Universität Heidelberg.

Novotny, S. (2008). 'Fragmentation of molecular ions in slow electron collisions.' PhD thesis. Ruprecht-Karls-Universität Heidelberg. DOI: 10.11588/heidok.00011597.

Novotný, O. et al. (2010). 'Fragmentation Channels in Dissociative Electron Recombination with Hydronium and Other Astrophysically Important Species.' In: *The Journal of Physical Chemistry A* 114 (14), pp. 4870–4874. DOI: 10.1021/jp9104097.

Novotný, O. et al. (2013). 'Dissociative Recombination Measurements of HCl^+ using an Ion Storage Ring.' In: *The Astrophysical Journal* 777 (1), p. 54. DOI: 10.1088/0004-637x/777/1/54.

Novotný, O. et al. (2015). 'Cryogenic micro-calorimeters for mass spectrometric identification of neutral molecules and molecular fragments.' In: *Journal of Applied Physics* 118 (10), p. 104503. DOI: 10.1063/1.4930036.

Novotný, O. et al. (2019). 'Quantum-state–selective electron recombination studies suggest enhanced abundance of primordial HeH^+.' In: *Science* 365 (6454), pp. 676–679. DOI: 10.1126/science.aax5921.

O'Connor, A. P. et al. (2016). 'Photodissociation of an Internally Cold Beam of CH^+ Ions in a Cryogenic Storage Ring.' In: *Physical Review Letters* 116 (11), p. 113002. DOI: 10.1103/PhysRevLett.116.113002.

O'Malley, T. F. and H. S. Taylor (1968). 'Angular Dependence of Scattering Products in Electron-Molecule Resonant Excitation and in Dissociative Attachment.' In: *Physical Review* 176 (1), pp. 207–221. DOI: 10.1103/PhysRev.176.207.

Orlov, D. A., H. Fadil, M. Grieser, and A. Wolf (2006). 'Cold Photocathode Electron Sources and Perspectives for Low-Energy Magnetically Guided Electron Beams.' In: *AIP Conference Proceedings* 862 (1), pp. 274–280. DOI: 10.1063/1.2387933.

Pastuszka, S. et al. (1996). 'Electron cooling and recombination experiments with an adiabatically expanded electron beam.' In: *Nuclear Instruments and Methods in Physics Research Section A: Accelerators, Spectrometers, Detectors and Associated Equipment* 369 (1), pp. 11–22. DOI: 10.1016/0168-9002(95)00786-5.

Plasil, R., T. Mehner, P. Dohnal, T. Kotrik, J. Glosik, and D. Gerlich (2011). 'Reactions of cold trapped CH^+ ions with slow H atoms.' In: *The Astrophysical Journal* 737 (2), p. 60. DOI: 10.1088/0004-637x/737/2/60.

Plašil, R., P. Dohnal, Á. Kálosi, Š. Roučka, D. Shapko, S. Rednyk, R. Johnsen, and J. Glosík (2018). 'Stationary afterglow apparatus with CRDS for study of processes in plasmas from 300 K down to 30 K.' In: *Review of Scientific Instruments* 89 (6), p. 063116. DOI: 10.1063/1.5036834.

Plašil, R., S. Rednyk, A. Kovalenko, T. D. Tran, Š. Roučka, P. Dohnal, O. Novotný, and J. Glosík (2021). 'Experimental Study on CH^+ Formation from Doubly Charged Carbon and Molecular Hydrogen.' In: *The Astrophysical Journal* 910 (2), p. 155. DOI: 10.3847/1538-4357/abe86c.

Poth, H. (1990). 'Electron cooling: Theory, experiment, application.' In: *Physics Reports* 196 (3-4), pp. 135–297. DOI: 10.1016/0370-1573(90)90040-9.

Rimmler, M. M. (2017). 'Operating a low-energy Electron Cooler at the Cryogenic Storage Ring CSR.' MA thesis. Ruprecht-Karls-Universität Heidelberg.

Sakurai, J. J. (1994). *Modern Quantum Mechanics*. Ed. by S. F. Tuan. 1st ed. Addison-Wesley Publishing Company. DOI: 10.1017/9781108499996.

Saurabh, S. (2019). 'Collision studies with internally cold ion beams and merged electron beams in a cryogenic storage ring.' PhD thesis. Ruprecht-Karls-Universität Heidelberg. DOI: 10.11588/heidok.00026791.

Schneider, I. F. and V. Kokoouline (2021). *Private communication*.

Shornikov, A. (2012). 'An electron cooler for ultra-low energy cryogenic operation.' PhD thesis. Ruprecht-Karls-Universität Heidelberg. DOI: 10.11588/heidok.00013459.

Singh, S. (2020). *Private communication*.

Snow, T. P. and B. J. McCall (2006). 'Diffuse Atomic and Molecular Clouds.' In: *Annual Review of Astronomy and Astrophysics* 44 (1), pp. 367–414. DOI: 10.1146/annurev.astro.43.072103.150624.

Spruck, K. et al. (2015). 'An efficient, movable single-particle detector for use in cryogenic ultra-high vacuum environments.' In: *Review of Scientific Instruments* 86 (2), p. 023303. DOI: 10.1063/1.4907352.

Stützel, J. (2011). 'Fragmentation of Small Multi-Electron Molecular Ions in Cold Electron Collisions.' PhD thesis. Ruprecht-Karls-Universität Heidelberg. DOI: 10.11588/heidok.00008531.

Takagi, H., N. Kosugi, and M. Le Dourneuf (1991). 'Dissociative recombination of CH^+.' In: *Journal of Physics B: Atomic, Molecular and Optical Physics* 24 (3), pp. 711–732. DOI: 10.1088/0953-4075/24/3/026.

Tennyson, J. (2010). 'Electron–molecule collision calculations using the R-matrix method.' In: *Physics Reports* 491 (2-3), pp. 29–76. DOI: 10.1016/j.physrep.2010.02.001.

Urbain, X., D. Bech, J.-P. Van Roy, M. Géléoc, S. J. Weber, A. Huetz, and Y. J. Picard (2015). 'A zero dead-time multi-particle time and position sensitive detector based on correlation between brightness and amplitude.' In: *Review of Scientific Instruments* 86 (2), p. 023305. DOI: 10.1063/1.4908597.

Vogel, S. (2016). 'Developments at an Electrostatic Cryogenic Storage Ring for Electron-Cooled keV Energy Ion Beams.' PhD thesis. Ruprecht-Karls-Universität Heidelberg. DOI: 10.11588/heidok.00020262.

von Hahn, R. et al. (2016). 'The cryogenic storage ring CSR.' In: *Review of Scientific Instruments* 87 (6), p. 063115. DOI: 10.1063/1.4953888.

Weigel, U. (2003). 'Cold Intense Electron Beams from Gallium Arsenide Photocathodes.' PhD thesis. Ruprecht-Karls-Universität Heidelberg. DOI: 10.11588/heidok.00004513.

Wilhelm, P. U. (2019). 'First Studies of Low-Energy Electron Cooling of keV Energy Ion Beams at the Electrostatic Cryogenic Storage Ring CSR.' PhD thesis. Ruprecht-Karls-Universität Heidelberg. DOI: 10.11588/heidok.00026821.

Wolfire, M. G. and D. A. Neufeld (2020). *Private communication.*

Zajfman, D., Z. Amitay, C. Broude, P. Forck, B. Seidel, M. Grieser, D. Habs, D. Schwalm, and A. Wolf (1995). 'Measurement of Branching Ratios for the Dissociative Recombination of Cold HD^+ Using Fragment Imaging.' In: *Physical Review Letters* 75 (5), pp. 814–817. DOI: 10.1103/PhysRevLett.75.814.

Zare, R. N. (1967). 'Dissociation of H_2^+ by Electron Impact: Calculated Angular Distribution.' In: *The Journal of Chemical Physics* 47 (1), pp. 204–215. DOI: 10.1063/1.1711847.

Danksagung

Das Zustandekommen der vorliegenden Arbeit verdanke ich einer Vielzahl an Personen, die mich sowohl in der experimentellen Phase als auch bei der Datenanalyse und Verfassen der Thesis wissenschaftlich, organisatorisch und moralisch unterstützt haben. Einen besonderen Dank möchte ich aussprechen an:

Prof. Dr. Andreas Wolf für die überaus engagierte Betreuung der Promotion. Seine visionäre, wissenschaftliche Ader ist stets hilfreich gewesen, bestmögliche Schlüsse aus experimentellen Resultaten zu ziehen. Außerdem möchte ich mich für die Diskussionen über die CH^+ und CH Molekülstruktur bedanken, die nicht nur sehr zu meinem Verständnis beigetragen, sondern auch weitere Nachforschungen auf dem Gebiet motiviert haben.
Dr. Oldřich Novotný für die herausragende Tag-für-Tag Betreuung der Promotion und nahezu ständige Erreichbarkeit. Durch seine pragmatische und durchgehend konstruktive Art und Unterstützung konnten einige problematische Schritte in der Analyse und beim Verfassen der Thesis geschickt gelöst werden. Weiterhin habe ich seine offene Kommunikation und seinen Weitblick für alle Experimente sehr zu schätzen gelernt.
Dr. Ábel Kálosi für die großartige Zusammenarbeit am Elektronenkühler und die Aufgeschlossenheit für Diskussionen jeglicher Art über Experimente, Imagine Analysen und das Duck. Seine Anschauung auf moderne Wissenschaft haben mir sehr weitergeholfen und ich konnte einige statistische Methoden mit seiner Hilfe erlernen und anwenden. Ein großer Dank gilt seinem Humor und Pannenverständnis, die beide den ein oder anderen Arbeitstag gerettet haben.
Dr. Patrick Wilhelm für den besten Mentor, den man sich wünschen kann. Sein offener und demütiger Charakter haben das Einarbeiten in die technische Seite des Elektronenkühlers sehr angenehm gestaltet - ungeachtet der Anzahl an wiederholten Nachfragen. Ein besonderer Dank gebührt seiner Empathie und seinem Humor, die Spaß an der und um die Arbeit herum gefördert haben.
Meine anderen Kollegen (Aigars, Damian, Felix, Julia, Lisa, Leonard, Naman und Viviane) für zahlreiche Mittags- und Eispausen, Gespräche über und fernab der Arbeit. Insbesondere möchte ich bedanken für den Zusammenhalt zu Beginn der

Pandemie, die kreativen Ideen, dennoch gemeinsam Freizeit zu gestalten, und ein paar schöne Wikingerschach-Abende in der (manchmal auch ohne) Sonne. Ich schätze den kollegialen Zusammenhalt, den wir beim Zusammenbau von so einigen Last-Minute-Doktorhüten gezeigt haben.

Das CSR Team für die enge Zusammenarbeit und den ständigen Austausch untereinander. Ein besonderen Dank möchte ich an die Techniker aussprechen, die fortwährend schnelle und unkomplizierte Hilfe geleistet haben. Ohne eine solche Unterstützung wäre das CSR Projekt nicht möglich!

Die Abteilung Blaum für die angenehme Arbeits- und Diskussionsatmosphäre. Lobenswert zu erwähnen ist der Einsatz von Prof. Dr. Klaus Blaum und Gabriele Weese zu Beginn der Pandemie und die Nachfrage nach Unterstützungsbedürfnis bei jedem einzelnen Mitarbeiter.

Meine langjährigen besten Freunde (Anıl, Jan, Marc, Marietta und Ricarda), die mich trotz Einschränkungen durch Thesis und Pandemie weiterhin begleitet und motiviert haben. Jegliche Gespräche und Freizeitgestaltungen haben als Gegenpol zum wissenschaftlichen Arbeiten gedient und mir sehr geholfen, einen freien Kopf zu bewahren.

Meine Schwester für ihre abfärbende positive Art, selbst wenn sie keine gute Laune hat, und für zahlreiche kulinarisch hochwertige Treffen. Großer Dank gilt ihrer stetigen Nachhilfe in badischem Dialekt, der mir die Kommunikation am Institut erleichtert hat. Soooe, weida zum neegschde.

Meine Eltern, die mir in Zeiten der Pandemie und des regelmäßigen Home-Office nicht nur ein zweites Zuhause sondern auch menschliche Nähe geboten haben. Ohne das Abwenden vieler, anderer Pflichten in dieser Zeit sowie ihre organisatorische Unterstützung und Vertrauen wäre das Verfassen der Arbeit erheblich schwerer (und meine Ernährung deutlich ungesünder) ausgefallen.

Allen anderen Bekannten, Freunden und Familienmitgliedern, die ich zuvor nicht erwähnt oder vergessen haben sollte.